

The basic angle monitoring system : picometer stability with silicon carbide optics

Citation for published version (APA):

Veggel, van, A. A. (2007). *The basic angle monitoring system : picometer stability with silicon carbide optics*. [Phd Thesis 1 (Research TU/e / Graduation TU/e), Mechanical Engineering]. Technische Universiteit Eindhoven. <https://doi.org/10.6100/IR621988>

DOI:

[10.6100/IR621988](https://doi.org/10.6100/IR621988)

Document status and date:

Published: 01/01/2007

Document Version:

Publisher's PDF, also known as Version of Record (includes final page, issue and volume numbers)

Please check the document version of this publication:

- A submitted manuscript is the version of the article upon submission and before peer-review. There can be important differences between the submitted version and the official published version of record. People interested in the research are advised to contact the author for the final version of the publication, or visit the DOI to the publisher's website.
- The final author version and the galley proof are versions of the publication after peer review.
- The final published version features the final layout of the paper including the volume, issue and page numbers.

[Link to publication](#)

General rights

Copyright and moral rights for the publications made accessible in the public portal are retained by the authors and/or other copyright owners and it is a condition of accessing publications that users recognise and abide by the legal requirements associated with these rights.

- Users may download and print one copy of any publication from the public portal for the purpose of private study or research.
- You may not further distribute the material or use it for any profit-making activity or commercial gain
- You may freely distribute the URL identifying the publication in the public portal.

If the publication is distributed under the terms of Article 25fa of the Dutch Copyright Act, indicated by the "Taverne" license above, please follow below link for the End User Agreement:

www.tue.nl/taverne

Take down policy

If you believe that this document breaches copyright please contact us at:

openaccess@tue.nl

providing details and we will investigate your claim.

**The Basic Angle Monitoring system:
picometer stability with Silicon Carbide optics**

Mariëlle van Veggel

This research has been conducted in cooperation with TNO Science and Industry and has been financially supported by the Netherlands Agency for Aerospace Programmes (NIVR).

A catalogue record is available from the Library Eindhoven University of Technology.

ISBN-13: 978-90-386-0874-7

Printed by Universiteitsdrukkerij, Technische Universiteit Eindhoven
Cover design by Mariëlle van Veggel
Typeset by the author with Microsoft® Office XP Word.

Copyright © 2007 by Anna-Maria Arnoldina van Veggel

**The Basic Angle Monitoring system:
picometer stability with Silicon Carbide optics**

PROEFSCHRIFT

ter verkrijging van de graad van doctor aan de
Technische Universiteit Eindhoven, op gezag van de
Rector Magnificus, prof.dr.ir. C.J. van Duijn, voor een
commissie aangewezen door het College voor
Promoties in het openbaar te verdedigen
op donderdag 8 maart 2007 om 16.00 uur

door

Anna-Maria Arnoldina van Veggel

geboren te Deurne

Dit proefschrift is goedgekeurd door de promotor:

prof.dr. H. Nijmeijer

Copromotor:

dr.ir. P.C.J.N. Rosielle

Table of contents

Nomenclature	v
1 Introduction	1
1.1 GAIA	1
1.1.1 Goals	1
1.1.2 Satellite general design	2
1.1.3 Basic Angle Monitoring system	4
1.2 Stability	7
1.2.1 Stable environment	7
1.2.2 Stable material	13
1.2.3 Stable opto-thermo-mechanical design	16
1.3 Aim of the thesis	17
1.4 Layout of the thesis	18
2 Silicon Carbide	21
2.1 History of Silicon Carbide	22
2.2 Manufacturing technologies	23
2.2.1 Acheson process	23
2.2.2 Sintered Silicon Carbide	23
2.2.3 Carbon felt Silicon Carbide	25
2.2.4 Chemical Vapour Deposited SiC	27
2.3 Properties of Silicon Carbide	27
2.3.1 Mechanical properties	27
2.3.2 Thermal properties	35
2.3.3 Optical properties	40
2.3.4 Other properties	41
2.4 Mechanical design with Silicon Carbide	41
2.4.1 Manufacturing limitations	42
2.4.2 Manufacturing accuracy	45

2.4.3	Design rules	46
2.4.4	Joining techniques	47
2.5	Conclusions	51
3	Optical design	53
3.1	Interference patterns	54
3.2	Causes for fringe shifts	55
3.3	The optical design	60
3.4	Requirements	62
3.4.1	Choice of the laser source	63
3.4.2	Beam requirements	63
3.4.3	Alignment accuracy and stability	64
3.4.4	Measurement stability	68
3.4.5	Stringency of stability	69
3.5	Alignment plan	70
3.5.1	Coarse alignment	71
3.5.2	Alignment possibilities	71
3.5.3	Alignment steps	73
3.6	Summary	74
4	Optical benches	77
4.1	Global optical bench design	77
4.1.1	Requirements	77
4.1.2	Honeycomb design	78
4.1.3	Manufacturability	80
4.1.4	Open- or closed-back honeycomb	84
4.2	Thermal stability	85
4.2.1	Spatial variations of α	87
4.2.2	xy-gradients	90
4.2.3	z-gradients	94
4.2.4	Conclusions	100
4.3	Final remarks	100
5	Mounting of optical components	103
5.1	Mounting plane	104
5.1.1	Coordinate system and critical DOF's	104
5.1.2	Mounting plane	105
5.1.3	Clamp to contact stiffness ratio	109
5.2	XY-mounted components	112
5.2.1	Beamsplitter	112

5.2.2	Mirror	115
5.3	YZ-mounted components	118
5.3.1	Beamsplitter	118
5.3.2	Mirror	120
5.4	Comparison of designs	121
5.4.1	Complexity of the design	121
5.4.2	Alignment complexity	122
5.4.3	Alignment stability	122
5.4.4	Measurement stability	123
5.4.5	Mass, preclamping force and stresses	123
5.5	Conclusions	124
6	Experiments	125
6.1	Beamsplitter breadboards	125
6.1.1	Goals	125
6.1.2	Breadboard design	126
6.1.3	Tests	127
6.1.4	Results	131
6.1.5	Discussion	133
6.2	Hydroxide catalysis bonding	134
6.2.1	Goals	134
6.2.2	Approach	134
6.2.3	Results	139
6.2.4	Discussion	144
6.3	Conclusions	146
7	Conclusions and recommendations	147
7.1	Introduction	147
7.2	Conclusions	148
7.2.1	Silicon Carbide	148
7.2.2	Optical design	148
7.2.3	Optical bench design	149
7.2.4	Optical bench thermal analysis	149
7.2.5	Design of optical components	150
7.2.6	Testing of optical components	151
7.3	Recommendations	151
Appendix A	Additional material properties	155
A.1	Hexoloy SA SSiC and Xycarb C/SiC	155
A.2	Fused silica	156

A.2.1. Thermal expansion	156
A.2.2. Stress birefringence of fused silica	157
A.3 TiAl ₆ V ₄	157
A.3.1. Creep	158
Appendix B Tunnel diagrams	161
B.1 Tunnel diagram technique	161
B.2 Equal OPD and base lengths	163
B.3 Influence of OPD	164
B.4 Influence of unequal base lengths	165
B.5 Influence of nonparallel incoming beams	167
Appendix C Optimizing flexural rigidity	169
C.1 Flexural rigidity of honeycombs	169
C.1.1. Open-back honeycomb	170
C.1.2. Closed-back honeycomb	171
C.2 Optimization of flexural rigidity	172
C.2.1. No limitations	172
C.2.2. With manufacturing limits	176
C.2.3. With manufacturing and building height limits	179
C.2.4. Hexagonal, square or triangular pockets	180
Appendix D Rolling kinematic couplings	183
D.1 Contact mechanics: rolling versus sliding	185
D.1.1. Sliding contact	186
D.1.2. Rolling contact	188
D.2 Axial stiffness of a ball in V-grooves	191
D.3 Accuracy of V-groove orientation	193
Appendix E Thermal contact conductance	201
Bibliography	207
Summary	217
Samenvatting	219
Dankwoord	221
Curriculum vitae	223

Nomenclature

Symbols

a	Base length	[m]
	Effective Hertz contact radius	[m]
	Creep constant	[-]
b	Width	[m]
c	Crack length	[m]
	Stiffness	[N m ⁻¹]
d_{fringe}	Fringe width	[m]
f	Focal length	[m]
h	Distance a beam travels in an optical component	[m]
	Height	[m]
h_c	Cell height	[m]
k	Propagation wave number	[-]
l	Length	[m]
m	Weibull modulus	[-]
	Mass	[kg]
q	Heat flux	[W m ⁻²]
r	Radius	[m]
t	Time	[s]

t_w	Wall thickness	[m]
t_f	Facesheet thickness	[m]
A	Surface area	[m ²]
	Auerbach constant	[N m ⁻¹]
	Creep constant	[-]
B	Stress optical coefficient	[N m ⁻²]
	Inscribed diameter of a honeycomb cell	[m]
C_p	Specific heat	[J kg ⁻¹ K ⁻¹]
D	Diameter	[m]
D_{Airy}	Airy disc diameter of the BAM system	[m]
E	Elastic modulus	[N m ⁻²]
E^*	Effective elastic modulus in Hertz contact	[N m ⁻²]
E_{photon}	Energy of a photon	[J]
F	Force	[N]
H_V	Vickers Hardness (500 g)	[N m ⁻²]
I	Irradiance	[W m ⁻²]
$J_1(x)$	First order Bessel function	
K_{IC}	Fracture toughness	[N m ^{-3/2}]
N	Number of fringes	[-]
	Number of photons detected	[-]
P	Power of the light beam	[W]
	Probability	[-]
R	Radius	[m]
T	Temperature	[K] or [°C]
T_{SR}	Thermal shock resistance	[K]
V	Volume	[m ³]
α	Coefficient of linear thermal expansion	[K ⁻¹]
	Localization accuracy	[rad]
γ	Fracture energy	[J m ⁻²]
	Bending	[m ⁻¹]
δ	Deflection	[m]
ε	(Creep) strain	[-]

$\dot{\epsilon}$	Creep strain rate	[s ⁻¹]
η	Rib solidity ratio	[-]
θ	Angle	[rad]
λ	Thermal conductivity	[W m ⁻¹ K ⁻¹]
	Wavelength	[m]
μ	Coefficient of friction	[-]
ν	Poisson ratio	[-]
ρ	Density of a material	[kg m ⁻³]
σ	Stress	[N m ⁻²]
σ_c	Compressive strength	[N m ⁻²]
σ_T	Tensile strength	[N m ⁻²]
σ_B	3- or 4- point bending strength	[N m ⁻²]
σ_I	Inert strength	[N m ⁻²]
σ_0	Scaling strength	[N m ⁻²]
τ	Integration time of the CCD	[s]
ψ	Angle	[rad]

Abbreviations

BAM	Basic Angle Monitoring
CCD	Charge Coupled Device
C/SiC	Carbon felt infiltrated Silicon Carbide
CVD	Chemical Vapour Deposited
CVI	Chemical Vapour Infiltrated
DOF	Degree-of-freedom
GAIA	Global Astrometric Interferometer
GCR	Galactic cosmic ray
HPSiC	Hot-pressed Silicon Carbide
HIPSiC	Hot Isostatically Pressed Silicon Carbide
LPSiC	Liquid-phase sintered Silicon Carbide
OP	Optical path length
OPD	Optical path length difference
PLM	Payload Module
PV	Peak-to-Valley

PVD	Physical vapour deposition
SiC	Silicon Carbide
SSiC	Sintered Silicon Carbide
RBSiC	Reaction Bonded Silicon Carbide
SVM	Service Module
ULE	Ultra-Low Expansion
WFE	Wave front error
YAG	Yttrium Aluminium Garnet

as	arcseconds
g	gravitational acceleration (= 9.81 m s ⁻²)
hr	hour
kg	kilograms
l	liter
m	meter
rad	radian
rms	root-mean-square
s	second

A	Ampère
Hz	Hertz
J	Joule
K	Degrees Kelvin
N	Newton
Pa	Pascal
V	Volt
W	Watt

°	Degrees (angle)
°C	Degrees Celcius
%	Percent

Prefix

p	pico
n	nano
μ	micro
m	milli
c	centi
k	kilo
M	Mega
G	Giga
Δ	Spatial difference
δ, d	Temporal change

1 Introduction

Space missions have always pushed the limits of what humans can achieve. In some missions the limits are pushed for political reasons and for some missions scientific curiosity is the motivation. Guided by space agencies, astronomers set extremely ambitious goals for future space missions and immediately start simulations on what they expect to learn from the mission. Engineers are given the task of building a satellite which can achieve these goals. The Hipparcos mission (1989 – 1993) was such a mission. Initiated by the curiosity of astronomers to learn more about the structure and evolution of our Galaxy, Hipparcos has been developed by engineers to suit the wish of the astronomers to make a 3D map of stars with an accuracy of 250 microarcseconds (μas). In retrospect it indeed has proven to give a wealth of information on the structure and evolution of the Galaxy. Astronomers now hope to push the limits again with Hipparcos' successor GAIA (Global Astrometric Interferometer for Astrophysics).

1.1 GAIA

The name GAIA not only is an acronym, but originates also from Greek mythology. GAIA is mother earth, an ancient primeval goddess who emerged at the creation of the universe, second only to Khaos (Air) [1].

1.1.1 Goals

The main goal of the GAIA mission (2012 – 2018) is to gather data on $\sim 10^9$ stars so that more understanding can be gained on the

origin and evolution of the universe, on star formation and evolution and on extra-solar planetary systems. This will be achieved by creating an extraordinarily precise three-dimensional map of stars throughout our Galaxy and beyond [2]. Additionally, the motion and several detailed physical properties of each star will be observed, such as luminosity, temperature, mass and elemental composition.

To reach these goals the measurement capabilities of the GAIA satellite will have to be:

- to catalogue $340 \cdot 10^3$ stars to magnitude 10, $26 \cdot 10^6$ stars to magnitude 15, $250 \cdot 10^6$ stars to magnitude 18 and $1 \cdot 10^9$ stars to magnitude 20;
- to handle a mean sky density of approximately $2.5 \cdot 10^4$ stars/degree and the maximum density of $\sim 3 \cdot 10^6$ stars/degree;
- to reach median parallax accuracies of $4 \mu\text{as}$ at magnitude 10, $11 \mu\text{as}$ at magnitude 15 and $160 \mu\text{as}$ at magnitude 20;
- to have distance accuracies of $21 \cdot 10^6$ stars better than 1%, $46 \cdot 10^6$ stars better than 2%, $116 \cdot 10^6$ stars better than 5% and $220 \cdot 10^6$ stars better than 10%;
- to measure radial velocities of 1 to 10 km/s to magnitude 16-17, and;
- to gather photometry data to magnitude 20 in the 320 – 1000 nm band.

1.1.2 Satellite general design

The GAIA satellite (Figure 1.1) consists of three modules [3]: the sun shield, the service module (SVM) and the payload module (PLM) covered with a thermal tent.

Sun shield

The function of the sun shield is to protect the SVM and the PLM from direct sunlight, because the solar radiation and light damage the CCD camera and reduce contrast of the star measurement. The sun shield is essentially a multi-layer insulation cover, which is stretched by a supporting structure on the shadow side. On the sunny side the shield is covered with second surface mirrors, to minimize the temperature of the cover and its effects on the SVM and PLM. The sunshield has a diameter of approximately 11 meters (m). In the centre, it contains a solar panel with a diameter

of 3 m, which provides for the necessary energy for satellite operation.

The sunshield is attached to the SVM central tube and folded against the PLM thermal tent for the launch. After separation it is deployed like an umbrella around and in the same plane as the solar array.

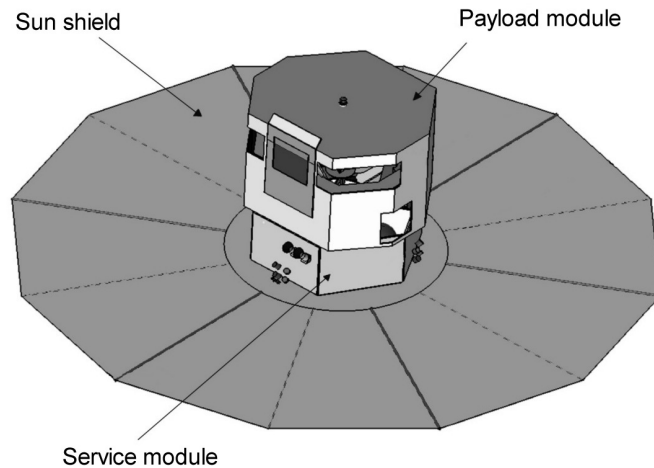


Figure 1.1 Artistic impression of the GAIA satellite

Service module

The SVM accommodates all avionics units and equipment for the support of the PLM. Its configuration is organized around a central tube, having a diameter compatible with the 1194 millimeter (mm) adapter between the Soyuz/ Fregat launcher and the satellite. The solar array is accommodated outside the central tube.

The tube is the direct supporter of two fuel tanks. The walls of the hexagonal box support the telemetry and telecommunication equipment, power distribution equipment, service module data handling system and payload video processing units.

Payload module

The payload module accommodates the scientific instrumentation (Figure 1.2):

- Two identical astrometric telescopes, which allow for the position and velocity of stars to be measured in a 320 – 1000 nm band. The basic angle (the angle between the lines of sight of the telescopes) will be ~ 106 degrees ($^\circ$);
- Focal plane assembly; a large CCD camera, which collects the light from the telescopes;
- Spectrometric instrument, which determines the radial velocity and the chemical composition of stars in the 847 – 874 nm band.

In the preliminary design, the scientific instruments are mounted on an octagonal optical bench. To ensure mechanical and thermal stability in the PLM, it has been decoupled from the SVM as much as possible by placing the optical bench on three V-shaped isostatic struts. The maximum diameter of the optical bench is 3 m. The payload module is covered with a multi-layer insulation tent providing insulation from solar and deep-space radiation.

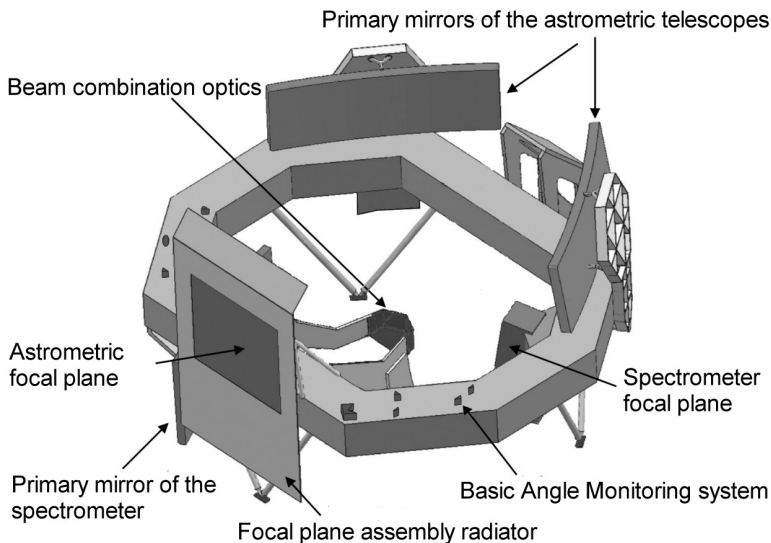


Figure 1.2 Payload module

1.1.3 Basic Angle Monitoring system

To be able to link the measured positions of stars of one telescope, to the measured positions of stars of the other telescope, it is very important to know the angle between the lines-of-sight of both

telescopes. This “basic angle” is measured prior to launch. Maximum variations of 15 prad are expected on the basic angle in the 6-hour cycle based on initial thermal analyses. However, this expected variation may be larger. Therefore, the satellite will be equipped with a metrology system, which will specifically measure the variations of the basic angle with maximum uncertainty of $\pm 0.5 \mu\text{as}$ ($\pm 2.5 \text{ prad}$), with the goal of mathematically correcting off-line for these variations in the measured positions of stars. The full name of this metrology system is the Basic Angle Monitoring (BAM) system. The measurement principle of BAM system is discussed in this section.

Measurement principle

In Figure 1.3, a top view is shown of the Payload Module of the satellite. The octagonal structure is visible on which the scientific instruments are mounted.

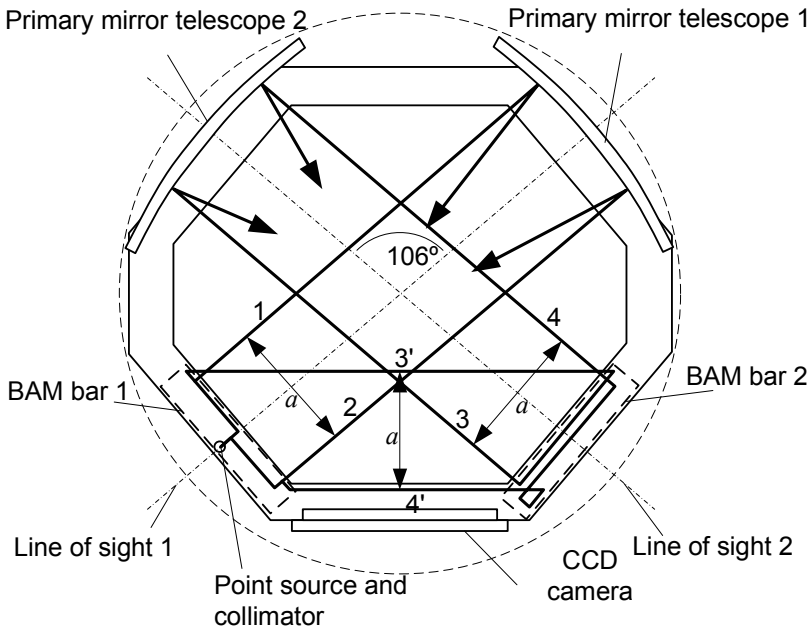


Figure 1.3 Top view of the Payload Module of GAIA with light paths of the metrology system

The primary mirrors of both telescopes are shown on the left- and right-hand side. The basic angle is the angle between the lines of

sight of both telescopes. Bars 1 and 2, which are facing the primary mirrors of the telescopes on the opposite side of the octagonal structure, contain the BAM system.

Essentially, on BAM bar 1 a collimator lens creates a beam with diameter D . Via a beamsplitter the light is split into two coherent beams, which are reflected against mirrors to create two parallel beams (1 and 2) with a center-to-center distance (base length) a . These beams travel through telescope 1 and create a fringe pattern on the CCD camera.

On BAM bar 1 the light is also split into two parallel coherent beams (3' and 4') traveling to a second bar (BAM bar 2). On this bar also some mirrors are positioned, such that two parallel coherent beams (3 and 4) are sent through telescope 2. This pair of beams creates a second fringe pattern on the CCD camera. The two fringe patterns are shown in Figure 1.4.

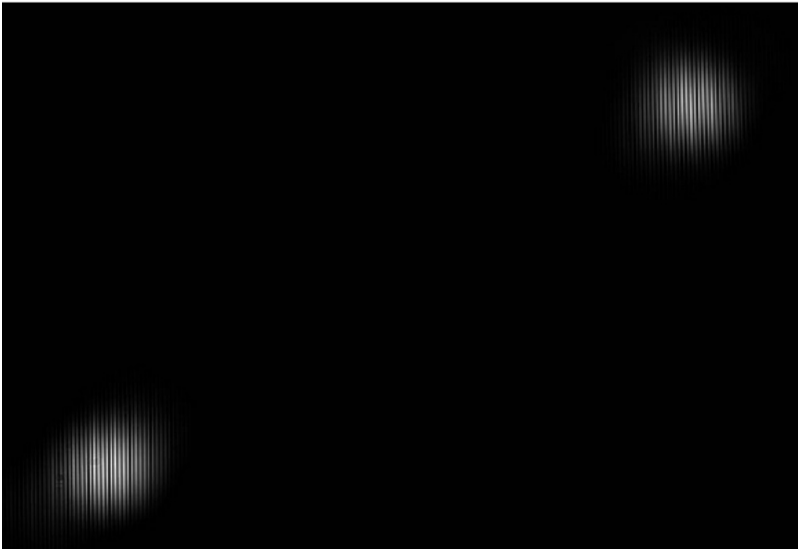


Figure 1.4 The interference patterns of two pairs of interfering laser beams made with the GAIA OPD Test Bench [4].

If one fringe pattern shifts with respect to the other fringe pattern, this is a measure for the change in angle between the lines-of-sight of the telescopes.

1.2 Stability

The measurements made by the scientific instrumentation on the GAIA satellite, like the $4 \mu\text{s}$ uncertainty in star position measurement, and the $0.5 \mu\text{s}$ uncertainty in the measurements of the basic angle variations, requires extreme stability during measurements.

To illustrate the statement of extreme stability, $0.5 \mu\text{s}$ is equal to 2.5 prad . If 2.5 prad is described as displacement, this is a movement of 2.5 pm over a distance of 1 m . 2.5 pm is much smaller than the radius of atoms: e.g. a Helium atom has a diameter of 50 pm .

This stability must be achieved in three steps. The first step is to send GAIA to a location, with extremely stable environmental conditions. The second step is to build the satellite of an extremely stable material, i.e. Silicon Carbide (SiC). The final step is a stable thermo-mechanical design of the instrumentation. Each step is of considerable importance for the success of the GAIA star position measurements.

1.2.1 *Stable environment*

The environmental conditions of the BAM system are essential in the design, especially since GAIA is a space mission involving Earth-like conditions prior to launch, launch conditions, and operational conditions in the vacuum of space.

Pre-launch conditions

The pre-launch conditions are relevant for the BAM system in the sense that the system will have to survive these conditions without changes in the system and without damage, which could impair the systems functionality in space. The BAM system will most likely be manufactured in regular Earth conditions at approximately room temperature. Prior to assembly and alignment, the parts will be thoroughly cleansed and the assembly and alignment will then be performed in clean room conditions. This is done because the optical components should remain clean for optimal optical performance. Also, the vacuum of space causes mainly organic substances to sublime, which could then precipitate on other optical systems in the GAIA satellite. Possibly, the BAM system will be transported from the assembly

and alignment location to the satellite assembly location. This will be performed in clean conditions, but with possible thermal changes and transportation vibrations. The satellite will be assembled and qualification tested on Earth in these clean room conditions at rather constant temperatures. However, just prior to launch the satellite will be transported over a large distance to the launch location. This will also be a clean transport but in less predictable thermal and vibration conditions. Finally, the satellite will be mounted onto the launch adaptor and into the launch vehicle. The launch vehicle will then be transported to the launch stage. This whole pre-launch procedure can take a year. A quantified summary of the pre-launch conditions is shown in Table 1.1.

Table 1.1 Pre-launch conditions [5]

Parameter	Values
Atmosphere	Air
Pressure	10^5 Pa
Temperature	-40 °C to +40 °C
Humidity	0 – 90 %
Vibrations	Same as during launch but less severe
Period	1 year

Launch conditions

During launch, the satellite will be maintained at ambient pressure and at constant temperature. The conditions, which make the launch environment severe, are the vibration loads. The vibration loads are transmitted from the launch rocket to the satellite via an interface on which the satellite is mounted in the rocket.

The loads on the BAM system itself will be altered due to the mechanical behavior of the satellite to the levels stated in Table 1.2. The vibration spectrum indicates that the lowest Eigen frequency of the BAM system should be well above 400 Hz and preferably above 1000 Hz in order not to risk resonance in high amplitudes followed by failure.

Table 1.2 Frequency environment for the BAM system [5]

Load case	Frequency	Qualification level
Quasi static		25 g
Sine-equivalent dynamics	5 – 23 Hz	11 g
	23 – 35 Hz	25 g
	35 – 60 Hz	6 g
	60 – 140 Hz	3 g
PSD of random dynamics	20 – 100 Hz	3 dB/oct
	100 – 400 Hz	0.3 g ² /Hz
	400 – 2000 Hz	-3 dB/oct
	Overall	17 g rms
Shock	0.5 ms	200 g

Not only vibrations, but also depressurization, temperature fluctuations and radiation are part of the launch procedure. During launch the temperature can rise up to 350 K and after the jettison of all rocket stages, the satellite will cool down to 120 ± 20 K. This leads to a required non-operational temperature range of 100 to 350 K. The depressurization rate is 3500 Pa/s from ambient to zero pressure. Complete depressurization is therefore achieved in 30 seconds (Table 1.3).

Table 1.3 Non-operational environmental conditions [5]

Parameter	Values
Depressurization rate from ambient to zero pressure	3500 Pa/s
Temperature range of payload module	100 – 350 K

The radiation environment can be split into a transfer phase environment and operational environment. The transfer phase consists of a 190 km parking orbit of the satellite and transfer from this orbit to the operational orbit, with a duration of approximately 3 months. Due to geomagnetic shielding effects and the short duration of this phase compared to the operational phase, the solar protons are neglected and instead are included in the operational phase of the mission. Similarly, due to geomagnetic shielding effects, the galactic cosmic ray (GCR) environment during the transfer phase is less harsh than during the operational phase and so the GCR environment of the operational phase can be considered the baseline spectra for the entire mission.

Operational conditions

The GAIA satellite is sent to the L_2 Lagrange point of the Sun-Earth system. According to the Keplerian Law's a planet close to the Sun has a shorter orbital period than a planet further away [6]. So if a satellite is put in orbit around the Sun, at a larger distance than the Earth, it will have a larger orbital period than the Earth. However, the satellite is then also subject to the gravitational force of the Earth. At certain locations in the Sun-Earth system the gravitational forces of Earth and Sun are in equilibrium with the centripetal acceleration of the satellite. These locations are called Lagrange points. The L_2 Lagrange point is about 1.5 million km from the Earth (Figure 1.5). In this point the satellite will move faster than the Earth, but will move with the same period (of a year) around the Sun.

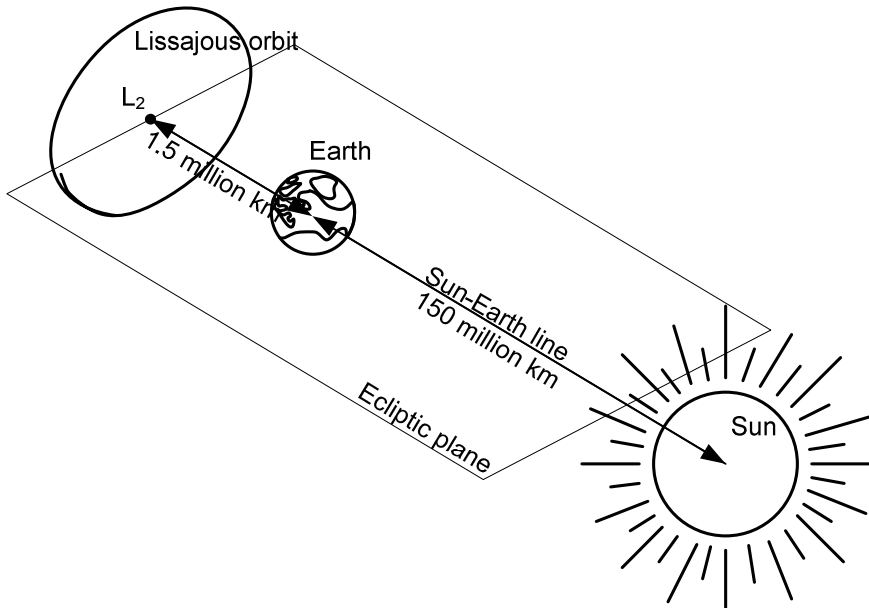


Figure 1.5 GAIA transfer trajectory to L_2

The satellite will orbit the Sun not exactly in the L_2 Lagrange point. The orbit that is being maintained is Lissajous curve around L_2 with a radius of about $5 \cdot 10^4$ km. The reason for this is twofold: first, the L_2 Lagrange point is inherently unstable, because small perturbations in the gravitational equilibrium can cause the satellite to be put off-course; the second reason is that

the satellite would at all times be in half shade of the Earth, if it would be maintained at L_2 , thus reducing solar energy supply drastically. The small amplitude Lissajous orbit will ensure constant power supply by the Sun and due to the quasi-periodic property only small course corrections are necessary to maintain orbit. Also, the L_2 Lagrange point makes daily contact possible for downloading measurement data from the GAIA satellite to the Earth.

The GAIA satellite is oriented with the solar shield in a 50° angle towards the Sun, such that the PLM is in the shade of the solar shield at all times (Figure 1.6). All instrumentation therefore sees only deep-space with background radiation temperature of 4 K. The design of the satellite is such that the optical bench with all scientific instrumentation is as much as possible decoupled from heat sources in the satellite. Nearly all heat sources are mounted in the SVM, except for the CCD camera's in the astrometric focal plane. The PLM is decoupled by using insulating isostatic rods for mounting.

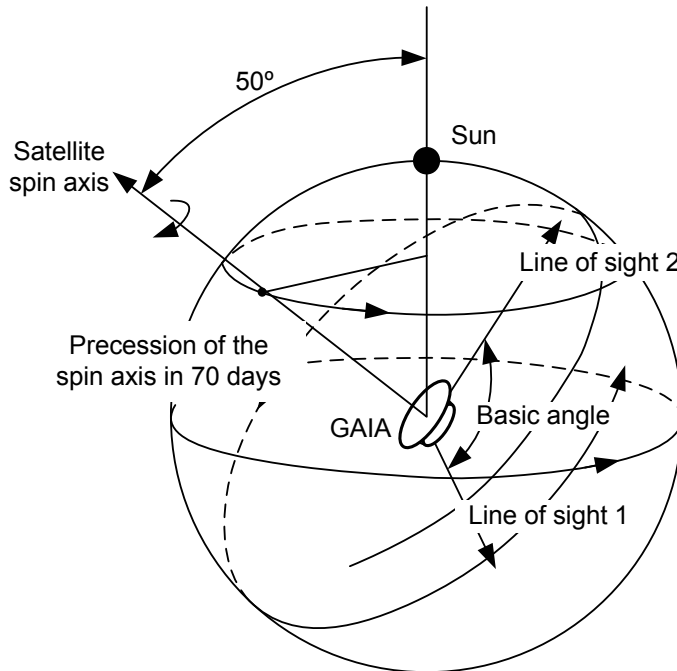


Figure 1.6 The orientation of the GAIA satellite with respect to the Sun

The combination of the vacuum of space, the isolating mounting and the deep-space orientation of the PLM leads to an expected overall temperature in the PLM of $120\text{ K} \pm 20\text{ K}$. The expected thermal stability in the 6-hour measurement cycle is $\pm 0.1\text{ mK}$. This thermal variation comprises both overall temperature fluctuations and temperature gradient variations.

The 6-hour measurement cycle time mentioned for the satellite in operation is important because the BAM system will have to show $0.5\text{ }\mu\text{s}$ stability. Since the rotation of the satellite around its own axis has an overlap in the field of view each succeeding cycle, the system can be calibrated every 6 hours. This is done by overlaying the position of a specific star measured in the previous cycle onto the measured position of the same star in the current cycle. Therefore, stability levels should be maintained in the periodic cycle of 6 hours.

Often satellites are subject to micro-vibrations during operation. However, the GAIA satellite will not be subject to micro-vibrations during measurements. Monthly, a small number of engine bursts will be needed to maintain the satellite in its position. This will cause some micro-vibrations in the satellite, but during these course corrections no measurements will be performed.

The BAM system will be shielded for thermal solar radiation by a large sun shield, but will be subject to cosmic rays and solar particle events. The L_2 point is outside of the region of effective geomagnetic shielding and the trapped radiation belts and can be considered to be an interplanetary environment.

The GCR environment originates outside the solar system. Fluxes of these particles are low, but they include heavy, energetic ions of elements such as iron, which can cause intense ionization as they pass through matter. This ionization is generally difficult to shield, but only affects electronics, like CCD cameras. This does concern the performance of the BAM system, but it does not concern the optical benches of the BAM system.

Solar protons are products of solar events, with extreme energy levels and flux densities. These events are relatively rare, occurring primarily in periods of eleven years. One event typically lasts several days. These solar protons affect electronics and detectors by introducing background noise.

Note finally, that the stability requirement of 2.5 pm is in the range where quantum effects become important. In fact atoms move in their crystal lattice in the range of a few tenths of picometers [7] due to thermal energy and surfaces change shape due to quantum effects and the impact of radiation. However, any of these effects are not expected to be a problem, because the vibration of atoms in crystalline solids lies in extremely high frequencies of $\sim 10^{13}$ Hz [7] in relation to the measurement frequency range of the BAM system. Each measurement is taken over 5 minutes averaging time. In combination with the 6 hours rotation time, this leads to a frequency range of 10^{-6} Hz to 10^{-3} Hz. It is therefore reasonable to assume that any quantum-mechanic effects will not harm the basic angle variation measurements in any way.

Operational conditions of the PLM and the BAM system are summarized in Table 1.4.

Table 1.4 Operational conditions of the PLM and BAM system [6]

Parameter	Values
Pressure	10^{-10} Pa
Temperature of payload module	120 K \pm 20 K
Temperature stability	± 0.1 mK
Micro-vibrations	Periodic engine bursts (no measurements during bursts)
Cycle time of the satellite around its axis	6 hours
Operation period of the satellite	6 years
Averaging period of a basic angle variation measurement	5 minutes

1.2.2 Stable material

The material of which the PLM and the BAM system are built, must be extremely stable during measurements. From a mechanical point of view, there are several demands that can be stated with regard to the material of the PLM and the BAM system of GAIA. To make full use of the very stable conditions in the L_2 -point in space, the material should have the following properties [8]:

- High specific stiffness E/ρ , meaning high Young's modulus E and low density ρ (such that the design can be light and stiff);

- Low sensitivity to spatial thermal gradients α/λ , meaning that the thermal expansion coefficient α should be small and thermal conductivity λ should be high, to get very small and uniform expansion on temperature increase;
- High volumetric thermal diffusivity $\lambda/\rho C_p$, meaning that the speed at which the structure as a whole changes temperature should be high;
- High volumetric stability $\lambda/\alpha\rho C_p$. This characteristic combines the sensitivity to spatial thermal gradients and the volumetric thermal diffusivity and expresses the capability of the material to maintain its shape due to temporal and spatial thermal variations;
- Low (micro-)creep level, meaning that under constant stress conditions the material should preferably not show creep.

The required properties of the material discussed up to this point are only focused on the stability during measurements, disregarding the environmental conditions. The material should also have some additional properties, because the launch environment and space itself are very harsh environments, like discussed in Section 1.2.1.

Therefore, materials applied in space must have the following characteristics:

- No sublimation for ambient pressures of 10^{-10} Pa;
- Oxidation resistant;
- Radiation resistant and;
- Corrosion resistant from atomic oxygen and high-energy particles.

Finally, there is one property that the material must have specifically for the PLM of GAIA. The material must be polishable to a low wave front error (WFE) of 25 nm. It should preferably be highly reflective for the visible wavelengths or at least be suitable for coating with a reflective coating to increase the reflectance.

The material that has been chosen by ESA for usage in the PLM of the GAIA satellite is SiC. To illustrate why SiC is a very suitable material for application in the PLM, the basic mechanical and thermal properties of several materials are shown in Table 1.5 and Table 1.6 for comparison. Three types of SiC, several ceramic

materials, some metals which are often applied for space applications and some glass-ceramic materials are compared.

Mechanical properties of the selected materials

For the mechanical stability of the BAM system it is necessary to have high specific stiffness E/ρ . Preferably, the material should thus have low density ρ in combination with a high Young's modulus E . As can be seen in Table 1.5, the ceramic materials generally have high specific stiffness, much higher than the more common metals – steel, aluminium and TiAl_6V_4 – and the glass-ceramic materials. Boron carbide has the highest specific stiffness, closely followed by beryllium and sintered SiC (SSiC). Reaction Bonded SiC (RBSiC) and C-felt SiC (C/SiC) have a somewhat smaller specific stiffness than SSiC.

Table 1.5 Mechanical properties of the selected materials

Material (supplier)	ρ [$\times 10^3 \text{ kg m}^{-3}$]	E [$\times 10^9 \text{ N m}^{-2}$]	E/ρ [$\times 10^6 \text{ N m kg}^{-1}$]
SSiC (Boostec)	3.1	410	132
C/SiC (Poco)	2.6	218	84
RBSiC (SSG)	2.9	310	107
Al_2O_3 (Ceratec)	3.9	370	95
B_4C (Ceratec)	2.5	450	180
Si_3N_4 (Ceratec)	3.2	275	96
302 stainless steel	7.9	193	24
Al alloy 6061	2.7	69	26
TiAl_6V_4 (grade 5)	4.4	114	26
Invar 36 (Carpenter)	8.1	148	18
HIP Be	1.8	303	168
Zerodur (Schott)	2.5	90	36
fused silica (Schott)	2.2	72	33

Thermal properties of the selected materials

In Table 1.6 the thermal properties of the materials at room temperature are presented. Only the volumetric thermal stability is used, because this parameter is most suitable for use in case of passive optics. Since the GAIA application is a passive optical application, this parameter is used in Table 1.6. All three types of SiC and Zerodur do have a high volumetric thermal stability.

Table 1.6 Thermal properties of selected materials at room temperature

Material (supplier)	α [$\times 10^{-6} \text{ K}^{-1}$]	λ [$\text{W m}^{-1} \text{ K}^{-1}$]	C_p [$\text{J kg}^{-1} \text{ K}^{-1}$]	$\frac{\lambda}{\alpha \cdot \rho \cdot C_p}$ [$\text{m}^2 \text{ K s}^{-1}$]
SSiC (Boostec)	2.5	180	680	34.1
C/SiC (Poco)	2.4	158	800	28.4
RBSiC (SSG)	2.4	157	670	33.4
Al ₂ O ₃ (Ceratec)	7.0	28	880	1.2
B ₄ C (Ceratec)	5.0	45	950	3.8
Si ₃ N ₄ (Ceratec)	3.2	35	680	5.0
302 stainless steel	17	16	500	0.2
Al alloy 6061	24	180	880	3.2
TiAl ₆ V ₄ (grade 5)	8.6	6.7	526	0.3
Invar 36 (Carpenter)	1.3	10	515	0.2
HIP Be	11.4	216	1925	5.5
Zerodur (Schott)	0.05	1.46	800	14.6
fused silica (Schott)	0.49	1.31	790	1.5

When comparing both the thermal and mechanical properties it is clear that only the three types of SiC score high both on mechanical and on thermal stability, which makes SiC the material of choice for application in GAIA.

1.2.3 Stable opto-thermo-mechanical design

The third and final step to make the BAM system stable enough to measure basic angle variation of $\pm 0.5 \mu\text{as}$, is to make a stable opto-thermo-mechanical design. This means that some design principles must be applied consistently and correctly, such that any instability of the optical paths in the BAM system will not occur. These instabilities are focused mainly on the stability of the optical path length differences (OPD) of the 2 interfering pairs of beams and on the angular stability of the beams. Causes for instabilities are:

- Thermal expansion effects;
- Hysteresis;
- Creep due to constant loading and;
- Failure.

The design principles follow mainly from many years of experience in precision design ([9] to [19]). Some relevant examples of these principles are:

- Make a statically determinate design. This means that a rigid component should be mounted in exactly six degrees of freedom (DOF). If the component is mounted in less DOF's it is under-constrained and will be able to move. If it is mounted in more than six DOF's it will be over-constrained. In that case the component will be subject to internal stress and will become bent or distorted [19];
- Make a thermally insensitive design as much as possible, making use of a statically determinate design with a thermal centre such that specific functional points of a component will stay in place relative to another component under temperature variations;
- Make a design based on stiffness. High stiffness will lead to low stresses and small deformations for equal loading. In the BAM system the stiffness should be high to avoid large deformations due to mechanical loading;
- Use as few joints between components as possible. Any joint gives the risk of either hysteresis, or stresses. Preferably the entire BAM system should be monolithic. Also any joint is a barrier which reduces the thermal diffusivity [20]. The thermal diffusivity should be as high as possible;
- Reduce any internal stresses to a minimum to prevent creep and;
- Make force loops as short as possible to reduce the number of error sources and to reduce deformation due to stresses in the parts.

1.3 Aim of the thesis

SiC is a material that has only been emerging as a construction material in the past few decades. The experience that has been obtained is focused mainly on refractory industry in extremely hot conditions. Only in the past decade some experience has been gained also in space industry, mainly in the form of SiC mirrors. More recently, the interest in SiC for structural applications for space missions is increasing, like is the case for the GAIA satellite. At the same time high precision industry (in the Netherlands) is calling for ever increasing accuracy. Now, picometer level accuracy is the next goal. Picometer level accuracy requires the consideration of more stable materials. SiC is a good candidate.

In the Netherlands experience in SiC is limited, both for mirrors and structural applications. The GAIA BAM system provides in this respect the perfect opportunity (for the Netherlands) to gain experience in picometer stable metrology systems in combination with the stable material SiC.

This thesis focuses on the integration of mechanical design principles for opto-mechanical structures with the stable material SiC, with the convenient case study of the GAIA BAM system. Six main topics are considered to be of importance for the successful application of a picometer stable metrology system. These are:

- knowledge of the properties and possibilities of SiC;
- the optical design of the metrology system;
- the optical bench design;
- the design of the optical component mounting;
- the detectors and;
- the software.

This thesis only considers the first four aspects, because these are directly considered relevant for the mechanical design of the system.

1.4 Layout of the thesis

In chapter 2 a more detailed investigation on SiC is made. Different manufacturing processes are investigated. For application in the BAM system, two main processes can be distinguished: SiC made by sintering a compressed SiC powder and SiC made by infiltrating a carbon felt with silicon. The possibilities and limitations of both manufacturing processes are mapped out. The mechanical, thermal and optical properties of the different types of SiC are discussed. These properties give insight into the possibilities and limitations of opto-mechanical design with SiC. Special attention is paid to the stability of SiC as a material. This includes creep and fault and fracture propagation.

The requirements on the optical design of the BAM system are discussed in chapter 3. They follow partly from the properties of the telescopes on GAIA and partly from the sensitivity to error sources. The concept of the optical design is presented and possible error sources are mapped out. For the sensitivity analysis of some of these error sources, the tunnel diagram technique is

used. The requirements are subdivided into laser requirements, initial alignment accuracy, lifetime alignment stability, and measurement stability. An alignment plan is made to achieve the initial alignment accuracy needed for each optical component.

The concept design process of the basic angle monitoring system can be subdivided in the design of the optical benches and the design of the optical components, more specifically focused on mounting the optical components. The design of the optical benches, treated in chapter 4, focuses on optimizing for stability. This is done by manufacturing the optical bench in one piece and by maximizing the bending stiffness. A comparison is made between closed-back and open-back honeycomb benches specifically keeping in mind the manufacturing limitations of SiC. The mounting of the optical benches is discussed as well.

The design of the optical components in chapter 5 is focused on a conceptual study in which a comparison is made of mounting planes, in which the optical component should be aligned and fixed to the optical bench for optimal stability. The different comparisons lead to two different designs, one of which is implemented by manufacturing fused silica beamsplitters in a SiC mount.

In chapter 6 the manufacturing and testing of these beamsplitters is discussed. The beamsplitters are subjected to 17g rms vibration levels and thermal cycling tests are performed. The position and wavefront of the beamsplitter compared to the mount, is measured before and after testing. In this way, the positional stability can be measured to nanometer accuracy.

Furthermore in chapter 6, an experimental bonding technique called hydroxide catalysis bonding is discussed. The technique is performed on SiC and some strength measurements are conducted.

The thesis will end in chapter 7 with concluding remarks on the topic of SiC and with recommendations on future research in the field of extremely stable metrology in SiC.

2 Silicon Carbide

To make full use of any material in the design of any mechanical structure it is necessary to know and understand the mechanical and thermal properties of the material, and the production processes needed to make the product. The understanding of the properties and production processes, gives an idea of the possibilities and impossibilities in a design. In this chapter these aspects of designing with SiC are discussed. First, in section 2.1, attention is paid to the history of SiC, meaning the discovery of the material and applications of the material through the years. In section 2.2, several manufacturing techniques for SiC are discussed. These manufacturing techniques are specifically focused on the Acheson process and the production of SSiC, C/SiC, CVD SiC for specialized products, like is the case for the BAM system. Next, in section 2.3, the properties of different types of SiC are discussed. The discussion is subdivided into mechanical properties, thermal properties, optical properties and other properties. Only properties which are relevant for the application in the BAM system are discussed. Therefore, special attention is focused on the properties relevant to a cryogenic and space environment.

Also some properties of fused silica and TiAl_6V_4 are shown, because these materials are used in the BAM system as well. Fused silica is used as semi-transparent material for the beamsplitter application and TiAl_6V_4 is used as an elastic material for clamping purposes.

The chapter will end in section 2.4 with a discussion on the direct implications of the use of properties and manufacturing processes of SiC on the design of an opto-mechanical structure like the BAM system.

2.1 History of Silicon Carbide

SiC has been reported for the first time in 1810 and 1821 by Berzelius. Later, it has been rediscovered during various electro chemical experiments.

Naturally occurring SiC has been discovered in 1905 by Moissan in a meteorite from the Diablo Canyon in Arizona. Note that the natural occurrence of SiC is very rare.

In 1891 Acheson discovered how to prepare SiC on a large scale [21]. This manufacturing process is discussed later in this section. Acheson believed the material was a compound of Carbon and Corundum (Al_2O_3), and he named it Carborundum.

Nowadays, SiC is produced at a rate of 900,000 tonnes a year. By far the largest amount of SiC is produced for the abrasive industry. Due to its great hardness (third hardest material) it is very suitable for application as an abrasive. Another large market for raw SiC is its application as a siliconizing and carburizing agent in iron and steel metallurgy.

The development of bonded SiC in molded form has only been conducted from the 1960's onwards. Nowadays, the hot-process industry makes use of SiC for refractories such as firebricks, setter tiles, heating elements and tubes.

Currently, SiC is used more than before as material for structural components in mechanical engineering. The material has already proved successful for use under extreme conditions involving abrasion, corrosion and high temperatures. Examples are: brake discs in F1 cars, seal rings for water pumps in cars, etcetera.

Parallel to high temperature application, the interest in SiC for structural parts is growing for application in completely different extreme environments or applications, e.g. space and semiconductor industry. These applications require extreme shape stability in vacuum (and possibly cryogenic) environments. The main applications of SiC in the space industry up to this point have been mirrors and some support structures for those mirrors.

Examples of SiC mirrors that are already in an Earth orbit are the Narrow Angle Camera of Rosetta and mirrors for Rocsat 2 [22].

2.2 Manufacturing technologies

A large number of different manufacturing technologies exists for SiC. It is not the intention of this thesis to discuss all manufacturing techniques in great detail, because some techniques are not of interest for application in the BAM system or in any space application. A small selection of manufacturing techniques is discussed, starting with the Acheson process, which is the first step towards different types of sintered SiC. The production of sintered SiC products is therefore the next topic. C/SiC, used here as a generic term for SiC with a carbon based production method is the third manufacturing technique discussed in this section. Finally, the production of CVD SiC is discussed.

2.2.1 Acheson process

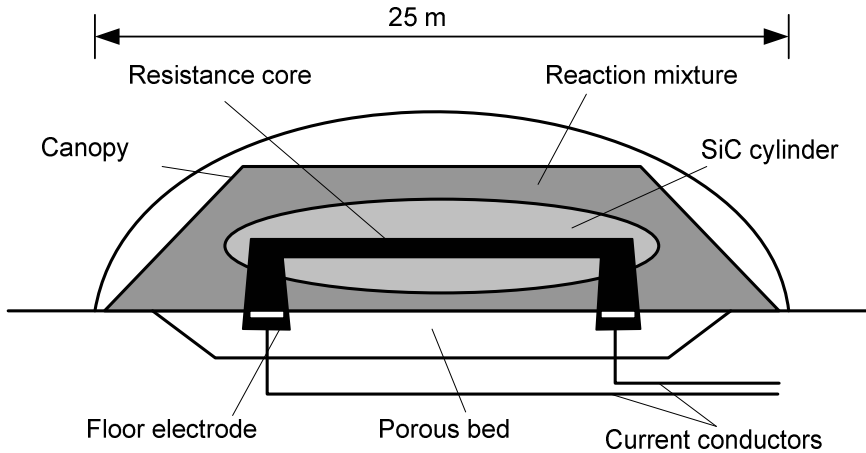
The production of α -SiC (SiC with hexagonal crystal structure) can be performed with the Acheson process. In this process, a mixture is made of high purity quartz (SiO_2) and petroleum coke (C). This mixture is piled on stacks of up to 25 m long, 4 m wide and 4 m high and covered by a rectangular furnace (Figure 2.1). At both ends of the furnace water-cooled graphite electrodes are present. A graphite rod in the middle of the mixture connects the two electrodes. A current of up to $25 \cdot 10^3$ A is led through the electrodes, heating the furnace up to 2500 °C.

This causes SiC to crystallize outward. The further out, the more difficult it is for the SiC to form, because of the temperature drop outwards. Therefore, high-purity large α -SiC crystals (hexagonal crystal structure) are created in the center of the mixture and further out fine crystals of β -SiC (cubic crystal structure) are created. After 16 hours the current is switched off. After cooling down, the mixture is removed layer by layer, so that different qualities are separated. For sintering the α -SiC crystals are used.

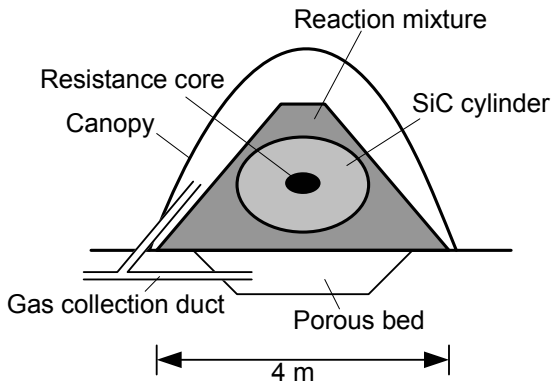
2.2.2 Sintered Silicon Carbide

Sintered SiC materials use the α -SiC crystals from the Acheson process as base material. There are several different forms of sintered SiC, e.g.: liquid-phase sintered SiC (LPSiC), hot-

(isostatically) pressed SiC (HPSiC or HIPSiC), and solid-state sintered SiC (SSiC).



a) longitudinal cross-section



b) radial cross-section

Figure 2.1 Silicon Carbide production by the Acheson process

The SSiC process is used by a manufacturer of SiC mirrors and other structural parts for space applications, called Boostec in France [23]. In more detail the Boostec SSiC production process can be subdivided in the following steps (see also Figure 2.2):

- α -SiC powder produced with the Acheson process, is mixed with organic binders and sintering aids (like carbon and boron);

- The mixed powder is compacted under cold isostatic pressing. This is done by putting the powder mixture in a large rubber bag. The bag is sealed and then submerged in a vessel filled with a fluid. This fluid with the powder bag is then subjected to a $200 \cdot 10^6$ Pa pressure. After pressing, this leaves a 'green' SiC block of compacted powder, which exhibits chalk-like behavior. The homogeneity of the 'green' SiC is verified by testing the strength of small dummies of the compacted powder.

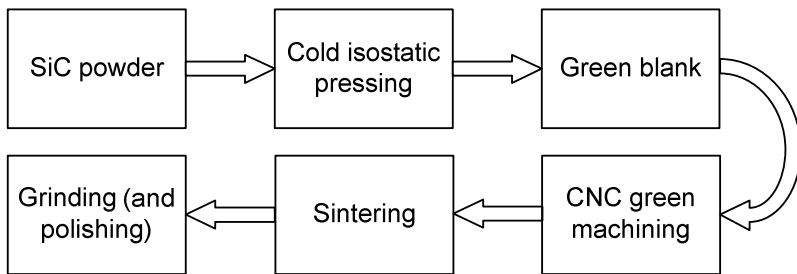


Figure 2.2 A flowchart of the sintered SiC manufacturing process

- The 'green' SiC block is machined to the desired shape (green shape);
- The green shape is pressureless sintered. The sintering is performed at approximately 2100 °C in a non-oxidizing environment in a graphite electrical furnace. The sintering process takes in the order of a day to a week depending on the thickness of the product. If the thickness is large, the cool-down trajectory after sintering should be long to keep the temperature difference between the core and edge of the product within limits, such that no micro-cracks occur due to thermal stresses. During sintering the product shrinks approximately 17 %.

2.2.3 Carbon felt Silicon Carbide

C/SiC is also called reaction-bonded SiC (RBSiC) in some literature [21]. Generally in this process gaseous SiO_2 or liquid silicon invades a carbon pre-form. Sometimes this pre-form also contains SiC fibers and a carbon-containing binder. The carbon reacts with the silicon to form SiC. If there is an excess of silicon

the pores are filled with silicon, and the material will have higher density and will be stronger than if there is an excess of carbon.

An American company called Poco Graphite makes C/SiC products for space and military applications according to the following process [24] (see also Figure 2.3):

- A graphite felt block with a very fine and open porous structure is produced;
- The graphite felt is purified;
- The graphite felt is machined to the desired shape (green shape);
- The carbon is infiltrated with silicon and converted into SiC. This conversion is performed by carbothermal reduction of silica. In this process solid carbon (C) and quartz (SiO_2) react at temperatures above ~ 1600 °C at atmospheric pressure, creating gaseous SiO. Thereupon, the SiO reacts with the carbon to form SiC. The maximum infiltration depth that can be achieved using this process is typically 6 mm. The infiltration process takes a few days, which is comparable to the process time for SSiC.

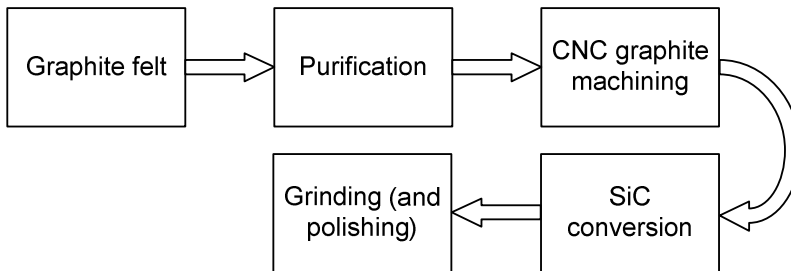


Figure 2.3 A flowchart of the C/SiC manufacturing process

The conversion can also be achieved by infiltration of liquid silicon in the graphite felt using capillary forces. This conversion technique is used by Xycarb Ceramics (Netherlands). The infiltration depth of silicon using capillary forces is not limited for graphite blocks like as large as a 1 m^3 cube.

C/SiC materials do not show any shrinkage. Generally, they can exhibit a small shape change of maximally 1 %.

2.2.4 Chemical Vapour Deposited SiC

Chemical Vapour Deposited (CVD) SiC is obtained by a chemical reaction of volatile silicon and carbon containing compounds in the presence of hydrogen in the temperature range of 1000 °C to 1800 °C. Gaseous precursors can be, for example, silicon tetrachloride or methane. CVD SiC is of high purity (99.999 %). It has a β -SiC structure and has very fine grains [21].

For the BAM system application CVD SiC can be used for coating an SSiC or C/SiC substrate for mirror applications, because it has higher reflectance in the visible spectrum and can be polished to 0.3 nm roughness.

Chemical Vapour Infiltrated (CVI) SiC and Physical Vapour Deposited (PVD) SiC can also be applied for coating, however no details on these techniques have been found in the literature.

2.3 Properties of Silicon Carbide

Due to slight variations in material properties from different manufacturers the material properties presented in this section are based on brands of which the largest amount of information is available and which are focused on space application. The SSiC material properties mentioned are Boostec SSiC material properties [25], the C/SiC material properties are Poco SuperSiC material properties [24]. In some instances the information is completed with the gathered data from Touloukian ([26], [27] and [28]). The presented properties of CVD SiC are based on the information from Rohm and Haas [29]. In experiments that are discussed in chapter 6, two other brands of SiC have been used for testing. These are Hexoloy SA SSiC and Xycarb C/SiC. The available information on these materials is shown in appendix A.

2.3.1 Mechanical properties

The most basic mechanical properties of SiC (density and Elastic modulus) have been compared to other materials in Chapter 1. These properties are not the only mechanical properties important for opto-mechanical design. Other properties are needed to make a good analysis of the opto-mechanical system. Nearly all room temperature mechanical properties of the three main types of SiC, which are important for BAM system application, are shown in Table 2.1.

The mechanical properties of SiC at room temperature can be assumed to be fairly constant in the temperature range of 100 K – 350 K, because in this temperature trajectory these SiC types will not undergo changes in crystallographic composition and do not have secondary phases.

The density of CVD SiC is $3.21 \cdot 10^3 \text{ kg m}^{-3}$, which is equal to the theoretical maximal density of SiC. The actual density of SSiC and C/SiC is lower than the theoretical density, due to a porosity of 3% and 20%, respectively. The porosity in C/SiC is also responsible for the strongly reduced elastic modulus.

The Poisson ratio of the SiC materials and fused silica is around a 0.17 which is lower than for most brittle materials ($\nu \approx 0.25$) and for metals ($\nu \approx 0.34$ for TiAl_6V_4).

Table 2.1 Mechanical properties of SiC and other relevant materials at room temperature

Property	Unit	SSiC	C/SiC	CVD SiC	Fused silica	TiAl ₆ V ₄
ρ	[$\times 10^3 \text{ kg m}^{-3}$]	3.1	2.55	3.21	2.2	4.4
E	[$\times 10^9 \text{ N m}^{-2}$]	420	218	460	72	114
ν	[-]	0.16	0.17	0.18	0.17	0.34
σ_C	[$\times 10^6 \text{ N m}^{-2}$]	3000	?	2500	1100	970
σ_T	[$\times 10^6 \text{ N m}^{-2}$]	200	130	?	50	880
σ_B (3-pt)	[$\times 10^6 \text{ N m}^{-2}$]	450	160	470	80	880
m	[-]	10	17	11	?	-
K_{IC}	[$\times 10^6 \text{ N m}^{-3/2}$]	3.5	2.3	?	0.8	75
γ	[J m^{-2}]	14.2	23.6	?	4.3	-
K	[$\times 10^{-12} \text{ N m}^{-2}$]	-	-	-	3.5	-

Average strength and probability of failure

Table 2.1 shows three strength values for all materials: compressive strength σ_C , tensile strength σ_T and bending strength σ_B . These strengths are all average strengths. It is shown that the compressive strength of all types of SiC is considerably larger than the tensile and bending strengths. This is also true for fused silica, but not for TiAl₆V₄. The explanation is found in the fact that the brittle nature of SiC and fused silica is such that flaws in the materials will cause micro-cracks when loaded. In tension these micro-cracks will open up, allowing them to grow until complete

failure, whereas in compression the micro-cracks will be closed, preventing them from growth.

The strengths are average strengths due to the fact that the strength of brittle materials is highly dependent on the size and distribution of these flaws, because brittle materials do not yield (significantly). It is therefore highly important to know how well the strength of a material can be guaranteed and for how long.

The variability in strength and lifetime is the basis for flaw statistics for brittle materials [30]. Herein, individual flaws are regarded as members of some determinable solution. The most commonly used flaw distribution is that due to Weibull, based on the notion of the weakest link. The Weibull flaw statistics approach is an empirical approach assuming that strength and toughness remain constant during the service life of the material.

In terms of inert strengths σ_i , the Weibull fracture probability is defined in its simplest form by [31]:

$$P = 1 - \exp \left[- \left(\frac{\sigma_i}{\sigma_0} \right)^m \right] \quad (2.1)$$

with:

m Weibull modulus;

$\sigma_0 = \frac{\bar{\sigma}}{\Gamma(1 + \frac{1}{m})}$ Scaling stress;

$\bar{\sigma}$ Average strength in a certain loading condition, and;

$\Gamma(z)$ Gamma function of z .

In Figure 2.4 and Figure 2.5 Weibull plots of SSiC and C/SiC are shown. The probability of failure is plotted directly in logarithmic scale against the stress, also in logarithmic scale. The strengths and Weibull moduli of each of the plots is depicted in Table 2.2.

The figures show that for SSiC the maximum bending stress should not exceed $225 \cdot 10^6 \text{ N m}^{-2}$, and for the two C/SiC types the maximum bending stress should not exceed $100 \cdot 10^6 \text{ N m}^{-2}$ for a failure probability of 1/1000. Especially, with the vibration loads of up to 25 g quasi-static during launch, it would be unwise to exceed these stress levels for bending.

Note that the data on the different SiC in Table 2.2 and Figure 2.4 and Figure 2.5 is very scattered. No conclusion can be drawn on

the temperature dependence of the Weibull modulus or the dependence on loading conditions, because no information is available on the flaw distribution and number of samples tested.

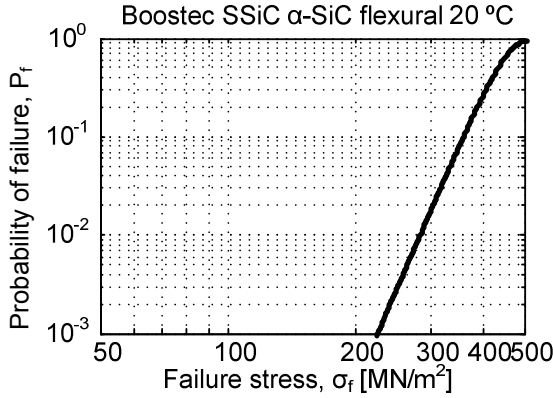


Figure 2.4 Weibull diagram for Boostec SSiC [23]

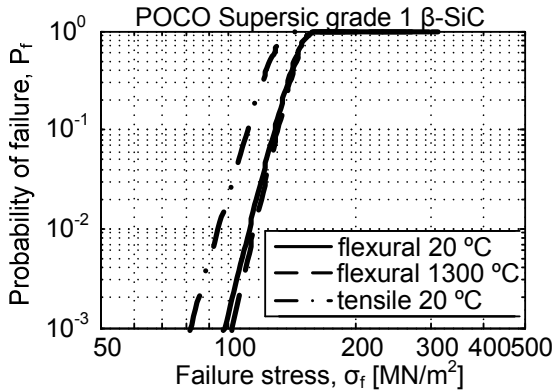


Figure 2.5, Weibull diagram for POCO C/SiC under different conditions [24]

Table 2.2 Scaling stress and Weibull modulus for the plots of Figure 2.4 and Figure 2.5

Type of SiC	Bending test	Temperature [°C]	Scaling stress [MPa]	Weibull modulus
Boostec α-SiC	3-point	20	450	10.0
POCO β-SiC	4-point	20	147	17.1
POCO β-SiC	4-point	1300	148	18.6
POCO β-SiC	4-point	20	129	15.1

SiC is able to resist much higher stress levels in compression than in bending or tension as all ceramics. For compressive loading the failure probability is not determined by any sub-critical crack growth [32]. However, for tensile or flexural loading, sub-critical crack growth is a determining factor for failure.

The maximum contact stress in Hertzian contact

Initial cracks in a Hertz ball-on-flat contact will be cone cracks in the flat surface. The tensile stress on the flat surface near the edge of the circle of contact is usually responsible for the initiation of cracks. The crack is a circle traveling perpendicular to the surface into the flat specimen for a short distance and will then evolve into a cone (Figure 2.6). The angle of the cone depends on the Poisson's ratio of the material and on the thickness of the specimen. This would imply that the tensile strength of the material is the limiting factor to the maximum load in a Hertzian ball on flat contact [33].

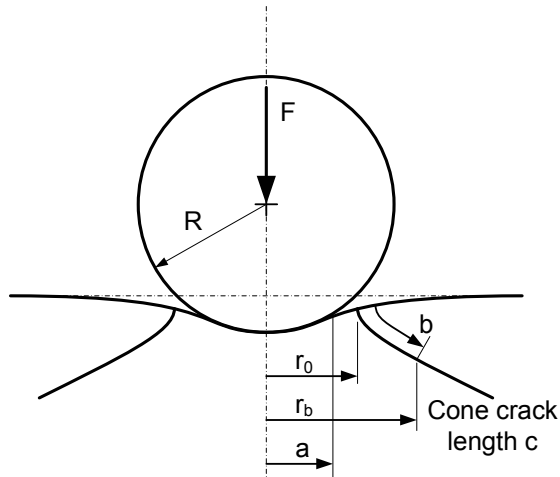


Figure 2.6 Geometry of a Hertzian cone crack [33]

The maximum tensile stress at the surface of a Hertzian ball-on-flat contact is [33]:

$$\sigma_T = \frac{(1-2\nu)}{2\pi} \cdot \left(\frac{4}{3} \cdot E^*\right)^{2/3} \cdot \left(\frac{F}{R^2}\right)^{1/3} \quad (2.2)$$

The cone crack begins to form, when the tensile stress is equal to the stress needed for growth of an existing flaw of length $2c$ in an infinite solid, which is given by [33]:

$$\sigma_a = \left(\frac{2 \cdot \gamma \cdot E}{(1 - \nu^2) \cdot \pi \cdot c} \right)^{1/2}, \quad (2.3)$$

where γ is the fracture energy of the material in J m^{-2} .

This is the Griffith criterion for fracture [33]. The fracture surface energy is a material property, which can be calculated from other material properties according to:

$$\gamma = \frac{K_{IC}^2 \cdot (1 - \nu^2)}{2 \cdot E}, \quad (2.4)$$

where K_{IC} is the stress intensity factor.

The values for K_{IC} and γ for the different relevant materials are shown in Table 2.1. If (2.2) and (2.3) are combined, a relation between the minimal load to induce a cone crack and the radius of the ball is obtained:

$$F = \left(\frac{2 \cdot \gamma \cdot E}{(1 - \nu^2) \cdot \pi \cdot c} \right)^{3/2} \cdot \left(\frac{2 \cdot \pi}{(1 - 2 \cdot \nu)} \right)^3 \cdot \left(\frac{4}{3} \cdot E^* \right)^{-2} \cdot R^2. \quad (2.5)$$

The Griffith criterion thus predicts that $F \sim R^2$. However, in 1891 Auerbach found empirically that for a wide range of brittle materials, the force F required to produce a cone crack is linearly proportional to the radius of the ball R , such that:

$$F = A \cdot R, \quad (2.6)$$

where A is the Auerbach constant ([33], [34]).

This empirical result has become known as Auerbach's law. The discrepancy between the theoretical prediction according to the Griffith criterion and Auerbach's can best be explained by the energy balance explanation. This explanation says that if the material contains flaws within a certain size range, namely within $0.01 < c/a < 0.1$, called the Auerbach range, the critical load F_c for which a cone crack will occur will be nearly constant for a number of starting radii r_0 of the crack and flaw sizes. For any other size distribution of flaws in the material, the critical load F_c will always be larger. This means that from the point of view of load

carrying capability without any cracks, the critical load within the Auerbach range of flaw sizes is a worst case scenario. For flaws within the Auerbach range the critical force is given by:

$$F_C = \left(\frac{3 \cdot \pi^3 \cdot K_{IC}^2}{16 \cdot \phi_a \cdot E^*} \right) \cdot R, \quad (2.7)$$

with ϕ_a a constant dependent only on the punch geometry, in this case a sphere: $\phi_a = 0.0011$.

The Auerbach constant A is thus:

$$A = \left(\frac{3 \cdot \pi^3 \cdot K_{IC}^2}{16 \cdot \phi_a \cdot E^*} \right). \quad (2.8)$$

For loads below the critical force, the probability of failure is nil. Above the critical load the probability of failure for a random distribution of flaw sizes increases with load according to the Weibull distribution.

In Table 2.3 the Auerbach constant has been computed for different contact situations between SSiC and fused silica. The actual maximum contact pressure is thus dependent on the radius of the ball on the flat surface. This information will be used in the design of the optical components of the BAM system in chapter 5.

Table 2.3 Fracture surface energy computed for SSiC and fused silica and Auerbach constants computed for SiC ball on silica flat contact and for SiC ball on SiC flat

Contact situation	Material	E^* [N m ⁻²]	K_{IC} [$\times 10^6$ N m ^{-3/2}]	γ [N m ⁻²]	A [N m ⁻¹]
SiC ball on silica flat	SSiC	$0.64 \cdot 10^{11}$	3.5	14.1	$1.0 \cdot 10^6$
	Fused silica	$0.64 \cdot 10^{11}$	0.8	4.4	$5.3 \cdot 10^4$
SiC ball on SiC flat	SSiC	$2.16 \cdot 10^{11}$	3.5	14.1	$3.0 \cdot 10^5$

Creep behavior

The Weibull function and Weibull diagram shown above do not reveal any time dependency of the failure behavior of a brittle material: i.e. creep or fatigue behavior.

It has never been shown that SiC (α -SiC and β -SiC) exhibits creep at room temperature or lower temperatures (operating temperatures of the BAM system). Creep experiments have been

performed at temperatures above 1300 °C. SSiC does show some creep and fatigue at these temperatures. At these temperatures SiC undergoes a phase change in which the SiC starts showing a liquid intergranular phase. This causes softening, and so (presumably) enables creep behavior in the SiC. This creep rate, even at these high temperatures, is of the order of 10^{-9} s^{-1} , which is rather low.

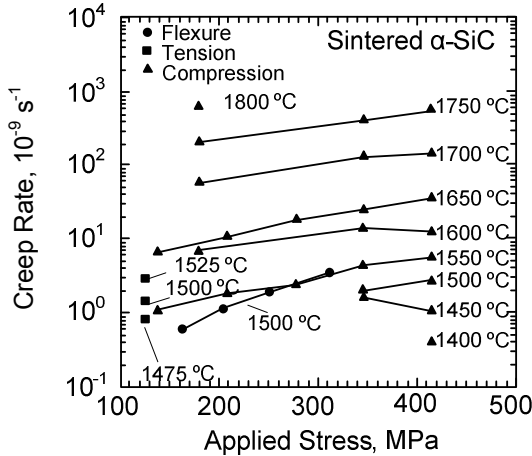


Figure 2.7 Creep rate of sintered α -SiC at elevated temperature [35]

Friction behavior

Literature on the experimental determination of friction and wear behavior of SiC is extensive. Especially in the late seventies and early eighties, extensive research has been performed in the tribological behavior of SiC ([35] to [45]). In the literature studied there are several aspects of the experiments that are general:

- The material studied is SSiC;
- Surfaces are polished or lapped beforehand to a roughness of $0.1 \mu\text{m}$;
- The temperature range of the experiments is 20 to 1000 °C;
- Almost all experiments are point-contact experiments;
- Normal forces vary from 0.1 N to 98 N.

In the literature studied the influence of several environmental aspects on the measured friction coefficients has been measured. Aspects of interest for the BAM system are: temperature, ambient pressure, normal force, humidity and sliding velocity. Literature

addresses all these aspects resulting in coefficients of friction of $\mu = 0.4$ to 0.8 . However, these aspects are mainly addressed outside the region in which the BAM system will operate.

The measurement data missing from the literature, but important for the BAM system, is the measurement of the friction of SiC-SiC contacts at temperatures below room temperature. Also, measurements at very slow velocities (of the order of mm s^{-1}) are of interest and high normal loads, because the BAM system is a steady state device. Furthermore, only α -SiC friction has been reported in the literature, whereas β -SiC is also considered in this thesis. Therefore, friction experiments have been conducted at room temperature and $-50\text{ }^\circ\text{C}$ (cooling with liquid nitrogen) at a velocity of 0.02 m s^{-1} , in pin on ring experiments with a contact pressure of $50 \cdot 10^6\text{ N m}^{-2}$ [46]. Different contacts involving SSiC, C/SiC, stainless steel 316 and aluminium 6061 have been tested, leading to the friction coefficients stated in Table 2.4. The friction coefficients are all in the range indicated by other experiments. The friction coefficients do alter at lower temperature, but for the the SSiC ring they increase slightly, whereas for the C/SiC ring they decrease. There is no explanation for this.

Table 2.4 Measured friction coefficients

Contact material		Friction coefficient	
ring	Pin	At $20\text{ }^\circ\text{C}$	At $-50\text{ }^\circ\text{C}$
SSiC	SSiC	0.45	0.50
	C/SiC	0.50	0.55
	Aluminium 6061	0.60	0.70
	SS 316	0.50	0.60
C/SiC	C/SiC	0.50	0.40
	Aluminium 6061	0.60	0.55
	SS 316	0.45	0.40

2.3.2 Thermal properties

The thermal properties that are generally of interest for the design of the BAM system are the coefficient of thermal expansion, the thermal conductivity and the heat capacity of the materials, not only at room temperature but in the entire trajectory of 100 K to 350 K . The thermal properties in this temperature trajectory are shown in Figure 2.8, Figure 2.9, Figure 2.10 and Figure 2.11 for Boostec SSiC [25], Poco C/SiC [24] and the recommended trajectories for SSiC from Touloukian ([26], [27]

and [28]). The coefficient of thermal expansion decreases with decreasing temperature from about $2 \cdot 10^{-6} \text{ K}^{-1}$ at room temperature to $0.2 \cdot 10^{-6} \text{ K}^{-1}$ at 100 K for both Boostec SSiC and Poco C/SiC.

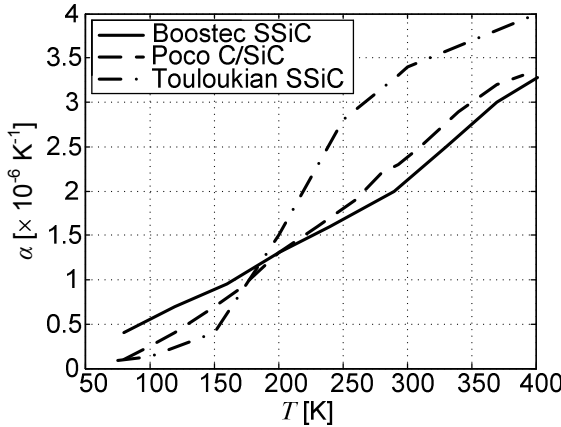


Figure 2.8 Coefficient of thermal expansion as a function of temperature

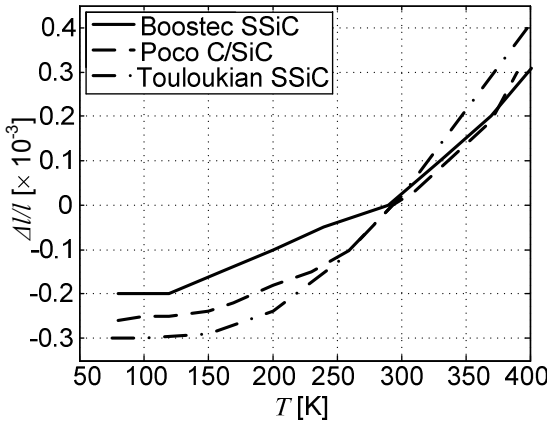


Figure 2.9 Thermal expansion from 293 K as a function of temperature

The recommended data from Touloukian shows a more extreme curve with larger coefficient of thermal expansion at room temperature. When looking at the thermal expansion data from room temperature, Boostec SSiC shows the smallest length change over a temperature trajectory of 293 K to 100 K.

Thermal conductivity data is available only for Boostec SSiC (Figure 2.10) and not for Poco or Xycarb C/SiC. The thermal conductivity of different SiC materials shows a large spread due to

the large influence of additive materials on this property. This is why Touloukian [27] does not provide a recommended value.

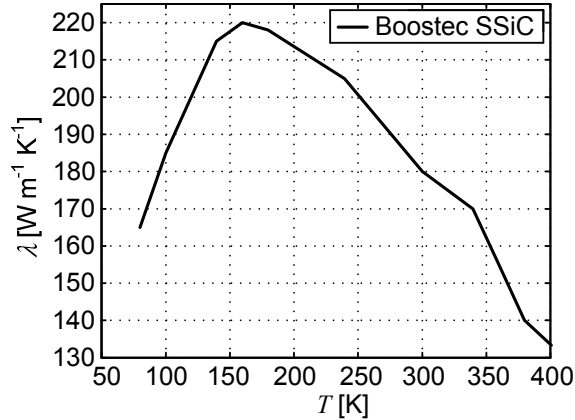


Figure 2.10 Thermal conductivity as a function of temperature [25]

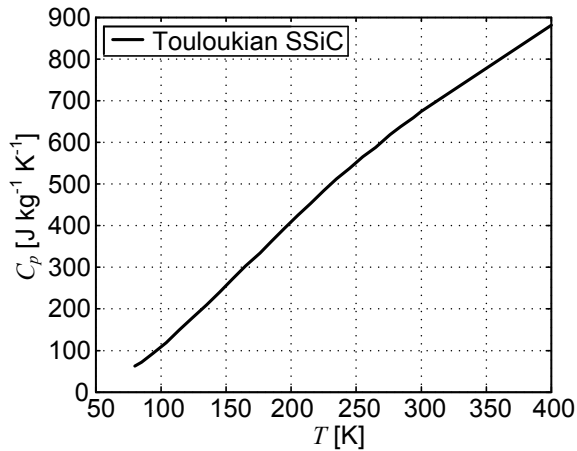


Figure 2.11 Specific heat as a function of temperature

Data on specific heat of Boostec SSiC and Poco C/SiC is not readily available. However, Touloukian shows that specific heat for several types of SSiC is very similar (Figure 2.11).

When combining Touloukian and Boostec SSiC data, a plot of the thermal stability (as defined in Section 1.2.2) as a function of temperature can be constructed (Figure 2.12). The thermal stability should preferably be as large as possible. The plot shows that the thermal stability increases exponentially with decreasing

temperature, which is beneficial for the stability of the BAM system at a working temperature of 100 K.

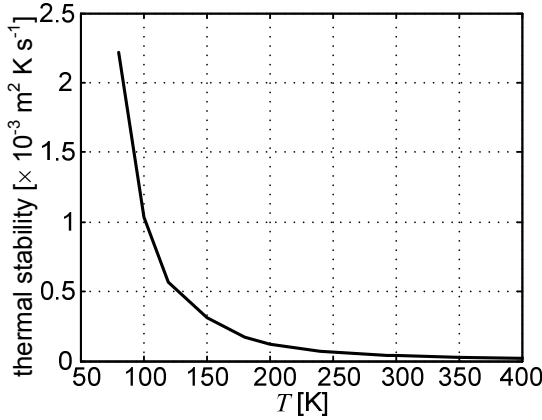


Figure 2.12 Volumetric thermal stability of SSiC as a function of temperature (data from Boostec and Touloukian combined)

Two thermal situations are of special interest for the BAM system:

1. The thermo-elastic behavior of the BAM system in 293 K to 100 K cool-down. Due to this temperature trajectory the optical components should not lose alignment with respect to each other.
2. The thermo-elastic behavior of the BAM system at 100 K with maximum temperature variation of ± 0.1 mK. Due to this thermal variation, the change of the OPD should be small enough to maintain measurement stability.

The length changes Δl over a distance l for the two types of SiC, fused silica and TiAl_6V_4 are shown in Table 2.5. This table will be used in chapters 4 and 5 to model the actual measurement stability of the BAM system.

Table 2.5 Thermal expansion of SSiC, C/SiC, fused silica and TiAl_6V_4 for a temperature change of 293 K to 100 K and the coefficient of thermal expansion at 100 K

	Boostec SSiC [25]	Poco C/SiC [24]	Fused silica (type I 1400 K) [26]	TiAl_6V_4 [26]
$\Delta l/l_{293-100\text{K}}$	$-2.0 \cdot 10^{-4}$	$-2.5 \cdot 10^{-4}$	$-0.13 \cdot 10^{-4}$	$-15.5 \cdot 10^{-4}$
$\alpha_{100\text{K}} [\text{m m}^{-1} \text{K}^{-1}]$	$0.5 \cdot 10^{-6}$	$0.25 \cdot 10^{-6}$	$-0.53 \cdot 10^{-6}$	$7.1 \cdot 10^{-6}$
$\Delta l/l_{+0.1\text{mK}@100\text{K}}$	$5.0 \cdot 10^{-11}$	$2.5 \cdot 10^{-11}$	$-5.3 \cdot 10^{-11}$	$71 \cdot 10^{-11}$

Thermal shock resistance

In a thermal shock situation, a large temperature gradient is created in a material. Temperature gradients lead to stresses due to expansion differences. If the thermal stresses due to a gradient are high enough, this can lead to micro-cracks in the part and even to failure. The thermal stress is expressed as follows [24]:

$$\sigma_{th} = \frac{\alpha \cdot E \cdot \Delta T}{1 - \nu} \quad (2.9)$$

According to Hasselman, the maximum temperature difference a material can absorb without the initiation of micro-cracks, is called the thermal shock resistance:

$$T_{SR} \approx \frac{\sigma_B \cdot (1 - \nu)}{\alpha \cdot E} \quad (2.10)$$

Note that the thermal shock resistance is in fact dependent on the geometry of the object and the velocity with which the thermal shock is applied. Therefore (2.10) provides only an indication. The measured thermal shock resistance of Poco C/SiC is $T_{SR} = 275$ K and of Boostec SSiC is $T_{SR} = 325$ K without knowledge of the geometry of the test object.

The actual temperature drop in the BAM system will be less than 200 K with a maximum cool-down rate of 10 K/min, which indicates that the exposure to space should not be a problem for the material itself.

Spatial variation in thermal expansion coefficient.

The variation in thermal expansion is an important parameter for the BAM system, because it can cause uneven thermal strains and stresses due to an overall temperature change. It might even cause misalignment of the optical components. According to Vukobratovich [47] at room temperature the variation of the coefficient of thermal expansion of CVD SiC is $\Delta\alpha = 88 \cdot 10^{-9}$ K⁻¹. The variation of the coefficient of thermal expansion of Boostec SSiC is $\Delta\alpha = 10 \cdot 10^{-9}$ K⁻¹ [48]. No information has been provided on the conditions in which these spatial variations of the coefficient of thermal expansion have been measured. No information is available on Poco C/SiC.

For ULE silica a value for the variation of the coefficient of thermal expansion is available: $\Delta\alpha = 20 \cdot 10^{-9} \text{ K}^{-1}$ [47]. An analysis on the influence of the variation of the coefficient of thermal expansion will be conducted in chapter 4.

2.3.3 Optical properties

α -SiC is birefringent due to its crystal structure ($n_o = 2.65$ and $n_e = 2.69$). Only under high pressures and temperatures can a partly transparent (100 – 800 nm) SiC crystal grow: Moissanite. Moissanite also has an α -SiC structure. β -SiC (CVD SiC) is not transparent and thus not birefringent and has a refractive index of ~ 2.63 .

The reflectivity of SiC in the visible spectrum (Figure 2.13) is nearly independent on the crystal structure and wavelength of the light. It is about 20 % ([49] and [50]). The reflectivity for infra-red increases to 40 %.

Due to the low reflectivity of SiC, it is often coated with a more reflective metallic layer, such as silver or gold. Gold does not adhere well to SiC. A CVD bonding layer of chrome/nickel or other reactive metals is usually applied first [49].

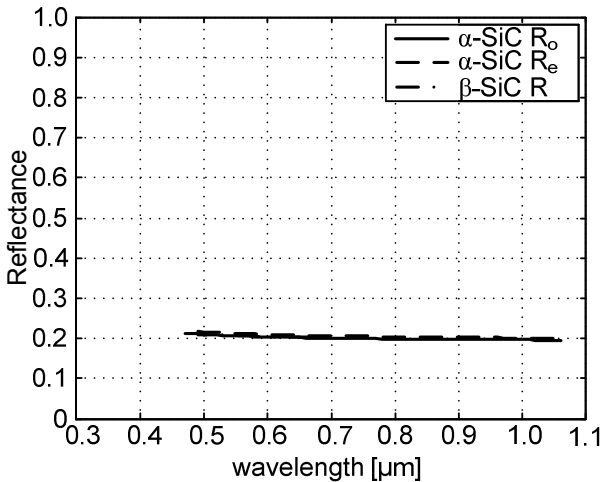


Figure 2.13 Reflectivity of SiC in the visible spectrum

2.3.4 Other properties

Oxidation resistance

SiC will not oxidate in temperatures of up to 600 °C in air, because a coating of SiO₂ is already formed on the surface of the SiC during sintering that prevents further oxidation. Above 1000 °C in a wet oxygen atmosphere, active oxidation takes place and the SiC will decompose. Still at high temperatures, SiC is twice as oxidation resistant as the best superalloys.

Aggressive chemicals

SiC is resistant to most chemicals (acids, alkali). Reaction with chemicals and metals only occurs at very high temperatures (> 1000 °C). Metals that can react with SiC at high temperatures are Zinc, Iron and Aluminium.

Radiation resistance

The (nuclear) radiation resistance of SiC is high in comparison to many metals, because of its resistance to the activation of dislocations and defects in the material. SiC/SiC composites are considered for application in fusion reactors in extreme radiation. SiC/SiC composites have larger reliability than un-reinforced SiC, but still have large radiation resistance, are applicable at high temperatures and have high thermal stability. However, still extensive research is being conducted to improve the radiation resistance of SiC/SiC composites and to overcome manufacturing challenges ([51], [52] and [53]) for fusion reactors.

In conclusion, the radiation and chemical resistance mentioned in this section are not of further concern for the BAM system, because it is unlikely that the stability of SiC will be affected by them. Oxidization of SiC will be used for a joining technique called hydroxide catalysis bonding, which is discussed in the next section and in chapter 6.

2.4 Mechanical design with Silicon Carbide

There are several aspects of SiC, which need special attention when designing structures with it. These are:

- Manufacturing limitations;
- Manufacturing accuracy;

- Design rules in dealing with SiC and;
- Bonding techniques.

2.4.1 Manufacturing limitations

Since the focus is especially on Boostec SSiC and Poco C/SiC, the main attention is paid to shapes which are made by CNC machining a block of green SiC or graphite, respectively. The limitations to shapes are therefore mainly governed by the limitations of standard CNC machining.

Green shape machining

In combination with the chalk-like behavior of the green material, the minimal wall thickness generally used by manufacturers like Boostec and Poco is 2 mm, although they are able to make also 1 mm thin walls. Due to machining forces thinner walls have a larger chance of breaking during green machining.

During green shape machining all sharp edges are rounded or chamfered, to prevent chipping during and after sintering and during product handling.

Machining after sintering

After sintering or Si-infiltration, the material attains full hardness. Because of the large hardness of SiC, any machining, grinding or polishing process after sintering means that diamond tools must be used. Because of the hardness, machining is a lengthy, and thus expensive, process. The wear rate of the tools is high. Furthermore, one should consider the fact that industrial machining will damage the surface, reducing the strength in the process.

To get an idea of the machining time: sawing 18 small blocks (35 mm × 22.5 mm × 10.5 mm) from an SSiC plate for example takes about a week (chapter 6). It is important to properly clamp the plate, such that bending and torque loads are limited.

C/SiC products need machining at all times after the infiltration process, because – inherent to the process – drops of free silicon will form on the surface of the material. Poco does this by grit blasting the product with high purity SiC. Xycarb does this by machining the part.

Grinding

Grinding can be performed to increase the surface flatness and decrease surface roughness after sintering. Typically 46 μm diamond crystals are used for grinding. Smaller grains will not decrease the roughness and micro-cracks in the surface caused by grinding [54]. Boostec SSiC exhibits a surface roughness of $R_a = \sim 0.5 \mu\text{m}$ after sintering. With grinding the roughness can be reduced to $R_a = \sim 0.3 \mu\text{m}$.

Polishing

For different types of SiC different surface properties (roughness and flatness figures) can be obtained by grinding and polishing. Three different types of SiC are considered: SSiC, C/SiC and CVD SiC. SSiC and C/SiC are SiC which can be applied in construction. CVD SiC is generally applied as a coating material on top of i.e. SSiC, C/SiC or carbon products.

Because of the high stiffness and the fact that SiC does not exhibit plasticity, the materials do not require any relaxation time. This makes polishing SiC a very controllable process.

The roughness of as-sintered SSiC (Boostec) is $R_a < 0.5 \mu\text{m}$. Grinding reduces roughness to $0.3 \mu\text{m}$ rms. Lapping allows to reduce this roughness below $0.1 \mu\text{m}$. SSiC is polishable to 1 nm surface roughness. However, because SSiC contains open porosity of about 3%, the micro-holes are excluded from this figure. This creates a light loss of about 3%. The light is scattered over wide angles, which may be a problem with the use of a large number of mirrors or applications sensitive to stray light.

For C/SiC the surface roughness after grinding is comparable to SSiC with $R_a < 0.5 \mu\text{m}$. The open porosity of C/SiC is 20% and of Xycarb C/SiC the porosity is 5%. The porosity of Xycarb C/SiC is lower due to the fact that holes remain filled with free silicon. Because of the high porosity C/SiC is generally coated with CVD SiC.

With CVD SiC ultra-low scatter surfaces of the order of 0.2 nm rms roughness can be achieved, due to the dense single phase surface. The rate of deposition of CVD SiC is $\sim 2 \text{ mm/day}$ ($\cong 72 \mu\text{m/hr}$) [55]. Typical CVD SiC coating thicknesses are $50\text{-}500 \mu\text{m}$ ([56], [57] and [58]).

To get an idea of the polishing achievements and times, the following examples are presented.

On small Xycarb C/SiC samples of 50 mm × 50 mm × 10 mm a 55 μm ± 5 μm CVD SiC coating has been applied. The samples have been ground first and then polished using conventional diamond slurry polishing techniques. In 55 hours polishing time a roughness of ± 0.4 nm rms has been achieved [59].

The 3.5 m SSiC Herschel primary mirror is not coated with CVD SiC. At Boostec grinding has been performed to reach a surface figure of 100 μm. At Opteon in Turku (Finland) the wavefront error has been lowered to 3 μm rms and the surface roughness to 30 nm by polishing.

The flatness that can be achieved for all types of SiC is comparable. Surface figures with ±20 nm rms uncertainty can be achieved [60].

Conventional grinding and polishing of SiC necessarily needs to be performed with diamond slurries, because SiC is extremely hard. Cerai and Zirconia based slurries will not polish SiC. Diamond-based slurries range from 8–12 μm to 0–1 μm grades. Due to the hardness of SiC diamond machining of SiC is performed with relatively shallow cuts [62]. The material removal rates for SiC are < 5 % that of conventional optical materials (e.g. glasses and simple metals).

Another polishing technique for SiC is ion beam figuring. The technique consists of rastering an ion beam across the mirror surface with a variable velocity to remove the desired shape and thickness of material from a substrate; it makes use of the ion sputtering process. The technique is usually used as the final step in optical manufacturing because the etch rate is low (10 nm/min at the beam centre). This rate is not very dependent on the hardness of the material. Also it introduces very little stress into the surface. Possible disadvantages are the introduction of heat and the increase of surface roughness due to the rastering. From an initial 243 nm rms roughness, after 6 ½ hours 28 nm rms is obtained and after another 8 ½ hours 13 nm rms roughness is obtained ([63] and [60]).

2.4.2 Manufacturing accuracy

The as-sintered accuracy of Boostec SSiC is determined by the accuracy with which the sintering shrinkage can be predicted. During sintering a predictable shrinkage of ~17 % occurs. Large dimensions can be predicted with 0.4% accuracy, caused by the slight variation of density for individual green blanks and after sintering the SiC product [23]. Boostec has stated the achievable as-sintered in ISO norms.

The tolerances according to these ISO norms on the as-sintered dimensions of SSiC products are depicted in tables 2.6 to 2.10 and Figure 2.14. The tolerances on C/SiC can be considered to be comparable after machining the residual silicon.

Table 2.6 Tolerances on linear size

Tolerance on linear size	Range of size	Tolerance
Holes diameter	if ≤ 37.5 mm	± 0.15 mm
	if > 37.5 mm	± 0.4 %
Ribs thickness		- 0.1 / +0.3
Other sizes	if ≤ 25 mm	± 0.1 mm
	if > 25 mm	± 0.4 %

Table 2.7 Angle tolerances according to ISO 2768-c

Tolerance class	Tolerances for a range of lengths of the small edge of the angle [mm]				
	≤ 10	$10 < \dots \leq 50$	$50 < \dots \leq 120$	$120 < \dots \leq 400$	> 400
Coarse	$\pm 1^{\circ}30'$	$\pm 1^{\circ}$	$\pm 0^{\circ}30'$	$\pm 0^{\circ}15'$	$\pm 0^{\circ}10'$

Table 2.8 Flatness and roughness tolerances according to ISO 2768-k

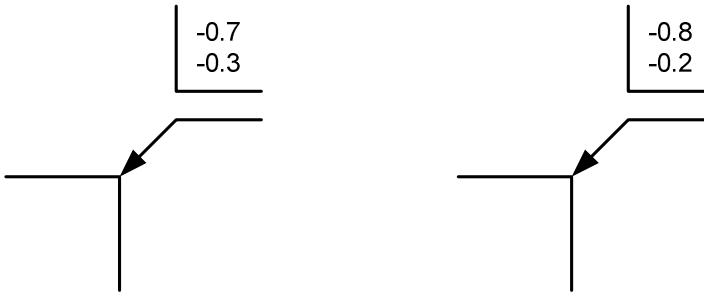
Tolerance class	Flatness and roughness tolerances for a range of nominal lengths [mm]					
	≤ 10	$10 < \dots \leq 30$	$30 < \dots \leq 100$	$100 < \dots \leq 300$	$300 < \dots \leq 1000$	$1000 < \dots \leq 3000$
K	0.05	0.1	0.2	0.4	0.6	0.8

Table 2.9 Orthogonality tolerances according to ISO 2768-k

Tolerance class	Orthogonality tolerances for a range of lengths of the small edge of the angle [mm]			
	≤ 100	$100 < \dots \leq 300$	$300 < \dots \leq 1000$	$1000 < \dots \leq 3000$
K	0.4	0.6	0.8	1.0

Table 2.10 Symmetry tolerances according to ISO 2768-k

Tolerance class	Symmetry tolerances for a range of nominal lengths [mm]			
	≤ 100	100 <...≤ 300	300 <...≤ 1000	1000 <...≤ 3000
K	0.6	0.6	0.8	1.0



a) Between as-sintered (not ground) faces

b) Between an as-sintered face and a ground face

Figure 2.14 Edge tolerances with sintered SiC according to ISO 13715

2.4.3 Design rules

Size limitations

The size of a monolithically sintered piece of SiC is limited mainly by the size of the existing sintering ovens. In the space industry typical limits are 1.5 m × 1.0 m × 1.0 m.

Because of the brittleness of the green material or the graphite, manufacturers generally consider 1 mm thickness of walls in a product to be the minimum thickness. If the wall thickness becomes lower, the chance of pieces of green material braking out during green machining, is considered to be too large.

Poco C/SiC also has a maximum wall thickness of 6 mm due to the maximum infiltration depth of silicon during SiC conversion.

The depth of holes and the complexity of shapes for SSiC and C/SiC products is dependent on the operating range for the CNC machining tools.

Compressive loading

The design should preferably be such that the material is loaded in the mode in which it is strongest, meaning compressive loading for SiC. The material is also strong in bending with $450 \cdot 10^6 \text{ N m}^{-2}$

for SSiC. However, the fracture probability suggests that it is unwise to apply bending stresses larger than $200 \cdot 10^6 \text{ N m}^{-2}$.

Rounded or chamfered edges

All edges of a product should be rounded or chamfered as much as possible, because the brittle nature of SiC, makes a SiC part very susceptible to chipping. This also means that SiC should not be loaded too close to the edges.

2.4.4 Joining techniques

Techniques which can be used for joining a SiC body to a SiC body are adhesive bonding, phenolic resin sintering, brazing, optical contacting, hydroxide catalysis bonding and clamping.

Adhesive bonding

In adhesive bonding an epoxy resin adhesive is used to bond two pieces of SiC together. For the BAM system application the epoxy adhesive needs to be space qualified, such that it will not outgas in space vacuum conditions. Also it will need to be able to cope with a – for adhesives – large temperature range of 100 – 350 K. Examples of space qualified epoxies are Araldite AV 138 and 3M EC 2216. The adhesive layer thickness can generally be reduced to 5 to 10 μm . The surface does not need to be very flat to achieve a good bond. However, great care has to be taken generally in preparing the adhesive surfaces before applying the adhesive. This is done by applying a primer, which is in most cases the adhesive but then strongly diluted to make the contact with the body more efficient. C/SiC has large porosity which makes it difficult to use an adhesive with low viscosity primer, because the primer will go into the pores. Adhesive can be applied at room temperature, although it is generally cured at slightly elevated temperature to speed up the curing process. Adhesives generally are subject to creep and relaxation. They are generally also sensitive to chemical influences and ageing.

Phenolic resin sintering

For the C/SiC production a technique exists to bond two machined graphite pieces of material together. In this technique a phenolic resin is applied at the interface and the pieces are glued together. During Si infiltration the organic compounds of the resin are

burned away leaving a SiC transfer. The distinction between the two pieces disappears completely, giving the bond exactly the same mechanical and thermal properties as the rest of the material. This method of phenolic resin sintering is practiced by companies like ECM and Poco Graphite.

This technique has also been applied for SSiC. However, during sintering SSiC shrinks with 17% and the shrinkage can vary with 0.4% throughout the body, which often leads to cracks in the bond layer during cool down.

Brazing

In brazing, two pieces of sintered SiC can be bonded together using cobalt silicide applied in between the two pieces. The piece is then placed in a vacuum oven and annealed at approximately 1250 °C.

Boostec uses a braze, which is thermally matched to the SiC material and the brazing temperature is 1450 °C. This brazing technique has already been successfully applied to the 3.5 m Herschel telescope primary mirror. After brazing the quality of the braze can be checked ultrasonically [22].

The typical thickness of such a braze is dependent on the initial surface roughness and figure. To create a good bond the surface is generally ground to 5 µm flatness. The braze thickness will be 5 – 10 µm.

Optical contacting

Direct bonding, also called optical contacting, uses the fact that two smooth and atomically flat surfaces of almost any material adhere to each other when brought into contact. Three kinds of forces determine the adhesion of the bond:

1. Van-der-Waals forces; caused by atomic and molecular dipoles and can be either dipole-dipole interaction (force between two polar molecules), dipole-induced interaction (force between a polar and a non-polar molecule) or dispersion interaction (force between two non-polar molecules resulting from instantaneous dipoles created by temporally uneven distributions of electrons in the electron clouds);
2. Electrostatic or Coulombic forces (if two objects are macroscopically charged);

3. Short range (0.1 – 0.2 nm) forces; which can be ionic, covalent or metallic overlap of electron clouds.

The parameters that influence bonding are:

1. Micro-roughness; the RMS roughness should be 0.1 nm to 0.5 nm depending on the main attractive force;
2. Presence of particles; they can cause circular non-bonded areas. Five 1 μm particles on a square centimeter can completely prevent bonding;
3. Waviness of the surfaces; at room temperature in clean room conditions the surface flatness must be < 50 nm to make the bond successful.

Hydroxide catalysis bonding

Hydroxide catalysis bonding or ‘silicate’ bonding is a bonding technique invented and patented by Gwo ([64] and [65]) at Stanford University. The technique has been used in the Gravity Probe B space experiment (successfully launched in 2004). The technique has been applied by the Institute of Gravitational Research at the University of Glasgow in the GEO 600 gravitational wave detector [66] and on the LISA Technology Package interferometer for LISA pathfinder ([67], [68] and [69]).

The hydroxide catalysis bonding technique is a technique that achieves bonding between a number of materials if a silicate-like network can be created between the surfaces, or in other words any silica containing material. Examples are silica, Zerodur, fused quartz, ULE glass and granite.

Any materials containing surface hydroxide groups, like iron, are not suitable for hydroxide catalysis bonding.

The two silicate based materials are bonded using an alkaline bonding solution: like sodium hydroxide (NaOH), potassium hydroxide (KOH) and sodium silicate (Na_2SiO_3) dissolved in water.

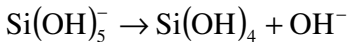
The bonding surfaces must have a peak-to-valley (PV) flatness of ≤ 60 nm if a hydroxide solution is used. Both bonding surfaces are cleaned in a clean environment to be free of chemical and particulate contaminants. The bonding solution is filtered and dispensed on the bonding surface with a volume of ≥ 0.4 $\mu\text{l}/\text{cm}^2$. The other piece is then placed gently on top of the piece with the bonding solution and is possibly slightly compressed to ensure a

uniform bond. At this moment the hydroxide catalysis commences and consists of three steps [64]:

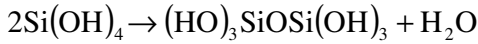
1. Hydration and etching: in which the OH^- ions in the bonding solution act as a catalyst and etch the silica surfaces in contact. This causes the liberation of silicate ions.



2. Polymerization: due to the hydration the active number of OH^- ions reduces and the pH of the solution decreases. If the $\text{pH} < 11$, the silicate ions disassociate:



And siloxane chains and water are formed:



Once the siloxane chains are formed the bond is rigid.

3. Dehydration: in which the water migrates or evaporates. After 4 weeks of curing at room temperature full strength is achieved.

For optimal strength the $\text{NaOH}:\text{H}_2\text{O}$ ratio is 1:256 in case of a silica to silica bond of 50 mm^2 . The first 2 steps of hydroxide catalysis are achieved after approximately 150 seconds. The bonding thickness is approximately 50 nm.

The roughness is not an issue. The roughness can even be $0.5 \mu\text{m}$ to avoid optical contacting during alignment.

SiC cannot be used directly for hydroxide catalysis bonding. During polishing to $\lambda/10$ PV flatness, any SiO_2 layer formed during sintering is removed. To make bonding of to SiC components possible, the surface must have a thin layer of SiO_2 . This layer is formed first cleaning the SiC pieces and then placing the pieces in a quartz tube furnace at $1150 \text{ }^\circ\text{C}$ in a wet oxygen environment. The SiO_2 layer thickness must be smaller than 250 nm to maintain the $\lambda/10$ PV flatness.

The layered structure of hydroxide catalysis bonded SiC pieces is shown in Figure 2.15.

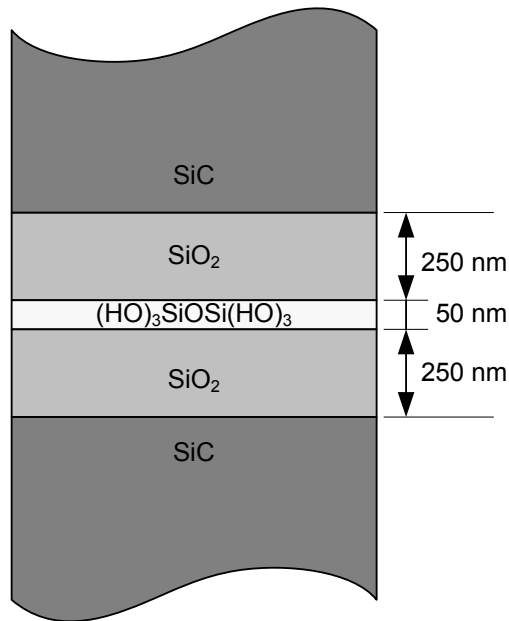


Figure 2.15 Layer structure of hydroxide catalysis bonded SiC pieces

Clamping

In clamping the two bodies are connected to each other by applying a mechanical force to the contacting surface, such that it is fixed on friction or is prevented from movement due to hitting a stop. Examples of clamping are a bolted joint or a metallic spring which is preloaded to tension the one body to the other. The design of such a clamping solution is very dependent on the design of the optical component itself.

2.5 Conclusions

The SiC material properties discussed in this chapter are essential for making an opto-mechanical design of the BAM system. Each of these properties is used for either the design of the optical benches in chapter 4 or the design of the optical components in chapter 5. On the one side, the presentation of these properties gives insight in the possibilities and impossibilities of designing opto-mechanical systems in SiC. On the other side, properties SiC are directly used in the analysis and design of the BAM system. The thermal properties as a function of temperature for example are used extensively in chapter 4 to assess the thermal stability of the

optical benches. The maximum allowable Hertzian contact stresses are used in chapter 5 for dimensioning SiC balls in V-grooves. Some of the properties will also be addressed in chapter 6 where some experiments are discussed, like experiments with hydroxide catalysis bonding.

3 Optical design

The measurement principle of the BAM system has been explained in chapter 1. Two parallel beams from two optical benches are sent through each telescope (Figure 1.3), which causes the beams to interfere, creating two interference patterns on the CCD focal plane of the PLM (Figure 1.4). If one pattern shifts with respect to the other, this is a measure of the variation of the basic angle. To be able to measure basic angle variations with $0.5 \mu\text{as}$ (2.5 prad) accuracy, the optical design of the BAM system will have to meet a number of requirements. The requirements for the optical design of the BAM system are the topic of this chapter.

In section 3.1, the mathematical background to the fringe patterns created by interference of 2 beams is discussed. The parameters which affect the size-characteristics of the fringe patterns are illustrated. Next, in section 3.2, attention is paid to the physical effects that can change the fringe position. The main attention here is paid to orientation changes of the optical benches or optical components. In section 3.3, the arrangement of optical components is examined, especially to cancel out any relative error due to relative rotation of the two subsystems. In section 3.4 then, the requirements are stated and quantified. After examining the telescope and focal plane properties, the laser requirements are stated, followed by alignment accuracy and stability of the BAM system properties. Finally, the measurement stability is discussed. Using the requirements information, in section 3.5, a rough alignment plan is constructed. Note that the alignment plan is focused only on determining an order of aligning the optical

components. The chapter ends with a summary of the requirements.

3.1 Interference patterns

Each beam $i = 1, 2$ traveling from one bar through a telescope has a flat wavefront with a truncated Gaussian intensity distribution. The irradiance of each beam i is then given by [70]:

$$I_i(x, y) = I_{0i} \cdot \left(\frac{2 \cdot J_1 \left(k \cdot \frac{D_i}{2} \cdot \sin \theta \right)}{k \cdot \frac{D_i}{2} \cdot \sin \theta} \right)^2, \quad (3.1)$$

with:

I_{0i}	Maximum irradiance at the centre of focus;
$J_1 \left(k \cdot \frac{D_i}{2} \cdot \sin \theta \right)$	First order Bessel function of the first kind;
$D_i, i = 1, 2$	Diameter of the i^{th} beam;
$k \equiv \frac{2\pi}{\lambda}$	Wave number;
λ	Laser wavelength in vacuum and;
$\theta = \tan^{-1} \left(\frac{\sqrt{x^2 + y^2}}{f} \right)$	The angular position of the irradiance, with respect to the centre of the focal plane at distance f .

By focusing these beams with the telescope, they act like double slit diffraction creating a two-beam interference pattern given by [71]:

$$I(x, y) = I_1(x, y) + I_2(x, y) + 2\sqrt{I_1(x, y) \cdot I_2(x, y)} \cos \left(\frac{2 \cdot \pi \cdot a \cdot x}{\lambda \cdot f} \right). \quad (3.2)$$

where a is the baselength.

In (3.2) it has been assumed that there is no optical path length difference between both beams and that both beams are exactly parallel and perpendicular to the focal plane. Also, the detector is located exactly in the focal point of the on-axis telescope with no aberrations.

The global picture of the double beam interference can be seen in Figure 3.1. The mirror in the picture represents the telescope. Note that the interference plot shows a pattern for which $a = 3D$.

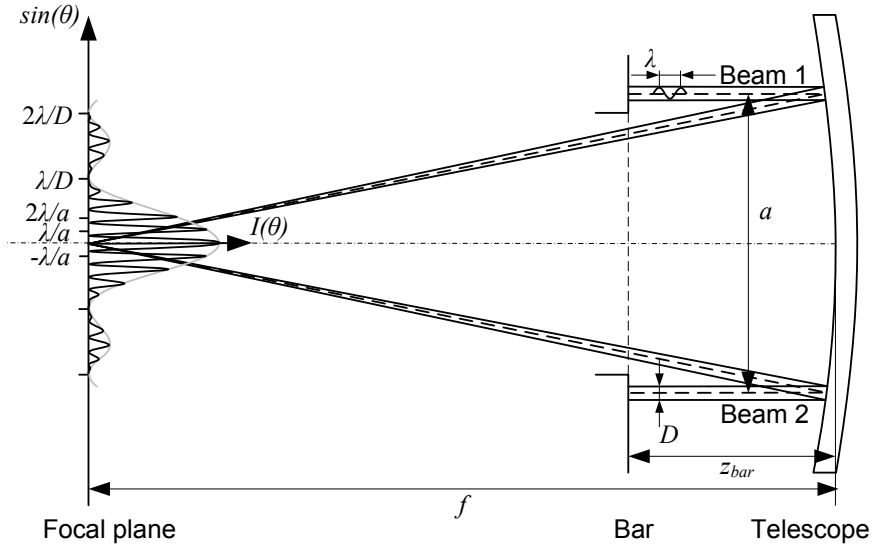


Figure 3.1 Double beam interference

For two beams with wavelength λ and diameter D and a base length a between the beams, which are send through a telescope with focal length f , the diameter of the Airy disc is given by:

$$D_{Airy} = \frac{2.44 \cdot f \cdot \lambda}{D} \tag{3.3}$$

The fringe width can be computed using:

$$d_{fringe} = \frac{f \cdot \lambda}{a} \tag{3.4}$$

The number of fringes within the Airy disc can then be calculated by dividing the Airy disc diameter with the fringe width:

$$N = \frac{D_{Airy}}{d_{fringe}} = \frac{2.44 \cdot a}{D} \tag{3.5}$$

3.2 Causes for fringe shifts

With the measurement method used, there are five possible causes for a shift of the fringes of one of the interference patterns on the CCD camera. These causes are:

1. Rotation $\delta\theta_{telescope}$ of the telescope, which is illustrated in Figure 3.2. Note that this is the actual variable that must be measured.

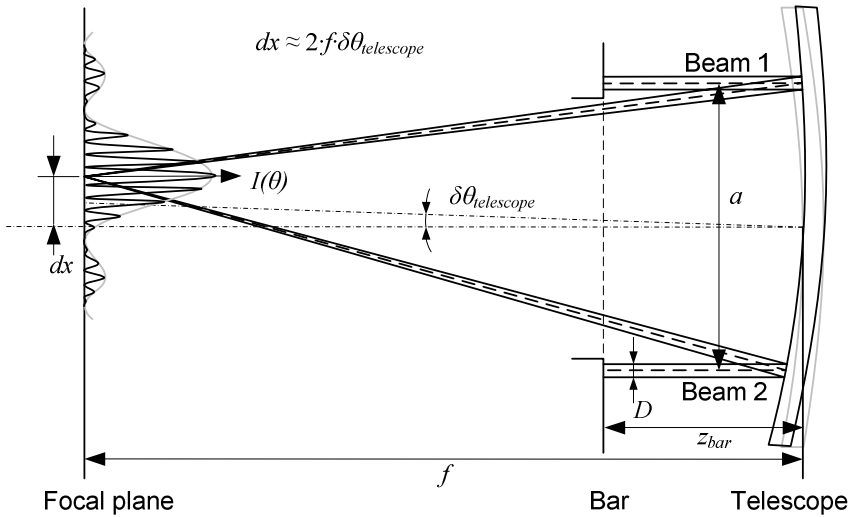


Figure 3.2 Relation between pattern shift and the rotation of the telescope mirror

This causes a shift of the entire Airy disc created by the two interfering beams of:

$$dx = f \cdot \tan(2 \cdot \delta\theta_{telescope}). \tag{3.6}$$

2. Rotation $\delta\theta_{bar}$ of the bar from which the beams are traveling (Figure 3.3).

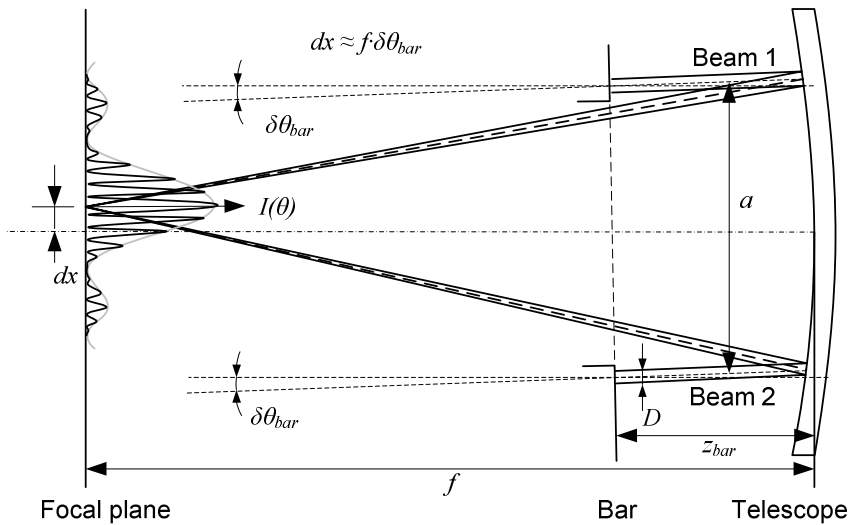


Figure 3.3 Relation between the rotation of the bar and a pattern shift

This causes a shift of the entire Airy disc created by the two interfering beams. The shift is equal to:

$$dx = f \cdot \tan(\delta\theta_{bar}). \tag{3.7}$$

When comparing (3.6) and (3.7) we see, that the fringe shifts are of the same order of magnitude for $\delta\theta_{bar} \approx \delta\theta_{telescope}$. This would mean that the rotation of a bar is a serious source of error for the measurement of $\delta\theta_{telescope}$. However, the measurement will be a relative measurement and by smart optical design this source of error can be cancelled out. This will be discussed in section 3.4.

3. An optical path length difference change δOPD between the two interfering beams (Figure 3.4).

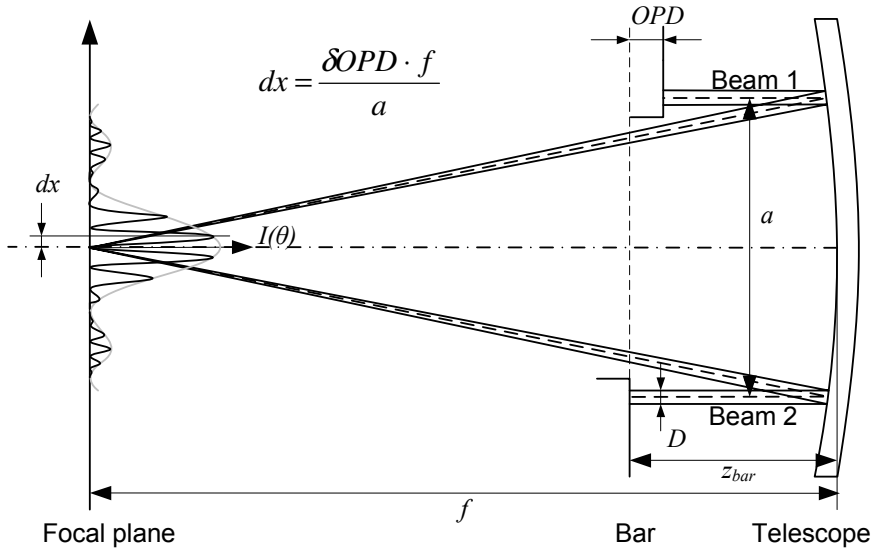


Figure 3.4 Relation between an OPD between the two beams and a pattern shift

This causes a shift of the fringes within the Airy disc of:

$$dx = \frac{\delta OPD \cdot f}{a}. \tag{3.8}$$

Compared to the other two causes for fringe shift, this is a different reaction. Therefore, if one would monitor the position of the entire Airy disc, the OPD source of error could be filtered out. However, it is very unlikely that the Airy disc itself can be monitored sufficiently accurate, because of a low signal/noise ratio

for low intensity fringes. Therefore, only the high intensity fringes will be monitored, making it impossible to differentiate between the three sources of fringe shifts mentioned up to this point. Another observation that can be made with regard to the OPD error is that it is a periodic error source, the fringe shift is at its maximum for an OPD equal to half the wavelength.

4. A tilt of one beam with respect to the other beam on the same bar. This error source is illustrated in Figure 3.5. The consequence of this tilt is that the overlap of the Airy discs of both beams is reduced. This also introduces a change in the optical path length difference:

$$\delta OPD_{\delta\theta_{beam}} = (z_{bar} + f) \cdot \left(\sqrt{1 + \delta\theta_{beam}^2} - 1 \right) \cong \frac{1}{2} \cdot (z_{bar} + f) \cdot \delta\theta_{beam}^2. \quad (3.9)$$

The shift of the fringes caused by this optical path length change can be computed using (3.8).

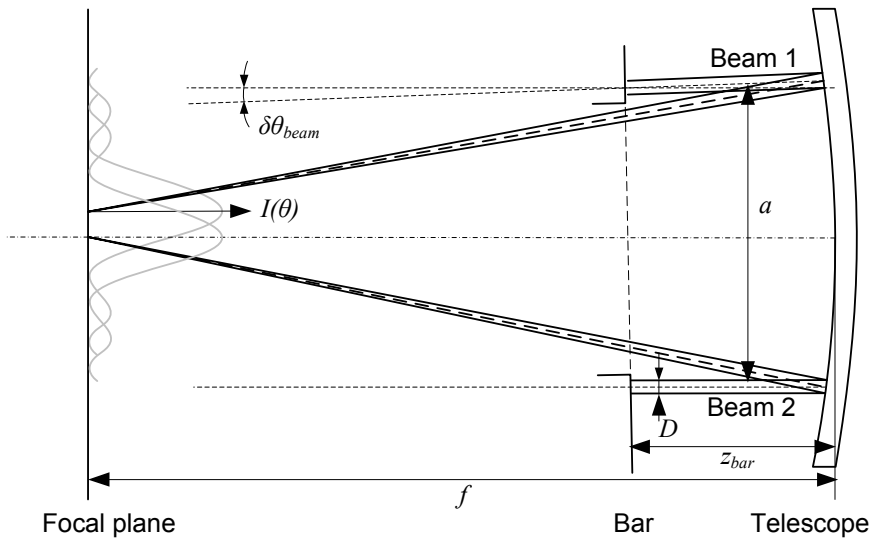


Figure 3.5 Relation between the rotation of one beam and the overlap of Airy discs

5. Laser wavelength instability. In case the initial OPD between two interfering beams is not exactly zero, wavelength change results in fringe position change. When the OPD is exactly zero, the zero optical difference fringe (white fringe) is centered exactly in the diffraction spot. In this case a wavelength change results in “breathing” of the fringes, where the white fringe position is fixed.

When the initial OPD is not exactly zero, the white fringe is decentered in the diffraction spot. The decenter of the white fringes can be expressed in the number of fringes:

$$N_d = \frac{OPD}{\lambda}. \quad (3.10)$$

In this case a wavelength change results in an average fringe shift, which can be explained as an additional apparent change of the OPD:

$$\delta OPD = N_d \cdot \delta \lambda = OPD \cdot \frac{\delta \lambda}{\lambda}. \quad (3.11)$$

The five error sources can be included in the diffraction equation by including angular errors $\delta\theta_{bar}$, $\delta\theta_{telescope}$ and $\delta\theta_{beam}$ and the OPD in the equation for one fringe pattern. Also the two-dimensional situation can be extended to a three-dimensional situation with angular errors $\delta\psi_{bar}$, $\delta\psi_{telescope}$ and $\delta\psi_{beam}$:

$$I(x, y) = I_1(x - f \cdot \theta_1, y - f \cdot \psi_1) + I_2(x - f \cdot \theta_2, y - f \cdot \psi_2) + \dots \\ \dots 2\sqrt{I_1(\dots) \cdot I_2(\dots)} \cos\left(\frac{2 \cdot \pi \cdot a \cdot x}{\lambda \cdot f} - \frac{2 \cdot \pi \cdot OPD}{\lambda}\right) \quad (3.12)$$

in which:

$$\theta_1 = \delta\theta_{bar} - 2 \cdot \delta\theta_{telescope} + \delta\theta_{beam1} \\ \psi_1 = \delta\psi_{bar} - 2 \cdot \delta\psi_{telescope} + \delta\psi_{beam1} \\ \theta_2 = \delta\theta_{bar} - 2 \cdot \delta\theta_{telescope} + \delta\theta_{beam2} \\ \psi_2 = \delta\psi_{bar} - 2 \cdot \delta\psi_{telescope} + \delta\psi_{beam2}$$

Note that there is one additional error source, which affects the fringe pattern. This source does not cause a fringe shift of the white fringe. However, it does affect the fringe period and fringe width. This is a translation of one beam with respect to the other along the x-axis. This translation does not affect the position of the fringe pattern on the focal plane, because the position of the fringe pattern is only dependent on the angular orientation of the beams.

The fringe width is dependent on the focal length of the telescope f , the base length a and the wavelength of the light λ , like:

$$d_{fringe} = \frac{f \cdot \lambda}{a}. \quad (3.13)$$

Any change δa in base length a will result in a change in fringe width δd_{fringe} according to:

$$\delta d_{fringe} = -d_{fringe} \cdot \frac{\delta a}{a + \delta a} \cong -\frac{d_{fringe}}{a} \cdot \delta a. \quad (3.14)$$

3.3 The optical design

The error created by rotation of a bar with respect to the focal plane can be cancelled out. This can be explained by the fact that the BAM system does not make a measurement of the rotational stability of each telescope, but a relative measurement of the stability of the basic angle between both telescopes. This means that the variation on the distance between both fringe patterns is measured instead of the absolute position of the fringe patterns on the focal plane. The requirement is thus that any rigid body movement of the bars should have no influence on the differential fringe pattern shift. Since the telescopes only measure the angular position of the fringe patterns, any rigid body translation of the bars will not affect the measurement regardless of the optical design. However, the optical design should be made such that no differential fringe pattern shift occurs due to rigid body rotations of the bar.

In Figure 3.6 a possible optical design of the BAM system is shown. In case bar 1 makes a rigid body rotation $\delta\theta_{bar1}$, this will result in a fringe shift of the pattern created by beams 1 and 2. This also results in a rotation of the beams traveling from bar 1 to bar 2 and consequently the beams 3 and 4 will rotate. The number of optical components in each path is even, such that the fringe shift created by beams 3 and 4 is equal to the fringe shift of the pattern created by beams 1 and 2. In turn this means that the rotation of bar 1 does not have any influence on the differential fringe pattern shift [72].

The rigid body rotation of bar 2 ($\delta\theta_{bar2}$ in Figure 3.6) does not have an effect on the fringe pattern position on the focal plane created by beams 3 and 4 as long as each beam is reflected by an even number of mirrors on bar 2, [72]. The first mirror introduces an error in angle of the reflected beam; however, this error is compensated for by the second mirror, which has rotated around the same point as the first mirror. Essentially each beam is traveling through a retro-reflector.

There is one other danger for the measurement of the basic angle variation due to rotation $\delta\theta_{bar2}$ of bar 2. This is the introduction of an optical path length difference between beams 3 and 4. However, the optical design shown in Figure 3.6 is insensitive to this optical path length change, because the base lengths between the pairs of beams 3'-4' and 3-4 are equal and the pairs of beams 3'-4' and 3-4 are parallel. The explanation for these requirements in the optical design is given in Appendix B using a tunnel diagram method.

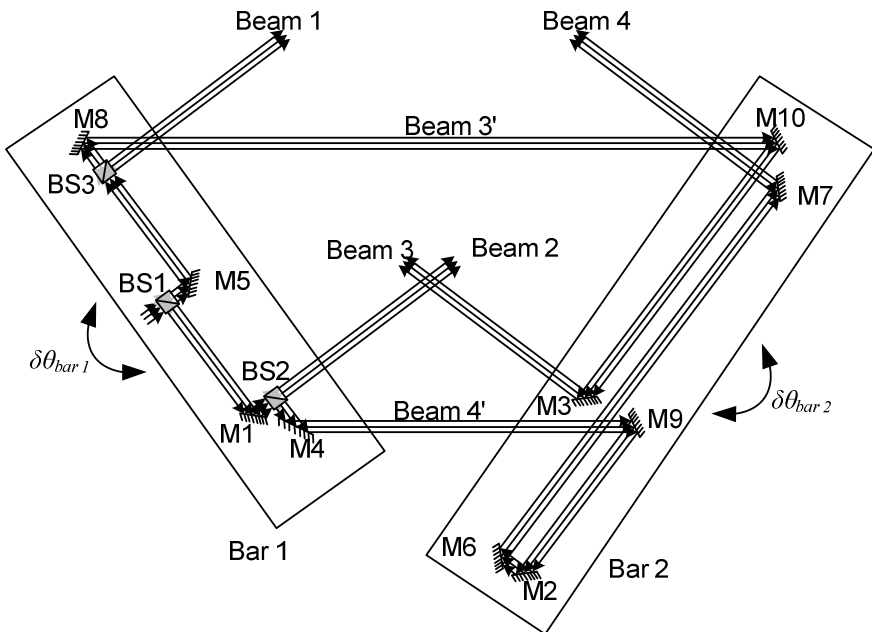


Figure 3.6 A possible optical design of the BAM system. *M* designates a mirror and *BS* a 50-50% beamsplitter.

In summary, there are several error sources which can cause a relative fringe shift between the two diffraction patterns on the focal plane. The error sources all cause a fringe shift within the pattern due to the fact that they cause a change in optical path length difference, whereas the rotation of the telescope will cause a shift of the entire diffraction pattern.

These error sources are:

- Rotation of bar 2 in combination with $\delta\theta_{bar}$

- Initial difference in base length between the pairs of beams 3'-4' and 3-4 ΔBL
- Initial non-parallelism of beam pair 3'-4' $\Delta\theta_{beam'}$
- A non-parallelism of beam pairs 1-2 or 3-4 $\delta\theta_{beam}$
- Wavelength instability in combination with $\frac{\delta\lambda}{\lambda}$
 - Initial optical path length difference OPD
- Optical path length variation independent on the optical design δOPD

The total variation in optical path length difference of bar 2 is now given by:

$$\delta OPD_{total} \approx (\Delta BL + (x_{Oi} + PL) \cdot \Delta\theta_{beam'}) \cdot \delta\theta_{bar} + \frac{1}{2} \cdot (z_{bar} + f) \cdot \delta\theta_{beam}^2 + \dots \cdot \left(\dots OPD \cdot \frac{\delta\lambda}{\lambda} + \delta OPD \right) \quad (3.15)$$

with:

- x_{Oi} x-distance of the rotation point to the first mirror on bar 2;
- PL total path length of the beam on bar 2.

For bar 1, the OPD error caused by rotation of the bar is not taken into account, because it will not cause a relative fringe shift. However, stability requirements for components on bar 1 are governed by pairs of beam 3'-4' and 3-4, because these beams travel through the components on bar 1 as well.

3.4 Requirements

The requirements analysis starts with an analysis of the laser source that should be used for the BAM system. The requirements analysis is continued by determining the properties of the beams traveling from the BAM system through the telescopes. From there, the requirements for individual optical components are determined. The latter requirements will be subdivided in alignment requirements including an alignment plan, alignment stability requirements and measurement stability requirements.

3.4.1 Choice of the laser source

There are several properties the laser source should have for the BAM system in GAIA. The properties are shown in Table 3.1.

With regard to the space qualified lasers, not very many space missions have flown with a low-power laser on board. For outgassing and pressure reasons, only solid-state lasers are an option for space applications. Lightwave Electronics and Tesat-Spacecom have space-qualified Nd:YAG lasers, which have been adapted to the NPRO (Non-Planar Ring Oscillator) laser. Such lasers have a 1064 nm wavelength, or, if applied with a frequency-doubling crystal, 532 nm. This wavelength is very suitable for the BAM system of GAIA.

Table 3.1 Requirements of the light source

Requirements	Quantity	Value
Output wavelength in visible spectrum ([3] p. 62)	$\lambda_{\min} - \lambda_{\max}$	380 – 780 nm
Pressure range	p	$10^5 - 10^{-10}$ Pa
Temperature range	T	100 – 293 K
Maximum power consumption ([3] p. 89).	$P_{in \max}$	20 W
Minimum lifetime ([3] p.3).	$lifetime_{\min}$	6 years

3.4.2 Beam requirements

When the metrology system in GAIA is considered, there are some properties and requirements, which determine the other dimensions of the system. These basic requirements are given in Table 3.2.

Table 3.2 Basic optical properties and requirements of the metrology system of GAIA

Property/ requirement	Symbol	Value
The width of each fringe is comparable to the width of a real star with the same wavelength as imaged by the telescope.	d_{fringe}	$50 \cdot 10^{-6}$ m
The focal length of the telescope	f	46.67 m
Wavelength of the double Nd:YAG laser diode	λ	$532 \cdot 10^{-9}$ m
Number of fringes in Airy disc	N	60

Based on these initial values, the base length a (distance between both beams), the diameter of the laser beams D and the Airy disc diameter D_{Airy} can be computed (Table 3.3).

The remaining requirements for the beams traveling from the bars through the telescopes can be subdivided in alignment accuracy and stability requirements, and in measurement stability requirements. Alignment accuracy indicates the uncertainty in the relative initial alignment of the components. Alignment stability indicates a lifetime requirement on the stability of the aligned components. Measurement stability indicates the stability of components during measurements to obtain the required minimal resolution of the BAM system of 0.5 μ as.

Table 3.3 Resulting data from basic requirements

Description	Equation	Value
Base length	$a = \frac{f \cdot \lambda}{d_{fringe}}$	0.50 m
Airy disc diameter along scan	$D_{Airy} = N \cdot d_{fringe}$	$3.0 \cdot 10^{-3}$ m
The diameter of each laser beam	$D = \frac{2.44 \cdot a \cdot d_{fringe}}{D_{Airy}}$	$20 \cdot 10^{-3}$ m

3.4.3 Alignment accuracy and stability

Angular accuracy of the beams

Bar 1 should be mounted onto the optical bench of the payload module with sufficient angular accuracy to make sure that the fringe pattern ends up on the CCD camera at the desired position. The mirrors on bar 2 should be aligned such that the fringe pattern from bar 2 is right above the fringe pattern from bar 1. In this way the thermal expansion variation of the CCD's will not affect the differential fringe shift between both patterns.

The empty space between the two fringe patterns in the CCD image field must be at least 1/3 of the Airy pattern size to prevent crosstalk between them. However, the distance between the fringe patterns must be so small that they fall on one CCD to cancel the movement of the CCD's with respect to each other. The width of a CCD is 45 mm. This corresponds to 1 mrad alignment angle. To align the fringe patterns with sufficient accuracy on the CCD, an angular uncertainty of ± 0.1 mrad is needed. The angular alignment stability of the bars should also be ± 0.1 mrad.

OPD between interfering beams

The white fringe of the interference pattern should preferably be in the centre of the diffraction spot. If a decenter of the white fringe of 10 fringes is allowed, the initial OPD is allowed to be 5 μm (see (3.10)).

For alignment stability there are three error sources which can cause a change in OPD:

- angular alignment change between bar 1 and 2 in combination with initial base length difference and parallelism errors between pairs of beams 3'-4' and 3-4;
- OPD change due to shifting of optical components;
- change in parallelism of the pair of beams 3-4.

Since each of these sources is uncoupled, their uncertainty budget can be determined by dividing the total budget of $\pm 5 \mu\text{m}$ by the square root of the number of error sources (3 in this case), leading to a budget of $\pm 2.9 \mu\text{m}$ for each source. However, the contribution of the change in parallelism of the pair of beams 3-4 to the OPD alignment stability is very small (an explanation follows in the next sections), and the contribution of the angular alignment change between bar 1 and bar 2 is also just $\pm 0.01 \mu\text{m}$, meaning that the random OPD alignment stability budget is $\pm 5 \mu\text{m}$.

Since most components are at 45° incident angle, a movement of the component of $3.5 \mu\text{m}$ in the direction perpendicular to the mirror surface will cause an OPD of $5 \mu\text{m}$. In the worst case there are 7 components in one optical path. The influence of each optical component on the OPD is uncoupled. Therefore, the root mean square value over 7 components can be taken over the OPD budget of $3.5 \mu\text{m}$. This leads to the necessary x-position alignment stability of each optical component:

$$\Delta x_{\text{alignment stability}} = \frac{3.5}{\sqrt{7}} \cong 1.3 \mu\text{m}. \quad (3.16)$$

Parallelism of pairs of interfering beams

The interfering beam pairs should have sufficient parallelism to ensure a 90% diffraction pattern overlap. The number of fringes depends on the amount of overlap. Since the Airy disc of the diffraction pattern is 3 mm in diameter, this corresponds to a diffraction size of the Airy disc of $60 \mu\text{rad}$ over 46.67 m focal

length. This leads to an angular alignment uncertainty of one beam with respect to the other of $\pm 6.0 \mu\text{rad}$. The alignment accuracy of the optical component should be a factor of two better, due to reflection.

Since every optical component in each optical path can disturb the alignment of the parallelism of the beam pairs, the alignment stability of the optical components is also an issue. In particular, the BAM system will have to survive launch vibrations and cool down from 293 K to 100 K without losing alignment. The maximum number of optical components is present in the path of beam 4, with a total of 7. Since the alignment stability for individual optical components is expected to be independent, and normally distributed, the necessary angular stability of optical components is:

$$\Delta\theta_{\text{alignment stability}} = \Delta\psi_{\text{alignment stability}} = \frac{3.0}{\sqrt{7}} \cong 1.2 \mu\text{rad}. \quad (3.17)$$

The OPD error caused by a parallelism error in the pair of beams 3-4 is computed with (3.9) and is 0.9 nm, which is a factor 5000 below the required OPD alignment stability. Therefore, it is not necessary to take this error source into account for the OPD alignment stability.

Parallelism of the beams travelling from bar 1 to bar 2

The parallelism required for the beams traveling from bar 1 to bar 2 (beams 3' and 4' in Figure 3.6) is dependent on the distance x_{O_i} of the rotation point along the direction of the incoming beam to the first mirror on bar 2 and on the distance PL the light travels under angular error in the system (see Appendix B). For the BAM system it is assumed that this distance is 10 m. The angular accuracy of the bar is 0.1 mrad.

The required parallelism of the pair of beams 3'-4' is governed by the measurement stability requirement in OPD of $\pm 0.65 \text{ pm}$. This level is discussed in the next section. In combination with angular measurement stability of bar 2 of $\pm 5 \text{ nrad}$ and with (B.2) and (B.3) from Appendix B, this leads to:

$$\Delta\theta_{\text{beam}} = \frac{0.65 \cdot 10^{-12}}{10 \cdot 5 \cdot 10^{-9}} = 1.3 \cdot 10^{-5} \text{ rad}. \quad (3.18)$$

With this parallelism alignment accuracy of the pair of beams 3'-4', the contribution to the OPD error for alignment accuracy is $\pm 0.01 \mu\text{m}$.

Base length accuracy between pairs of beams

The base length, i.e. the distance between the two small interfering beams, shall be similar for the two pairs of beams, i.e. $1-2 \approx 3-4$ at better than $\pm 5 \text{ mm}$, because preferably both interference patterns should be similar.

The base length equality between the beams 3' and 4' and beams 3 and 4 can be computed by using the sensitivity to a difference in base length creating OPD between the beams, when bar 2 is rotated. As shown in Appendix B with (B.1), the OPD introduced by a difference in base lengths is directly dependent on the rotation angle of bar 2 $\delta\theta_{\text{bar}2}$. Aligning the base lengths to $\pm 0.1 \text{ mm}$ uncertainty, leads to a required angular alignment stability of bars 1 and 2 during measurements of 5 mrad , in order not to introduce an optical path length difference change of more than 0.65 pm .

In combination with angular alignment stability of bar 2 of $\pm 0.1 \text{ mrad}$, this would lead to an OPD error of $0.01 \mu\text{m}$, which is not significant.

Beam diameter accuracy

It is sufficient to state that the beam diameter uncertainty should be $\pm 0.5 \text{ mm}$ at the CCD to prevent fringe pattern overlap, since the beam diameter affects the Airy disc diameter. Note that it also affects the number of fringes in the Airy disc, but not the fringe width. From this beam diameter accuracy the maximum divergence of the beam can be computed taking into account a 50 m traveling distance of the beams. The maximum divergence should therefore be $10 \mu\text{rad}$. This maximum divergence is also the required alignment stability.

Beam properties

The wavefront of the beams should be flat to $\lambda/20$ with Gaussian intensity distribution to create a clean fringe pattern, with clean intensity distribution.

The light should be polarized in the \mathcal{P} plane, because in that case the CCD detector is less sensitive to crosstalk between pixels. Therefore, a linear polarizer appropriate for the useful laser output power should be used. The light is polarized to have an as pure interference as possible, with as little light as possible not interfering and creating background noise on the CCD. The polarizer extinction ratio must be such that no interference effect by light in the \mathcal{S} plane is seen by the CCD.

3.4.4 Measurement stability

δOPD between interfering beams

The required measurement uncertainty of the BAM system will be $\pm 0.5 \mu\text{s}$ or 2.4 prad. Any physical optical path length change should not bring this measurement accuracy down. The three main sources of bias on the measurement, namely OPD variation, angular stability of one beam with respect to the other and wavelength stability, are independent biases and therefore, the maximum apparent rotation of the telescope, due to either one of these errors may be 1.3 prad. The requirement on the OPD stability during measurements can now be determined by combining (3.6) and (3.8), leading to:

$$\delta OPD = 2 \cdot a \cdot \delta \theta_{\text{telescope}} \quad (3.19)$$

With $a = 0.5 \text{ m}$ this leads to an OPD stability requirement of 1.3 pm for each of the four beams. The OPD stability is affected by four possible error sources, namely random OPD variation, parallelism variations in the pairs of beams 1-2 or 3-4, angular stability of bar 2 to bar 1 and wavelength stability of the laser. The OPD budget of 1.3 pm must be divided over these four error sources. This leads to an OPD budget per error source of:

$$\delta OPD_{\text{specific error source}} = \frac{1.3}{\sqrt{4}} \cong 0.65 \text{ pm}. \quad (3.20)$$

With most optical components at a 45° incident angle, the total OPD should be divided by $\sqrt{2}$. The random position stability of an individual optical component should thus be:

$$\delta x_{\text{measurement stability}} = \frac{0.65}{\sqrt{2} \cdot \sqrt{7}} \cong 0.17 \text{ pm}. \quad (3.21)$$

$\delta\theta_{beam}$ between interfering beams

The maximum apparent rotation of the telescope that may be caused by the rotation of one of the interfering beams with respect to the other is 1.3 prad, like stated in the previous subsection, corresponding with a maximum OPD change of 0.65 pm. Using (3.9), the maximum relative rotation of the beams can be calculated. The maximum rotation is 0.16 μ rad.

The angular measurement stability of an individual optical component should therefore be:

$$\delta\theta_{beam\ measurement\ stability} = \frac{0.16}{\sqrt{7}} \cong 0.06\ \mu\text{rad}. \quad (3.22)$$

$\delta\theta_{bar}$ between bar 2 and bar 1

In case the base lengths are aligned with ± 0.1 mm uncertainty and the parallelism uncertainty of the pair of beams 3'-4' is ± 13 μ rad, the required angular alignment stability of bars 1 and 2 during measurements is 5 nrad. In this case an optical path length difference change of less than ± 0.65 pm is introduced.

Laser wavelength stability

The maximum apparent OPD any laser wavelength instability may cause is: 0.65 pm. Combined with the initial OPD requirement of 5 μ m, the laser wavelength stability needed can now be computed using (3.11). This gives a minimum laser wavelength stability of $\delta\lambda/\lambda = 1.3 \cdot 10^{-7}$. Since there are lasers which have wavelength stabilities of 10^{-9} over several hours, this requirement can realistically be met.

3.4.5 Stringency of stability

The alignment stability requirement of 1.3 μ m appears easy to achieve in comparison to the 0.17 pm measurement stability requirement. However, this conclusion is drawn without considering the environmental conditions. The alignment requirements are stated over a large temperature range of about 200 K. The measurement stability is required over a much smaller temperature variation of 0.1 mK. If the required alignment and measurement stabilities per Kelvin are computed, the results below the double line in Table 3.4 are obtained. Between the brackets the angular stability requirements are converted into

displacements over a distance of 50 mm, which is taken as a typical size value for the optical components. This table shows that if the requirements are investigated as a function of temperature variation, the angular alignment stability is the most stringent alignment requirement with a factor of at least 10.

Table 3.4 Requirements summarized for the critical degrees of freedom of 1 optical component

Critical DOF	Alignment stability	Measurement stability
ΔT	200 K	0.1 mK
x	1.3 μm	0.17 μm
ψ	1.2 μrad	60 nrad
θ	1.2 μrad	60 nrad
$x/\Delta T$	6.5 nm/K	1.7 nm/K
$\psi/\Delta T$ (-50 mm)	6 nrad/K (0.3 nm/K)	0.6 mrad/K (30 $\mu\text{m}/\text{K}$)
$\theta/\Delta T$ (-50 mm)	6 nrad/K (0.3 nm/K)	0.6 mrad/K (30 $\mu\text{m}/\text{K}$)

Note also however, that the OPD stability during measurements will be largely determined by the thermal gradient stability through the optical bench. This will be illustrated in section 4.2. This means that the 0.17 μm budget for OPD stability must be given largely to the stability of the optical bench. Therefore, the x-stability budget for the optical components should be at least a factor 5 better than stated in Table 3.4, which makes it an equally important factor to the angular alignment stability requirement.

3.5 Alignment plan

In the previous section, it was shown that for alignment there are requirements on the OPD, parallelism of the beams, the base length uncertainty and angular alignment of the bars. These requirements can be met by aligning the optical components to sufficient accuracy. Since it is preferred to achieve alignment with as little effort as possible, an alignment plan has to be made. Also, an alignment plan will aid in good design choices of optical components and alignment mechanisms.

For the alignment plan, we first assume that the components can be aligned in angle and position and that they either have coarse or fine alignment capability. The alignment accuracy of the coarsely aligned components is directly related to the alignment range needed for the fine alignment.

Furthermore, the alignment plan should include methods to measure the achieved alignment.

3.5.1 Coarse alignment

The coarse alignment of the optical components will be performed with SiC as-sintered manufacturing accuracy. This means that the individual optical components will be aligned with positional coarse accuracy of ± 1 mm and angular coarse uncertainty of ± 17 mrad. The angular coarse alignment should be performed with lower uncertainty of ± 0.3 mrad to avoid having to make large mirrors.

Only the OPD error of beams 3 and 4 (Figure 3.6) could be dependent on another factor, namely the angular alignment uncertainty of bar 2 with respect to bar 1, which is 0.1 mrad. Over a distance of 3 m of the beams 3' and 4', a maximum OPD between beams 3 and 4 of 0.3 mm can occur. This means that manufacturing uncertainty of ± 1 mm of the SiC is still the limiting factor.

3.5.2 Alignment possibilities

Aligning the BAM system entirely on the satellite versus as much as possible away from the satellite

In considering the alignment possibilities, two main options can be chosen:

- Assembling the entire BAM system on the PLM (in other words mounting optical components directly on the octagonal ring);
- Assembling the BAM system as much as possible away from the satellite.

The advantages of the first option are that:

- most probably less alignment steps would be necessary;
- the focal plane and telescopes themselves can be used as alignment tools.

The disadvantages of this option are that:

- building the PLM would become very sequential, and this would considerably slow down the building process;

- initial vibration and systems tests would have to be performed on the PLM, with increased risks.

The latter arguments are more important for space applications, which leads to the conclusion that assembly and alignment of the BAM system should be performed as much as possible away from the satellite.

If the greatest part of the alignment is performed before installing the BAM system on the satellite, the only three alignment steps that should be performed on the satellite are:

- Align bar 1 with ± 0.1 mrad uncertainty with respect to telescope 1;
- Align bar 2 with ± 0.1 mrad uncertainty with respect to bar 1;
- OPD alignment with ± 5 μm uncertainty of beams 3 and 4.

OPD alignment

The OPD must be limited to ± 5 μm uncertainty for each of the beam pairs 1-2 and 3-4. Therefore, at least one optical component in a pair of optical paths must be fine aligned to ± 5 μm uncertainty. For beams 1 and 2 (see Figure 3.6), mirrors M1 or M5 or beamsplitters BS2 and BS3 could be used for this purpose.

For beams 3 and 4, ideally the combination of mirrors M2 and M6 could be used.

Parallelism of the beam pairs

The parallelism of the beams to ± 6 μrad for beam pairs 1 and 2 and 3 and 4 (Figure 3.6) can be achieved by using one optical component per beam pair for fine angular alignment:

- For beams 1 and 2, mirrors M1 or M5 or beamsplitters BS2 or BS3 can be used for this purpose;
- For beams 3 and 4, either one of the mirrors M3, M7, M9 or M10 can be used.

For the alignment of the parallelism of for beam pair 3' and 4' to ± 1 mrad uncertainty, either mirror M8 or M4 can be used for angular alignment.

Base length

The base length alignment of 3'-4' and 3-4 (Figure 3.6) should be performed with ± 0.1 mm. This means that either mirror M4, M8, M3 or M7 can be used for this purpose.

Spreading alignment tasks versus concentrating alignment tasks

The possible components which can be used for alignment of three main alignment issues have now been pointed out: OPD, base lengths and parallelism. Generally the alignment should be performed such that these three main issues are decoupled, e.g.: OPD and base length alignment are both achieved by a translation of the optical component along the same axis. These alignments should be conducted with separate optical components if the order of magnitude of both OPD and base length required alignment is close to each other.

If for example the required uncertainty of the OPD is ± 1 μm , whereas the required base length uncertainty is ± 1 mm (3 orders of magnitude difference) and achieving base length accuracy will put the OPD error within ± 1 mm as well, one can choose to use the same optical component for base length and OPD alignment. Base length alignment is achieved first in that case, and the OPD alignment is achieved by fine tuning the component. OPD alignment can then be achieved without risking losing baselength alignment.

Angular alignment of an optical component to achieve the required parallelism of the beams is a different alignment action than for example OPD alignment (translation), if the alignment mechanism is such that any angular alignment effort does not cause OPD translation or vice versa, alignment of both degrees of freedom can be performed on the same optical component.

Alignment should also be performed in the correct order, meaning in general that one should start aligning at the beginning of the light paths and align the paths in parallel.

3.5.3 Alignment steps

The following alignment steps should be performed:

- Coarsely assemble all optical components on bars 1 and 2;

- Use beamsplitter BS3 for OPD and parallelism alignment of beam 2 with respect to beam 1;
- Use mirror M4 for parallelism alignment of beam 4' with respect to beam 3';
- Align bar 2 with 0.1 mrad accuracy with respect to bar 1;
- Use mirror M3 for parallelism alignment of beam 3 with respect to beam 4 and for base length alignment of 3-4 with respect to 3'-4' and;
- Use mirror pair M2-M6 for OPD alignment of beam 4 with respect to beam 3.

3.6 Summary

The measurement principle of the BAM system uses interference of two beams per telescope, creating two fringe patterns of which the relative position will be measured, to determine the basic angle variation.

In Figure 3.6 the optical design of the BAM system is shown. The remaining error source of a rotation of the bar is canceled out, by positioning the mirrors on bar 2 such that no relative fringe shift between the two patterns occurs.

The error sources for the alignment are:

- Optical path length difference;
- Parallelism of the beam pairs 1-2, 3-4 and 3'-4';
- Base length difference between beams 3'-4' and 3-4;
- Beam diameter and divergence.

Table 3.5 shows the alignment accuracy and stability for these elements in the BAM system.

The error sources for the measurements are:

- Angular stability of bar 2 with respect to bar 1;
- Variation in optical path length difference;
- Variation of the base lengths between two diffracting beams;
- Variation of the beam pair parallelism;
- Wavelength stability.

The measurement stability budgets for these elements in the BAM system are summarized in Table 3.6.

Table 3.5 Alignment accuracy and stability criteria and requirements for the BAM system

Criterion	Alignment uncertainty/ stability budget
Bar 1 angular alignment	0.1 mrad
Bar 2 angular alignment w.r.t. bar 1	0.1 mrad
OPD beams 1-2	5 μm
Parallelism beams 1-2	6 μrad
Parallelism beams 3'-4'	13 μrad
OPD beams 3-4	5 μm
Parallelism beams 3-4	6 μrad
Base length beams 1-2 to 3-4	5 mm
Base length beams 3'-4' to 3-4	0.1 mm
Beam diameter	0.5 mm
Beam divergence	10 μrad

Table 3.6 Measurement stability criteria and requirements for the BAM system

Criterion	Measurement stability budget
Angular stability bar 2 with respect to bar 1	5 nrad
OPD beams 1-2	0.65 μm
Parallelism beams 1-2	0.16 μrad
Parallelism beams 3'-4'	0.16 μrad
OPD beams 3-4	0.65 μm
Parallelism beams 3-4	0.16 μrad
Wavelength stability	$3 \cdot 10^{-7}$

The methods, which will aid in aligning the optical components, are not discussed here. This is a recommended subject for investigation. Because of the large distances inside the metrology system it seems very likely that the telescopes of the GAIA satellite themselves will have to be used as aids to achieve alignment.

4 Optical benches

The optical benches of the BAM system are the bodies connecting the optical components to create the optical paths defined in chapter 3. Because of the relatively large distances between the optical components, the optical benches play at least an equally important role for the OPD stability in the measurements of the basic angle variation as the mounting of the optical components. Although the focus of this thesis is on the mounting of optical components, the design of the optical benches is discussed briefly in section 4.1. Three main topics are discussed: requirements, honeycomb design and manufacturability. This discussion is made to be able to continue the chapter in section 4.2 with an assessment of the thermal stability of the optical benches. This assessment gives insight into the relative influence of the optical benches on the required measurement stability and what stability budget remains for the mounting of the optical components.

4.1 Global optical bench design

4.1.1 Requirements

The BAM system must meet several dimensional restrictions, which limit the size and the mass of the system. They are stated in Table 4.1. The total mass of 20 kg, must be divided over the optical components, the mounts and 2 optical benches. In this analysis the mass budget is taken as 8 kg for each optical bench, leaving 2 kg per bench for mounts and components. The 8 kg mass per optical bench must be distributed over a surface area of 0.2 m², leading to a mass to surface area ratio of 40 kg m⁻².

Table 4.1 Dimensional requirements [5]

Requirement	Parameter	Value
Total mass of the BAM system	m_{BAM}	20 kg
Maximum length of each bench	l_{bench}	1.0 m
Maximum width of each bench	b_{bench}	0.20 m
Maximum height of each bench	h_{bench}	0.07 m

The beams traveling to the telescopes are positioned in the starlight, to make incidence with the CCD's on the focal plane possible. However, any optical component which is positioned in the starlight reduces the light intensity of the stars and thus the accuracy of the star position measurements. The BAM system should therefore be in the starlight as little as possible. This provides a restriction on the height of a bar of 70 mm.

4.1.2 Honeycomb design

With the mass available for each optical bench the stiffness should be maximized, such that the risk of alignment instabilities due to vibrations is reduced to a minimum. In this respect, the stiffness can be subdivided into flexural stiffness and torsional stiffness. The torsional stiffness is very important for the PLM optical bench, due to the fact that large masses are suspended on the optical bench with their centre of mass at a considerable distance from the optical bench. These masses thus have sufficient arm to create considerable torsional moments on the optical bench, which asks for a stiff optical bench in torsion. According to Rosielle [18] a closed box easily can be a factor 1000 stiffer than an open box in torsion, which is illustrated by the following equation:

$$\frac{c_{openbox}}{c_{closedbox}} \cong \frac{1}{12} \cdot \left[\frac{V_{SiC}}{V_{box}} \right]^2, \quad (4.1)$$

in which c_i denotes the stiffness, V_{SiC} is the material volume in the box and V_{box} is the box volume.

For an isostatically mounted BAM optical bench, the flexural stiffness or rigidity is also important. Because the mirrors and beamsplitters suspended on the optical bench are relatively close to the optical bench and their masses are relatively small, the risk for torsion is considered to be small. Thus under vibration loads, the largest risk is flexural deflection under its own mass.

Also, the mounting surface of the optical bench should not deflect (especially under the mass of the optical components), because this can cause OPD variations. Therefore, a simple box with low-stiffness face sheets is not sufficient. In mirror design these arguments also hold and there, honeycomb structures are used to increase the face sheet stiffness. In Vukobratovich [47], the flexural rigidity of a body is used as a means of comparing several concepts of light-weighted mirrors. A comparison is made between open- and closed-back honeycomb mirrors (Figure 4.1 and Figure 4.2, respectively).

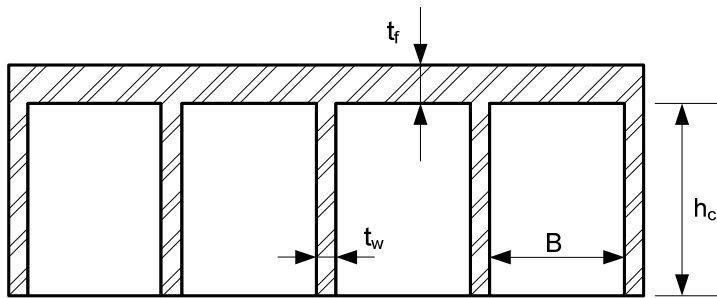


Figure 4.1 Cross-section of an open back optical bench

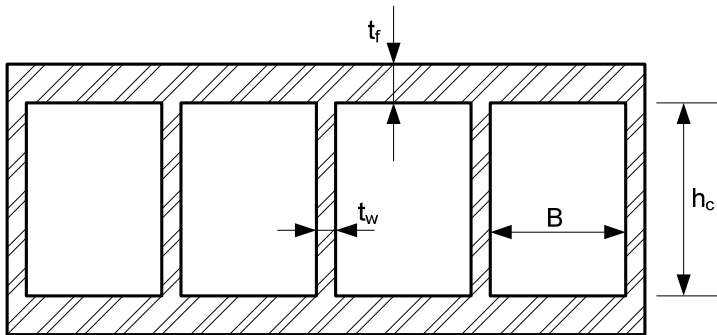


Figure 4.2 Cross-section of a closed back optical bench

Also the shape of the cells is compared. The references used for this comparison are Mehta [73] and Barnes [74]. For the BAM optical benches either open- or closed-back honeycomb structures are also considered. In the next section the manufacturability of such a structure is discussed, followed by a discussion on whether to use a closed- or open-back honeycomb.

4.1.3 Manufacturability

In section 2.4 the most general manufacturing aspects and limitations have been discussed, like wall thickness limitations, round-off and chamfering and bonding methods suitable for making closed back honeycomb optical benches (brazing and phenolic resin sintering). However, some topics specific for the optical bench production remain, which are discussed here.

Maximum machining depth

The maximum machining depth is dependent on the available machining tools. The deeper the machining depth, the larger is the minimum radius of the tool. With 10 mm diameter tools, typically a depth of 100 – 150 mm can be reached.

Areal density

Manufacturers often use areal density (mass to front surface area ratio) to illustrate how light-weight they can go in mirror design. Manufacturers of SiC mirrors have shown large mirror bodies with 22 kg/m² areal density in which the mirror is tapered back to the edges. For mirrors which are not tapered back, typically values between 30 and 50 kg/m² have been shown in the literature [22].

Rib solidity ratio

To determine the best design for the SiC optical bench, the minimal rib solidity ratio η is an important parameter. The rib solidity ratio is defined as the ratio between rib surface area and honeycomb hole surface area. It is dependent on the wall thickness and diameter of the honeycomb cells. The minimal rib thickness mentioned by manufacturers is 1 mm, for cells with wall length L of maximally 30 mm and height h_c of the order of 50 mm. For larger cells manufacturers like to use 2 to 3 mm rib thickness t_w . For the GAIA primary mirror triangular cells are mentioned with 55 mm inscribed diameter B and 2 mm rib thickness t_w , leading to a rib solidity ratio $\eta = 10 \%$ (Table 4.2). For large untapered mirrors in SiC this appears to be the minimal rib solidity ratio. For smaller mirrors the rib solidity ratio can be reduced to 8 % ([22] and [75]).

Table 4.2 Some size data on manufactured SiC mirrors ([22] and [75])

Name	Aladin primary mirror	GAIA primary mirror	RB SiC mirror blank 1	RB SiC mirror blank 2
Type	Open-back circular with triangular pockets	Open back rectangular with double layer triangular pockets	Open-back hexagonal with triangular pockets	Open-back rectangular with square- triangular pockets
A [m ²]	1.8	0.8	0.09	0.9
m [kg]	50	36	?	27
m/A [kg/m ²]	28	46	?	31
t_f [mm]	3	3	2.4	2.3
B [mm]	35	55	50	50
h_c [mm]	122	147	41	46
t_w [mm]	2	2	1.7	2.3
η [%]	10	10	6.5	8.6

Face sheet thickness

The face sheet thickness should be sufficient to prevent quilting during polishing of the face sheet surface and to prevent quilting in the cool down process of the satellite (293 to 100 K). Manufacturers mention a face sheet thickness t_f of less than 3 mm for large mirrors (\varnothing 1 to 3.5 m) [22].

Optimizing for equal density and material properties

The production of SiC parts is a batch process. This means that products made from the same batch of material, will generally have very similar characteristics. If the products are made in different batches, this can lead to differences in the material properties.

For the BAM optical benches this means that both benches and the optical components should preferably be made from the same block of green material, and that the sintering or infiltration of both benches must preferably be performed simultaneously.

Manufacturing of a closed-back optical bench

A completely monolithic closed-back optical bench cannot be built. A semi-closed back optical bench however, can be made monolithically by using T-shaped machining tools to make the semi-closed back structure. Such a semi-closed back bench is shown Figure 4.3. It shows an optical bench with 2 rectangular pockets. To make it, a T-tool enters at the top pocket and removes material from underneath the edge of the pocket, connecting the honeycomb walls with a perforated face sheet. The size of the holes in the face sheet is minimally the diameter of the T-tool. The distance that the T-tool can get underneath the edge is the radius of the T-tool minus the radius of the tool-shaft.



Figure 4.3 SSiC semi-closed back blank (courtesy Boostec, France)

The minimal radius of the pocket is the radius of the T-tool, which means that quite a large amount of material remains in the connection of the cell walls. Because a relatively large amount of material remains at the centre of the optical bench and not in the face sheets, this means that the material is not located mostly near the face sheets, which is significantly less effective for the stiffness of the optical bench. This even means that such semi-closed-back structure is less effective in mass-stiffness ratio than an open-back optical bench.

A closed back honeycomb structure can also be made by machining two halves into two equal open-back honeycomb benches or by

machining one open-back honeycomb structure and one plate. There are then two options. The two halves can be phenolic resin sintered (only for C/SiC) or brazed together. In case of phenolic resin sintering, the lower face sheet must have holes to let redundant silicon flow out of the pockets, making it a semi-closed back structure [76]. Note that this structure has a better material distribution than the monolithic semi-closed back discussed above for stiffness. An example is shown in Figure 4.4.

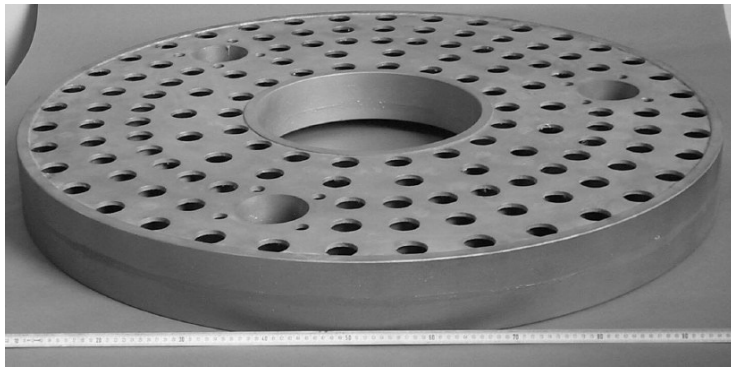


Figure 4.4 \varnothing 1 m semi-closed back Solar Lite Primary Mirror, manufactured by glueing two halves together in the green stage and infiltrating the complete mirror ([76], courtesy ECM)

When brazing the halves together, the high temperatures and the vacuum environment require that the pockets are interconnected with small venting holes, and that there should be holes in either a face sheet or a side sheet to prevent the optical bench from imploding due to the pressure difference after removing the bench from the vacuum.

The drawback of a closed-back structure is the difficulty of inspection for cracks as small as 1 mm in length. Crack inspection can be done by spraying a phosphorizing liquid onto the SiC piece after sintering. The liquid is absorbed by cracks and holes, and when inspected under UV light after removal of the external excess, the cracks will become visible. In a closed-back structure the pockets cannot be inspected inside after brazing. Therefore the manufacturer cannot guarantee the optical bench is 100 % crack-free. However, this is imperative for a space mission like GAIA, with extreme vibrational launch loads. This problem can be overcome by qualification testing at higher loads than the launch

loads. If the optical bench does not fail during these tests it will have only a very small chance of failure during launch. The brazes can be inspected ultrasonically, as was done for example in the Herschel primary mirror [22].

4.1.4 Open- or closed-back honeycomb

Whether to use an open- or closed-back honeycomb solution for the BAM optical benches is dependent on the manufacturing difficulty and stiffness. The manufacturing challenges have been discussed in the previous section. This leaves the stiffness. The goal is to reach maximum flexural rigidity. In Appendix C, an exercise is made using the method of Mehta [73] to maximize the flexural rigidity. Three steps are made to optimize flexural rigidity of SiC honeycomb optical benches; first by an optimization without face sheet thickness and height limitations, followed by fixing the pocket size and cell wall thickness and facesheet thickness according to the current manufacturing limits. Finally also, a limit is set to the height of the optical bench. The analysis is performed over a large range of mass per surface area for the optical bench. Also both SSiC and C/SiC are considered. The conclusion from this analysis is that a closed-back optical bench is 2 to 3 times stiffer than an open-back optical bench for equal mass to surface area ratio at 40 kg m^{-2} in case of a free optimization. If the manufacturing limits on face sheet thickness and cell wall thickness ($t_f = 3 \text{ mm}$, $t_w = 2 \text{ mm}$ and $B = 50 \text{ mm}$) are taken into account, the difference in flexural rigidity is marginal. The height difference between the open-back and closed-back optical bench is however, considerable. The open-back optical bench height is not considered to be realistic for the BAM optical bench. On the basis of this analysis the closed-back optical bench is therefore preferred over the open-back optical bench.

If a height limit of $h_c = 70 \text{ mm}$ is implemented, the mass of a closed-back optical bench with a surface area $A = 0.2 \text{ m}^2$ is $m = 8 \text{ kg}$, whereas the mass of an open-back optical bench is $m = 6 \text{ kg}$. In that case the flexural rigidity of a closed-back optical bench is two times that of the open-back optical bench. Note that the stiffness to mass ratio of the closed-back optical bench is still higher than for the open-back optical bench.

The conclusion from the analysis in appendix C for the specific case of the BAM optical benches is that for both torsional stiffness and flexural rigidity, a closed-back optical bench should be used.

For manufacturing difficulty an open-back optical bench is a better solution, because it is not necessary to join two halves. However, it is recommended to use a closed-back optical bench, because the requirement to obtain maximal stiffness is considered to outweigh manufacturing complexity (Figure 4.5).

The cells should be triangular in shape, because triangular cells are stiffest in themselves, which is especially important for an open-back optical bench. Also six triangles provide the 6-axes symmetry needed for isotropic thermal behavior of the optical bench and less cells are needed than for rectangular or hexagonal cells.

In order to introduce as little bending moments as possible into the optical bench the isostatic mounts must be joined to the optical bench at the neutral axis of the optical bench.

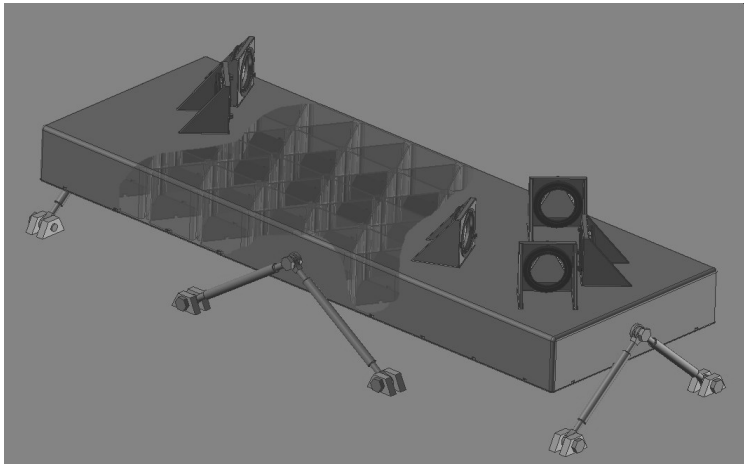


Figure 4.5 Impression of the closed-back optical bench, mounted at the neutral axis with isostatic rods.

4.2 Thermal stability

The thermal instability of the BAM optical benches with the mounting of the optical components is considered to be the most important influence of the measurement accuracy of the BAM system.

The optical benches will cool down over a rather large temperature trajectory, and this should be performed without losing alignment or without any development of cracks. Finally, the optical bench should be very stable under small temperature variations during measurements, so that the OPD changes do not impair measurement accuracy.

Essentially, for the optical bench the thermal stability requirement is that the shape of the optical bench may not change due to thermal fluctuations. The requirement is not that the overall size of the optical bench may not change.

There are many terms in the literature which cover shape changes in a mirror body due to thermal variations. These terms are thermal bowing, imprinting of honeycomb structures (also called quilting), thermal deformation, thermal figuring, thermo-elastic deformation etc. For this section, the term thermo-elastic deformation is used ([47] and [77] to [81]).

To get an understanding of thermo-elastic deformation, first the effects which could cause it are discussed:

- A temporal thermal variation: i.e. a temperature change of a body over time;
- A thermal gradient, or spatial thermal variation.

Obviously, also a combination of both can occur.

A temporal thermal variation can cause a deformation if the material exhibits anisotropic behavior in the coefficient of thermal expansion or if the body consists of more than one material (for example a coated mirror), which causes a bimetallic effect. The effect on mirror shape due to differences in coefficient of thermal expansion has been addressed by Paquin [79], Jacobs [81] and Vukobratovich [47] and [80]. The bimetallic effect is considered by Barnes [82]. The argument of anisotropic coefficient of thermal expansion is important since Vukobratovich [47] mentions that the spatial variation on the coefficient of thermal expansion within a piece of material is often 4 to 5% of the materials coefficient of thermal expansion. This can cause uneven thermal strains and thus OPD variations in the optical bench.

The bimetallic effect can be important for a C/SiC optical bench, because this material is coated with CVD SiC by most manufacturers, because the C/SiC itself is very porous. However,

the coating thickness is very small in comparison to the optical bench thickness, which makes it unlikely that bimetallic bending will occur. Therefore bimetallic bending is not considered further.

Thermal gradients occur due to the fact that a body can be loaded thermally at different ways on different sides of the body. Deformation due to thermal gradients has been addressed by Pearson and Stepp [78], Barnes [82] and Mehta [83]. In section 1.2.1 it was already mentioned that the BAM system will operate in a very stable environment, but still with temperature gradients of 0.1 mK. Over a distance of 1 m at 100 K, a temperature change of 0.1 mK can cause a thermal expansion of 50 pm in Silicon Carbide, which is larger than the allowed 1.3 pm OPD.

The sensitivity to temporal thermal fluctuations is influenced by the effective conductivity of the mirror, which has been addressed by Daryabeigi [84] and Swann and Pittman [85]. The larger the thermal conductivity, the smaller are temporally induced thermal gradients induced by conductive heat flow.

The influence of spatial variations of the coefficient of thermal expansion α , the influence of gradients in the plane of the mounting surface (xy-gradients) and gradients in the direction perpendicular to the mounting surface (z-gradient) are investigated in the following subsections.

4.2.1 Spatial variations of α

In section 2.3.2 some numbers have been mentioned for the spatial variation of the coefficient of thermal expansion for Boostec SSiC ($\Delta\alpha = 10 \cdot 10^{-9} \text{ m m}^{-1} \text{ K}^{-1}$) and for CVD SiC ($\Delta\alpha = 88 \cdot 10^{-9} \text{ m m}^{-1} \text{ K}^{-1}$). The variation is caused by density variations in the material and is in principle independent on the design of the optical bench.

To obtain an idea of the impact of spatial variations of the coefficient of thermal expansion on the OPD error between two paths, consider the BAM optical design of bar 1 (see Figure 4.6).

As discussed in chapter 3, beams 1 and 2 must have equal path lengths to 5 μm accuracy and to 0.65 pm stability from beamsplitter BS1 to beamsplitter BS3 for beam 1 and to beamsplitter BS2 for beam 2. The optical path length of each path is 300 mm. The paths are not parallel but are essentially in line with each other, creating a total length of 600 mm. This situation is considered worst case, since the spacing between these paths is

the largest spacing in the entire optical design. Therefore, the risk of spatial differences in coefficient of thermal expansion and temperature gradients is considered largest for these two optical paths.

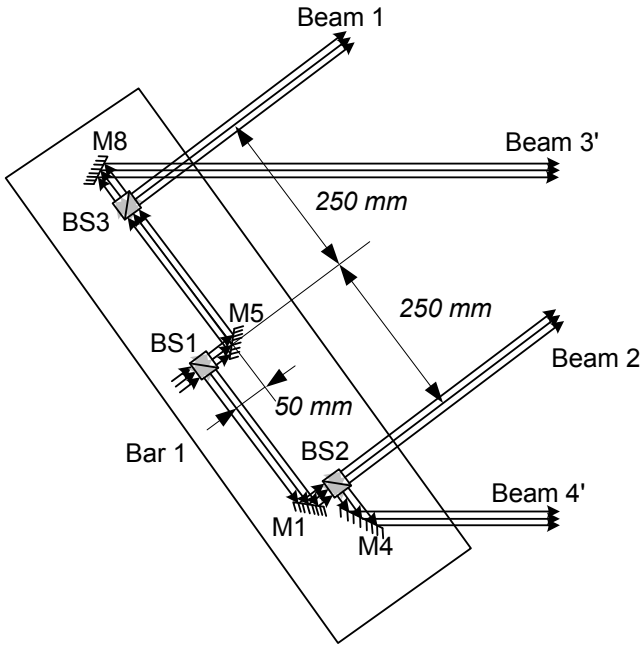


Figure 4.6 Important distances in the optical design of BAM bar 1

Now, translate the configuration described above to a 1-dimensional model, in which the two optical paths are drawn in line (Figure 4.7).

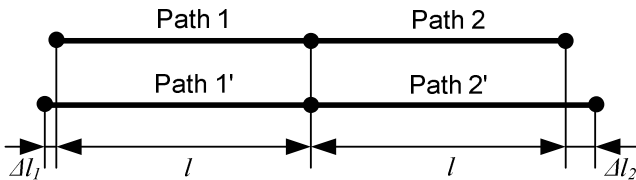


Figure 4.7 Original paths 1 and 2 and paths 1' and 2' after temperature change in a 1D situation.

Path 1 has a different coefficient of thermal expansion than the other optical path. The changes in optical path length are computed for two situations. The first for a temperature drop of 193 K. SiC has a typical thermal expansion of $-2.00 \cdot 10^{-4}$ over this

temperature range. This corresponds to an average coefficient of thermal expansion of $\alpha_l = 1.04 \cdot 10^{-6} \text{ m m}^{-1} \text{ K}^{-1}$. If path 2 has a $10 \cdot 10^{-9} \text{ m m}^{-1} \text{ K}^{-1}$ higher coefficient of thermal expansion, this gives $\alpha_2 = 1.05 \cdot 10^{-6} \text{ m m}^{-1} \text{ K}^{-1}$. This corresponds to a thermal expansion of $-2.03 \cdot 10^{-4}$ over 193 K in path 2. The optical path length change between paths 1 and 2 may not be larger than $5 \text{ }\mu\text{m}$ over this temperature range. With a $-0.03 \cdot 10^{-4}$ thermal expansion difference, the computed optical length difference of paths 1 and 2 is $0.9 \text{ }\mu\text{m}$, which is within the limit (see the fourth column in Table 4.3).

The same computation is performed for the case of measurement stability with temperature stability of 0.1 mK . In this case a $10 \cdot 10^{-9} \text{ K}^{-1}$ difference in coefficient of thermal expansion causes an optical path length difference change of 0.3 pm (see the fifth column in Table 4.3), which is also just below the required 0.65 pm . This would mean that due to the spatial difference in coefficient of thermal expansion, the budget on stability of the mounting of the individual optical components is smaller. The conclusion of this analysis is, that the risk of disturbed measurement stability and alignment stability is real and therefore the BAM system necessarily should be tested at 100 K , to confirm that alignment is not lost. If this is confirmed, it is very unlikely that measurement stability is impaired, because the spatial variation of the coefficient of thermal expansion is probably smaller than $10 \cdot 10^{-9} \text{ K}^{-1}$ at 100 K , due to the fact that the coefficient of thermal expansion is smaller at 100 K .

Table 4.3 Changes in optical path length difference due to spatial variations in the coefficient of thermal expansion

			Alignment stability	Measurement stability
Temperature change	ΔT	[K]	-193	$0.1 \cdot 10^{-3}$
Path length	l	[m]	0.300	0.300
Path 1	α_1	[$\cdot 10^{-6} \text{ K}^{-1}$]	$1.04 \cdot 10^{-6}$	$0.50 \cdot 10^{-6}$
	$\Delta l_1 / l$	[$\cdot 10^{-4}$]	$-2.00 \cdot 10^{-4}$	$50 \cdot 10^{-12}$
	Δl_1	[m]	$-60 \cdot 10^{-6}$	$15 \cdot 10^{-12}$
Path 2	α_2	[$\cdot 10^{-6} \text{ K}^{-1}$]	$1.05 \cdot 10^{-6}$	$0.51 \cdot 10^{-6}$
	$\Delta l_2 / l$	[$\cdot 10^{-4}$]	$-2.03 \cdot 10^{-4}$	$51 \cdot 10^{-12}$
	Δl_2	[m]	$-60.9 \cdot 10^{-6}$	$15.3 \cdot 10^{-12}$
Path 2 – Path 1	$\Delta l_2 - \Delta l_1$	[m]	$0.9 \cdot 10^{-6}$	$0.3 \cdot 10^{-12}$

4.2.2 *xy-gradients*

1-D analysis

To obtain an idea of the impact of gradients in the mounting plane (x- and y-gradients) on the OPD error between two paths, consider again the 1-D situation of Figure 4.7. Now, one optical path has a different temperature change than the other optical path. Consider the occurrence of a linear thermal gradient of 0.1 mK over the entire length $2l$ of the 1-D optical bench. The temperature change over path 1 is on average $\Delta T_{path\ 1} = 0.025$ mK and the average temperature change over path 2 is $\Delta T_{path\ 2} = 0.075$ mK. The thermal expansion coefficient for both paths is $\alpha = 0.5 \cdot 10^{-6}$ K⁻¹. The optical path length change of path 1 is thus $\Delta l_1 = 3.8$ pm and of path 2 $\Delta l_2 = 11.3$ pm. This leads to a change in optical path length difference of $\Delta l_2 - \Delta l_1 = 7.5$ pm, which is more than the 1.3 pm which is allowed during measurements.

In order not to lose OPD alignment of 5 μ m maximum OPD, the steady-state temperature gradient in this 1-D investigation may not be larger than 67 K over 0.6 m. The chance, that this temperature gradient occurs, is considered to be extremely small.

2-D analysis

A similar analysis is performed in 2-D space of the octagonal PLM optical bench subject to 0.1 mK thermal gradient change. These temperature fluctuations are most likely caused by power fluctuations in the electronics and detectors in the CCD focal plane. To investigate the influence of these variations in temperature on the shape of the PLM optical bench, a FEM thermal analysis has been made of the PLM optical bench with the ANSYS software package.

The FEM analysis was made, making a number of assumptions:

- 2-D (see Figure 4.8);
- The thermal expansion coefficient of the bench is $0.5 \cdot 10^{-6}$ K⁻¹;
- The thermal conductivity is 180 W m⁻¹ K⁻¹;
- A steady state heat flux of $15 \cdot 10^{-3}$ W m⁻² (grey square marked with 15 mW/m² in Figure 4.8) is applied to create an 0.1 mK thermal gradient. The heat flux is introduced at a surface area of 1 cm², which is located at the CCD detector location. Over a

period of 6 hours, the transient thermal behavior of the optical bench is monitored.

- The optical bench is fixed in six degrees of freedom, so that no mechanical load can introduce a bending strain in the bench. Bending can only occur due to non-uniform thermal effects.

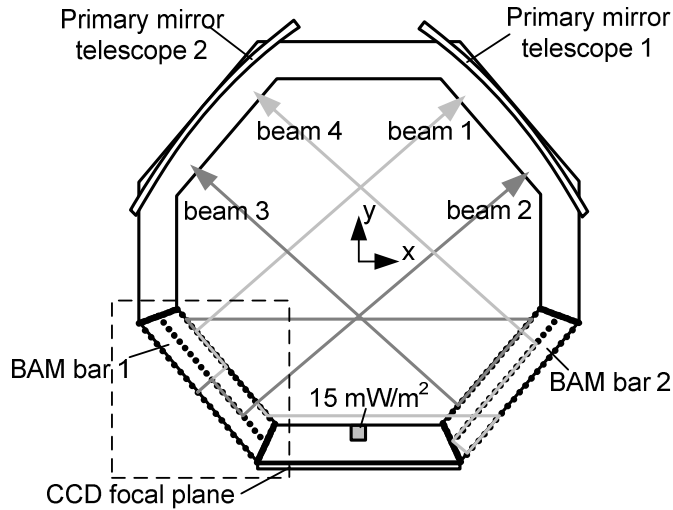


Figure 4.8 2-D thermal analysis of the PLM octagonal optical bench

The optical bench with the thermal load is symmetric. Also, the only interest is in the behavior of the parts on which the BAM system will be mounted. Therefore, on one side, the optical bench is equipped with 6 nodes. The 6 nodes are used to span 5 lines, which – in their turn – consist of 21 points. This grid of points gives the displacement due to the transient thermal gradient at each hour. Together with the original positions, this information can be used to investigate the influence of the thermal expansion on the optical paths of the BAM system. Two aspects of the BAM system are considered: OPD and angle; e.g. the OPD between beam 1 and beam 2 and the variation of angle of beam 1 leaving the BAM bar and the variation of the angle difference between beam 1 and beam 2 leaving the BAM bar.

The thermal gradient traveling through the PLM optical bench is very symmetric, meaning that BAM bar 1 expands in the same manner, but mirrored to BAM bar 2. In Figure 4.9 the shape of BAM bar 1 is plotted in black. The x- and y-coordinates indicate

the size of BAM bar 1. In grey the deformed shape of BAM bar 1 after 6 hours is plotted with scaling factor of $5 \cdot 10^9$.

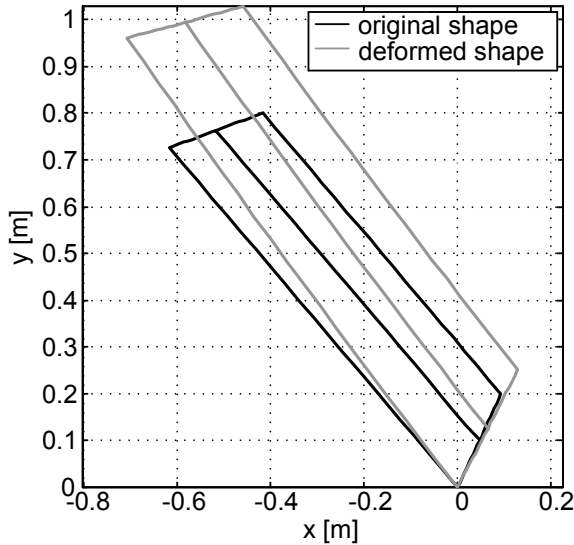


Figure 4.9 Original shape of BAM bar 1 and deformed shape after 6 hours with deformation scaling factor $5 \cdot 10^9$ for visualisation.

With respect to the origin (0,0) the maximum displacement due to 0.1 mK temperature change of any point on BAM bar 1 will be 47 pm after 6 hours. This displacement is mainly caused by the expansion of the beam. Part of this displacement is counteracted by a rotation of the BAM bar which is about 20 prad or equivalently a displacement of 20 pm over 1 meter.

If the BAM bar 1 optical design is now considered, shown in Figure 4.10, the displacements and rotations of each mirror and beamsplitter can be determined, through linear extrapolation of positions of mirrors from the positions of nodes. The results in Table 4.4 show that the individual components in the course of 6 hours, sometimes move 20 pm. However, the critical displacement is the relative displacement of optical component with respect to each other, which can cause OPD change.

Using optical software, the OPD change and fringe shift due to the displacement and rotation of the optical components is determined. The OPD change caused by the 0.1 mK local heating for BAM bar 1 is computed to be 8 pm, which corresponds rather

well with the 7.5 pm OPD computed in the 1-D analysis. The OPD change of BAM bar 2 is even higher with 29.3 pm. This large OPD is caused by the OPD change on bar 1 and by bending of bar 2, which causes shortening of beam 3 and stretching of beam 4.

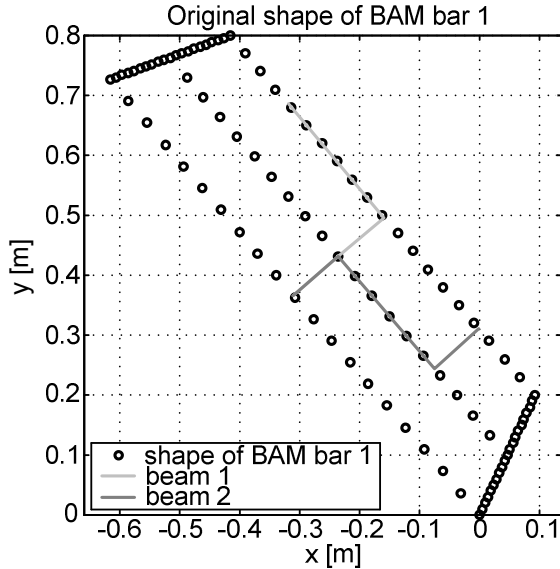


Figure 4.10 Optical paths of BAM bar 1

Table 4.4 Rotations and displacements of the optical components

Component on bar 1	dx [$\times 10^{-12}$ m]	dy [$\times 10^{-12}$ m]	$d\theta$ [$\times 10^{-12}$ rad]
S	-13.2	29.2	18.3
BS1	-8.5	30.9	15.8
M5	-4.0	32.6	16.4
BS3	-7.8	43.6	18.5
M8	-8.5	46.0	18.0
M1	-3.7	19.2	13.8
BS2	1.0	21.5	13.8
M4	3.3	17.1	11.5
Component on bar 2			
M10	8.5	46.0	-18.0
M3	-1.0	21.5	-13.8
M9	10.1	20.7	-18.6
M2	1.9	3.4	-10.5
M6	-3.1	6.2	-10.8
M7	12.2	42.3	-21.1

Only 0.65 μm OPD change is allowed during measurements. Therefore, the conclusion from this analysis is that if the 0.1 mK stability shows itself as a variation on the thermal gradient in the xy-plane causing an OPD change of 29.3 μm , the measurement uncertainty of the BAM system will at least $\pm 22.5 \mu\text{s}$ instead of the required $\pm 0.5 \mu\text{s}$. Note that measurement uncertainties due to mounting instabilities are not taken into account in this figure.

The analysis above has been conducted presuming that the optical components of the BAM system are mounted directly on the PLM octagonal ring. The bending due to a 0.1 mK gradient can be reduced if the components are mounted on special BAM optical benches, which are then mounted onto the octagonal ring and effort is put into ensuring that thermal gradients occur along the axis of the optical bench.

4.2.3 z-gradients

Gradients perpendicular to the mounting surface (z-gradients) can cause bending of the optical bench, and thus measurement instability of the optical components. Two aspects should be considered with regard to z-gradients:

- The fact that the thermal conductivity of the optical bench is reduced due to the application of a honeycomb structure, which makes the probability of the occurrence of thermal gradients and variations on the thermal gradients larger.
- The resulting actual instabilities of the OPD and angular alignment in the BAM system.

Thermal conductivity of a honeycomb optical bench

The thermal conductivity of a honeycomb optical bench, also called effective thermal conductivity λ_e can be described by the Swann-Pittman model modified by Daryabeigi [84]:

$$\frac{(n \cdot t_f + h_c)}{\lambda_e} = n \cdot \frac{t_f}{\lambda_f} + n \cdot \frac{t_{ad}}{\lambda_c \cdot \eta + \lambda_{ad} \cdot (1 - \eta)} + \frac{h_c}{\lambda_c \cdot \eta + \lambda_g \cdot (1 - \eta) + \lambda_r}, \quad (4.2)$$

where,

n = 1 for open back section;

= 2 for sandwich section;

λ_f face sheet material thermal conductivity;

λ_{ad}	adhesive thermal conductivity;
t_{ad}	adhesive layer thickness;
λ_c	cell material thermal conductivity;
λ_r	radiation effective conductivity of the cells, and;
λ_g	thermal conductivity of gas in cells.

In the context of the BAM optical benches, the Swann-Pittman model is simplified. The radiation effective conductivity of the cells is neglected. Since the BAM optical benches will operate in space, no heat flow will occur due to gas conduction or convection ($\lambda_g = 0$ W m⁻¹ K⁻¹). Also, the optical benches are made from a monolithic piece of material, thus not containing any adhesive layer ($t_{ad} = 0$ m). Furthermore, the monolithic property of the optical bench also means that $\lambda_f = \lambda_c$.

By discounting gas conduction, adhesive layer conduction and the effective radiative conductivity, (4.2) can be simplified to:

$$\lambda_{ez} = \frac{\lambda_f \cdot \eta \cdot (n \cdot t_f + h_c)}{n \cdot t_f \cdot \eta + h_c} \quad (4.3)$$

The relation shows that the contributions of the face sheets and honeycomb structure are put in series for the axial heat flux. This relation also shows that if the face sheet thickness is small with respect to the rib height, the effective thermal conductivity scales linearly with the rib solidity ratio. This is shown in Figure 4.11.

The reduction factor in effective thermal conductivity with respect to the honeycomb material thermal conductivity is approximately equal to the rib solidity ratio η . The honeycomb structure thus works as an insulator. It should also be noted that for small face sheet thickness with respect to the rib height, there is little difference in thermal conductivity between open-back and closed-back mirrors. Therefore, there will be little difference in bending due to axial temperature gradients between the open-back and closed-back option. The actual effective thermal conductivity of a honeycomb optical bench with $h_c = 70$ mm, $\eta = 0.1$ and $t_f = 3$ mm and $\lambda_f = 180$ W m⁻¹ K⁻¹ is $\lambda_{ez} = 19$ W m⁻¹ K⁻¹.

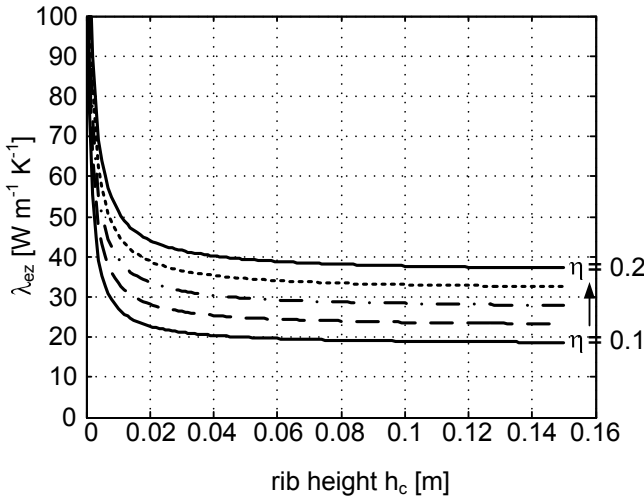


Figure 4.11 Effective axial thermal conductivity of a closed-back optical bench with $\lambda = 180 \text{ W m}^{-1} \text{ K}^{-1}$ for varying rib heights and rib solidity ratio's

Bending due to a thermal z-gradient

A thermal gradient in z-direction causes bending γ in m^{-1} of the optical bench according to [47]:

$$\gamma = -\left(\frac{1}{R} - \frac{1}{R_0}\right) = \frac{\alpha \cdot q}{\lambda_{ez}}. \quad (4.4)$$

The change in curvature of a nearly flat mirror ($R_0 > 1 \text{ km}$) is in approximation directly inversely proportional to the effective thermal conductivity in z-direction.

For small changes in curvature, the maximum deflection δ in m of a mirror with radius r due to a thermal gradient in z-direction can be approximated by:

$$\delta \cong \frac{r^2 \cdot \gamma}{2} \quad (4.5)$$

The bending of the optical bench can cause ψ -errors on the optical components. It can also cause displacements due to a lever effect.

Angular stability

The maximum ψ -error of the optical components can be approximated by:

$$\Delta\psi \cong \frac{r \cdot \gamma}{2} \quad (4.6)$$

For the measurement stability a worst case scenario is taken of a gradient change of 0.1 mK over the height of the optical bench $h_c = 70 \cdot 10^{-3}$ m. This corresponds with a heat flux $q = 28 \cdot 10^{-3}$ W m⁻² according to:

$$q = \frac{\lambda_{ez} \cdot \Delta T}{h_c}. \quad (4.7)$$

For the alignment stability a worst case scenario is taken of a temperature difference of 3 K over the height of the optical bench h_c . The corresponding heat flux is $q = 814$ W m⁻². This heat flux is extreme. It is therefore unlikely that a gradient of 3 K over 70 mm is created. However, requirements state this maximum temperature difference [5]. In Table 4.5 the bending of the optical bench due to the gradients mentioned above are summarized.

Table 4.5 Bending due to a temperature difference in z-direction

			Measurement stability	Alignment stability
Temperature difference	ΔT	[K]	$0.1 \cdot 10^{-3}$	3
Heat flux	q	[W m ⁻²]	$28 \cdot 10^{-3}$	814
Bending	γ	[m ⁻¹]	$7.1 \cdot 10^{-10}$	$2.1 \cdot 10^{-5}$

OPD stability

The OPD error due to bending of the optical benches occurs due to the lever effect. This lever effect is illustrated in Figure 4.12. The actual bending of the optical bench occurs along a neutral line.

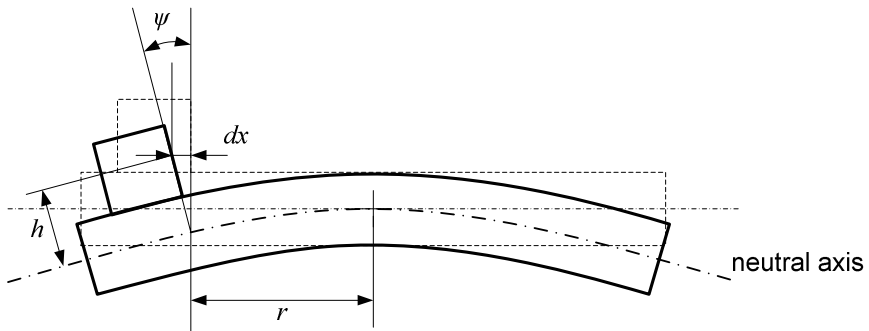


Figure 4.12 Bending of the optical bench and lever effect on the optical component

The displacement of a component, which is at distance d from the neutral line, is then given by:

$$dx \cong d \cdot \psi. \quad (4.8)$$

Influence of z-gradient on the BAM system

The influence of z-gradients on the BAM system is assessed in a similar way as was done in the 2-D analysis of the OPD variations caused by x-gradients in the PLM optical bench. First, displacements and rotations of the components due to the bending of the optical benches are computed. In the second step, these displacements and rotations are applied in the optical design, described with optical software and the resulting OPD variations and rotations of the beams are calculated.

In Table 4.6 the displacements and rotations of the individual components due to the bending of the optical benches with $\gamma = 7.1 \cdot 10^{-10} \text{ m}^{-1}$ due to a 0.1 mK gradient are shown. Note that the displacements exceed the required positional stability of 0.19 μm by up to a factor 50. The rotations of the individual components remain far below the required rotational stability of 60 nrad.

Table 4.6 x- and y-displacements and ψ - and φ - rotations (around y- and x- axis respectively) of the optical components with $d = 70 \text{ mm}$ due to bending of the optical benches with $\gamma = 7.1 \cdot 10^{-10} \text{ m}^{-1}$

Component	dx [$\times 10^{-12} \text{ m}$]	dy [$\times 10^{-12} \text{ m}$]	d φ [$\times 10^{-9} \text{ rad}$]	d ψ [$\times 10^{-9} \text{ rad}$]
S	-1.96	-0.50	-0.028	-0.007
BS1	-0.96	0.25	-0.014	0.004
M5	0.03	0.99	0.000	0.014
BS3	-3.71	5.96	-0.053	0.085
M8	-4.65	7.21	-0.067	0.103
M1	2.77	-4.71	0.040	-0.067
BS2	3.77	-3.97	0.054	-0.057
M4	4.71	-5.22	0.067	-0.075
M10	6.19	10.28	0.088	0.147
M3	-2.23	-0.89	-0.032	-0.013
M9	-0.06	-2.14	-0.001	-0.031
M2	-4.57	-8.14	-0.065	-0.116
M6	-5.57	-7.39	-0.080	-0.106
M7	6.24	8.28	0.089	0.118

When these displacements and rotations are applied in the optical design, the OPD stability and parallelism variation of the interfering beams can be computed. The resulting OPD variation of beams 1 and 2 is 7.4 μm and of beams 3 and 4 is 17.2 μm . Both exceed the required OPD stability of 0.65 μm by far. The parallelism of the interfering beams is affected with 8 μrad but that is not significant. Due to the OPD variation the heat flux through the optical bench in z-direction should not be larger than $1 \cdot 10^{-3} \text{ W m}^{-2}$.

The same analysis is performed for alignment stability. The displacements and rotations of the optical components due to the bending of the optical benches in case of 3 K gradient over the height of the optical benches are shown in Table 4.7. The combination of these displacements and rotations gives a change in OPD between beams 1 and 2 of 0.22 μm and a change of 0.51 μm between beams 3 and 4. This OPD change is within the budget of 5 μm . The parallelism of the interfering beams is affected with 0.36 μrad between beams 1 and 2 and 0.27 μrad between beams 3 and 4. This parallelism change is also within the budget of 6 μrad .

Table 4.7 x- and y-displacements and ψ - and φ - rotations of the optical components with $d = 70 \text{ mm}$ due to bending of the optical benches with $\gamma = 2.1 \cdot 10^{-5} \text{ m}^{-1}$

Component	dx [$\times 10^{-6} \text{ m}$]	dy [$\times 10^{-6} \text{ m}$]	d φ [$\times 10^{-6} \text{ rad}$]	d ψ [$\times 10^{-6} \text{ rad}$]
S	-0.058	-0.015 $\cdot 10^{-6}$	-0.83 $\cdot 10^{-6}$	-0.21 $\cdot 10^{-6}$
BS1	-0.029	0.007 $\cdot 10^{-6}$	-0.41 $\cdot 10^{-6}$	0.10 $\cdot 10^{-6}$
M5	0.001	0.029	0.01	0.42
BS3	-0.110	0.176	-1.57	2.52
M8	-0.138	0.213	-1.97	3.05
M1	0.082	-0.140	1.17	-1.99
BS2	0.111	-0.117	1.59	-1.68
M4	0.139	-0.154	1.99	-2.20
M10	0.183	0.304	2.62	4.34
M3	-0.066	-0.026	-0.94	-0.38
M9	-0.002	-0.063	-0.03	-0.91
M2	-0.135	-0.241	-1.93	-3.44
M6	-0.165	-0.219	-2.35	-3.12
M7	0.184	0.245	2.64	3.50

4.2.4 Conclusions

In conclusion the alignment stability is considered to be threatened only by a spatial variation of the coefficient of thermal expansion through the optical bench. A variation of $\Delta\alpha = 10 \cdot 10^{-9}$ K can cause an OPD instability of $0.9 \mu\text{m}$, which is rather close to the maximum allowed alignment OPD variation of $5 \mu\text{m}$. It is therefore necessary to measure the alignment stability of the BAM system by measuring the fringe shift after cool down to 100 K for verification. The occurrence of gradients due to the transition to space environment is expected not to be a problem, because this would require thermal gradients of 44 K m^{-1} for the z-direction and even higher gradients for the xy-direction.

Furthermore, the measurement stability is most certainly affected by heat flux variations in both xy- and z-directions. The effects of heat flux variations in xy- and z- directions are uncoupled in the first order, which means that they can be added. The heat flux variations of $15 \cdot 10^{-3} \text{ W m}^{-2}$ simultaneously in xy- and z-direction can therefore cause OPD variations of as much as $\sim 50 \text{ pm}$ between interfering beams. This leads to the following conclusion regarding basic angle variation measurement.

In order to obtain $0.5 \mu\text{as}$ measurement accuracy with the BAM system, the maximum heat flux variation through the optical benches during measurements may not exceed than $0.2 \cdot 10^{-3} \text{ W m}^{-2}$, provided that the mounting stability of the optical components is negligibly small.

The spatial variations of the coefficient of thermal expansion are considered to be small relative to the gradient variation problem. However, the OPD variations caused by this effect are with 0.3 pm close the required 0.65 pm , which means that this effect should be considered as a serious factor during measurements.

4.3 Final remarks

A realistic question after the presentation of closed-back honeycomb optical benches mounted with isostatic mounts at the neutral axis and the presentation of the thermal stability risks is whether or not the design of the optical benches can and should be adapted to reduce thermal effects. An adaptation that one can think of is: increasing the rib solidity ratio, because this will increase the effective thermal conductivity in z-direction, thus

reducing the gradients in z-direction. The consequence of this adaptation is that the stiffness of the optical benches will reduce with constant weight, because the mass is located more to the center and not at the face sheets of the optical bench.

Another adaptation is reducing the height of the optical bench, because this will reduce the lever effect in z-gradient variations. The consequence of this adaptation is a reduction of stiffness of the optical bench as well. Note that the height can also be reduced by building the optical components as low as possible onto the optical benches.

Note that the two adaptations will only reduce OPD variations due to z-gradients. The OPD variations due to xy-gradient fluctuations will not reduce. For this reason, and because launch vibrations and shock loads warrant maximal stiffness of the optical benches, the reduction of height and increase of rib solidity ratio are not recommended.

The most effective means of adapting the optical bench design to reduce OPD variations due to thermal effects is considered to be the reduction of the heat flow variations. This can be done by isolating the optical benches from the environment as much as possible. The isostatic mounts should be made of an isolating material, such that heat flux variations in the PLM optical bench will not be conducted to the BAM optical benches. Also, the BAM optical benches can be equipped with thermal covers, to reduce the effects of radiative heat flux variations.

5 Mounting of optical components

The thermal analyses in chapter 4 have shown that variation on the thermal gradients in the optical benches will have a large influence on the measurement stability (in particular OPD stability) of the BAM system. It is therefore imperative to focus on optimal measurement stability in the design of the optical components themselves. The mounts of the components to the optical bench are the critical factor here. However, at the same time the dynamic and thermal loading of launch must not be underestimated. This chapter will discuss mounting of optical components for stability. Note, that the attention goes to the mirrors and beamsplitters. The collimating optics are not discussed.

The optical components are mounted onto the optical bench by mechanical clamping. This technique introduces stresses, which are in principal not beneficial for stability. However, this technique is reversible, which is especially beneficial during aligning.

Section 5.1 addresses the mounting plane of the optical components. First the local coordinate system of the optical components is defined and the DOF's are subdivided in critical and non-critical axes. Next, the mounting plane and required clamping force stability is discussed. These general considerations lead to two different design philosophies, which are discussed in

sections 5.2 and 5.3 by specifying the design. The chapter ends with a comparison of the designs in section 5.4.

5.1 Mounting plane

The definition of a mounting plane is the plane at which body-to-body contact of the optical component to the optical bench is achieved relative to the reflective surface of the component. One could consider using multiple mounting surfaces. However, this option is in principle not considered, because the argument is that the more body-body joints, the lower the stability.

The choice of the mounting plane is dependent on the alignment possibilities when clamping the component to the optical bench on the specified mounting plane. Also it is dependent on the measurement stability that can be achieved when mounting the component on the specified mounting plane.

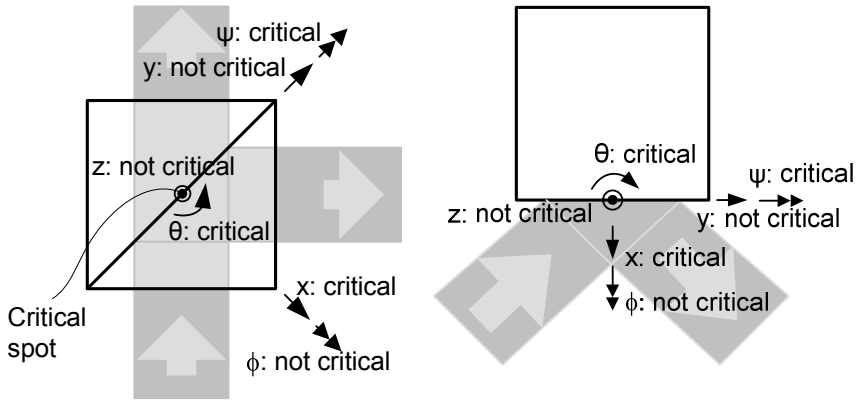
Before an assessment of the measurement stability of either mounting plane can be made, it is necessary to determine which DOF's affect the OPD and angular stability of the BAM system

5.1.1 *Coordinate system and critical DOF's*

The local coordinate systems for the beamsplitter and mirror are shown in Figure 5.1. The grey areas with arrows illustrate the light paths. The origin of the coordinate systems is in the critical spot, which is the center of the beam coinciding with the reflective surface of the component. For the beamsplitter this reflective surface is in fact a 50% reflective surface (Figure 5.1 a). For both components the x-direction is perpendicular to the reflective surface. The y- and z-direction thus define the reflective surface. The xy-plane is the plane in which all beams of the ideal BAM system travel.

The requirements in section 3.4 have been stated for only three DOF's (x , ψ and θ), which are critical DOF's for the optical components. If the beamsplitter (Figure 5.1 a) rotates around the ψ - and θ -direction, this will cause an error in the direction of travel of the reflected and transmitted beam. The ϕ -rotation will not cause any OPD change or angular errors in the light and is therefore not critical. This argument also holds for the positional stability of the beamsplitter in the z- and y-direction. These DOF's are therefore not critical either. The x-direction is critical, because

a displacement in x-direction will cause an OPD and therefore a displacement of the fringes in the interference pattern. In summary, the x-, ψ -, and θ -directions are the critical directions, for which requirements must be stated. For a mirror (Figure 5.1 b) exactly the same arguments can be used to determine that the x-, ψ -, and θ -directions are the critical directions.



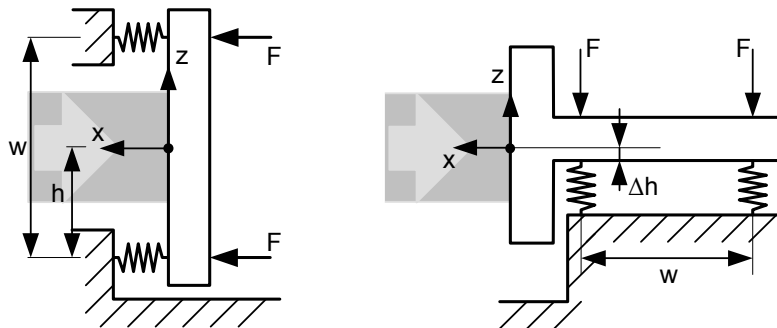
a) Beamsplitter

b) Mirror

Figure 5.1 Critical and non-critical degrees of freedom of the beamsplitter and the mirror

5.1.2 Mounting plane

Two mounting planes are considered for mounting the optical components: the yz-mount (Figure 5.2 a) and the xy-mount (Figure 5.2 b). In these figures they are shown in a 2-D situation.



a) yz-mounting plane

b) xy-mounting plane

Figure 5.2 Schematic representation of the two mounting planes

In these figures the mirror body is considered to be a rigid body with infinite stiffness. The contact areas have finite stiffness and are represented by the springs, each with stiffness c_{Hz} . The dot represents the critical spot. The maximum displacement of this spot in x-direction allowed during measurements is $\Delta x = 0.17 \cdot 10^{-12}$ m and the rotation around the y-axis of the mirror surface $\psi = 60 \cdot 10^{-9}$ rad.

Note that in the yz-mounting the critical point is located on the mounting plane. This will prevent lever effects on the stability of the optical components due to force variations. In the xy-mounting the critical point is at distance Δh from the mounting plane.

yz-mounting plane

In Figure 5.2 a) the mirror is mounted on the yz-plane which is the plane of the reflective surface. Mounting forces are applied in the x-direction. In practice, the optical component is mounted against three Hertzian contact points with finite stiffness and therefore variations in the mounting forces can cause x-, θ - and ψ -variations in position. These are exactly the critical directions shown in Figure 5.1 b).

The influence of mounting force variations can be quantified in the 2-D situation in two analyses. First each of the springs is subjected to an extra force level ΔF (Figure 5.3 a), causing a translation of the rigid body, for the yz-mounting in x-direction:

$$\Delta x = \frac{\Delta F}{c_{Hz}} \quad (5.1)$$

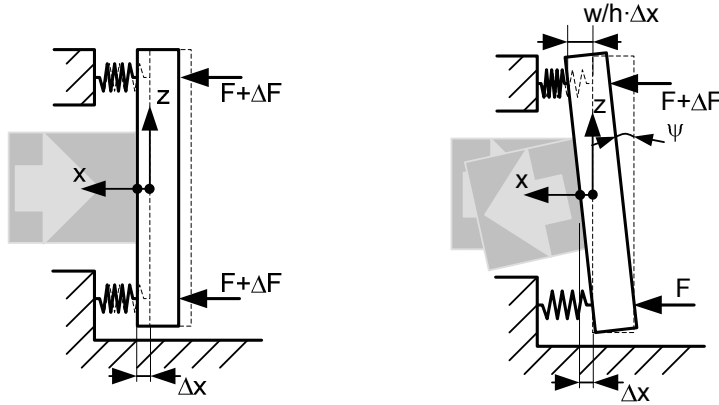
In the second analysis one of the springs is subjected to an extra force level ΔF (Figure 5.3 b), causing a translation of the critical point Δx of:

$$\Delta x = \frac{h}{w} \cdot \frac{\Delta F}{c_{Hz}}, \quad (5.2)$$

and a rotation ψ of:

$$\psi = \frac{1}{w} \cdot \frac{\Delta F}{c_{Hz}}. \quad (5.3)$$

A bracket on the optical bench is needed to be able to mount the component on the yz-plane. The component itself does not need to have a large thickness in the x-direction.



a) ΔF on both contact points

b) ΔF on 1 contact point

Figure 5.3 Displacement and rotation of critical point due to force variation in the yz-mounted component

xy-mounting plane

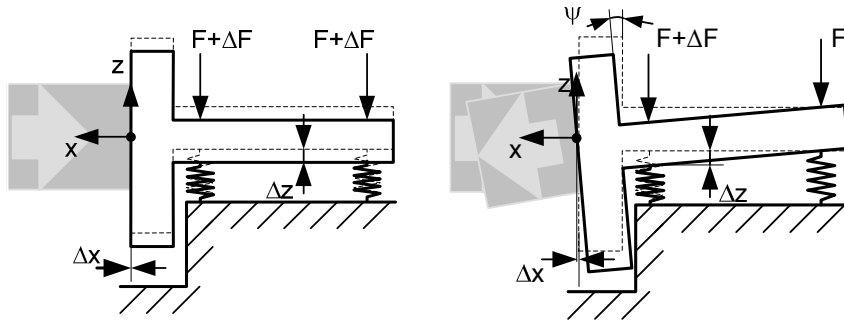
In Figure 5.2 b) the mirror is mounted at distance Δh from the xy-plane. Mounting forces are applied in the z-direction. In practice variations in the mounting forces can cause z-, ψ - and ϕ -variations and due to the lever effect also x-variations can occur. ψ and x are critical directions.

In the 2-D situation a force variation on both springs (Figure 5.4 a) will cause a displacement Δz . This does not result in a displacement Δx or in rotation ψ .

A force variation on 1 spring (Figure 5.4 b) will cause a tilt ψ according to (5.3). The force variation on 1 spring will also cause a displacement Δx :

$$\Delta x = \frac{\Delta h}{w} \cdot \frac{\Delta F}{c_{Hz}} - \frac{1}{w} \cdot \left(\frac{\Delta F}{c_{Hz}} \right)^2 \quad (5.4)$$

The first order effect is the lever effect due to Δh and a second order effect due to the rotation.



a) ΔF on both contact points

b) ΔF on 1 contact point

Figure 5.4 Displacement and rotation of critical point due to force variation in the xy-mounted component

Comparison

In Table 5.1 the maximum allowed force variation for both yz-mounting and xy-mounting in the plane of light with uncertainty $\Delta h = 0.1 \text{ mm}$ is shown.

Table 5.1 Allowed maximum force variation ΔF for maximum displacement Δx of the component for the two realistic mounting options

Force variation	yz-mounting	xy-mounting in plane of light with uncertainty Δh
	$w = 50 \cdot 10^{-3} \text{ m}$ $h = 25 \cdot 10^{-3} \text{ m}$	$w = 50 \cdot 10^{-3} \text{ m}$ $\Delta h = 0.1 \cdot 10^{-3} \text{ m}$
All contact points (translation of component)	$\Delta F = c_{Hz} \cdot \Delta x$	$\Delta x = 0 \ \forall \ \Delta F \in \Re$
1 point (tilt)	$\Delta F = c_{Hz} \cdot \frac{w}{h} \cdot \Delta x$ $= 2 \cdot c_{Hz} \cdot \Delta x$	$\Delta F = c_{Hz} \cdot \frac{w}{\Delta h} \cdot \Delta x$ $= 500 \cdot c_{Hz} \cdot \Delta x$

For the yz-mount both a force variation on all contact points and on 1 contact point can cause measurement instability. For the xy-mounted component only a force variation on 1 contact point can cause measurement instability. The maximum allowed force variation for the xy-mount is 500 times the allowed force variation for the yz-mounting. This means that xy-mounted components are

preferable over yz-mounted components from a measurement stability point of view. The next question to answer is whether or not force variations are a problem for measurement stability.

5.1.3 Clamp to contact stiffness ratio

The clamping force variations can have several causes:

1. (Micro-)creep;
2. Stress relaxation;
3. Temperature variations.

Creep and temperature variations cause an effective length change of the clamp Δl , which leads to a clamping force variation in combination with the stiffness of the clamp c_{clamp} :

$$\Delta F = c_{clamp} \cdot \Delta l \quad (5.5)$$

In stress relaxation there is no effective length change in the clamp. However, the clamping force changes due to a reduction in stress. Creep and stress relaxation effects are time (and temperature) dependent effects. The creep and relaxation rate decrease with the passing of time if temperature and loading conditions are constant. Stress relaxation is generally conducted intentionally at elevated temperatures to remove residual machining stresses.

The clamp material is $TiAl_6V_4$ because it has relatively low density and can absorb large strains. No data is available on stress relaxation of $TiAl_6V_4$ at room temperature, which is why the assumption is made that stress relaxation will have a comparable effect on the pre-clamping force as creep does. Therefore, only creep and temperature variations are considered for both measurement and alignment stability.

The next problem is to define a criterion to determine whether force stability will be enough. Assuming that the component is tensioned to the mount using a clamp, the criterion is the ratio between the stiffness of the clamp and the contact stiffness. To be able to absorb a force variation with as little displacement on the contacts as possible, the clamp should have low stiffness. At the same time the stiffness of the contact should be as high as possible. The ratio between the stiffness of the clamp and stiffness of the contact should therefore be as small as possible and it should certainly be below a certain level. This maximum can be

determined by integrating (5.5) with the equations shown in Table 5.1. For the yz-mounting this leads to the following criterion:

$$\frac{c_{clamp}}{c_{Hz}} < \frac{\Delta x}{\Delta l} \quad (5.6)$$

For the xy-mounting this leads to the more relaxed criterion:

$$\frac{c_{clamp}}{c_{Hz}} < 500 \cdot \frac{\Delta x}{\Delta l} \quad (5.7)$$

To get some idea of the stiffness ratio's needed to make the mounting options work, an indication of a length change Δl of the clamp should be computed.

Creep

Quantifying creep for either alignment or measurement stability is conducted with large uncertainties. Because it involves a number of assumptions on the design of the component, clamp and mount. Also creep data are not readily available for all materials and the available data should be treated with caution because creep rates are dependent on the loading and environmental conditions.

Although little data is available on creep of SiC and fused Silica at low temperatures (room temperature and below), it is assumed that the creep rate will remain below 0.1 nm/s even in the first 1000 hours and that the TiAl₆V₄ clamp will exhibit a significantly larger creep rate. Note that Titanium alloys are often chosen as a construction material because of their low creep rate in comparison to other metal alloys. The creep behavior of TiAl₆V₄ is discussed in Appendix A for measurement stability in which creep strain is calculated for a period of 6 hours after 0.5 years (allowed displacement $\Delta x = 0.17$ pm) and for alignment stability in which the creep strain is calculated for a period of 6 years (allowed displacement $\Delta x = 1.9$ μm).

The final assumption of this analysis is an assumption on the length of the TiAl₆V₄ clamp, over which the creep strain occurs. Assume that a fused Silica beamsplitter with thickness $l_{BS} = 10$ mm is mounted against a SiC mount with thickness $l_M = 10$ mm using a TiAl₆V₄ clamp with length $l = 20$ mm. Using this length and the creep data in Appendix A, the length change Δl can be

calculated. In combination with the allowed displacement Δx the maximum stiffness ratio between the clamp and the Hertz contact can be computed. These are shown for best- and worst-case creep conditions in Table 5.2.

Table 5.2 Maximum stiffness ratios to maintain measurement and alignment stability for yz- and xy-mounting

Case	maximal c_{clamp}/c_{Hz} for yz-mount		maximal c_{clamp}/c_{Hz} for xy-mount	
	after 6 years constant stress	in a 6 hour period after 0.5 years constant stress	after 6 years constant stress	in a 6 hour period after 0.5 years constant stress
Best	$1.5 \cdot 10^1$	$1.7 \cdot 10^{-2}$	$7.4 \cdot 10^3$	$8.9 \cdot 10^0$
Worst	$2.7 \cdot 10^{-3}$	$1.8 \cdot 10^{-6}$	$1.4 \cdot 10^0$	$8.8 \cdot 10^{-4}$

Realistically the stiffness of a Hertzian contact is of the order of 10^7 N m^{-1} to 10^8 N m^{-1} . Depending on the pre-clamping force needed, the clamp can have a minimal stiffness of 10^4 N m^{-1} to 10^5 N m^{-1} , which leads to a stiffness ratio of at least $1 \cdot 10^{-3}$. Table 5.2 shows that the maximal stiffness ratio is always larger than $1 \cdot 10^{-3}$ in the best creep conditions, for both yz- and xy-mounting. However, for worst case creep conditions for TiAl_6V_4 , the measurement stability of the yz-mount cannot be met, because the required stiffness ratio is below the minimal ratio of $1 \cdot 10^{-3}$. Note that the xy-mount also does not meet the limit with a stiffness ratio of $0.88 \cdot 10^{-3}$. The conclusion drawn from this analysis is that it is necessary to give the TiAl_6V_4 clamp anti-creep treatment like aging and chempolishing. If the anti-creep actions are performed properly, both yz- and xy-mounts should maintain measurement stability.

Temperature variation

Force variations due to temperature variations occur due to a mismatch in the coefficient of thermal expansion between the component, mount and clamp. Important temperature variations for this force variation are the cool down trajectory from 293 K to 100 K ($\Delta T = -193 \text{ K}$) for alignment stability and a temperature variation of $\Delta T = 0.1 \text{ mK}$ during measurements.

Assume again that a fused silica beamsplitter with thickness $l_{BS} = 10 \text{ mm}$ is mounted against a SiC mount with thickness $l_M = 10 \text{ mm}$ using a TiAl_6V_4 clamp with length $l = 20 \text{ mm}$. For the

environmental conditions mentioned above, the relative length change of the clamp with respect to the Silica beamsplitter in the SiC mount is 29 μm for the 193 K cool down and 14.4 μm length change for the 0.1 mK temperature variation at 100 K.

Using the length changes the maximal stiffness ratios can be determined for the beamsplitter mounted in either the yz- or the xy-plane. As expected the stiffness ratio between the clamp and the contact can be higher for the xy-mount, but stiffness ratios for the yz-mount are also values which can be met.

Table 5.3 Maximum stiffness ratios to maintain measurement and alignment stability for yz- and xy-mounting

Case	Stiffness ratio	
maximal c_{clamp}/c_{Hz} for yz-mount	293 K to 100 K cool down	$6.5 \cdot 10^{-2}$
	0.1 mK temperature variation at 100 K	$1.7 \cdot 10^{-2}$
maximal c_{clamp}/c_{Hz} for xy-mount	293 K to 100 K cool down	$3.3 \cdot 10^1$
	0.1 mK temperature variation at 100 K	$8.7 \cdot 10^0$

The conclusion that can be drawn from this analysis is that force variations due to creep and temperature variations have a significantly larger effect in optical components mounted in the yz-plane than they do on components mounted in the xy-plane. However, it is expected that these variations will not cause force variations that are large enough to cause measurement or alignment instability, in either yz- and xy-plane mounting. yz- and xy-mounting are therefore both still an option. It should be noted however, that creep can pose a threat for the measurement stability in yz-mounting. Therefore, proper anti-creep precautions should be taken, like aging or chempolishing.

5.2 XY-mounted components

5.2.1 Beamsplitter

In Figure 5.5 a 3-D colour view of a possible design of the xy-mounted beamsplitter is shown. It is a cubic beamsplitter made of fused silica. This material has been chosen because it is transparent for optical wavelengths and the coefficient of thermal expansion closely matches that of SiC. The size of the beamsplitter is $\sim 65 \text{ mm} \times 65 \text{ mm} \times 25 \text{ mm}$ and the mass is $\sim 0.2 \text{ kg}$.

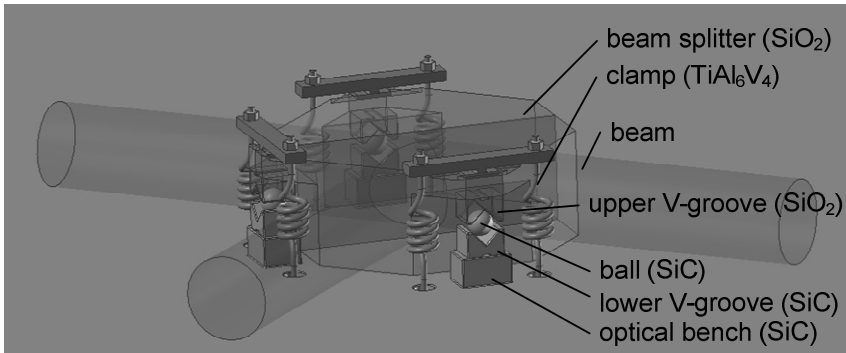


Figure 5.5 XY-mounted beamsplitter

The beamsplitter mass consists of two parts. One part is coated with 50% – 50% reflective coating on the bonding surface. The two parts are optically contacted at the bonding surface. Optically contacted parts have the thinnest possible interlayer, meaning that this kind of bond poses the smallest risk for losing measurement stability due to bond related effects like expansion of an interlayer.

The beamsplitter is mounted on three V-grooves-ball combinations (Figure 5.6). The centre of two of the balls is located on the x-axis and one ball is on the y-axis. This arrangement makes it least sensitive to variations of the clamping forces.

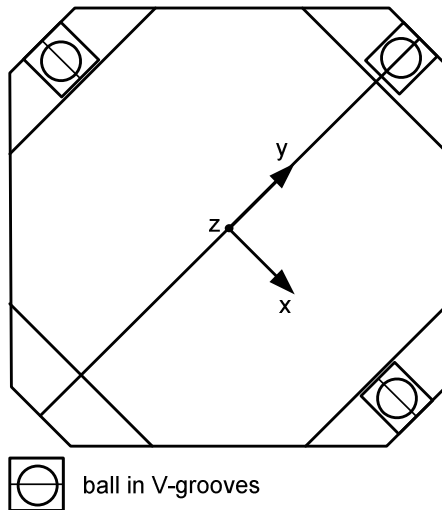


Figure 5.6 Position and orientation of the V-groove ball combinations on the xy-mounted beamsplitter

The clamping force at each of the contact areas is chosen such that the balls will not lose contact with the V-grooves when the beamsplitter is quasi-statically loaded during launch with 25g acceleration. In combination with a friction constant $\mu = 0.4$ [46], this leads to 155 N clamping force per V-grooves-ball combination. The V-grooves are pointing towards the centre of the beamsplitter, such that the critical point is the thermal centre (the origin of the coordinate system in Figure 5.6). Note that generally sliding balls in single V-grooves are used for kinematic mounts. However here, rolling balls in double V-grooves are used, because theoretically the 6.9 μm thermal expansion difference between the fused silica beamsplitter and the SiC mount can be absorbed without hysteresis when using rolling balls, whereas it cannot be absorbed using sliding balls (Appendix D). The V-grooves ensure that the optical component remains aligned after the temperature drop from 293 K to 100 K. The required alignment accuracy of the V-grooves is ± 2 mrad (Appendix D).

To survive a 155 N dynamic load in the SiC ball on the silica flat, the radius of the SiC ball must be at least 2.9 mm according to Auerbachs law (section 2.3.1). The radius taken for the ball in the beamsplitter mount shown in Figure 5.5 is 3 mm. Note that each contact point absorbs 109 N, which gives a safety factor of 1.4. In this situation the Hertzian contact pressure is $2.1 \cdot 10^9 \text{ N m}^{-2}$ [86].

Note that this is a high contact pressure, certainly since the compressive strength of silica for long duration loading is $350 \cdot 10^6 \text{ N m}^{-2}$, which is considerably lower than the Hertzian contact pressure mentioned above [47]. The strength of glass is highly dependent on flaw sizes. The flaws can be reduced in size and number by grinding, polishing and acid etching. At cryogenic temperatures ($\sim 80 \text{ K}$) glass has a breaking strength which is twice the strength at room temperature [87].

For either xy- and xz-mounting, the clamping mechanism cannot be equipped with one central pulling rod, since the light will need to travel through the center of the beamsplitter. Therefore, the beamsplitter is tensioned against the optical bench using separate clamps for each contact point.

The upper and lower contacts of the clamp are fixed to the beamsplitter and base respectively, in 6 DOF's. A realistic uncertainty for ball position relative to the clamp is $\pm 0.1 \text{ mm}$. The

deviation of the ball position relative to the clamp causes a bending moment of $15 \cdot 10^{-3}$ Nm on the beamsplitter at each contact point.

The force is ideally applied as a purely compressive force. Therefore the clamp is symmetrical, to prevent additional bending moments in the beamsplitter.

The total axial stiffness for the ball in V-grooves combination suggested for the beamsplitter mount is $c_{A,total} = 2.7 \cdot 10^7$ N m⁻¹ [88]. Therefore, the chosen spring has a stiffness of $7.8 \cdot 10^4$ N m⁻¹, such that the stroke is 2 mm for a 155 N load.

In the clamp design custom made TiAl₆V₄ coil springs with round wire (thickness 1.53 mm) and 4 windings are applied to achieve this stiffness. The spring force is relayed to the contact area via levers on the bottom underneath the optical bench and the on top of the beamsplitter. The levers are relatively stiff. To make sure that the force is applied above the contact points in a clean flat contact, the upper lever is equipped with an elastic hinge to level out force variations. The contacts of the levers to the optical bench and the beamsplitter are glued into slits, such that rotation of the clamp around the z-axis is prevented (Figure 5.7).

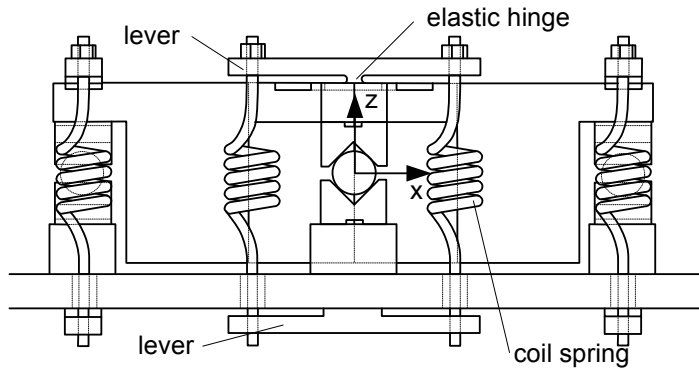


Figure 5.7 xz side view of the beamsplitter with clamps

5.2.2 Mirror

The mirror mounted in the xy-plane is shown in Figure 5.8. The mirror is designed for a light incidence angle of 45°, which is the case for most mirrors in the BAM system. The clear aperture size of the 45° mirror is rectangular with a height of 25 mm and a width of 34 mm for a Ø 20 mm beam. The mass of the mirror body

is $m = 0.044$ kg. Like for the beamsplitter, hysteresis may not occur with a 25 g quasi-static load, leading to a preclamping force of ~ 40 N per contact point.

The mirror is suspended on V-grooves with balls, like the xy-mounted beamsplitter. Note that the mirror body is made of SiC like the optical bench, and there is no difference in thermal expansion coefficient. However, the suspension on V-grooves with balls is considered to be necessary, because point contact mounting has the drawback that the thermal conductance of point contacts is so low that the temperature difference between the mirror body and the optical bench can increase such that alignment stability is lost (Appendix E). By applying V-grooves with balls this problem can be solved. The difficulty of this solution is that it is more complex than simply clamping the mirror against the optical bench. However, the advantage is that the mirror is truly fixed in 6 DOF's, because the V-grooves provide fixation also for tangential forces larger than the friction force in the x- and y-direction. Also, the mirror bases can be manufactured at the same height as the bases of the beamsplitter, which makes grinding to 0.1 mm height accuracy and to 0.1 μm flatness significantly easier.

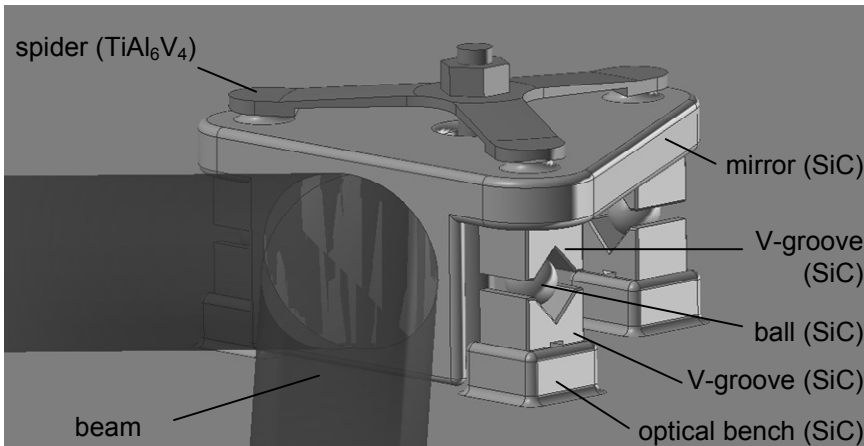


Figure 5.8 XY-mounted mirror

The V-grooves are not pointing towards the reflective surface of the mirror, because this would reduce the rotational stiffness provided by the V-grooves to zero. The front V-grooves are aligned

towards each other instead, to keep the thermal centre as close as possible to the reflective surface, while still maintaining sufficient rotational stiffness (Figure 5.9).

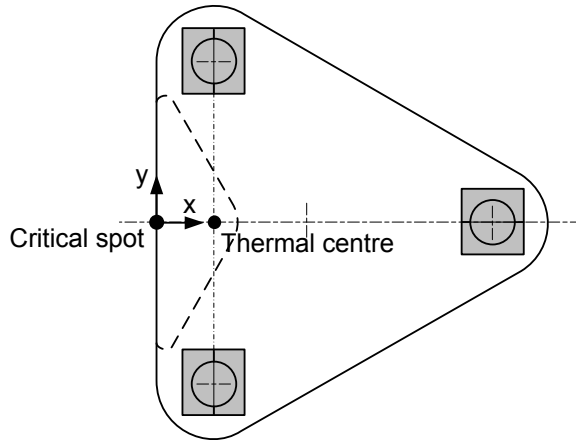


Figure 5.9 Orientation of the V-grooves in the xy -mounted mirror

The spider, a single clamping mechanism has three arms. The angle between each of the three spider arms is equal and the arms are of equal length, the total clamping force is divided equally to each contact point. The spider clamp is tensioned by shortening the central pulling rod.

The total axial stiffness of the combination with a SiC ball of radius $R = 3 \text{ mm}$ and SiC V-grooves at a 45° angle at a clamping load of 40 N is $7.3 \cdot 10^7 \text{ N m}^{-1}$ (D.2). The three ball in V-grooves combinations are applied in parallel leading to a total axial stiffness of $2.2 \cdot 10^8 \text{ N m}^{-1}$ for the mirror. The required stiffness ratio between the clamp and the axial stiffness of the mirror is $8.8 \cdot 10^{-4}$, in worst case creep conditions. The axial stiffness of the spider should therefore be maximally $1.9 \cdot 10^5 \text{ N m}^{-1}$, this leads to a minimal deflection of each spider 0.28 mm at 110 N load. The required deflection and the load give a means of dimensioning the spider.

The TiAl_6V_4 spider will shrink more than the SiC mirror due to the temperature drop from 293 K to 100 K . However, the clamping force must be applied through the centre of the ball. Therefore, the top of the mirror and the bottom of the optical bench face sheet are equipped with SiC semi-spheres which are made in one piece with

the mirror and glued to the face sheet, respectively. This way the spider can shift over the semi-spheres. The clamp is shown in cross-section in Figure 5.10.

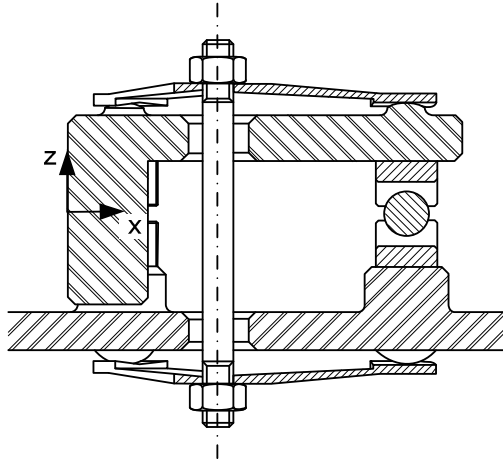


Figure 5.10 xz cross-section of the xy-mounted mirror

The alignment and assembly procedure is equal to the procedure used for the xy-mounted beamsplitter.

5.3 YZ-mounted components

5.3.1 Beamsplitter

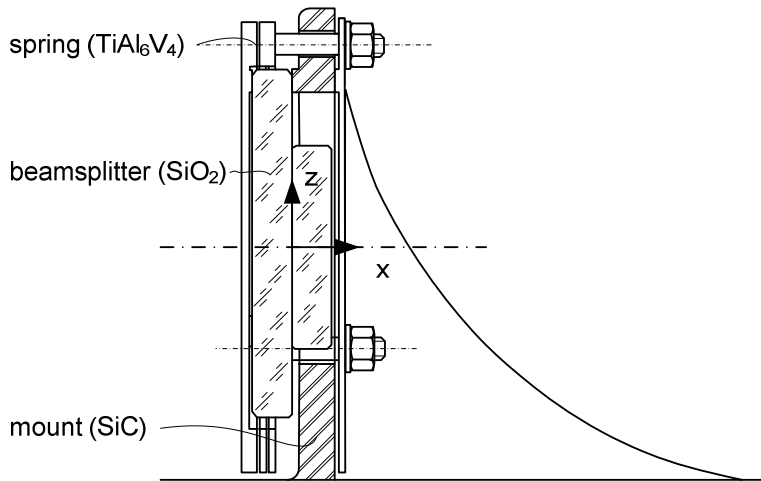
Figure 5.11 shows a design of a beamsplitter mounted in the yz-plane. It shows a beamsplitter consisting of 2 plates of equal thickness. One of the plates is larger, such that the beamsplitter can be mounted on the beam splitting plane. The spring tensions the beamsplitter against the mount.

The contact points for the yz-mounted beamsplitter are located at equal distance from the centre at angles of 120° . These contact point locations allow for applying equal contact force to each contact point more easily.

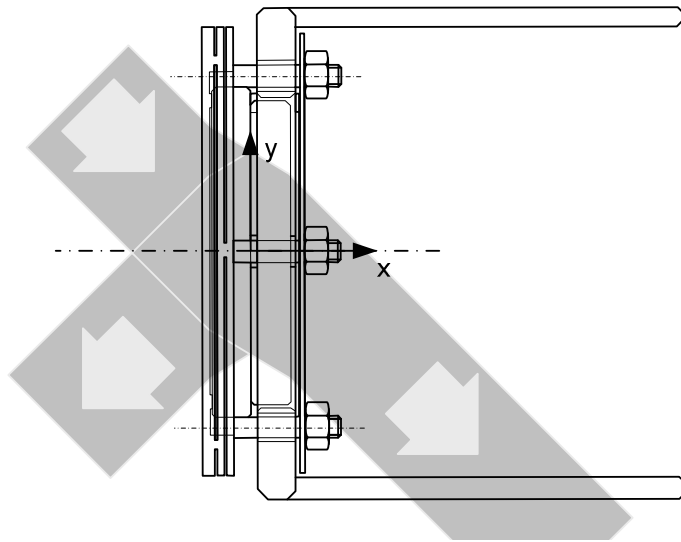
The beamsplitter splitting surface is the contact plane against the mount, and contact points in the SiC mount are spherical with radius $R = 3$ mm.

The beamsplitter size must be large enough to transmit the beam with radius 20 mm. Each half of the beamsplitter glass must be

sufficiently flat to allow optical contacting to take place between the two halves. The required flatness for optical contacting is $\lambda/10$.



a) *xz*-cross-section



b) *xy*-view

Figure 5.11 yz-mounted beamsplitter

In order to achieve this flatness, each half of the beamsplitter should have sufficient thickness to diameter ratio. Optics manufacturers usually use a thickness to diameter ratio of $1/5$ to $1/7$. Sometimes the thickness to diameter ratio is stretched to $1/10$.

The fact that the incident angle of the beam is 45° , means that the beam shows refraction when entering and leaving the beamsplitter leading to a shifted beam. This shift needs to be taken into account as well when determining the size of the beamsplitter. This is illustrated in Figure 5.11 b.

The mass of the beamsplitter is $m = 0.033$ kg. The clamping force is calculated such that the beamsplitter does not loose contact at a 25 g quasi-static load, leading to 12 N per contact point. The force is, however, not high enough to prevent the beamsplitter from shifting over the contact point during these loads. The beamsplitter will shift anyway due to the thermal expansion difference. To center the beamsplitter three drops of low stiffness adhesive RTV 566 are used around the circumference.

The clamp for clamping the beamsplitter against the mount can only be applied around the edges of the beamsplitter, where it does not hinder the optical path.

The clamp design is focused on providing equal clamping force at all contact points, while at the same time using as small force loops as possible, such that no unnecessary bending forces are introduced into the beamsplitter mount. This is done by a concertina spring with three contact points like in the cross-section of the side view in Figure 5.11 a. On the back side of the mount a ring is present such that the force loop is as small as possible, creating as little as possible bending forces in the spring and in the mount.

5.3.2 Mirror

The yz-mounted mirror design (Figure 5.12) is very similar to the yz-mounted beamsplitter design, with the same arguments on the location of the contact points. The mass of the mirror is about the same as the mass of the beamsplitter, leading to equal clamping force. Adhesive is used for maintaining yz-alignment. The spring which tensions the mirror against the mount is a harmonica spring like the yz-mounted beamsplitter spring except that it is mounted against the back side of mirror mounted. The mirror is mounted against the reflective surface, so that alignment instability due to poor thermal contact conductance is prevented.

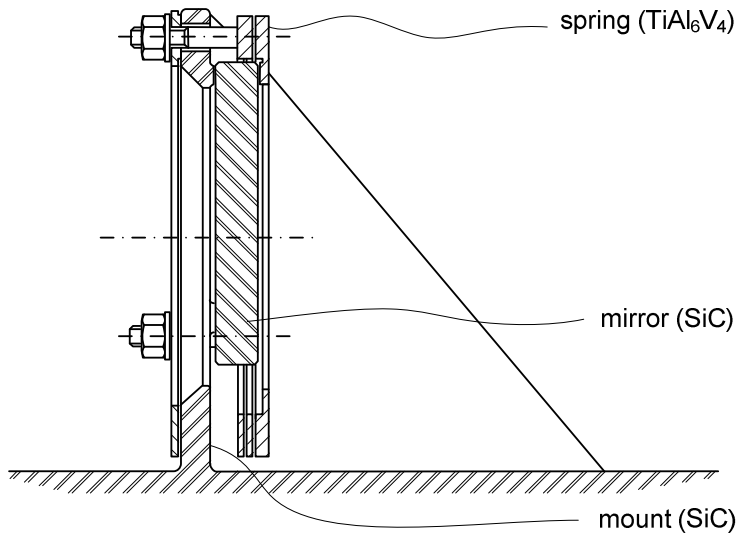


Figure 5.12 Side cross-section yz-mounted mirror

5.4 Comparison of designs

The most important aspects for the mirror and beamsplitter design in both mounting in the xy -plane and the yz -plane have been discussed in sections 5.2 and 5.3. In this final section a comparison is made between mounting on the xy -plane and the yz -plane. Criteria for this comparison are: overall complexity of the design, alignment complexity, alignment stability, measurement stability, mass and clamping force, and stresses.

5.4.1 Complexity of the design

The xy -mounted optical components are considered more complex than the yz -mounted optical components, because the complete optical component consists of more parts (the V-grooves and balls), which must be accurately aligned to create an accurate thermal centre. The parts in themselves are not considered to be difficult to manufacture. The V-grooves do not need to be extremely flat ($\sim 1 \mu\text{m}$). The same goes for the roundness of the balls. The roughness must be much smaller than the contact radius of the ball on flat ($\ll 0.1 \text{ mm}$). 100 nm rms roughness would suffice.

For the yz -mounted optical component, the most complex part is considered to be the mount. Preferably, it is machined together with the optical bench from one monolithic piece of green SiC. The

holes in the mount, which are only just above the optical bench are, however, not well reachable by machining tools. The mount is machined separately and brazed to the optical bench in a later stage.

5.4.2 Alignment complexity

Alignment complexity is that of aligning the component and clamping it. The xy-mounted components are aligned with one or several dedicated tools, which first align and fix the upper V-grooves to the optical components. In the next step the balls and lower V-grooves are placed in the alignment tool and aligned with respect to the upper V-grooves. The alignment tool can then be placed on the optical bench, to align the optical component with respect to other components. For most components this is only a rough alignment but for some it is a fine alignment step as well. Finally, the lower V-grooves are fixed to the optical bench by gluing with EC 2216, and possibly another tool is used to apply the clamping force. The preclamping force of the xy-mounted components is considerably larger than the preclamping force of the yz-mounted optical components.

The alignment of the yz-mounted optical components is performed by polishing the contact areas on the mount in case of the beamsplitter, or on the mirror bodies in case of the mirror. This polishing does not need to be conducted on all optical components. It must only be performed on components which need fine alignment. The rough alignment is considered to be achieved on the manufacturing accuracy of the mount. Polishing is an iterative process, which is lengthy and irreversible. The contact areas of the beamsplitter mount are somewhat harder to reach with a polishing tool than those on the mirror. However, it is not considered impossible. Polishing SiC is considered to be well-controllable.

5.4.3 Alignment stability

The alignment stability of the yz-mounted optical components is better than the alignment stability of the xy-mounted optical components. Due to the clamping against extremely stiff point contacts in the critical directions (x , ψ and θ), these directions are truly fixed. Force variations will not be large enough to disturb the

alignment stability. Due to the flatness of the optical components, which are mounted against the contact points, it is very unlikely that the optical components will lose alignment in the critical directions due to either the launch vibrations or the temperature drop from 293 K to 100 K.

The alignment stability of the xy-mounted optical components is partly dependent on friction between the ball and V-grooves, and between the V-grooves and optical component or optical bench. This means that possibly there is hysteresis. The design of the components has been made on force levels of 25 g quasi-static. However, it is possible that the component is exposed to shock loads of 200 g in 0.5 ms. In this case the hysteresis might have a disastrous effect on the alignment stability. Also the alignment stability after the temperature drop is dependent on the alignment accuracy of the V-grooves.

5.4.4 Measurement stability

The measurement stability of the xy-mounted optical components is considered to be between 50 and 500 times better than the measurements stability of the yz-mounted beamsplitter, because force variations affect mostly non-critical directions and much less the critical DOF's. Also the clamps for xy-mounted components have been dimensioned to take into account creep of the clamp, whereas this was not possible for the yz-mounted components.

5.4.5 Mass, preclamping force and stresses

The mass of the components mounted in the xy-plane is considerably higher than the mass of the components mounted in the yz-plane. This is not beneficial for the overall mass budget in the BAM system, because this means less material can be used for the large optical bench, which should be as stiff as possible. Additionally, larger masses lead to larger forces due to launch vibrations, which in turn means, that the clamping forces needed for components mounted in the xy-plane are an order 10 higher than the clamping forces needed for the yz-mounted components. These higher clamping forces induce a need for heavier clamps. Also, the Hertzian contact stresses are considerably larger. The ball-on-flat contact stresses between the fused silica V-grooves and the SiC balls can be as high as $2 \cdot 10^9$ N m⁻². Theoretically, the

contact should be able to withstand this kind of stress. However, many engineers will not design glass products in which compressive stresses exceed $300 \cdot 10^6 \text{ N m}^{-2}$, because of its brittle nature. In the yz-mounted components it is possible to keep the stresses below this practical limit. This is not the case for the xy-mounted components.

5.5 Conclusions

In this chapter the focus has been on achieving optimal measurement stability in mounting the optical components, because the BAM optical bench has a major effect on the measurement stability. Analysis shows that an optical component mounted in the xy-plane (plane of light path) will have a 500 times higher measurement stability than a component mounted in the yz-plane. However, when making an actual design of xy-mounted components and yz-mounted components, the result is that xy-mounted components are more complex than yz-mounted components due to the fact that there are more joints between parts and the alignment procedure is rather complex. Also xy-mounted components have a significantly larger risk of losing alignment during launch, especially due to shock loads, where yz-mounted components are not expected to lose alignment. Therefore despite the worse measurement stability, the yz-mounted components are preferred over the xy-mounted components.

6 Experiments

The previous chapter has shown that the yz-mounting plane for optical components is chosen as preferable over the xy-mounting plane because it is expected that components mounted in the yz-plane will maintain alignment stability after launch and cool-down. In order to test this, experiments have been performed on beamsplitters mounted on breadboards in a similar fashion as discussed in the previous chapter. Several configurations of beamsplitters have been tested. These experiments are discussed in section 6.1.

In chapter 4, however, also has shown that the optical bench will have such a large influence on the measurement accuracy of the BAM system, that no instability budget is available for the optical components. In chapter 5 it is shown that it is not possible to achieve absolutely stable optical components with a clamping solution. However, bonding techniques with low stresses like hydroxide catalysis bonding might be a solution here. As stated in chapter 2, however, this technique is promising but still very experimental for bonding SiC. In section 6.2 experiments with HCB bonding and bending experiments on the bonded pieces of SiC are discussed to aid in the development of the HCB technique.

6.1 Beamsplitter breadboards

6.1.1 Goals

The goal of the beamsplitter breadboard experiments is to test the survivability and angular alignment stability of yz-mounted

beamsplitters in severe environmental loading (random vibrations, shock and thermal cycling) representative for launch.

6.1.2 Breadboard design

Three breadboards, as shown in Figure 6.1, have been made at TNO. The breadboards consist of a SiC baseplate with two beamsplitters mounted on to the breadboard. Each beamsplitter is supported on three polished SiC studs, which are part of the SiC structure, and preloaded with a TiAl_6V_4 concertina spring. Radial movement and rotation around its optical axis during transport, handling and vibration, is constrained by adhesive spots. Two breadboards are made of Boostec SSiC and one of Xycarb C/SiC with CVD SiC coating. Each breadboard has been tested in 2 different beamsplitter configurations.

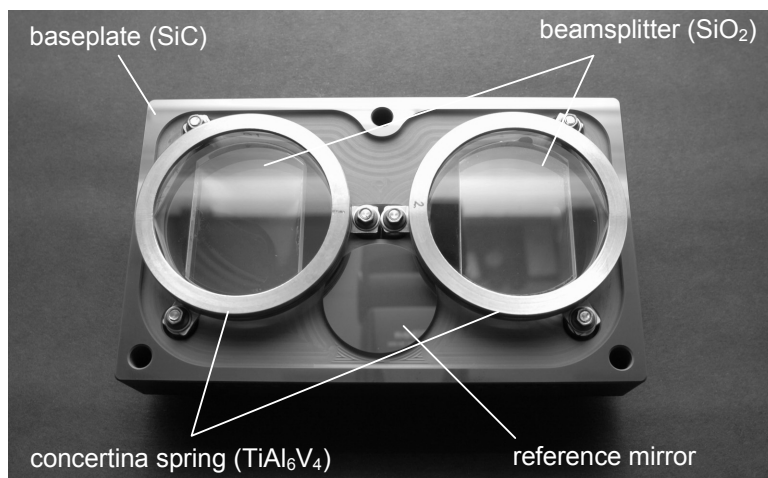
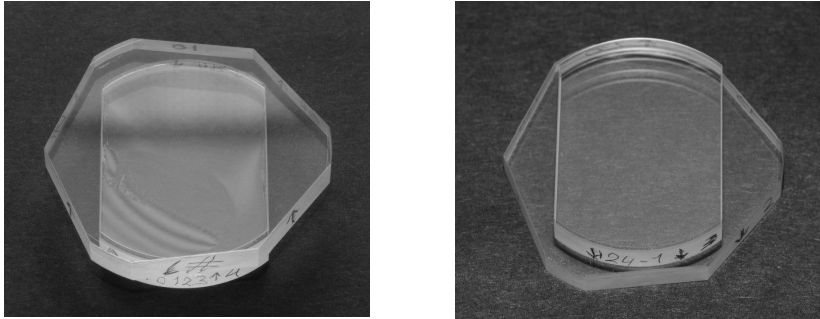


Figure 6.1 Beamsplitter breadboard

The breadboards contain two beamsplitters which have been bonded using the HCB technique at the University of Glasgow, or which have been optically contacted or joined with a transparent adhesive at TNO.

The HCB bonding was not performed with complete success. Due to flatness problems the bonds were successful over maximally 90 % of the surface. In the remaining part delamination or air bubbles occurred. An example of delamination is shown by the fringes in Figure 6.2 a). The optically contacted beamsplitters have been made successfully (Figure 6.2 b).



a) HCB bonded (30% delamination) b) Optically contacted

Figure 6.2 Beamsplitters

The three beamsplitter breadboards have been tested with 2 different preload levels, adhesives and beamsplitter radial plays, which is shown in Table 6.1.

Table 6.1 Details on breadboards

Test specimen	Beamsplitter serial number	Beamsplitter bond	SiC material	Glass contact diameter [mm]	Beamsplitter radial play [mm]	Adhesive	Spring preload [N]
A1	1	HCB	Boostec	1	0.5	RTV 566	20
	2	HCB		2	0.5	RTV 566	20
B1	4	optical	Boostec	1	0.5	RTV 566	20
	5	optical		2	0.5	RTV 566	20
C1	6	optical	Xycarb	1	0.1	EC 2216	20
	7	optical		2	0.1	EC 2216	20
A2	12	kit	Boostec	1	0.1	EC 2216	20
	13	kit		2	0.1	EC 2216	30
B2	14	kit	Boostec	1	0.1	RTV 566	20
	15	kit		2	0.1	RTV 566	30
C2	16	optical	Xycarb	1	0.1	None	20
	17	optical		2	0.1	None	30

6.1.3 Tests

The test program consists of 4 experiments:

- Thermal cycling test;
- Thermal vacuum test;
- Vibration test and;
- Shock test.

Optical alignment measurements and visual inspections have been performed prior to and after each experiment to assess possible damage and measure alignment stability.

Optical alignment measurements

The optical alignment measurements are performed with a Wyko 400 laser interferometer (beam diameter 100 mm) and a 45° mirror, with the breadboard horizontally installed on a kinematic mount (Figure 6.3). Homogenous temperature of the breadboard is achieved by at least 1 hour acclimatization in the test facility. The interferometer is autocollimated on the SiC reference mirror and the tilt of the beamsplitters is measured with respect to the reference mirror. For each test run, three to five separate measurements are taken, with removal of the test specimen in between measurements to verify the test setup reproducibility. The reproducibility of the test setup is 1.3 μrad , which is close to the required alignment stability of the optical components on the optical bench.

The reproducibility of the set-up is affected by thermal and airflow instabilities, and by stresses in the breadboards caused by hysteresis in the three contactpoints of the kinematic mount.

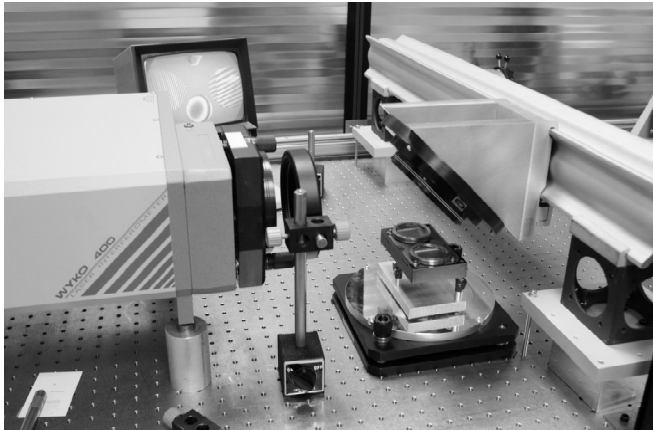


Figure 6.3 Optical alignment set-up

Thermal cycling

Thermal cycling is performed in a nitrogen gas environment in a climate chamber at Dutch Space in Leiden. The breadboards are all equipped with thermocouples to monitor their temperature.

The temperature extremes are 350 and 100 K, with cool-down and heat-up rates limited to 10 K/min. 5 thermal cycles have been performed on each test specimen. The thermal cycle profile of one thermocouple is shown in Figure 6.4.

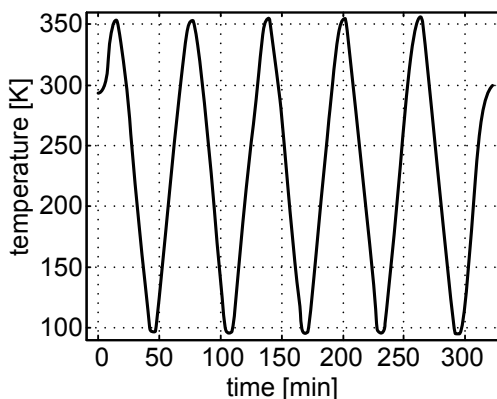


Figure 6.4 Temperature-time trajectory of one of the thermocouples

Thermal vacuum

In order to verify the beamsplitter bond (optical contacting or HCB) at low temperature (120 K) and low pressure ($5 \cdot 10^{-6}$ mbar), an inspection has been done under monochromatic light in a thermal vacuum chamber at 120 K (Figure 6.5).

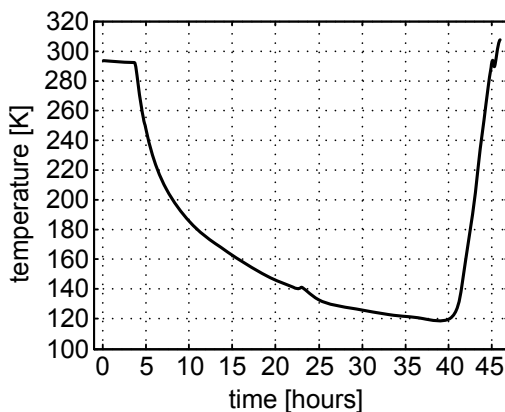


Figure 6.5 Cool-down trajectory of one thermocouple in thermal vacuum

The beamsplitters have been supported on a small trolley, to position them, one by one, in front of a small window.

Vibration testing

Random vibration testing has been performed on a single axis electro-magnetic shaker and a cube test interface (Figure 6.6) at NLR in Marknesse. This allows for testing of three test specimens simultaneously. By rotating the position on the cube, all three axes are tested on all specimens. The random vibration spectrum has an overall level of 17.3 g rms and is shown in Figure 6.7. It is representative for vibrations during launch. Low level sine sweeps have been done before and after each random vibration run to monitor changes in mounting conditions. Each breadboard is equipped with a tri-axial accelerometer.

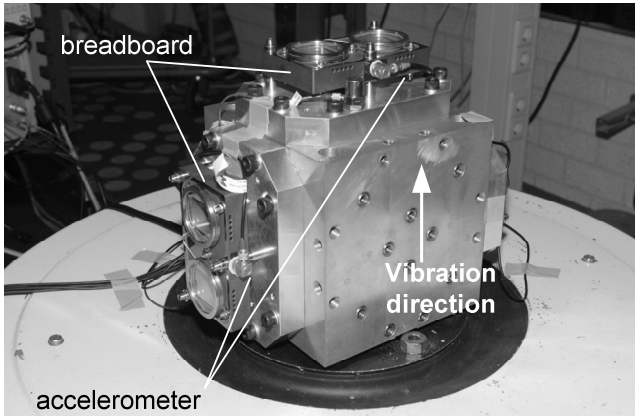


Figure 6.6 Three breadboards mounted on the vibration adaptor on a shaker

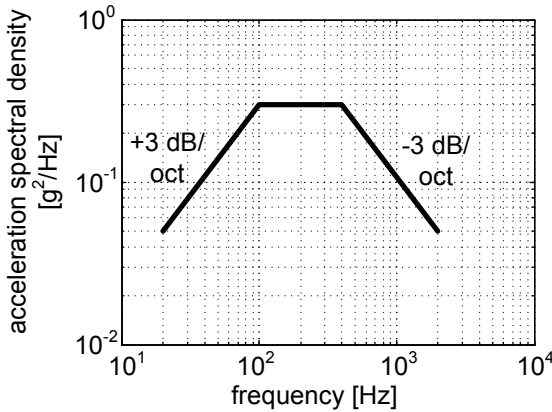


Figure 6.7 Random vibration input

Shock testing

Shock testing has been performed on a drop table (Figure 6.8) at Sebert Trillingstechniek in Berschenhoek in accordance with standard IEC 68-2-27 (3 test runs in 6 directions, 18 test runs total per specimen). The measured input level at the table base is 200 g half sine wave with a duration of 0.5 ms. Figure 6.9 shows a typical response of the accelerometer on the breadboard during the shock test.



Figure 6.8 Beamsplitter shock testing on a drop table

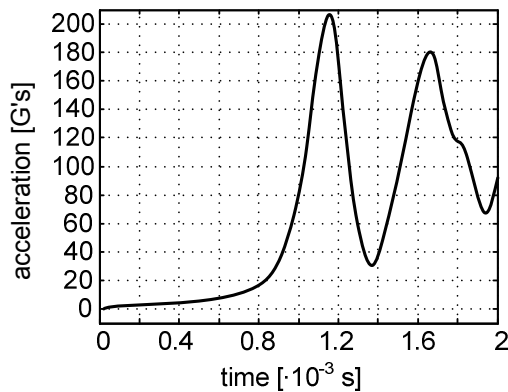


Figure 6.9 Typical acceleration on breadboard during shock test

6.1.4 Results

The results of the optical alignment measurements are shown in Table 6.2. The table shows which experiments have been performed on the breadboards and the maximum measured tilt

variations. The tilt variations are all close to the repeatability of measurement of 1.3 μrad , except for the beamsplitters on breadboard C2 and the tilt around the y-axis for beamsplitter BS1 on breadboard A1, which have an order of magnitude higher tilt.

Table 6.2 Test results. X indicates that the test has been performed.

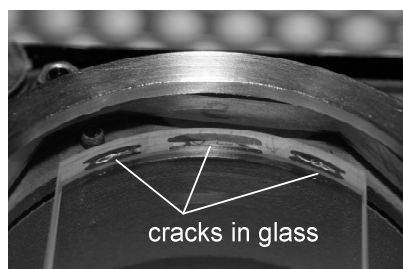
	A1	B1	C1	A2	B2	C2
Thermal cycling	X	X	X	X	X	X
Thermal vacuum	X	X	X	-	-	-
Random vibration	X	X	X	X	X	X
Shock test	-	-	-	X	X	Failed
Measured tilt variation [μrad]						
Beamsplitter 1	BS1	BS4	BS6	BS12	BS14	BS16
Bond	HCB	optical	optical	kit	kit	optical
x	-3.5	-4.5	-1.8	0.9	0.8	49.6
y	26.9	3.5	-0.1	1.5	6.2	-11.9
Beamsplitter 2	BS2	BS5	BS7	BS13	BS15	BS17
Bond	HCB	optical	optical	kit	kit	optical
x	-0.5	3.7	3.2	1.1	-1.7	62.1
y	-5.8	-3.2	1.2	3.6	1.8	11.6
Remark no.	1	2	3	4	5	6

The observations for each breadboard are:

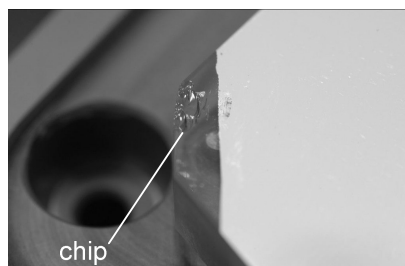
1. The HCB bonds in the beamsplitters of breadboard A1 have shown air bubbles and delaminations before the start of the test program. The contact points show severe surface degradation after random vibration tests (Figure 6.10 a).
2. The contact points of breadboard B1 show severe surface degradation after random vibration tests.
3. Breadboard C1 shows cracks in the EC2216 connection after thermal cycling (Figure 6.10 b).
4. Breadboard A2 shows a slight surface degradation of the contact points after random vibrations. Some chips have come off the beamsplitters after shock test (Figure 6.10 c).
5. Breadboard B2 has a slight surface degradation of the contact points after random vibrations.
6. Breadboard C2 shows severe surface degradation of the contact points after random vibrations. The beamsplitters have failed during shock test (Figure 6.10 d).



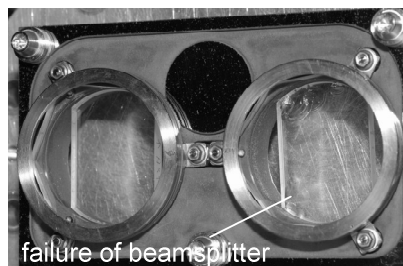
a) Surface degradation of contact point



b) Cracks in glass at EC2216 connection



c) Chips from glass after shock test



d) Failure of beamsplitter in shock test

Figure 6.10 Photographs of damage due to the test program.

6.1.5 Discussion

The surface degradation of the contacts during vibrations is explained by the fact that the clamping force is, with 20 N per contact point for most beamsplitters, so low that the vibration forces on the beamsplitter are higher than the friction forces. This means that the beamsplitter will slip over the contacts during vibrations, causing an abrading effect on both the glass and the SiC contacts (Figure 6.10 a). The lateral movement is restricted by the adhesive around the perimeter. The stiffer the adhesive, the less severe is the abrading effect. The higher clamping force of 30 N on beamsplitters BS13, BS15 and BS17, should theoretically be enough. However, some abrasion has still been observed.

The cracks in the glass at the EC2216 adhesive in breadboard C1 (Figure 6.10 b) are thought to be caused by stresses in the relatively stiff epoxy due to the thermal expansion difference between the SiC breadboard and the fused silica beamsplitter.

The large tilt variation in beamsplitter BS1 on breadboard A1 may be caused by the fact that the air bubble in the HCB bond closed

partly during thermal cycling. Beamsplitter BS2 has also been bonded with HCB and shows a delamination in the form of an airbubble. However, the delamination in this beamsplitter does not affect the tilt variation. Therefore, the tilt variation of beamsplitter BS1 cannot conclusively be appointed to the delamination of the bond.

The large tilt variations on the beamsplitters of breadboard C2 are caused by the failure during shock tests (Figure 6.10 d). The failure is explained by the fact that the lateral movement of the beamsplitters has not been restricted with adhesive. This allowed the beamsplitter to smash against the SiC.

The glass chips on breadboard B2 is more difficult to explain. It is unlikely that the silica has smashed against the SiC breadboard, because RTV566 adhesive has been applied to restrict lateral movement. Possibly, the silica chipped due the release of internal stresses upon shock.

The tilt variations are promisingly close to the required alignment stability of $1.2 \mu\text{rad}$. However, they are still above the required level. Improvement can possibly be made by increasing the clamping force, such that the contact points will not abrade during vibrations.

A more detailed discussion of the experiments with the SiC beamsplitter breadboards can be found in [89].

6.2 Hydroxide catalysis bonding

6.2.1 Goals

The goals of the HCB bonding experiments are threefold:

- Gain experience in polishing SiC to $\lambda/10$ PV flatness;
- Gain experience in bonding SiC with the HCB technique, and;
- Determine the strength of the HCB bond of SiC-SiC bonds.

6.2.2 Approach

The HCB bonding experiments consist of 7 steps:

- Sawing SiC blocks;
- Polishing SiC blocks;
- Oxidization of SiC blocks;
- HCB bonding SiC blocks;
- Sawing bars from SiC blocks;

- Viewing bonds under the scanning electron microscope (SEM), and;
- 4-point bending experiments on SiC bars.

Sawing SiC blocks

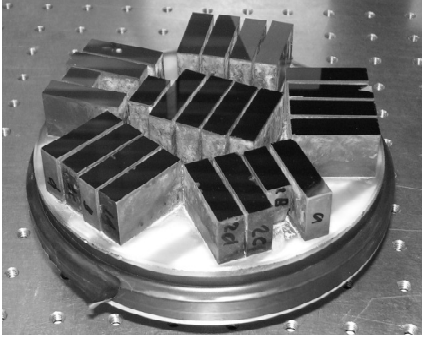
First blocks have been sawed from three different types of SiC (Boostec SSiC with and without CVD SiC coating, Xycarb C/SiC with CVD SiC coating and Hexoloy SA SSiC without SiC coating). For a representative measurement of the bending strength at least 25 bars per material should be tested, such that a reliable statistics analysis can be performed. Because the HCB technique is an experimental technique as well, enough surface area is bonded to make 50 bars. The dimensions of the blocks are shown in Table 6.3.

Table 6.3 Dimensions of the blocks

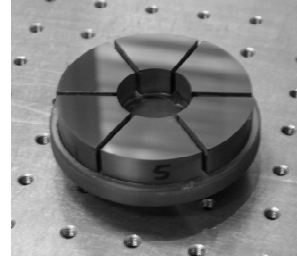
Material	Number of blocks	h [mm]	b [mm]	$\frac{1}{2}l$ [mm]
Boostec SSiC + CVD SiC	8	35.0 ± 0.2	10.5 ± 0.2	22.5 ± 0.2
Boostec SSiC + CVD SiC	8	35.0 ± 0.2	10.5 ± 0.2	22.5 ± 0.2
Boostec SSiC	8	35.0 ± 0.2	10.5 ± 0.2	22.5 ± 0.2
Boostec SSiC	8	35.0 ± 0.2	10.5 ± 0.2	22.5 ± 0.2
Xycarb C/SiC +CVD SiC	8	35.0 ± 0.2	10.5 ± 0.2	22.5 ± 0.2
Hexoloy SSiC	6	6 equal (± 0.5 mm) wedges from a $\varnothing 76$ mm disc		13.0 ± 0.2

Polishing SiC blocks

The bonding surfaces have been polished to $\lambda/10$ PV flatness. To achieve this flatness the blocks of Boostec material and Xycarb material have been bonded with an adhesive onto one pan like shown in Figure 6.11 a). The Hexoloy blocks already form a ring, and have been polished on a separate pan (Figure 6.11 b). The polishing has been conducted with $3 \mu\text{m}$ diamond powder type O of Kemet on a siphon machine with 38 rotations per minute and 3 kg load for 80 hours.



a) Boostec SSiC and Xycarb C/SiC



b) Hexoloy SSiC

Figure 6.11 Polishing pans

Oxidization of SiC blocks

After ultrasonic cleaning in an acetone bath, the blocks are oxidized in a quartz tube oven at 1100 °C in an oxygen deficient environment. This environment is created by bubbling zero-grade nitrogen through demineralised water at 80 °C. This wet nitrogen mixture is pumped through the oven. The oven heating scheme is shown in Figure 6.12. The bubbling is initiated slowly at 900 °C. At 1100 °C the flow is increased to 60 l/hr. This flow level and temperature is maintained for 2 hours. The oxidization set-up is shown in Figure 6.13.

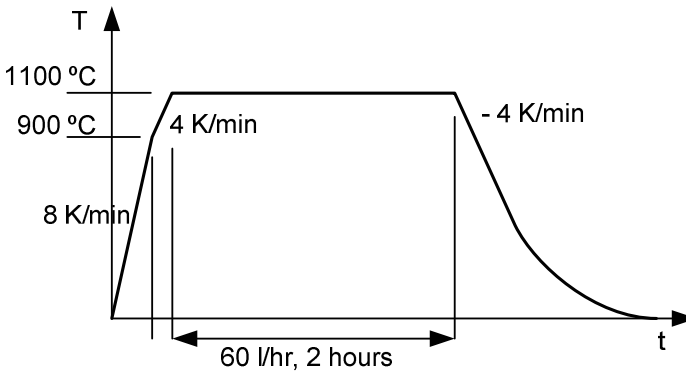


Figure 6.12 Oxidization temperature scheme

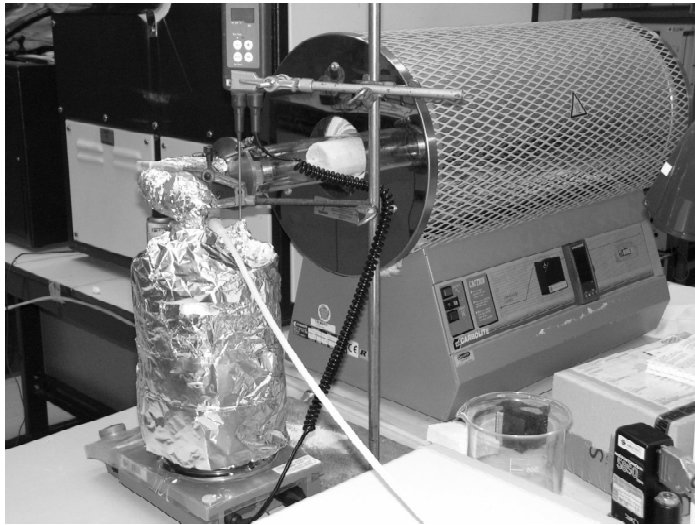


Figure 6.13 Oxidization set-up

HCB bonding

The blocks have been bonded using the HCB technique. Prior to bonding the blocks are thoroughly cleaned with cerium oxide and sodium bicarbonate powder in de-ionised water to make the bonding surfaces hydrophilic. The bonding is performed in clean-room conditions by mixing a sodium silicate solution (14% NaOH and 27% SiO₂) with de-ionised water with a volume ratio 1:6. The bonding solution is applied in the volume of 0.4 $\mu\text{l}/\text{cm}^2$ to one of the bonding surfaces upon which the other bonding surface is placed on top. The sodium silicate, the water and the silicon oxide on the bonding surfaces immediately form siloxane chains bonding the two surfaces together. The bonds have been made partly at the University of Glasgow, department of Astronomy and Physics. The other bonds have been made at TNO Science and Industry in Eindhoven. The bonds have been cured for 3 weeks in air one week of which the bonds have been held at 50 °C.

Sawing bars

The blocks are sawed and ground into bars, such that the HCB bond is in the center as shown in Figure 6.14. The desired dimensions of the bars for each material are shown in Table 6.4. However, the final dimensions are dependent on the success during sawing.

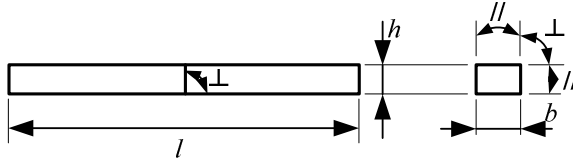


Figure 6.14 Dimensions of a bar

Table 6.4 Bars with dimensions and tolerances according to the ASTM norm (use Figure 6.14 for understanding of the symbols)

Material	h [mm]	b [mm]	l [mm]	\perp [mm]	$//$ [mm]
Boostec + CVD	3.00 ± 0.13	4.00 ± 0.13	45	0.015	0.015
Boostec	3.00 ± 0.13	4.00 ± 0.13	45	0.015	0.015
Xycarb + CVD	3.00 ± 0.13	4.00 ± 0.13	45	0.015	0.015
Hexoloy	1.58 ± 0.07	2.1 ± 0.07	26	0.015	0.015

Viewing bonds with the SEM

The bonds are inspected under the SEM after sawing to assess the SiO₂ layer thicknesses and the HCB bonding thickness.

4-point bending experiments

The bars have been subjected to a 4-point bending experiment according to ASTM norm C1161-2C [90]. A schematic illustration of a 4-point bending set-up is shown in Figure 6.15.

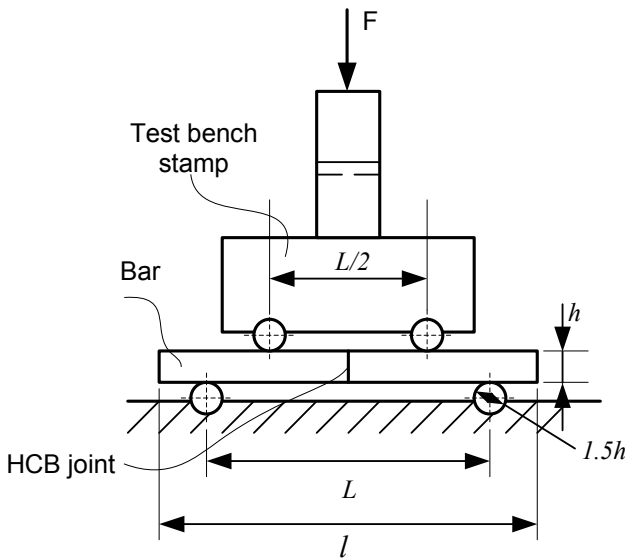


Figure 6.15 Schematic representation of the 4-point bending set-up

The ASTM norm is focused on determining the bending strength of ceramic materials. In the 4-point bending experiment the force F is increased slowly with prescribed crosshead speed of 0.55 mm/min. The applied force and crosshead speed are measured. Between the upper two rods the moment on the bar is uniform, and thus the stresses through the cross-section. The maximum stress upon fracture during the bending experiment is calculated using [90]:

$$\sigma_{\max} = \frac{3 \cdot F \cdot L}{4 \cdot b \cdot h^2} \quad (6.1)$$

6.2.3 Results

Polishing the blocks

After polishing for 1.5 week the required flatness of $\lambda/10$ PV or 0.1 waves has been obtained for all Hexoloy blocks and all but one Xycarb blocks. The flatness achieved for the Boostec blocks is in most cases worse than 0.1 wave (Table 6.5). The largest deformation of the surfaces is seen at the long edges of the polished surfaces. The surfaces of Boostec SSiC and Xycarb C/SiC are generally convex.

Table 6.5 Measured flatness in waves

Block	Overall flatness [waves]	Block	Overall flatness [waves]
Boostec SSiC + CVD SiC		Xycarb C/SiC + CVD SiC	
UAcvd1	0.119	UB1	0.105 ok
UAcvd2	0.077 ok	UB2	0.088 ok
UAcvd3	0.164	UB3	0.061 ok
UAcvd4	0.159	UB4	0.096 ok
UAcvd5	0.130	UB5	0.115
UAcvd6	0.089 ok	UB6	0.109 ok
UAcvd7	0.103 ok	UB7	0.076 ok
UAcvd8	0.148	UB8	0.104 ok
Boostec SSiC		Hexoloy SSiC	
UA1	0.127	UC1	0.098 ok
UA2	0.088 ok	UC2	0.099 ok
UA3	0.161	UC3	0.097 ok
UA4	0.151	UC4	0.092 ok
UA5	0.152	UC5	0.099 ok
UA6	0.095 ok	UC6	0.098 ok
UA7	0.134		
UA8	0.155		

Oxidization

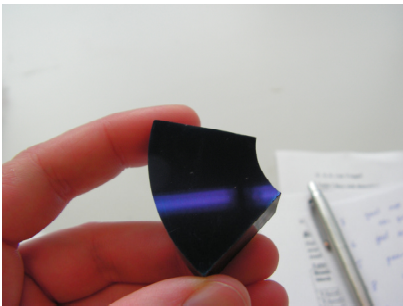
The blocks have been oxidized in 4 sessions. In the first 2 sessions the coloration of the polished surface due to oxidization shows a dependency of the position in the oven. In the front of the wet air flow the discoloration is less than further in the flow. This has, however, not been observed in the last two sessions.

In the first two sessions the color change of the Xycarb and Hexoloy blocks is yellow (Figure 6.16 a) and the color change of Boostec material is increasingly orange to blue (Figure 6.16 b). However, in the latter two sessions the discoloration of all materials varied from yellow to purple to blue. Some blocks show small spots of different color (Figure 6.16 b). The Hexoloy blocks show the most uniform color changes (Figure 6.16 c). Finally, marker residuals to indicate the nonflat parts of the reflective surface, which have visually been removed during cleaning, have become visible again after oxidization (Figure 6.16 d).

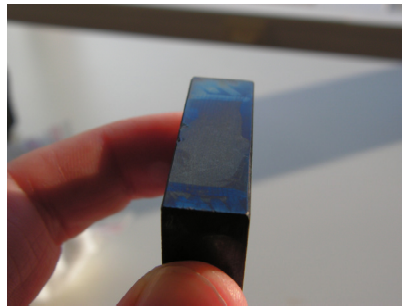


a) Yellow on Xycarb C/SiC with CVD SiC

b) Orange to purple on Boostec SSiC with CVD SiC



c) Uniform blue on Hexoloy SSiC



d) Marker residuals on Boostec SSiC with CVD SiC

Figure 6.16 Some examples of oxidized blocks

Bonding the blocks

Of each material one half has been bonded in Glasgow and the other half has been bonded in Eindhoven. The bonding has been performed successfully for 13 of 15 bonds. The two remaining bonds (both made in Eindhoven) proved unsuccessful after 3 weeks curing (Table 6.6). The failure of these bonds is attributed to dust and a hair on the bonding surface, which prevented good bonding. There are some small differences between the bonding in Glasgow and Eindhoven:

- In Glasgow the blocks have been kept wet after cleaning and have been wiped with methanol just before bonding because they had to be transported from a cleaning facility to a clean room facility. In Eindhoven the blocks have been cleaned in clean room conditions and have been blown dry with clean air. The blocks have not been wiped with methanol.
- In Glasgow the bonding solution has been filtered. In Eindhoven the bonding solution has not been filtered.
- In Glasgow the bonds have been made with exactly 1.4 μl bonding solution for the Boostec and Xycarb blocks and with 2.4 μl for the Hexoloy blocks. In Eindhoven all bonds have been made with ~ 5 μl bonding solution (Table 6.6).

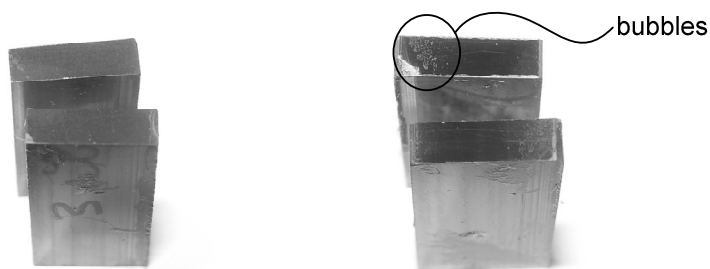
Table 6.6 Blocks bonded in Glasgow with bonding time and the amount of bonding fluid used.

Bonded block	Block 1	Block 2	Location	Amount of solution (μl)	Successful
VAcvd1	UAcvd6	UAcvd7	Glasgow	1.4	yes
VAcvd2	UAcvd4	UAcvd8	Glasgow	1.4	yes
VAcvd3	UAcvd3	UAcvd3	Eindhoven	5	yes
VAcvd4	UAcvd1	UAcvd5	Eindhoven	5	no
VA1	UA4	UA8	Glasgow	1.4	yes
VA2	UA3	UA5	Glasgow	1.4	yes
VA3	UA1	UA6	Eindhoven	5	yes
VA4	UA7	UA2	Eindhoven	5	yes
VB1	UB1	UB2	Glasgow	1.4	yes
VB2	UB3	UB4	Glasgow	1.4	yes
VB3	UB5	UB6	Eindhoven	5	yes
VB4	UB7	UB8	Eindhoven	5	no
VC1	UC1	UC4	Glasgow	2.4	yes
VC2	UC2	UC6	Glasgow	2.4	yes
VC3	UC3	UC5	Eindhoven	5	yes

Sawing bars

The sawing of the blocks which have been bonded in Glasgow has been largely unsuccessful. Initially, bonded blocks – VAcvd1, VAcvd2, VA1, VA2, VB1 and VB2 – have been sawed simultaneously into bars with dimensions: 45 mm × 10.5 mm × 3.2 mm. The bars have been sawn with a speed of 8 μm per stroke. After removal from the pan by heating the resin, only 16 bars had survived the sawing of which 7 and 8 bars came from bonded block VA1 and VB2, respectively. All other bars had failed on the bonding surface.

The broken bars have been cleaned with alcohol to remove the resin. Next the bonding surfaces have been inspected. Most surfaces appear to have only the SiO₂ layers (Figure 6.17 a). Residuals of the siloxane bond layer do not appear to be present, except on the bars of VB1 and VAcvd2. On them, some small bubbles are visible (Figure 6.17 b).



a) A bar from block VA2

b) A bar of block VAcvd2

Figure 6.17 Bonding surfaces of samples that failed during sawing

SEM inspection

A photograph has been taken with a SEM of the bond layer of bar from VB2, which survived the sawing (Figure 6.18). The sample has not received any additional treatment (like polishing) to get an optimal image. Because of this and because the bond is not present along the edges, the thickness of the bond layer can only be estimated at 260 nm. This thickness is in the same order of magnitude as the expected thickness, which was less than 550 nm (see the discussion in section 2.4.4 on page 50 and 51).

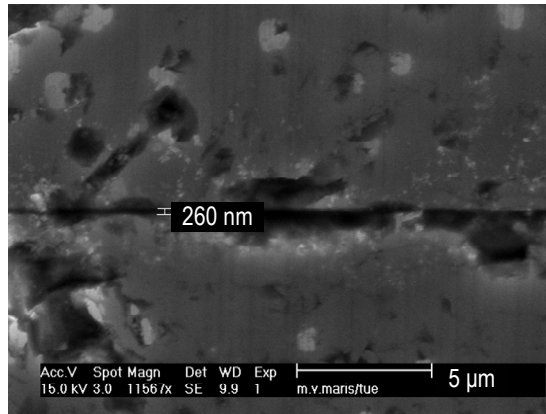


Figure 6.18 SEM image of the bond layer of a bar from block VB2

4-point bending

Due to the fact that the sawing was not totally successful, the 4-point bending experiments have not been conducted completely according to the ASTM-norms. The experiments have been performed on 11 bars with a 10 kN tensile testing bench with contact cylinders of \varnothing 3 mm.

The conditions during measurements are:

1. Room temperature: 20 °C;
2. Outside air pressure: 1003 mbar;
3. $L = 40$ mm;
4. $l = 20$ mm;
5. Crosshead speed: 0.5 mm/min;
6. The bars have dimensions: 45 mm \times 10.5 mm \times 3.2 mm and;
7. 11 bars have been broken.

The results of the experiments are shown in Table 6.7. The force-time diagrams for 2 specimens are shown in Figure 6.19. The table shows that maximum forces that have been measured for the bars from VA1 with an average maximum force of 103.9 N and a maximum deviation of 7.4 N. This is equivalent with an average strength of 29.3 N mm⁻² provided that 100% of the surface has bonded successfully. The maximum forces that have been measured for the bars from VB2 seem to be divided into two groups: one with average 23.1 N and one with average 48.6 N corresponding with 6.3 N mm⁻² and 13.3 N mm⁻², respectively.

Table 6.7 Results of the bending experiments

Bonded block	Bar	Maximum force [N]	Maximum stress [N mm ⁻²]
VB2	22	23.0	6.3
VB2	23	26.1	7.6
VB2	24	20.2	5.4
VA1	62	109.6	30.7
VA1	63	105.8	31.5
VA1	64	96.4	27.0
VB2	25	57.8	15.9
VB2	26	41.1	11.0
VB2	27	46.9	12.9
VA1	65	97.6	27.3
VA1	66	109.8	29.8

When viewing Figure 6.19 one can see that the force does not increase smoothly. This is due to the fact that the specimens have not been ground to remove standing edges in fear of fracture of the bond during grinding. These standing edges fracture first, resulting in a sudden reduction in measured force. The final reduction of the force shows the fracture of the bond.

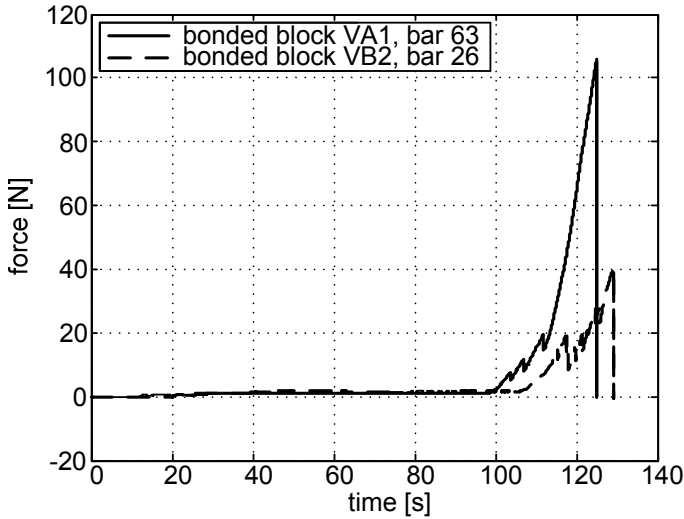


Figure 6.19 Force-time diagram of 2 samples

6.2.4 Discussion

Every step of the HCB bonding of SiC has been an experiment. This leads to a large number of uncertainties regarding the

fracture of most bars during sawing and measuring the strength of HCB SiC-SiC bonds:

- The achieved flatness of the bonding surfaces was not in all cases the desired $\lambda/10$ PV due to the difficult geometry of the samples. This might have contributed to bonds that are successful over only part of the bonding surface.
- The oxidization process is not very well controllable. It appears that there is a large dispersion of the SiO₂ layers and that the formation of the layers is sensitive to contamination using the wet-oxidization process. This technique has been used because the SiO₂ layer have grown in situ from the SiC, making the SiO₂ bond to SiC most probably much stronger than the HCB bond between the SiO₂ layers. However, creating a SiO₂ layer using chemical vapour deposition is thought to be weaker but is also considered to be much better controllable. This means that CVD SiO₂ can be applied with a controllable and more even thickness, and the process is less sensitive to contamination.
- The bonding process of the 13 blocks that have been bonded successfully, are not a complete success in the sense that the bond may well have not occurred over 100% of the bonding surface, due to a lack of flatness of the bonding surfaces, due to contaminations or due to a lack of bonding solution in the interface. The blocks bonded in Glasgow may not have bonded over 100% of the surface due to the latter argument.
- The fracture of the bonds during sawing can be explained by each of the arguments above in combination with two possible properties of the sawing process:
 1. During sawing forces are applied to the samples, which cause stresses larger than the strength.
 2. The cooling fluid (95% water) attacks the bond. The argument is that free OH⁻ ions in the water have a tendency to reverse the formation of siloxane chains, thereby reducing the strength of the bond [92]. To test this, 4 samples that have survived sawing initially, have been subjected to the cooling fluid (pH = 7.8) and to a buffer with a pH of 4.1 for 12 hours. After this period the bonds failed at the slightest handling.

It is recommended that sawing forces are reduced by using a thinner sawing blade and by reducing the sawing speed and to use an oily cooling fluid.

The measured strengths of the bonds in a range of 5 to 30 N mm⁻² can not be subjected to any statistics, because only 11 samples have been tested and because there are too many uncertainties regarding the true bonding surface area. What can be said is that the maximum strength of ~30 N mm⁻² is encouraging. This strength is in the region of the strongest epoxy adhesive and it is likely to be higher.

6.3 Conclusions

The experiments with yz-mounted beamsplitters have shown that the beamsplitters survive the thermal cycling and thermal vacuum tests without damage provided that the adhesive used, is not too stiff. During random vibrations abrasive damage occurred due to too low clamping forces. The damage can possibly be reduced by reducing lateral play of the adhesive and by increasing the clamping force.

The HCB bonding experiments have shown that polishing to $\lambda/10$ PV flatness is not trivial, but it is possible. The oxidization has been performed with success but the color differences suggest large differences in layer thickness. Possibly coating the SiC with SiO₂ using a CVD process might be better controllable than the wet-oxidization process.

The HCB bonding itself has been performed with reasonable success. The sawing process has proven to be largely unsuccessful, possibly due to: a less than 100 % effective bond over the entire bonding surface; a reduced bonding surface area due to the erosive characteristics of the cooling fluid during sawing; and the sawing forces may be too high.

Nonetheless some 4-point bending experiments have been conducted, yielding a maximum strength of ~30 N mm⁻², which is calculated presuming a 100% effective bond. Since 30 N mm⁻² is in the range of the strongest epoxy, this is encouraging.

7 Conclusions and recommendations

7.1 Introduction

The BAM system of GAIA is required to measure the variations on the basic angle between the lines-of-sight of two telescopes with $0.5 \mu\text{as}$ ($= 2.5 \text{ prad}$) accuracy. To obtain this accuracy, three precautions are made:

- GAIA is sent to a very stable location in space (L_2 -point);
- the Payload Module and thus also the BAM system is constructed in a highly stable material, i.e. Silicon Carbide, and;
- a stable opto-mechanical design of the BAM system is made.

This thesis has focused on the integration of mechanical design principles for stable opto-mechanical design with SiC as a highly stable, construction material.

Four main topics have been discussed with regard to this integration:

- properties and possibilities of SiC as a constructive material;
- optical design of the metrology system;
- optical bench design and thermal analysis, and;
- design and testing of optical components.

The conclusions drawn for each topic are discussed in section 7.2. Naturally, many questions still remain or have arisen during this research. Therefore, recommendations are made in section 7.3.

7.2 Conclusions

7.2.1 Silicon Carbide

SiC is a very suitable material for application in the BAM system, based on its mechanical and thermal properties. Two main types of SiC are used: SSiC and C/SiC. In SSiC a compressed block of SiC powder is sintered. In C/SiC a graphite block is infiltrated with silicon, which reacts with the graphite to form SiC. The combination of high specific stiffness with high thermal stability gives either material the advantage over other materials like aluminium and beryllium. The material also does only show negligible creep and is chemically highly resistant. The material is, however, extremely hard and brittle. This has to be taken into account when designing opto-mechanical structures in SiC. The material must preferably be loaded in compression, because possible cracks do not grow in this situation.

Also blanks can best be made by machining shapes in blocks of green (unsintered) material, because this material is softer and thus easier to remove.

Furthermore, edges must be rounded or chamfered to prevent chipping. Grinding and polishing of SiC must be limited because it is a time-consuming and thus expensive process.

7.2.2 Optical design

The BAM system consists of two optical benches (bar 1 and bar 2). A single laser is used to make four beams, two of which travel to telescope 1 and the remaining two beams travel to telescope 2. Each pair creates an interference pattern. The relative shift between the patterns is a measure of the variation of the basic angle. An investigation has been carried out to determine what properties the optical design must have to prevent a relative rotation of the optical benches themselves from influencing the measurement and what the stability requirements are. It has been found that:

- The number of mirrors of each optical path on bar 2 must be even.
- The beams traveling from bar 1 to bar 2 must be parallel to within $6 \mu\text{rad}$ for alignment stability and $0.16 \mu\text{rad}$ for measurement stability.

- The distance between the beams traveling from bar 1 to bar 2 must be equal to the distance between the interfering beams from bar 2 to within 0.1 mm for alignment stability.
- The optical path length difference must be zero to within 5 μm for alignment stability and 0.65 pm for measurement stability.

The alignment stability requirements must hold over 6 years including launch vibrations and cool down from 293 K to 100 K. Measurement stability requirements must hold for 6 hours.

7.2.3 Optical bench design

The optical bench must be both light and stiff and the surface on which the optical components are mounted must be especially stiff. A honeycomb optical bench is very suitable for this.

The design rule for making the basic shape in the green SiC can be utilized very well with a honeycomb optical bench. The honeycomb structure is made by machining chambers in a block of green SiC.

An optimization analysis has been made on whether to use a closed-back or an open-back optical bench. For a maximum flexural stiffness to mass ratio and torsional stiffness the optical bench must be closed-back. This is considered to outweigh the added difficulty of having to make the closed-back by brazing a lid on the open side of the honeycomb.

7.2.4 Optical bench thermal analysis

The alignment and measurement stability requirements have been used in a thermal analysis of the optical benches to determine what kind of thermal variations will cause errors in the measurements. The alignment stability is threatened by spatial variations of the coefficient of thermal expansion of SiC in the optical bench, which can cause OPD variations of 0.9 μm .

Measurement stability is affected by heat flux variations in all directions. Heat flux variations of 15 mW m^{-2} (based on a stated 0.1 mK thermal variation) can cause OPD variations of ~ 50 pm, which exceed the allowed OPD variation with more than a factor 75. In order to meet the required 0.65 pm OPD stability, assuming it is only determined by the optical benches, the maximum heat flux variation must be no larger than 0.2 mW m^{-2} .

7.2.5 Design of optical components

The conceptual design of the optical components has been focused mainly on achieving measurement stability of 0.17 μm per component. Preferably, the components must be mounted without introducing stresses. Hydroxide catalysis bonding is a promising but still highly experimental technique for mounting mirrors and due to required surface flatness, highly expensive bonding technique in this respect. Therefore, clamping has been used as the joining method of choice. Also, the HCB cannot be used for mounting a fused silica beamsplitter to SiC for the BAM system application, due to the thermal expansion difference.

The first step in the design of the optical components is utilizing the compressive strength of SiC and fused silica by loading the parts in compression when mounting the components against the mounts.

It has been shown that mounting in the xy-plane (plane in which all beams travel) will provide a 500 times better measurement stability than mounting in the yz-plane (plane of reflective surface of the component). TiAl_6V_4 clamps are used for providing the needed clamping force, for their insensitivity to creep. However, still creep in the clamp is the most threatening influence for measurement stability. However, theoretically both xy-mounted and yz-mounted components still can meet the 0.17 μm stability requirement.

The xy-mounted components are mounted on ball in double V-groove combinations to form kinematic clamps with a large hysteresis free stroke, to cope with the thermal expansion difference between the beamsplitter and the mounted or the low thermal contact conductance. Alignment is achieved by shifting the component over the mounting surface with a separate alignment mechanism.

The yz-mounted components are mounted with the reflective surface against three SiC studs to fix the x-direction and θ - and ψ -rotation. The movements in y-, z- and ϕ -direction are restricted by adhesive spots.

The yz-mounted components have been chosen for manufacturing over the xy-mounted components, because the xy-mounted components have more joints between parts, which are in principle unstable. Also, the alignment procedure of the xy-

mounted components is considered to be more complex. Finally, the risk of losing alignment during launch vibrations is considered to be larger for the xy-mounted components than for the yz-mounted components, especially due to hysteresis after shock loads.

7.2.6 Testing of optical components

The alignment stability of the yz-mounted beamsplitters has been tested on breadboards with two beamsplitters and one reference mirror. The breadboards have been subjected to thermal cycles from 100 K to 350 K, thermal vacuum at 100 K, 17.3 g rms random vibrations and to shock loads. Due to friction forces smaller than the vibration forces and due to limited stiffness of the adhesive, wear of the contact points occurred causing tilt of the beamsplitters which is larger than the required 1.2 μ rad.

HCB bonding experiments have been conducted because it is a promising technique for stable mounting of optical components. The HCB bonding technique has been conducted largely successfully on blocks of different types of SiC. In the process polishing is lengthy and sensitive to the shape that must be polished. The oxidization process lacks good control over the SiO₂ layer thickness. Sawing the bonded block for making bars for bending experiments has, however, been largely unsuccessful. Most bars fractured at the bond due to a number of possible reasons: a less than 100% effective bonding surface, erosion of the bond due to a chemical attack by the cooling fluid and too large sawing forces.

7.3 Recommendations

The optical design (chapter 3) contains a thorough sensitivity analysis of the BAM optical design. Also, some global alignment steps have been identified. However, these alignment steps have been stated without taking into account the aids needed to achieve alignment. An alignment plan including the tools and detailed steps must be made.

The thermal analyses made in chapter 4 have been made with the single assumption that the thermal stability in the PLM is 0.1 mK. This number has been used as a gradient over any distance, it has been used to estimate a heat flux variation and it has been

used as an absolute temperature variation in order to get some idea of the effect on the measurement and alignment stability of the BAM system. Although the analyses made are insightful, they do not tell a completely objective story on the thermal behavior of the BAM system. For a more objective analysis knowledge of the temperature stability is not sufficient, rather the heat flux stability at the base of the isostatic mounts of the BAM optical benches must be determined. Furthermore, a detailed FEM thermo-elastic analysis must be made for both the cool down and the steady-state in space, to determine the gradients. Also, FEM thermo-elastic analyses must be made for the measurement stability of the BAM system. Note that in these models, the thermal behavior of the optical benches and of the optical components should be combined, because they have been analyzed separately in this thesis.

Because even heat flux variations of 0.2 mW m^{-2} can cause OPD variations of 0.65 pm , it is essential to measure this heat flux variation. However, the problem arises that no heat flux sensor equipment has been found that can measure this kind of heat flux variation. Note that this fact makes it impossible to prove that the BAM system actually measures the basic angle variation instead of OPD variations.

In chapter 5 two types of designs have been made for the optical components. yz-mounted components have actually been built and their alignment stability has been tested. The xy-mounted components however, have not been built. For a truly objective comparison between the two, the xy-mounted beamsplitter must be built as well and subjected to the same tests the yz-mounted beamsplitter has been subjected to.

This thesis has focused for a large part on the theoretical analysis of the measurement stability of the BAM optical benches and the components. However, the measurement stability has not been determined in an experimental study. Preferably, measurements of this stability can distinguish the contribution of the optical bench and the components. For these measurements a possibility is to use a Michelson interferometer with two arms of equal length like discussed in [91]. The interferometer consists of an optical bench with a beamsplitter, and three mirrors. Two mirrors stand next to each other in one arm, and the third mirror stands in the

other arm. Each arm has four beams, making it possible to distinguish OPD variations caused by the optical bench and by the mirrors. This interferometer contains all essential elements that the BAM system contains, but is smaller and has a simpler optical design, because it is not used for the purpose of measuring the basic angle variations but for measuring OPD variations.

The hydroxide catalysis bonding technique has proven to be promising for application in highly stable systems, because it does not introduce stresses. Further research is necessary to optimize the oxidization process. Also, the bonding itself must be optimized to ensure 100% effective bonds. Considering HCB bonding in a broader view, experiments must be performed to determine how mirrors can be bonded with the HCB technique without affecting the reflective surface, because of the necessary oxidization of the bonding surface. In a further step, but already relevant for bonding silica optics, effort must be put in designing alignment mechanisms which can align components prior to bonding.

Appendix A

Additional material properties

This appendix contains some material properties additional to those presented in chapter 2 on SiC. The material properties presented here provide either some additional information for the interested reader or is relevant for experiments performed in chapter 6. The basic material properties of Hexoloy SA SSiC, Xycarb C/SiC and some more in depth properties of fused silica and TiAl_6V_4 are presented in this appendix.

A.1 Hexoloy SA SSiC and Xycarb C/SiC

Hexoloy SA SiC is a pressureless sintered SiC mainly focused on standard mass production industry for process industry tubing, mechanical seals etc.

Xycarb C/SiC is a C/SiC very much in development with a focus on the semi-conductor industry for wafer carrying.

The material properties of Hexoloy SA SiC and Xycarb C/SiC are shown with Boostec SSiC and Poco C/SiC in Table A.1.

Table A.1 Material properties of SiC at room temperature

Property	Unit	Boostec SSiC	Poco C/SiC	Hexoloy SA SiC	Xycarb C/SiC	CVD SiC
ρ	$[\times 10^3 \text{ kg m}^{-3}]$	3.1	2.55	3.1	2.6	3.21
E	$[\times 10^9 \text{ N m}^{-2}]$	420	218	410	213	460
ν	[-]	0.16	0.17	0.14	?	0.18
σ_C	$[\times 10^6 \text{ N m}^{-2}]$	3000	?	3800	?	2500
σ_T	$[\times 10^6 \text{ N m}^{-2}]$	200	130		?	?
σ_B (3-pt)	$[\times 10^6 \text{ N m}^{-2}]$	450	160	550	133	470
m	[-]	10	17	8	?	11
K_{IC}	$[\times 10^6 \text{ N m}^{-3/2}]$	3.5	2.3	4.6	2.4	?
γ	$[\text{J m}^{-2}]$	14.2	23.6		?	?
α	$[\times 10^{-6} \text{ K}^{-1}]$	2.5	2.4	4	~ 2.5	2.2
λ	$[\text{W m}^{-1} \text{ K}^{-1}]$	180	158	125	~ 100	300
C_p	$[\text{J kg}^{-1} \text{ K}^{-1}]$	680	800	?	?	640

A.2 Fused silica

A.2.1. Thermal expansion

The thermal expansion plots of fused silica as a function of temperature are shown in Figure A.1 and Figure A.2.

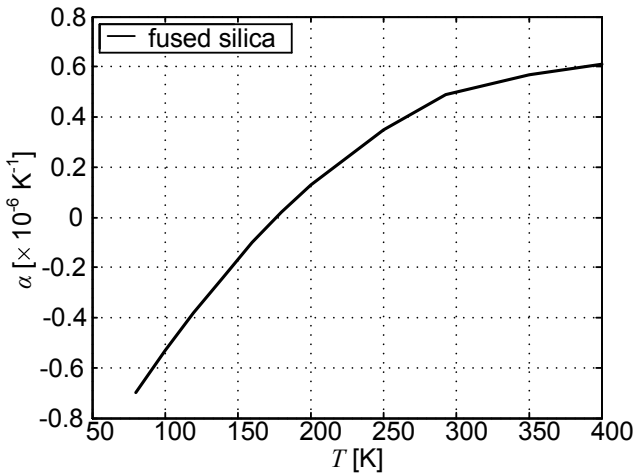


Figure A.1 Coefficient of thermal expansion of fused silica as a function of temperature

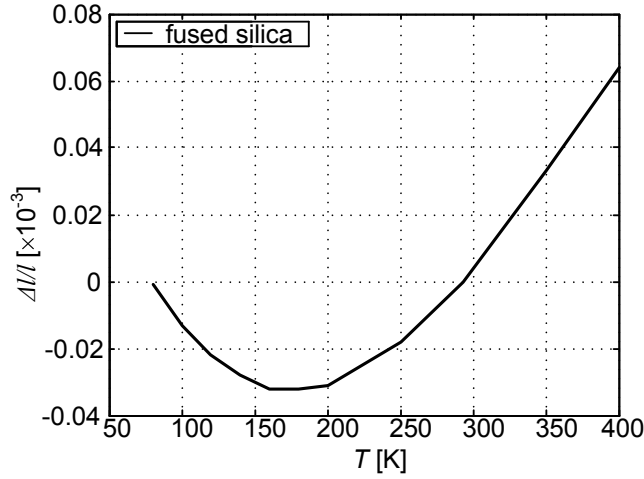


Figure A.2 Thermal expansion of fused silica as a function of temperature from 293 K

A.2.2. Stress birefringence of fused silica

Stress applied to optical materials induces a change in the optical path of a light beam passing through the material. This stress induced optical path change causes an optical aberration known as stress birefringence. A material property, the stress-optical coefficient, determines the amount of stress birefringence is given by [47]:

$$OPD = B \cdot h \cdot \sigma, \quad (\text{A.1})$$

where

OPD the stress birefringence or optical path length difference;

B the stress-optical coefficient;

h the distance the beam travels in the optical element and;

σ the stress in the optical element.

The stress optical coefficient of fused silica is $B = 3.5 \cdot 10^{-12} \text{ N m}^{-2}$.

A.3 TiAl₆V₄

The thermal expansion plots of TiAl₆V₄ as a function of temperature are shown in Figure A.3 and Figure A.4.

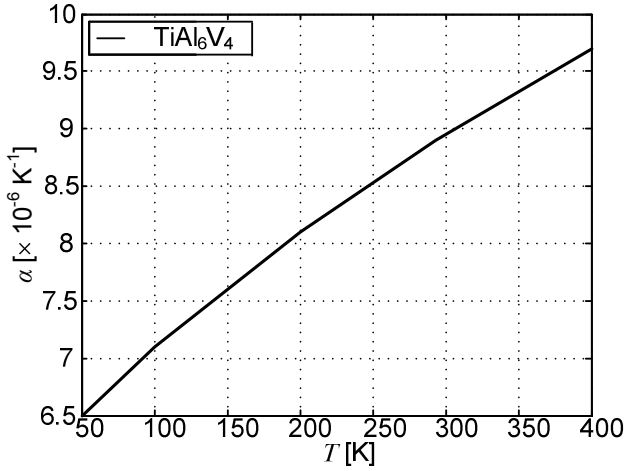


Figure A.3. Coefficient of thermal expansion of TiAl_6V_4 as a function of temperature

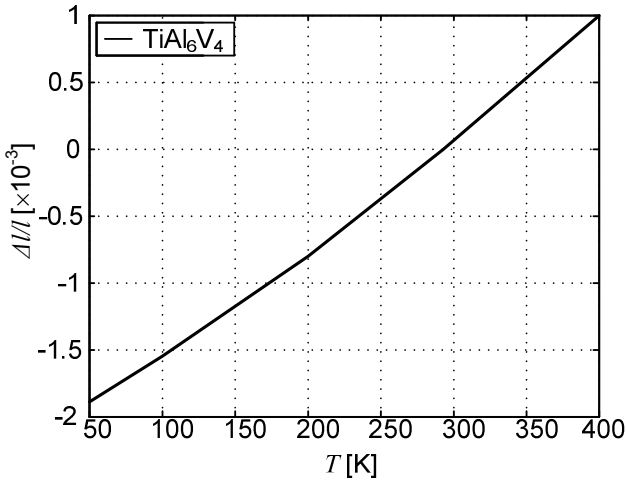


Figure A.4. Thermal expansion of TiAl_6V_4 as a function of temperature from 293 K

A.3.1. Creep

Creep experiments at room temperature on TiAl_6V_4 have been conducted by Odegard and Thompson [93]. They have conducted experiments on TiAl_6V_4 with different treatments to remove surface damage and on material which was pre-strained. Experiments have been performed for different stress levels,

ranging from 60% to 90% of the yield stress. Generally creep results obey a relation of the form:

$$\varepsilon = A \cdot t^a \quad (\text{A.2})$$

where A and a are constants and t is the time period in hours. This behavior is characteristic for primary creep behavior.

The strain rate after time period t is:

$$\frac{d\varepsilon}{dt} = a \cdot A \cdot t^{(a-1)}. \quad (\text{A.3})$$

The creep parameters for TiAl_6V_4 in the best and worst case conditions empirically determined by Odegard and Thompson are shown in Table A.2.

Table A.2 Creep curve parameters for the best and worst case conditions according to [93]

Case	Material	Stress, % σ_Y	A	a
Best	Aged & chempolished	60	$2.08 \cdot 10^{-6}$	0.1033
Worst	Pre-strained, $1 \cdot 10^{-3}$	90	$406.9 \cdot 10^{-6}$	0.4101

Important time periods for the GAIA BAM system are 6 years (or 53000 hours) lifetime and a 6 hour cycle starting after approximately 0.5 years (4400 hours). After 6 years the alignment stability $|\Delta x| < 1.9 \mu\text{m}$ should be ensured. In time periods of 6 hours, the measurement stability $|\Delta x| < 0.25 \text{ pm}$ should be ensured. Creep strains for these conditions are shown in Table A.3.

Table A.3 Creep strains for best and worst case conditions for two different time periods

Case	Material	Stress, % σ_Y	Creep strain after 6 years constant stress	Creep strain in a 6 hour period after 0.5 years constant stress
Best	Aged & chempolished	60	$6.4 \cdot 10^{-6}$	$7.0 \cdot 10^{-10}$
Worst	Pre-strained, $1 \cdot 10^{-3}$	90	$3.5 \cdot 10^{-2}$	$7.1 \cdot 10^{-6}$

Appendix B

Tunnel diagrams

The optical design shown in Figure 3.6 is insensitive to an optical path length change in beams 3 and 4 due to rotation of bar 2, because each beam has an even number of mirrors on bar 2, the base lengths between the pairs of beams 3'-4' and 3-4 are equal and the pairs of beams 3'-4' and 3-4 are parallel.

The goal of this appendix is to explain the reason for the latter two properties and to quantify the sensitivity to inaccuracy. This is done by considering simplified 2-D optical systems, in which the tunnel diagram technique is used to determine changes in OPD.

First in section B.1, an explanation of the tunnel diagram technique is given in a 2-mirror system with one optical path. In section B.2, the system is extended with a second 2-mirror path. Here the paths have equal lengths, the base lengths between in- and outgoing beams are equal and the incoming and outgoing beams are parallel. Next in section B.3, a similar analysis is performed. However, now the beams have unequal path lengths. The fourth step is a system in which the incoming and outgoing beams have unequal base lengths. In the final analysis the incoming beams are not parallel.

B.1 Tunnel diagram technique

Consider a 2-D optical system (Figure B.1) with two mirrors and only 1 optical path (single arrow) [72]. The optical system is rotated around a point O1. Instead of rotating the mirror system

around point O_1 , also the incoming beam can be rotated around point O_1 . This results in the beam with the double arrow.

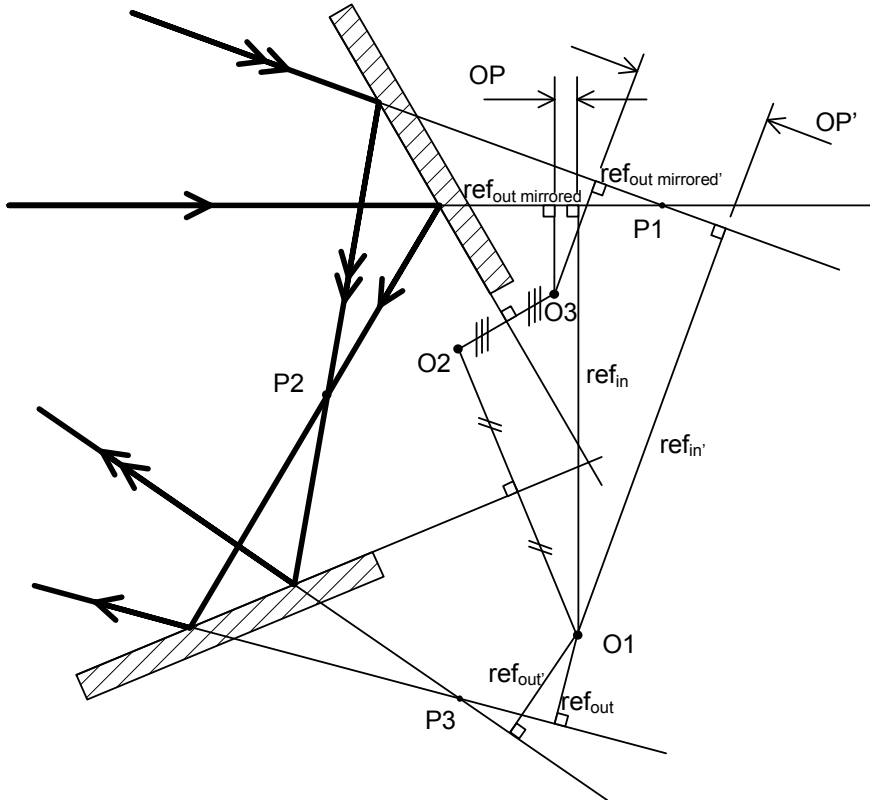


Figure B.1 Two mirror optical system rotation about point O_1

Perpendicular to the incoming beam (single arrow) a plane ref_{in} is placed from which the optical path length of the beam through the optical system will be measured. Since only optical path length differences are considered, the plane position can be chosen freely, as long as it is perpendicular to the direction of the incoming beam. In Figure B.1 the plane is drawn through point O_1 . Such plane $ref_{in'}$ can also be drawn for the rotated beam (double arrow).

We can construct the path of the unrotated and rotated beams through the optical system, by mirroring the intersection point P_1 of the two incoming beams in the first mirror. This leads to point P_2 . Point P_2 is then mirrored in the second mirror, creating point P_3 .

The reference planes at the exit can be drawn in a similar way as for the incoming beams. The reference planes ref_{out} and ref_{out}' are perpendicular to the outgoing beams and intersect rotation point O1.

The optical path length is now measured between ref_{in} and ref_{out} *mirrored* for the unrotated situation, and between ref_{in}' and ref_{out} *mirrored'*, for the rotated situation. For this purpose the outgoing reference planes ref_{out} and ref_{out}' are mirrored back to the incoming situation. This action will not change the optical path lengths between the incoming and outgoing reference planes. Mirroring back the reference planes is performed by mirroring rotation point O1 in the second mirror to point O2 and then mirroring point O2 in the first mirror to create point O3. The outgoing reference planes which have been mirrored back are also shown in Figure B.1 (ref_{out} *mirrored* and ref_{out} *mirrored'*). The optical path lengths can then be plotted easily for both the unrotated and the rotated situation (OP and OP' respectively). In the situation shown here the optical pathlengths are negative and unequal.

Note that the optical path lengths OP and OP' only depend on the relative positions of O1, O3, the nominal and rotated incoming beams. This means that for any optical system, for which the rotation point O1 coincides with the point O3, which is mirrored back to the start, the optical path OP will not change due to rotation of the system. Therefore, OP will be equal to OP' .

B.2 Equal OPD and base lengths

Now, consider two optical systems (1 and 2 in Figure B.2) with equal path lengths $OP_{beam\ 1}$ and $OP_{beam\ 2}$, equal base lengths BL_{in} and BL_{out} , and parallel beams entering the systems and leaving the systems. If any arbitrarily chosen rotation point O1 is mirrored back through each optical system, system 1 is mirrored back via point O2 to point O3 and system 2 is mirrored back via point O4 to point O5. Note that points O3 and O5 coincide. If both systems are simultaneously rotated around point O1, the change in optical path length of both systems is equal. Thus, the optical path lengths of both systems do change. However, no optical pathlength difference will occur. Thus, a double system with equal pathlengths $OP_{beam\ 1}$ and $OP_{beam\ 2}$, equal baselengths BL_1 and BL_2 and

parallel incoming and outgoing beams will be insensitive to a rotation about any arbitrary point O1.

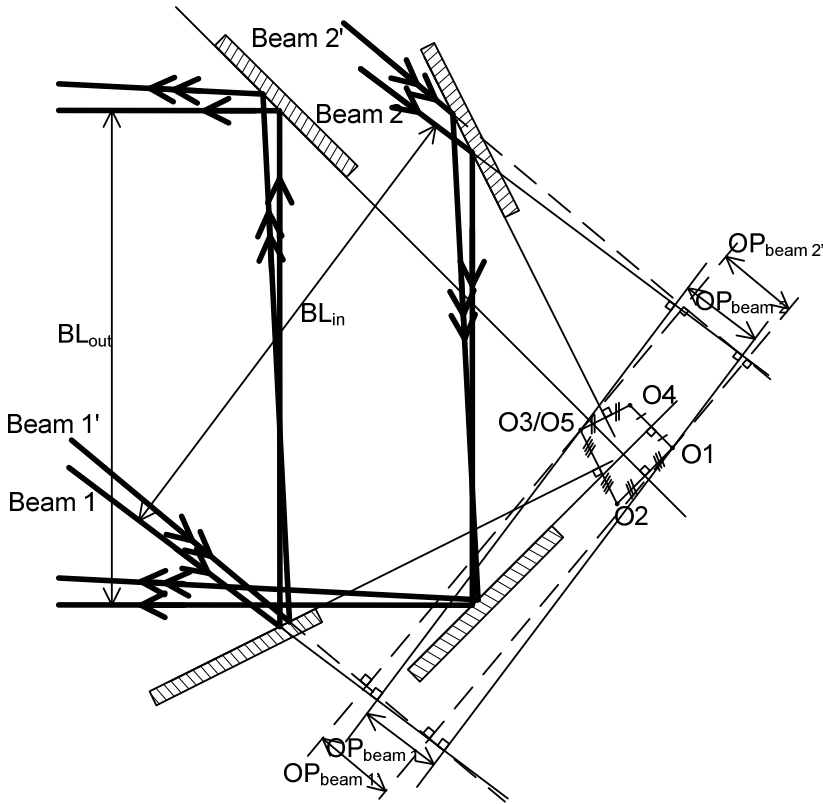


Figure B.2 Two optical systems for which $OP_{beam 1} = OP_{beam 2}$, $BL_{in} = BL_{out}$, the incoming beams are parallel and the outgoing beams are parallel

B.3 Influence of OPD

Next, consider two optical systems (1 and 2) with unequal path lengths $OP_{beam 1}$ and $OP_{beam 2}$. The optical path length difference between both paths is defined as: $OPD = OP_{beam 1} - OP_{beam 2}$. The incoming beams are parallel and outgoing beams are parallel as well. The distance between incoming and outgoing beams is equal (Figure B.3).

If any arbitrarily chosen rotation point O1 is mirrored back through each optical system, system 1 creates a point O5 and system 2 creates O3. In this case, points O3 and O5 can be connected by a line l , which is parallel to the incoming beams. The distance between O3 and O5 is equal to the path length difference

OPD. If both systems are rotated around point $O1$, the optical path length of system 1 will change equally, but in opposite direction as the optical path length of system 2, meaning that there will be no change in optical path length difference. Thus, $OPD = OPD'$. This latter argument is also true for the system shown in Figure 3.6. The optical design of bar 2 of the BAM system does therefore not need to have equal pathlengths.

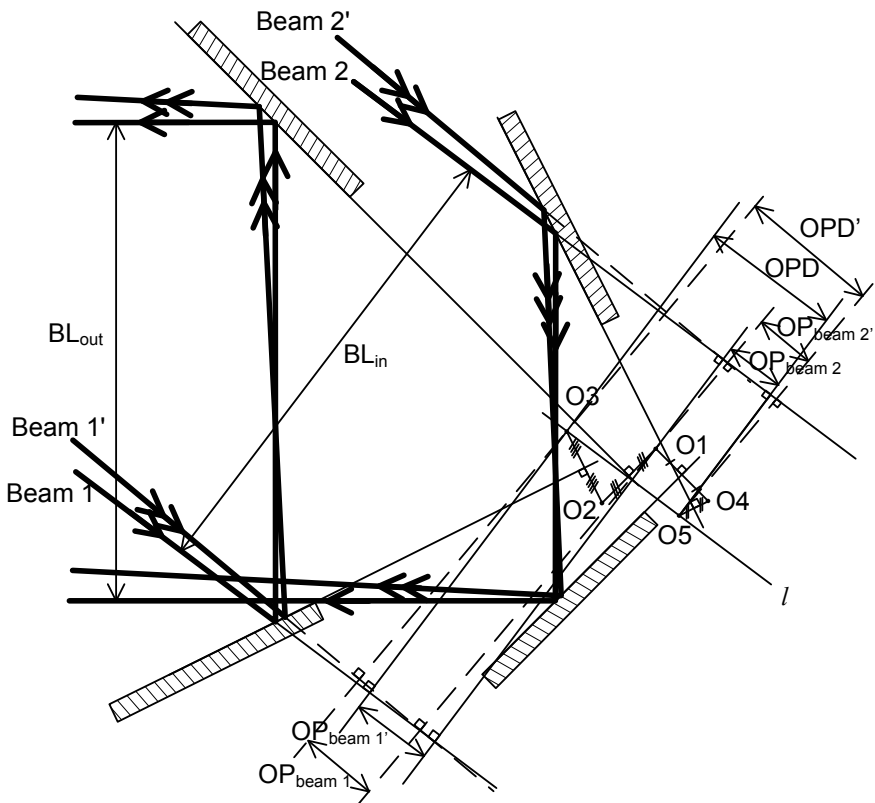


Figure B.3 Two optical systems (1 and 2), with equal base lengths ($BL_{in} = BL_{out}$) and with parallel incoming and outgoing beams, but with optical path length difference OPD ($OP_{beam 1} \neq OP_{beam 2}$)

B.4 Influence of unequal base lengths

The analysis of rotation insensitivity can be extended by analyzing the influence of inequality of the distances between the incoming and outgoing beams, or base lengths. In Figure B.4 such combination of systems is shown. The incoming beams are parallel and the outgoing beams are parallel as well. However, the base

lengths between the incoming and outgoing beams are not equal ($BL_{in} \neq BL_{out}$). Also the optical path lengths of both systems are not equal. In Figure B.4, rotation point O1 is mirrored back through both systems, creating point O5 for beam 1 and point O3 for beam 2.

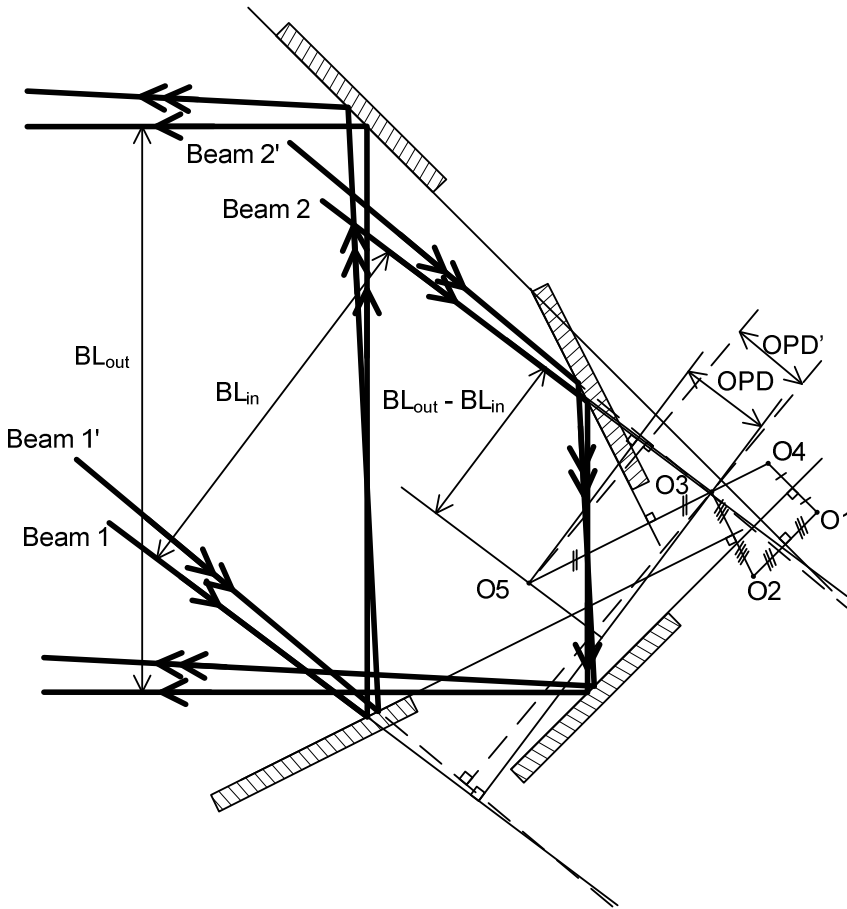


Figure B.4 Two optical systems (1 and 2), with unequal base lengths, with parallel incoming and outgoing beams, and with optical path length difference OPD

Parallel to the incoming beams the distance between O3 and O5 is the optical path length difference between beams 1 and 2. Perpendicular to the incoming beams, the distance between O3 and O5 is equal to the difference in base lengths of the incoming and outgoing beams ($BL_{out} - BL_{in}$). In case the systems are rotated

around point O1, the optical path length difference between beams 1' and beams 2' is OPD' , and is unequal to OPD . The change in optical path length difference is given by:

$$\delta OPD = |OPD' - OPD| = |BL_{out} - BL_{in}| \cdot \tan \delta\theta, \quad (\text{B.1})$$

with $\delta\theta$ the rotation of the systems.

(B.1) does show that the change of optical path length difference remains independent on the initial optical path length difference between the beams. It also gives a means of defining the required base length accuracy of the beams traveling from bar 1 to bar 2, with respect to the beams traveling from bar 2 to telescope 2.

B.5 Influence of nonparallel incoming beams

Finally, the influence of nonparallel beams travelling through a retroreflector system should be investigated. In the ideal situation the incoming beam has direction $-x$ (see Figure B.5). The beam travels into the retroreflector system from a point in the positive x region. At the point at which the beam hits mirror A: $x = 0$.

Assume that another 'rotated' beam (double arrowed beam in Figure B.5) travels through the retroreflector system which is rotated around point O1 with respect the ideal beam (single arrowed beam in Figure B.5).

The rotated beam leaves the system parallel to the ideal beam, because the last mirror in the system is rotated such that the beams leaving the systems are parallel. Note that the mirror is rotated around the intersection point of the ideal beam with the mirror by an angle which is half the rotational angle of the rotated beam with respect to the ideal beam.

In case both systems are rotated around an arbitrary mutual rotation point O2 (see Figure B.5), a change in path length difference between both systems occurs which is approximated by

$$\delta OPD \cong a_{O2} \cdot \delta\theta_{bar}. \quad (\text{B.2})$$

with $\delta\theta_{bar}$ the rotational angle of the system in radians and a_{O2} is the OPD arm length.

The OPD arm length is dependent on the x -position of the rotation point x_{O2} of the system, of the distance PL that the light of the

ideal beam travels inside the system between the first and the last mirror and of the rotational angle of the beam $\delta\theta_{beam}$:

$$a = (x_{O_i} + PL) \cdot \Delta\theta_{beam} \tag{B.3}$$

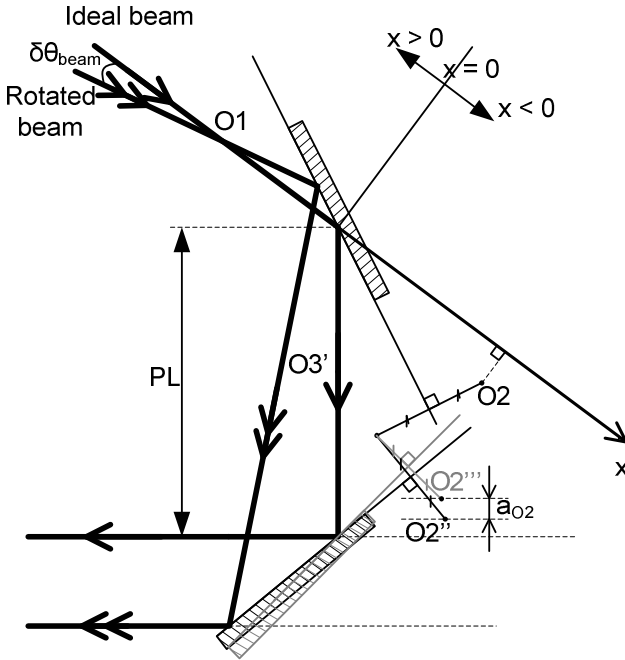


Figure B.5 Two optical systems with an ideal beam and rotated beam. Points O2 is mirrored back to the end mirror of both systems. This results in O2''' for the ideal system and in O2'' for the rotated system. The distance a_{O2} between the mirror back points of both systems is the OPD arm length creating a change in OPD when rotating both systems around point O2.

The change in optical path length due to a rotation of the bar between these two systems is equal to the change in optical path length between the rotated beam system and another system which is located such that the base lengths between the incoming beams and outgoing beams in the non-rotated situation are equal and the incoming beam pairs and outgoing beam pairs in the ideal situation are parallel.

Appendix C

Optimizing flexural rigidity

The flexural rigidity of a honeycomb optical bench of a certain mass can be maximized by optimal distribution of the available material. In this appendix first a means of optimizing the flexural rigidity of open- and closed-back honeycomb benches is summarized. Next the SiC material available for the optical benches is optimized for three different situations:

- No manufacturing limitations, nor height limitation of the optical bench;
- Manufacturing limitations, but no height limitation on the optical bench;
- Manufacturing limitations and a height limitation.

In each optimization both the open-back and closed-back option is optimized and they are compared. Finally, conclusions are drawn on recommended optical bench design.

C.1 Flexural rigidity of honeycombs

According to [47], the flexural rigidity of a honeycomb structure can be determined by computing the equivalent plate thickness of a honeycomb structure for a solid plate.

This leads to the following equation for the flexural rigidity of either an open back honeycomb or closed back honeycomb mirror or optical bench of:

$$D_{\text{honeycomb}} = \frac{E \cdot t_b^3}{12 \cdot (1 - \nu^2)} \quad (\text{C.1})$$

with t_b the equivalent bending thickness of the optical bench [m].

C.1.1. Open-back honeycomb

Let us first consider an open back honeycomb optical bench like shown in Figure C.1. It has a face sheet thickness t_f [m], rib height h_c [m] and rib thickness t_w [m].

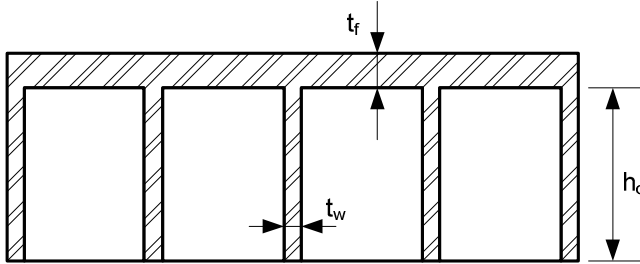


Figure C.1 Cross-section of an open-back honeycomb optical bench

The cell design can be square, triangular or hexagonal. These three cell configurations are shown in Figure C.2 for equal inscribed cell diameter B [m] and cell wall thickness t_w [m].

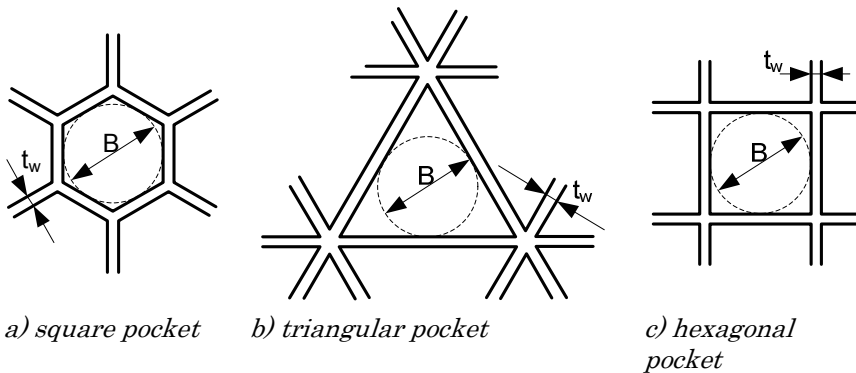


Figure C.2 Three different pocket geometries with equal inscribed cell radius B and wall thickness t_w

The amount of material in the honeycomb structure itself as opposed to a solid piece of material is expressed with the rib solidity ratio:

$$\eta = \frac{(2 \cdot B + t_w) \cdot t_w}{(B + t_w)^2} \quad (\text{C.2})$$

For a top surface area A [m²] and material density ρ [kg m⁻³] the mass of such an open back honeycomb optical bench is:

$$m = \rho \cdot A \cdot (t_f + \eta \cdot h_c) \quad (\text{C.3})$$

The equivalent bending thickness of an open back honeycomb optical bench is given by:

$$t_b^3 = \frac{\left(1 - \frac{\eta}{2}\right) \cdot \left(t_f^4 - \frac{\eta \cdot h_c^4}{2}\right) + (t_f + h_c)^4 \cdot \frac{\eta}{2}}{\left(1 + \frac{\eta \cdot h_c}{2}\right)} \quad (\text{C.4})$$

For an open back optical bench an optimum distribution of material exists, that provides the highest rigidity for a given bench mass. This equation should be solved numerically [73]:

$$4 \cdot \left(t_f + \frac{\eta \cdot h_c}{2}\right) \cdot \left[\left(1 - \frac{\eta}{2}\right) \cdot \left(t_f^3 + \frac{1}{2} \cdot h_c^3\right) + \frac{(\eta - 1) \cdot (t_f + h_c)^3}{2}\right] - \frac{1}{2} \cdot \left[\left(1 - \frac{\eta}{2}\right) \cdot \left(t_f^4 + \frac{1}{2} \cdot h_c^4\right) + \frac{\eta \cdot (t_f + h_c)^4}{2}\right] = 0 \quad (\text{C.5})$$

C.1.2. Closed-back honeycomb

The same analysis can be performed for the closed-back honeycomb optical bench, like shown in Figure C.3. Assuming that both face sheets have equal thickness, the equivalent bending thickness of a closed back honeycomb optical bench is given by:

$$t_b^3 = (2 \cdot t_f + h_c)^3 - \left(1 - \frac{\eta}{2}\right) \cdot h_c^3 \quad (\text{C.6})$$

The mass of a closed back optical bench is:

$$m = \rho \cdot A \cdot (2 \cdot t_f + \eta \cdot h_c) \quad (\text{C.7})$$

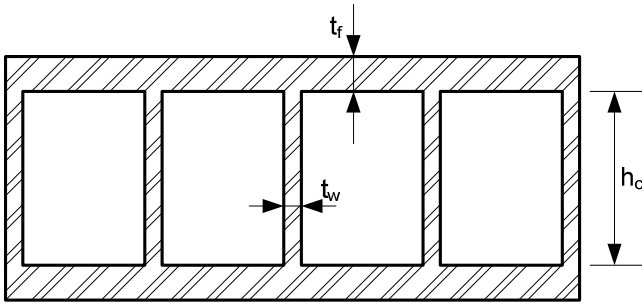


Figure C.3 Cross-section of a closed back honeycomb bench

The optimum distribution of material for the highest stiffness for a given mass of the optical bench in the closed-back optical bench is [73]:

$$t_f = \frac{m \cdot \left(\sqrt{1 - \frac{\eta}{2}} - \sqrt{1 - \eta} \right)}{2 \cdot \rho \cdot A \cdot \left(\sqrt{1 - \frac{\eta}{2}} - \sqrt{(1 - \eta)^3} \right)} \quad (\text{C.8})$$

C.2 Optimization of flexural rigidity

To make a usable trade-off in the design of the BAM optical benches, the method of Mehta [73] is used. A similar trade-off analysis was made by Kishner et al. [77] in a comparison of glass, beryllium and silicon carbide. The analysis is conducted in three steps and compares flexural rigidities of both open-back and closed-back solutions in both SSiC and C/SiC material.

First in section C.2.1 a free optimization of flexural rigidity on specified mass per unit area is made, without taking into account any manufacturing limitations. Secondly, manufacturing limitations on rib solidity ratio, face sheet thickness and rib wall thickness are taken into account. The height of the benches is not limited. In the final trade-off analysis, both a maximal rib height and manufacturing limits are taken into account.

C.2.1. No limitations

Each BAM optical bench has a mass of 8 kg as stated in section 4.1.1. With a top surface area of 0.2 m² per bench, this leads to a mass per unit area of 40 kg m⁻². For such mass per unit area the optimal material distribution can be computed using (C.8) for the

closed back bench. For the open-back bench (C.3) can be inserted in (C.5) leaving a fourth order polynomial (C.9), of which the roots can be computed numerically. Only one of these 4 roots yields the realistic value for the face sheet thickness.

$$C_1 \cdot t_f^4 + C_2 \cdot t_f^3 + C_3 \cdot t_f^2 + C_4 \cdot t_f + C_5 = 0 \quad (\text{C.9})$$

The coefficients of the polynomial are:

$$C_1 = -\frac{3}{2} + \frac{9}{2 \cdot \eta} - \frac{21}{8 \cdot \eta^2} \quad (\text{C.10})$$

$$C_2 = \left(\frac{3}{2 \cdot \eta^2} \right) \cdot \left(\frac{m}{\rho A} \right) \quad (\text{C.11})$$

$$C_3 = \left(3 + \frac{15}{2 \cdot \eta} - \frac{21}{4 \cdot \eta^2} \right) \cdot \left(\frac{m}{\rho A} \right)^2 \quad (\text{C.12})$$

$$C_4 = \left(\frac{3}{\eta} - \frac{9}{2 \cdot \eta^2} \right) \cdot \left(\frac{m}{\rho A} \right)^3 \quad (\text{C.13})$$

$$C_5 = \left(\frac{3}{8 \cdot \eta^2} \right) \cdot \left(\frac{m}{\rho A} \right)^4 \quad (\text{C.14})$$

The optimization is performed for the SSiC material and the C/SiC material. The results in flexural rigidity for different rib solidity ratios are shown in Figure C.4 and Figure C.5 for SSiC and C/SiC respectively. In both figures the optimized flexural rigidities of the closed-back option and the open-back option are compared.

Both figures show that in ideal circumstances the closed-back optical bench option can reach higher flexural rigidity over the entire range of masses per unit area. The figures also show that the lower the rib solidity ratio is, the higher is the flexural rigidity. The flexural rigidity increases slightly with the mass per unit area. Furthermore, when comparing Figure C.4 and Figure C.5, it can be seen that the SSiC material can reach higher flexural rigidity, which is mainly due to the larger Young's modulus of SSiC compared to C/SiC. To assess the realistic possibilities of these optimised designs, it is however important also to compare the resulting face sheet thickness and the rib height as a function of the mass per unit area. The face sheet thickness and the rib height are plotted in Figure C.6 and Figure C.7, respectively.

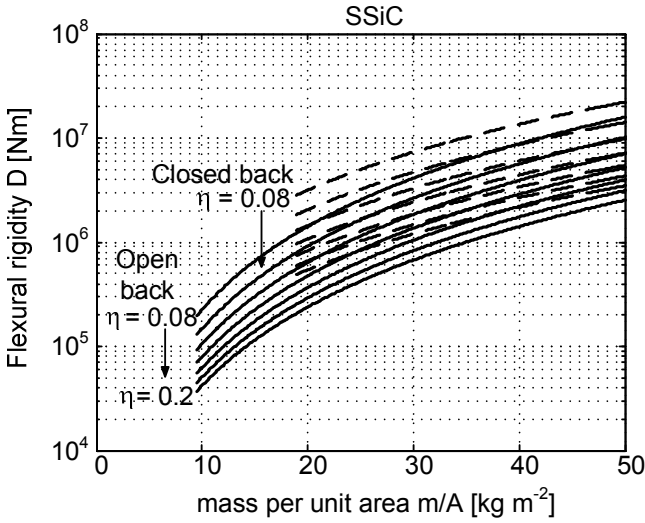


Figure C.4 Optimized flexural rigidity as a function of the mass per unit area for closed back and open back SSiC optical benches

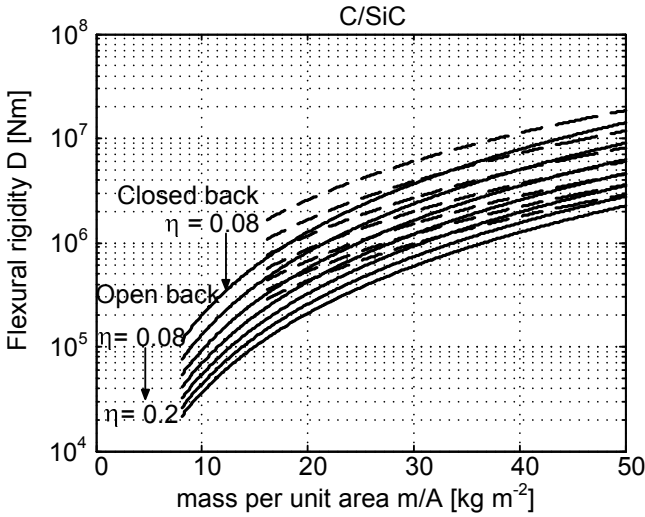


Figure C.5 Optimized flexural rigidity as a function of the mass per unit area for closed back and open back C/SiC optical benches

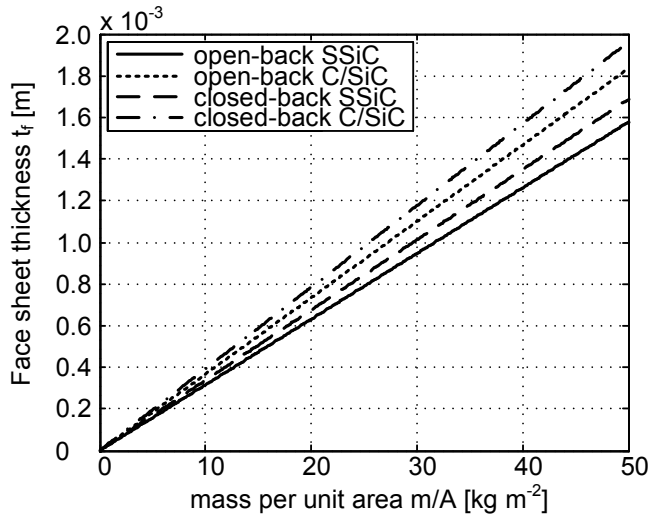


Figure C.6 Optimized face sheet thickness, for open-back and closed-back, SSiC and C/SiC optical benches

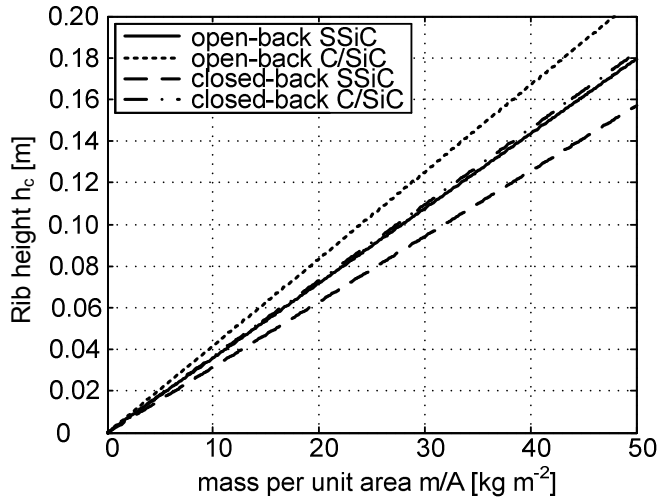


Figure C.7 Optimized rib height for open-back and closed-back, SSiC and C/SiC optical benches

Figure C.6 shows that for the open-back and closed-back optical benches, the optimal face sheet thickness does not differ much. The figure shows that the optimal face sheet thickness of the closed-back optical benches is higher than the open-back optical benches. The difference increases linearly with mass per unit area, but even at 50 kg m^{-2} the difference in face sheet thickness

between an open-back and a closed-back SSiC optical bench is only 0.1 mm, which is about 1/18 of the optimal face sheet thickness.

The values of optimal face sheet thickness are close to but below the current manufacturing capabilities with 1 mm, although in the future it is expected to be feasible to obtain face sheet thicknesses of 1 mm, which would make it possible to truly optimize mirrors and optical benches with masses per unit area higher than 30 kg m^{-2} for flexural rigidity. However, decreasing face sheet thickness will increase quilting during polishing.

The optimized rib heights range from 0.07 m at 20 kg m^{-2} to 0.2 m at 50 kg m^{-2} . These values appear to be realistic, be it that $h_c = 0.2 \text{ m}$ at 50 kg m^{-2} is considered a top limit. In the optimised solution especially the rib height of the closed back solution has increased in comparison to the trade-off which has been presented above. The difference in rib height between the open-back and closed-back solution now is only 15 %.

C.2.2. With manufacturing limits

For the purpose of deciding whether to use an open-back or closed-back solution, the minimal face sheet thickness, the minimal rib thickness and the minimal rib solidity ratio are summarized in Table C.1.

Table C.1 State-of-the-art fabrication constraints of two types of SiC

Material	$t_{f \min}$ [mm]	$t_{w \min}$ [mm]	η_{\min} [%]	Core(rib) fabrication process
SSiC	3	2	10	Machining green SiC blocks, and pressureless sintering, post grinding
C/SiC	3	1.5	8	Machining carbon blocks, and Si infiltrating, post machining and grinding

These fabrication constraints inherently pose limits on the light-weighting possibilities of both open-back and closed back optical benches. This can be visualized by using (C.3) and (C.7), for the open-back and closed-back solution respectively, to plot the rib-height as a function of the mass per unit area (see Figure C.8).

The mathematical limit to light-weighting is the point where the rib height $h_c = 0$. Realistically the minimal rib height for either SSiC or C/SiC should be 20 mm. Figure C.8 also shows that for a

bench with face sheet thickness $t_f = 3$ mm and rib solidity ratio $\eta = 10$ %, the rib height of an open-back becomes 1.4 times the rib-height of a closed-back optical bench. Both mathematical and practical limits to the mass per unit area are summarized in Table C.2.

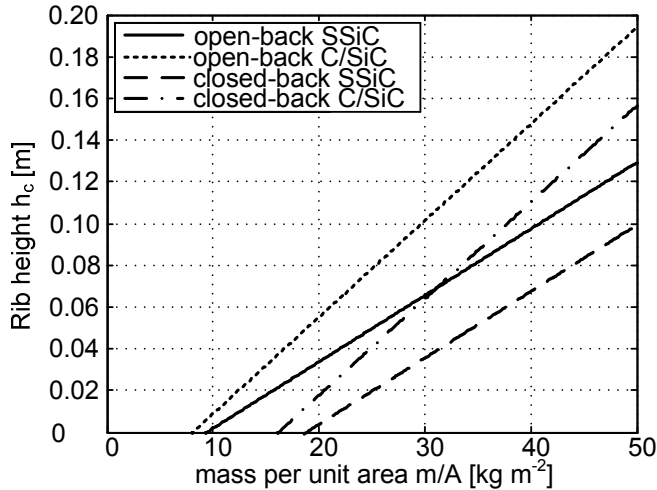


Figure C.8 Variation of the rib height with mass per unit area (limit values from Table C.1 are taken for rib solidity and face sheet thickness)

Table C.2 Limiting values for m/A at which light-weighting becomes impossible mathematically ($h_c = 0$ mm) and practically ($h_c = 20$ mm)

Material	Minimum m/A [kg m^{-2}]			
	Closed-back		Open-back	
	Mathematically	Practically	Mathematically	Practically
SSiC	18	25	9	16
C/SiC	16	21	8	12

With the material properties, the minimal face sheet thicknesses and rib solidity ratio's from Table C.1, and the computed rib heights shown in Figure C.8, the flexural rigidities can be computed from (C.4), (C.6) and (C.1). The flexural rigidities are plotted as a function of the mass per unit area in Figure C.9 and Figure C.10. The figures show that for masses per unit area below a limit value, open-back mirrors or optical benches have larger flexural rigidity than open-back benches. In this case the rib height of the closed-back optical benches is so small, that the optical bench resembles a solid plate, which has lower flexural

rigidity than an open-back optical bench. However, above a certain value the flexural rigidity of closed-back optical benches becomes larger. For SSiC this transition point is located at 38 kg m^{-2} and for C/SiC this point is located at 34 kg m^{-2} .

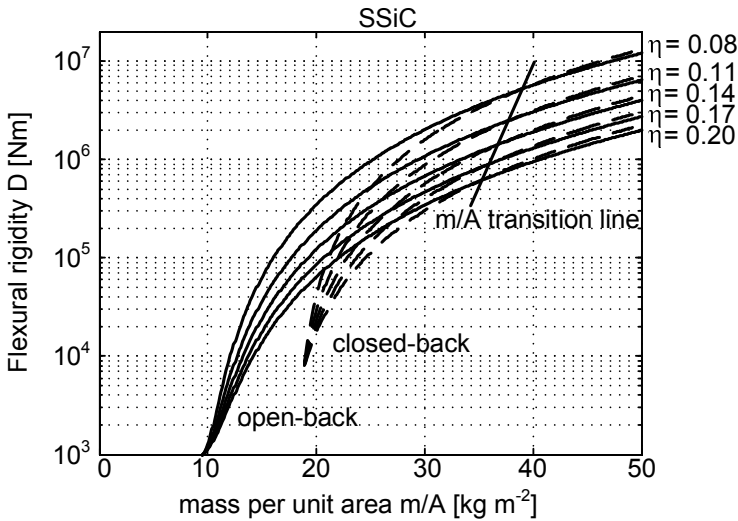


Figure C.9 Flexural rigidity as a function of mass per unit area for SSiC optical benches produced to the manufacturing limits (Table C.1)

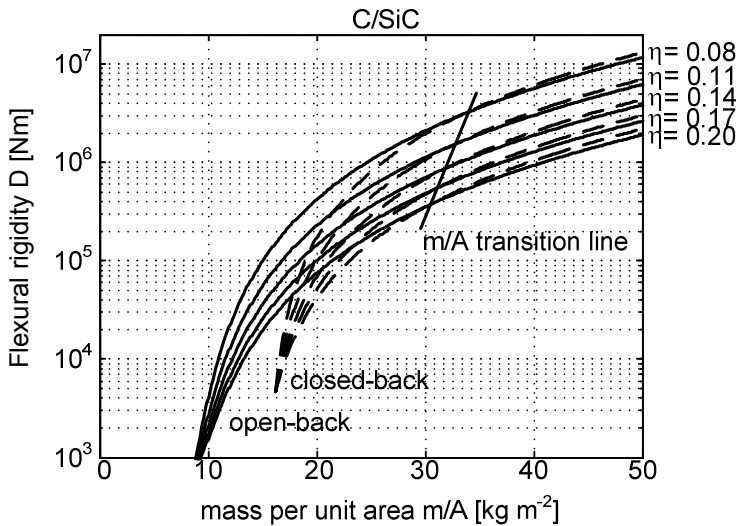


Figure C.10 Flexural rigidity as a function of mass per unit area for C/SiC optical benches produced to the manufacturing limits (Table C.1)

The figures also show that for equal rib solidity ratio and increasing mass per unit area the flexural rigidities of the C/SiC and the SSiC optical bench become equal. Because of manufacturing limitations C/SiC will be able to reach lower rib solidity ratio and thus higher flexural rigidity.

Finally, the flexural rigidity of the benches increases with decreasing rib solidity ratio. This is due to the fact that for increasing mass per unit area the height of the ribs increases.

From the minimal rib wall thickness in combination with minimal solidity ratio the honeycomb inscribed diameters can be computed with C.2, leading to 55 mm for SSiC and 53 mm for C/SiC. These dimensions very closely meet the size of the optical components which will be mounted on top of the optical bench, which means they can be supported rather well.

Note that for the same flexural rigidity for a specific mass per unit area in the range of 30 – 50 kg m⁻² an open-back optical bench will need twice the rib height compared to a closed back optical bench. In the third analysis the difference in flexural rigidity will be shown for equal building height.

C.2.3. With manufacturing and building height limits

In the final analysis no optimization is performed, except to minimize face sheet thickness and to minimize the rib solidity ratio. Flexural rigidities of closed-back and open-back optical benches for equal rib height are compared in this analysis. The minimal face sheet thickness taken is $t_f = 3$ mm and the rib solidity ratio is $\eta = 0.1$. The results are shown in Figure C.11. The flexural rigidity of a closed back optical bench either in SSiC or C/SiC is three times the flexural rigidity of an open back optical bench for equal rib height. Furthermore, the flexural rigidity of an SSiC optical bench is larger than of a C/SiC optical bench for equal rib height.

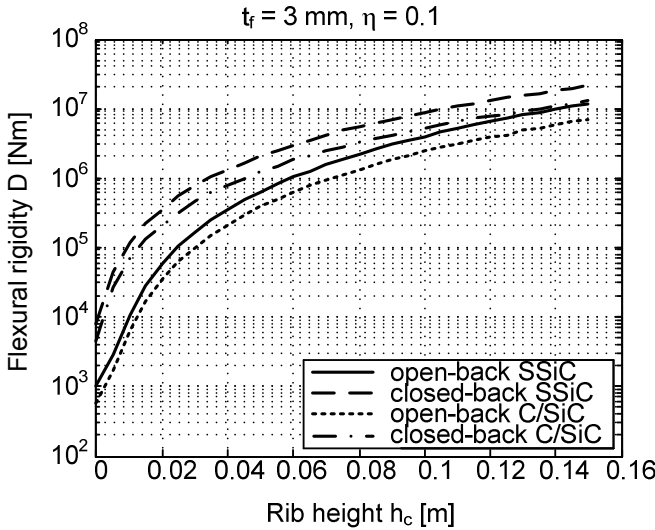


Figure C.11 Flexural rigidity as a function of rib height for a fixed face sheet thickness $t_f = 3$ mm and rib solidity ratio $\eta = 0.1$

C.2.4. Hexagonal, square or triangular pockets

The mechanical analysis above does not indicate which pocket shape should be used for optimal mechanical performance. For the material distribution only inscribed cell diameter and rib thickness, leading to a rib solidity ratio, are used. The inscribed cell diameter does not lead to a conclusion on the pocket shape. Generally in mirror production three types of pockets are used: hexagonal, square and triangular pockets.

Square pockets should not be used because they only have 4 axes of symmetry instead of 6, which is necessary for isotropic thermal expansion. Hexagonal and triangular pockets have 6 axes of symmetry.

For an open back structure, the choice should be triangular pockets, because only triangular pockets have inherent torsional stiffness, preventing them from folding, which can be used to increase bending stiffness. This advantage disappears when using a closed back mirror.

For quilting during polishing, hexagonal pockets can best be used, because with equal inscribed diameter, they span the smallest surface area. This makes it stiffer and thus less sensitive to deflections during polishing.

The fact that hexagonal pockets with equal inscribed diameter do span a smaller mirror surface area, means that more pockets must be machined in the green material. In fact, for equal inscribed diameter, the number of cells needed when using hexagonal pockets is 1.5 times the number of pocket needed for triangular pockets.

It was also shown that during manufacturing a round-off radius is necessary which leaves additional material in the corners. This additional material cannot be used for heightening the cells, such that it is an inefficient usage of material for stiffening the optical bench as a whole. For the triangular pockets the largest amount of material is left in the intersection, whereas for the hexagonal pockets the lowest amount of material is left in the intersections, making the hexagonal pockets more efficient. However, one should also consider the geometry of the entire mirror or optical bench. If the optical bench is square, triangular cells might be less efficient for flexural rigidity than square cells, because a lot of material remains around the edges.

Appendix D

Rolling kinematic couplings

One difficulty occurring for the xy-mounted beamsplitter is that the beamsplitter will show a thermal expansion difference on the optical bench. The mounting will have to absorb thermal expansion differences between the silica beamsplitter and the SiC mount in a way which least affects the function of the BAM system. This can be achieved with a kinematic coupling.

Kinematic couplings, e.g. the Kelvin clamp in Figure D.1, are widely used for locating one rigid body with respect to another. The coupling between the two bodies occurs in exactly 6 DOF, because contact between the ball body (body B in Figure D.1) and the groove body (body A in Figure D.1) occurs at six contact points. It has been shown by analyses and experiments that the one body can be coupled to the other body using kinematic couplings with a repeatability as low as $0.2\ \mu\text{m}$ ([88], [94] and [95]). Extensive work has been put in the modeling stresses and error motions due to manufacturing tolerances of the kinematic couplings to predict the repeatability ([96], [97], [98] and [99]). The effects that are taken into account in these analyses are the normal contact compression and tangential friction effects.

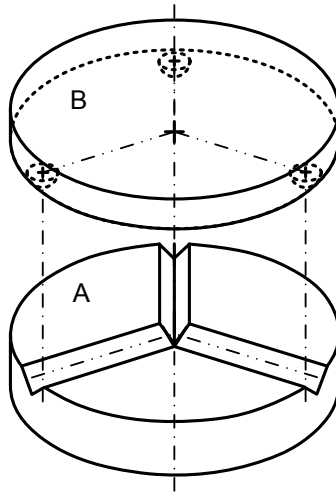
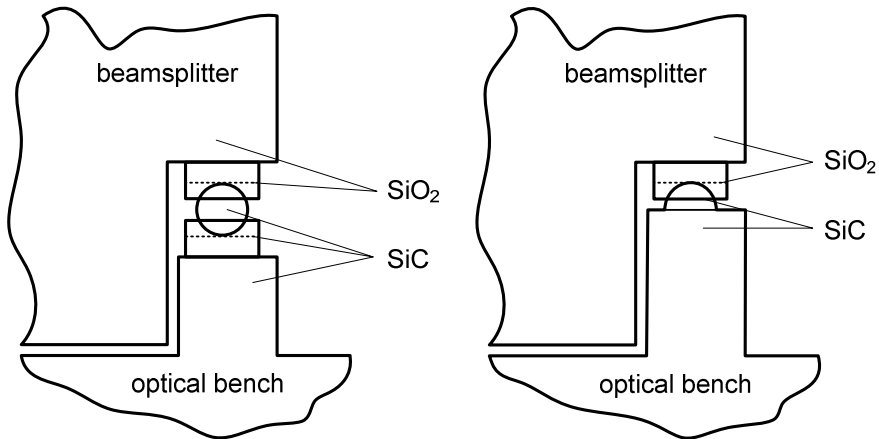


Figure D.1 A symmetric kinematic coupling

Two Kelvin clamp-like mountings can be considered for absorbing the thermal expansion difference between the SiC mount and the fused silica beamsplitter. One technique consists of a SiC ball enclosed in two V-grooves (of which the lower V-groove is SiC and the upper V-groove is fused Silica). The other technique is a sliding SiC semi-sphere in a fused silica V-groove. Figure D.2 shows one contact point for both mounting techniques.



a) Rolling ball in V-grooves

b) Sliding semi-sphere in V-groove

Figure D.2 Kelvin mounting possibilities

Both mounting techniques are symmetric, meaning that all contact points are equal in design and therefore theoretically they have equal stiffness, which is beneficial for the stability. In both options each V-groove is aligned towards the critical point of the beamsplitter. In case of thermal expansion, the critical point will remain in place with respect to the optical bench, i.e. the critical point is the thermal centre.

Alignment is achieved for both techniques by shifting the beamsplitter with ball and V-grooves over the optical bench. After achieving alignment, the beamsplitter is tensioned at the contact points.

D.1 Contact mechanics: rolling versus sliding

The comparison of the Kelvin mounting with rolling balls and with sliding semi-spheres can be made given the fact that the thermal expansion should be absorbed preferably without contact hysteresis. Contact hysteresis occurs when macro-scale slip occurs. Macro-scale slip will only occur when the front and back slip fronts in a contact touch each other [86].

A theoretical investigation is made on the amount of thermal expansion difference Δx that can be absorbed without contact hysteresis. The investigation is made using only the Hertz theory of normal contact of elastic bodies. Both sliding and rolling situations are shown for a single point contact in Figure D.3.

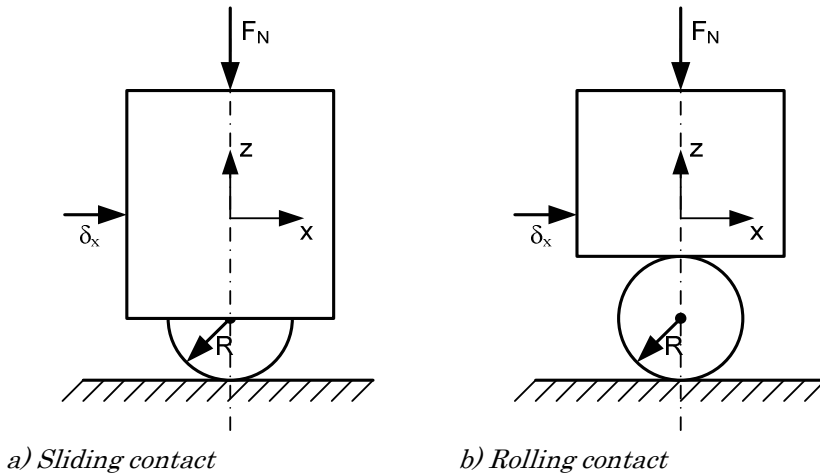


Figure D.3 Schematic representation of the sliding and rolling contact situation on macro-scale

The contacts are preloaded with normal force F_N . Both the semi-sphere in the sliding contact and the ball in the rolling contact have equal radius R to keep the contact stiffness the same for both situations.

D.1.1. Sliding contact

In reality, normal contact of an elastic spherical body on an elastic flat body will cause a deformation of both the flat body and the sphere. The elastic modulus and Poisson ratio of the spherical body and flat body are E_1 and ν_1 , and E_2 and ν_2 , respectively. In Hertz theory of normal contact of elastic bodies, this situation is simplified by assuming that the flat body is infinitely stiff (e.g. rigid) and the sphere is elastic with effective elastic modulus E^* [86]:

$$E^* = \left(\frac{1-\nu_1^2}{E_1} + \frac{1-\nu_2^2}{E_2} \right)^{-1}. \quad (\text{D.1})$$

This is illustrated in Figure D.4 by the deformed ball on a flat surface. The radius of the contact circle is given by [86]:

$$a = \left(\frac{3 \cdot F_N \cdot R}{4 \cdot E^*} \right)^{1/3}. \quad (\text{D.2})$$

The compression of the sphere in z-direction, called approach of distant points δ_z is given by [86]:

$$\delta_z = \frac{a^2}{R} = \left(\frac{9 \cdot F_N^2}{16 \cdot R \cdot E^{*2}} \right)^{1/3}. \quad (\text{D.3})$$

When a tangential force F_T is applied to the sphere with respect to the flat body, slip fronts will start to migrate inwards. This is visualized in Figure D.4.

A sliding contact will always have at least one contact point, which has stuck at all times from time $t = 0$, if the tangential force F_T does not exceed the limiting friction force $\mu \cdot F_N$ at any time t [86]. The width of the stick region in the direction of the tangential force is:

$$c = a \cdot \left(1 - \frac{F_T}{\mu \cdot F_N} \right)^{1/3}. \quad (\text{D.4})$$

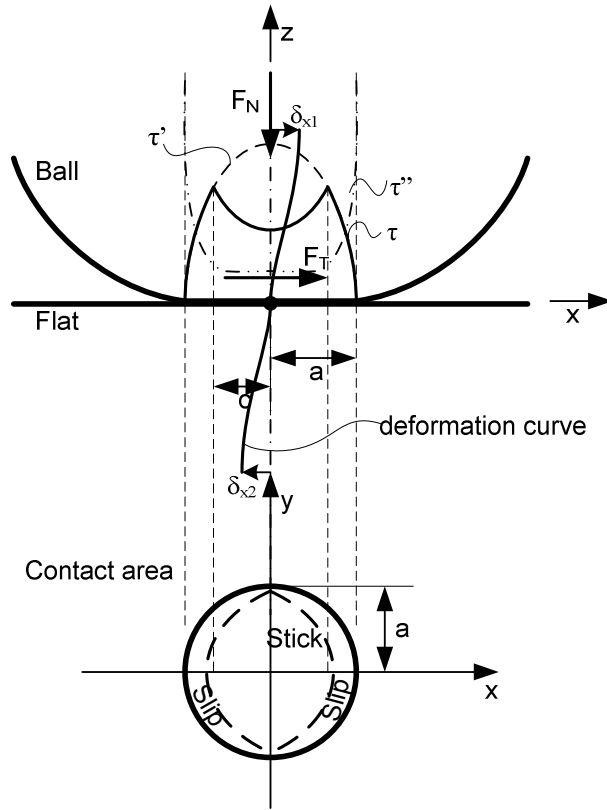


Figure D.4 Traction stress curve of a non-sliding contact, showing also the stick and slip regions

The corresponding shear stress distribution is indicated with τ . It is built up of the limiting shear stress τ' (Figure D.4) on the point of complete sliding (when $F_T = \mu \cdot F_N$) and of the shear stress τ'' occurring when no tangential force is applied ($F_T = 0$).

The tangential displacement of the ball is δ_{x1} and of the flat it is δ_{x2} (Figure D.4). The relative tangential displacement of the contacting bodies in x-direction ($\delta_x = \delta_{x1} - \delta_{x2}$) due to the tangential load is given by:

$$\delta_x = \frac{3 \cdot \mu \cdot F_N}{16 \cdot a} \cdot \left(\frac{2 - \nu_1}{G_1} + \frac{2 - \nu_2}{G_2} \right) \cdot \left\{ 1 - \left(1 - \frac{F_T}{\mu \cdot F_N} \right)^{2/3} \right\}, \quad (\text{D.5})$$

with:

G_1 the shear modulus of the sphere [N m^{-2}], and

G_2 the shear modulus of the flat [N m^{-2}].

The maximum relative tangential displacement that can be absorbed without hysteresis is achieved when $F_T = \mu \cdot F_N$:

$$\delta_x = \frac{3 \cdot \mu \cdot F_N}{16 \cdot a} \cdot \left(\frac{2 - \nu_1}{G_1} + \frac{2 - \nu_2}{G_2} \right). \tag{D.6}$$

D.1.2. Rolling contact

The rolling situation can best be explained by assuming that at time $t = 0$, the tangential force is $F_T = 0$ N. In that situation, the contact with contact radius a , is in complete stick. No slip exists, since no tangential force exists.

From $t = 0$, the tangential force is increased, and progressing slip fronts occur towards the centre of the contact region, exactly like is the case for sliding contact (see Figure D.5).

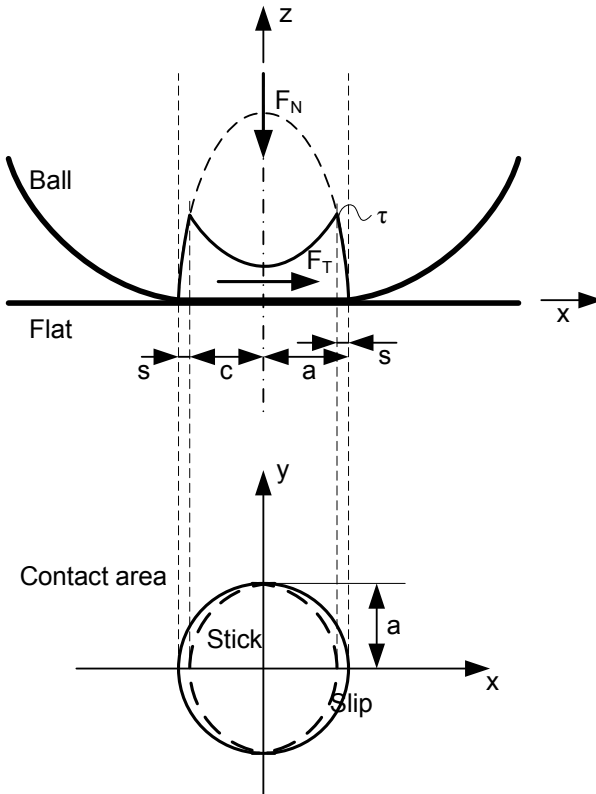


Figure D.5 Traction stress curve of a rolling contact, at the point that actual rolling starts: $F_T \leq \mu_{roll} \cdot F_N$. The rolled distance is $d_r = 0$. Ball is rolling from right to left over the flat surface.

It is assumed that the rolling resistance is much lower than the sliding resistance; $\mu_{roll} \ll \mu$. Therefore, at $F_T = \mu_{roll} \cdot F_N$, the sliding slip fronts have reached their maximum width and the ball will start rolling. The ball is moving from right to left over the flat surface.

From this point $F_T = \mu_{roll} \cdot F_N$ and the rolling contact will create a new stick region, shown in Figure D.6, while the original stick region shrinks.

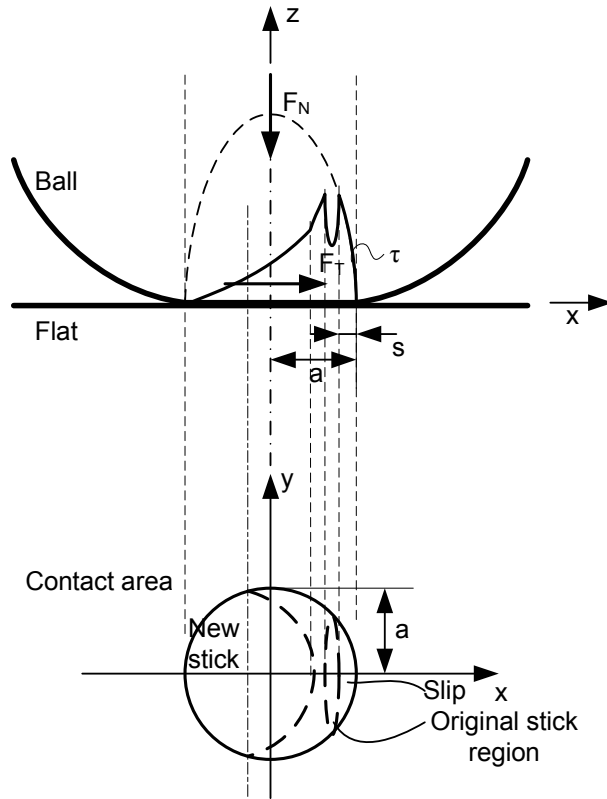


Figure D.6 Traction stress curve of a rolling contact, at the point that actual rolling starts: $F_T = \mu_{roll} \cdot F_N$. The rolled distance is $d_r < 2 \cdot c$. Ball is rolling anti-clockwise over the flat surface.

Finally, after achieving rolling distance $d_r = 2 \cdot c$, the final point in the original stick region is released (Figure D.7). At this point:

$$c = a \cdot \left(1 - \frac{\mu_{roll}}{\mu} \right)^{1/3}. \tag{D.7}$$

The maximum length change which can be absorbed by a rolling ball on a flat body without hysteresis is given by:

$$\delta_x = 2 \cdot c = 2 \cdot a \cdot \left(1 - \frac{\mu_{roll}}{\mu}\right)^{1/3}. \tag{D.8}$$

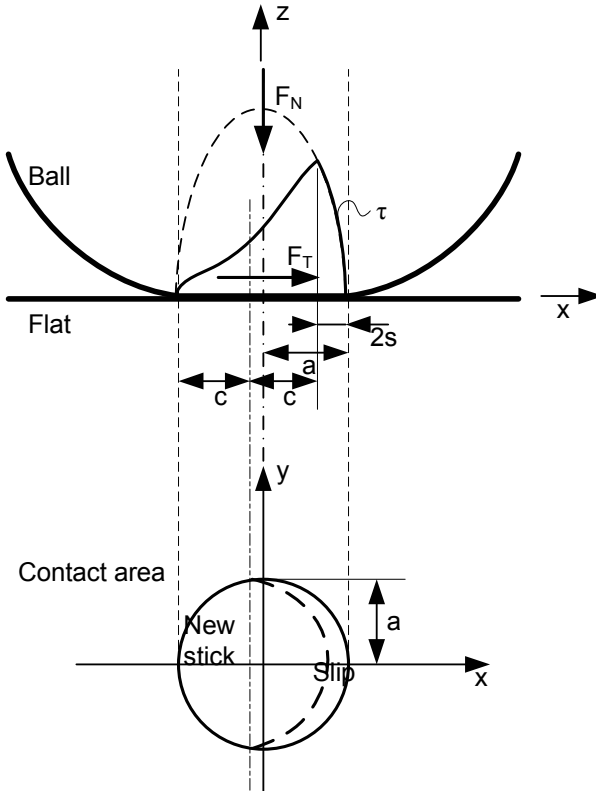


Figure D.7 Traction stress curve of a rolling contact, at the original stick region has disappeared; i.e. hysteresis occurs. $F_T = \mu_{roll} \cdot F_N$. The rolled distance is $d_r = 2 \cdot c$. Ball is rolling from right to left over the flat surface.

To compare the thermal expansion difference that can be absorbed by the rolling and sliding contact without hysteresis, consider a normal contact force $F_N = 150 \text{ N}$ in combination with a ball radius $R = 5 \text{ mm}$ for both the sliding and rolling contact. Consider an SSiC sphere on a fused silica flat. This gives an effective Young's modulus of $E^* = 0.64 \cdot 10^{11} \text{ N m}^{-2}$. The effective contact radius $a = 0.21 \text{ mm}$ is computed with (D.2). The friction coefficient of fused

silica on SiC is assumed to be $\mu = 0.3$. Furthermore, the rolling friction coefficient is estimated to be $\mu_{roll} = 0.003$.

Using (D.6) and (D.8) the maximum thermal expansion difference without hysteresis, for the sliding and rolling contact respectively, can be computed. For sliding this distance is $\delta_x = 2.9 \mu\text{m}$, whereas for rolling it is $\delta_x = 0.41 \text{ mm}$. This result makes the rolling ball pre-eminently the solution for absorbing the thermal expansion difference of $15 \mu\text{m}$ without hysteresis.

Note additionally, that the tangential forces in the rolling contact will not be larger than $F_T = \mu_{roll} \cdot F_N$, whereas the tangential forces in the sliding contact will increase to $F_T = \mu \cdot F_N$. The tangential force in the rolling contact is estimated to be a factor 100 smaller than in the sliding contact. The smaller are the tangential forces, the smaller will be the stresses in the beamsplitter, which will reduce the stress birefringence.

The Hertz theory of contact can be applied even for rough surfaces in contact when the surface roughness is less than 5% of the bulk elastic compression δ_0 . According to O'Connor and Johnson [100], who performed an experimental study with a smooth hard steel ball on a rough flat, the tangential and normal compliance under the action of a superimposed tangential force, changes very little with the roughness of the surface. This can be explained by the fact that in the central region of the contact area, the tangential traction shows a minimum, whereas the normal compression shows a maximum. The real contact area in this region will be high and, in consequence, the compliance of the asperities will be small. Since the tangential traction in that region is also small, the contribution of the asperity deformation to the bulk compliances is negligible.

D.2 Axial stiffness of a ball in V-grooves

The axial stiffness of a semi-sphere in a V-groove (like shown in Figure D.8) is given by [88]:

$$c_A = 2 \cdot \cos^2 \alpha \cdot c_N + 2 \cdot \sin^2 \alpha \cdot c_T \quad (\text{D.9})$$

where c_N is the Hertzian normal contact stiffness and c_T is the tangential stiffness due to friction given by:

$$c_N = \frac{3}{2} \cdot \left(\frac{16}{9} \cdot R \cdot E^{*2} \cdot F_N \right)^{1/3} \quad \text{and}; \quad (\text{D.10})$$

$$c_T = 8 \cdot a \cdot \left(\frac{G_1}{2 - \nu_1} + \frac{G_2}{2 - \nu_2} \right) \tag{D.11}$$

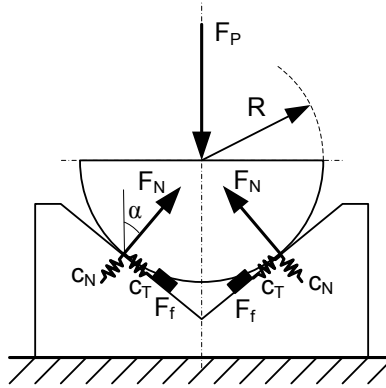


Figure D.8 Semi-sphere in a V-groove

The friction force also introduces hysteresis. The maximum hysteresis in the direction of the preload is given by:

$$s_v = \frac{\mu \cdot F_P \cdot \tan \alpha}{c_A} \tag{D.12}$$

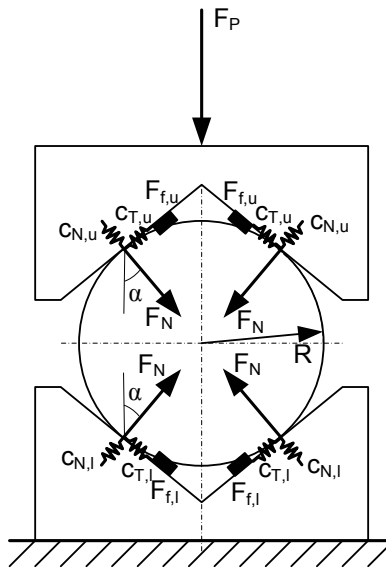


Figure D.9 Ball between 2 V-grooves

In the case of a ball clamped between two V-grooves (Figure D.9) like for the beamsplitter, the total axial stiffness is given by:

$$c_{A,total} = \frac{c_{A,u} \cdot c_{A,l}}{c_{A,u} + c_{A,l}} \quad (\text{D.13})$$

The maximum hysteresis due to the friction force is now given by:

$$s_{v,total} = s_{v,u} + s_{v,l} \quad (\text{D.14})$$

D.3 Accuracy of V-groove orientation

The kinematic coupling has been chosen for mounting the cubic beamsplitter, to absorb the thermal expansion between the fused silica beamsplitter and the SiC mount, such that the critical point of the beamsplitter remains fixed with respect to the optical bench. Tolerancing of the kinematic couplings can be focused on manufacturing cost reduction, which has been done in [98]. Some effort has been made to design quasi-kinematic couplings with replacements for the balls [102]. More recently attention is focused on the interchangeability of kinematic couplings [99]. However, no attention has been paid to the effect of tolerancing errors on the thermal centre of the kinematic coupling. Two tolerances are considered: a ψ -error and a θ -error in the V-groove, like shown in Figure E.10.

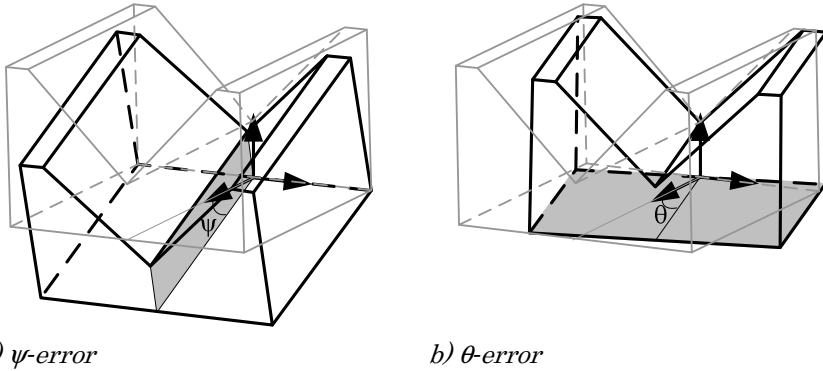


Figure D.10 Possible orientation errors of the V-grooves

Consider a kinematic coupling with a desired thermal center T_0 but with θ -errors in each of the V-grooves, like shown in Figure D.11. In the ideal situation the V-grooves coincide with lines $l_1(x)$, $l_2(x)$ and $l_3(x)$. The coupling is considered in a 3D space, i.e. \mathcal{R}^3 .

Points A_0 , B_0 and C_0 indicate the centers of the balls. Point S_0 indicates an arbitrary point on the ball body.

The assumption is made that there is uniform thermal expansion, meaning that the distance between any set of points is the original distance multiplied by one plus the thermal expansion.

Also, the fact that the center of each ball is always on the line, which defines the V-groove, is used to compute the position of the balls. In the next step the position of the thermal center after thermal expansion is computed. And finally a line in the plane of the ball body is projected on the xy -plane, the xz -plane and the yz -plane to compute the θ -, φ - and ψ -rotation of the ball body with respect to the V-groove body.

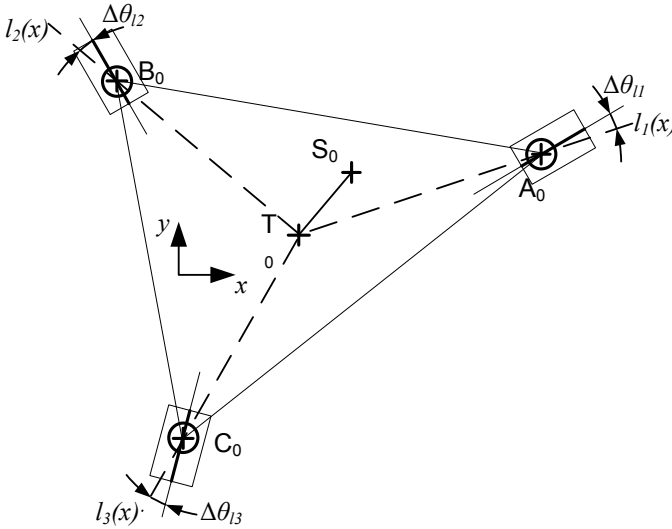


Figure D.11 General kinematic coupling with a θ -error at each V-groove

The original points are defined by (see Figure D.11):

$$A_0 \Rightarrow [x_{A_0}, y_{A_0}, z_{A_0}]; \quad (D.15)$$

$$B_0 \Rightarrow [x_{B_0}, y_{B_0}, z_{B_0}]; \quad (D.16)$$

$$C_0 \Rightarrow [x_{C_0}, y_{C_0}, z_{C_0}] \text{ and}; \quad (D.17)$$

$$T_0 \Rightarrow [x_{T_0}, y_{T_0}, z_{T_0}]. \quad (D.18)$$

The vectors of the lines defining the V-groove are defined by angles ψ and θ in radians:

$$\begin{aligned} \vec{n}_{l_4} = (T_0 - A_0) + \tan(\theta_4)[y_{T_0} - y_{A_0}, x_{A_0} - x_{T_0}, 0] \\ + \left\| [y_{T_0} - y_{A_0}, x_{A_0} - x_{T_0}, 0] \tan(\theta_4) \right\| \tan(\psi_4) [0, 0, 1] \end{aligned} \quad (D.19)$$

$$\begin{aligned} \vec{n}_{l_5} = (T_0 - B_0) + \tan(\theta_5)[y_{T_0} - y_{B_0}, x_{B_0} - x_{T_0}, 0] \\ + \left\| [y_{T_0} - y_{B_0}, x_{B_0} - x_{T_0}, 0] \tan(\theta_5) \right\| \tan(\psi_5) [0, 0, 1] \end{aligned} \quad (D.20)$$

$$\begin{aligned} \vec{n}_{l_6} = (T_0 - C_0) + \tan(\theta_6)[y_{T_0} - y_{C_0}, x_{C_0} - x_{T_0}, 0] \\ + \left\| [y_{T_0} - y_{C_0}, x_{C_0} - x_{T_0}, 0] \tan(\theta_6) \right\| \tan(\psi_6) [0, 0, 1] \end{aligned} \quad (D.21)$$

The following relations show that point A is on line l_4 , B is on line l_5 and C is on line l_6 :

$$A = A_0 + \vec{n}_{l_4} t_4; \quad (D.22)$$

$$B = B_0 + \vec{n}_{l_5} t_5 \text{ and}; \quad (D.23)$$

$$C = C_0 + \vec{n}_{l_6} t_6. \quad (D.24)$$

To solve this problem, the distance equations of A to B, B to C and A to C are introduced:

$$\|A - B\| = (1 + \gamma) \|A_0 - B_0\|; \quad (D.25)$$

$$\|B - C\| = (1 + \gamma) \|B_0 - C_0\| \text{ and}; \quad (D.26)$$

$$\|A - C\| = (1 + \gamma) \|A_0 - C_0\|. \quad (D.27)$$

This combination of equations is used to solve the points A, B and C. In the next step the new position of the thermal center is computed, using:

$$\|A - T\| = (1 + \gamma) \|A_0 - T_0\|; \quad (D.28)$$

$$\|B - T\| = (1 + \gamma) \|B_0 - T_0\| \text{ and}; \quad (D.29)$$

$$\|C - T\| = (1 + \gamma) \|C_0 - T_0\|. \quad (D.30)$$

The additional requirement that T should be in the same plane as A, B and C, is also implemented:

$$\begin{vmatrix} x_T & y_T & z_T & 1 \\ x_A & y_A & z_A & 1 \\ x_B & y_B & z_B & 1 \\ x_C & y_C & z_C & 1 \end{vmatrix} = 0. \quad (\text{D.31})$$

In the final step a line in the plane of the ball body, which is (preferably) not perpendicular to the xy-plane, or the xz-plane, or the yz-plane, is projected orthogonally onto each of these planes.

If a line with points B_0 and T_0 and a line with points B and T is taken, the following vectors are obtained:

$$\vec{k}_0 = B_0 - T_0 = [x_{B_0} - x_{T_0}, y_{B_0} - y_{T_0}, z_{B_0} - z_{T_0}] = [k_{x0}, k_{y0}, k_{z0}] \text{ and}; \quad (\text{D.32})$$

$$\vec{k} = B - T = [x_B - x_T, y_B - y_T, z_B - z_T] = [k_x, k_y, k_z]. \quad (\text{D.33})$$

With orthogonal projection of these vectors onto the xy-plane the following vectors are obtained:

$$\vec{u}_0 = [k_{x0}, k_{y0}, 0] \text{ and} \quad (\text{D.34})$$

$$\vec{u} = [k_x, k_y, 0]. \quad (\text{D.35})$$

From these vectors the rotation of the ball-body around the z-axis, or in other words the angle θ can be computed using:

$$\theta = \arccos\left(\frac{\vec{u} \bullet \vec{u}_0^T}{\|\vec{u}\| \|\vec{u}_0\|}\right) \quad (\text{D.36})$$

with $0 < \theta < \pi$.

The orthogonal projection on the xz-plane gives the ψ -rotation via:

$$\vec{v}_0 = [k_{x0}, 0, k_{z0}] \text{ and} \quad (\text{D.37})$$

$$\vec{v} = [k_x, 0, k_z]. \quad (\text{D.38})$$

The ψ -rotation is now:

$$\psi = \arccos\left(\frac{\vec{v} \bullet \vec{v}_0^T}{\|\vec{v}\| \|\vec{v}_0\|}\right) \quad (\text{D.39})$$

with $0 < \psi < \pi$.

The projection on the yz-plane gives the ϕ -rotation via:

$$\vec{w}_0 = [0, k_{y0}, k_{z0}] \quad \text{and} \quad \text{(D.40)}$$

$$\vec{w} = [0, k_y, k_z] . \quad \text{(D.41)}$$

The ϕ -rotation is now:

$$\phi = \arccos \left(\frac{\vec{w} \bullet \vec{w}_0^T}{\|\vec{w}\| \|\vec{w}_0\|} \right) \quad \text{(D.42)}$$

with $0 < \phi < \pi$.

Alignment instability of the beamsplitter

Using the 3-D method the alignment stability of a V-groove arrangement like used in the beamsplitter due to specified tolerances on the V-grooves orientations can be computed.

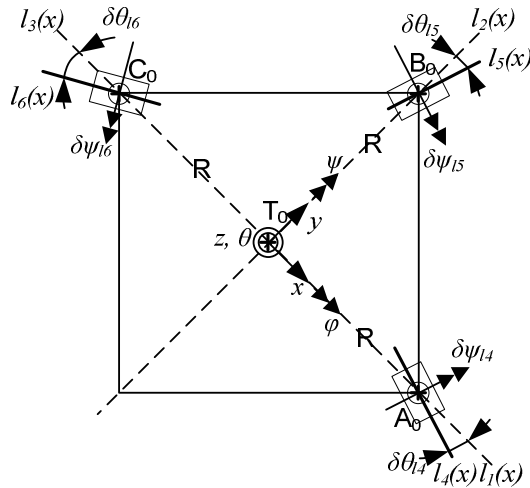


Figure D.12 Tolerances on V-grooves for the beamsplitter

Figure D.12 shows the beamsplitter arrangement with tolerances on the V-groove orientations. The distance between the balls and the thermal center is R . For quantifying the error on the orientation and position of the beamsplitter $R = 42.4$ mm, initially the θ -rotation error and ψ -rotation error are varied separately. The results are shown in Table D.1 and Table D.2. In each column of Table D.1 a combination of errors of the V-grooves around the θ -axis is shown, and below the double line, the resulting rotation of

the beamsplitter around the φ -, ψ -, and θ -axis, is shown and the displacement of the thermal center T . In Table D.2 the same has been done for combinations of errors of the V-grooves around the ψ -axis. Table D.1 shows that the errors caused by θ -errors in the V-groove alignment, only influence the θ -alignment of the ball-body and xy-position of the thermal center. ψ -errors in the V-groove alignment, only influence the ψ - and φ -alignment of the ball-body and z-position of the thermal center. This means that each error source has an independent influence on the position and the angular alignment of the ball body.

Table D.1 The influence of variation of $\delta\theta_4$, $\delta\theta_5$ and $\delta\theta_6$ on the beamsplitter kinematic coupling ($R = 42.4$ mm, $\gamma = 2.87 \cdot 10^{-4}$ and $\delta\psi_{l_4} = \delta\psi_{l_5} = \delta\psi_{l_6} = 0$ rad) on the angular orientation of the ball-body and on the position of the thermal centre

$\delta\theta_4$ [mrad]	0	2	2	2	2	2	2
$\delta\theta_5$ [mrad]	0	0	2	-2	2	-2	-1
$\delta\theta_6$ [mrad]	0	0	0	0	2	2	2
$\delta\theta$ [μ rad]	0	0.3	0.3	0.3	0.6	0.6	0.6
$\delta\varphi$ [μ rad]	0	0	0	0	0	0	0
$\delta\psi$ [μ rad]	0	0	0	0	0	0	0
δx_T [nm]	0	0	12	-36	0	-48	-36
δy_T [nm]	0	-12	-12	-12	0	0	0
δz_T [nm]	0	-12	0	0	0	0	0
$\delta\varphi_T$ [nm]	0	17	17	38	0	48	36

When comparing the required alignment stability of $\theta = 1.2$ μ rad, $\varphi = 1.2$ μ rad and $x = 1.3$ μ m to the found alignment stability in case of 2 mrad misalignment of the V-grooves Table D.1 shows that the x-alignment error remains of the order of tens of nanometers, which is well below the $x = 1.3$ μ m requirement. More critical are the angles θ and φ . In the worst case combination of alignment errors for the V-grooves within a limit of ± 2 mrad, the θ - and φ -alignment stability will be 0.6 μ rad, which is just half the required alignment stability of the beamsplitter. The conclusion is thus that the V-grooves should be aligned with maximally ± 2 mrad uncertainty, in order not to lose alignment due to the thermal expansion difference between the fused silica beamsplitter and the SiC mount. This conclusion is drawn without

taking into account other possible error sources for the alignment stability of the beamsplitter.

Table D.2 The influence of variation of $\delta\psi_{i_4}$, $\delta\psi_{i_5}$ and $\delta\psi_{i_6}$ on the beamsplitter kinematic coupling ($R = 42.4$ mm, $\gamma = 2.87 \cdot 10^{-4}$ and $\delta\theta_{i_4} = \delta\theta_{i_5} = \delta\theta_{i_6} = 0$ rad) on the angular orientation of the ball-body and on the position of the thermal centre

$\delta\psi_{i_4}$ [mrad]	2	0	2	0	0	2	2	-2
$\delta\psi_{i_5}$ [mrad]	0	2	2	2	2	2	-2	2
$\delta\psi_{i_6}$ [mrad]	0	0	0	2	-2	2	2	2
$\delta\theta$ [μ rad]	0	0	0	0	0	0	0	0
$\delta\varphi$ [μ rad]	0.3	0	-0.3	0.3	0.3	0	0	0.6
$\delta\psi$ [μ rad]	0.3	0.6	0.3	0.3	0.8	0	1.1	0.6
δx_T [nm]	0	0	0	0	0	0	0	0
δy_T [nm]	0	0	0	0	0	0	0	0
δz_T [nm]	-12	0	-12	-12	12	-24	-24	0
δp_T [nm]	12	0	12	12	12	24	24	0

Appendix E

Thermal contact conductance

Like the optical bench, the mirror is constructed of SiC; i.e. there is (in principle) no difference in material properties between the mirror and this optical bench. From this point of view no effort is needed to absorb the thermal expansion difference between the mirror and the optical bench. Contact between the mirror and the optical bench can therefore be conducted directly without the ball-in-V-grooves solution, which is used for the beamsplitter. However, since a clamping solution is chosen, there are only 3 points of contact. This can cause a severe drop in thermal contact conductance from the optical bench to the mirror or vice versa, which can in turn cause considerable temperature difference between the mirror and the optical bench. This temperature difference can cause a thermal expansion difference, causing misalignment of the mirror. This is not desirable.

Therefore, two steps are taken. First, an analysis is made of the expected thermal contact conductance and second, the expected thermal contact conductance is used in a hypothetical case to determine an expected temperature difference between the mirror and the optical bench and thereby assessing the risk of losing alignment. A large number of models exists to describe the thermal contact conductance of two bodies in contact ([103] to

[112]) Thermal contact conductance h is defined as the ratio of the heat flux to the temperature difference over the contact.

In the scope of the design of the optical components of the BAM system, thermal conductance of non-conforming surfaces is of interest. For non-conforming surfaces roughness has an insignificant effect on the conductance [108], which is why it is not considered here.

The thermal conductance over a elastic non-conforming smooth surface contact (Figure E.4) is predicted by Clausing and Chao [107]:

$$h_L = \lambda_s \cdot \frac{a_L}{\pi \cdot b_L^2 \cdot \psi}, \quad (\text{E.1})$$

In (E.5) a_L is the elastic Hertzian contact radius according to:

$$a_L = \left[\frac{3 \cdot P}{4} \left(\frac{1 - \nu_1^2}{E_1} + \frac{1 - \nu_2^2}{E_2} \right) \left(\frac{1}{r_1} + \frac{1}{r_2} \right)^{-1} \right]^{1/3}, \quad (\text{E.2})$$

λ_s is the harmonic mean of the thermal conductivities [$\text{W m}^{-1} \text{K}^{-1}$]:

$$\lambda_s = \frac{2 \cdot \lambda_1 \cdot \lambda_2}{\lambda_1 + \lambda_2}, \quad (\text{E.3})$$

and ψ is the constriction parameter for $0 < a_L/b_L < 0.4$ according to:

$$\psi = \left[1 - \left(\frac{a_L}{b_L} \right) \right]^{1.5}. \quad (\text{E.4})$$

To achieve a sense of the reduction of thermal conductance a case study is made. Consider SiC as the material of both bodies, with $E_1 = E_2 = 420 \cdot 10^9 \text{ N m}^{-2}$, $\nu_1 = \nu_2 = 0.16$ and $\lambda_1 = \lambda_2 = 180 \text{ W m}^{-1} \text{K}^{-1}$.

A curved surface with $r_1 = 3 \cdot 10^{-3} \text{ m}$ pressed against a flat surface ($r_2 = \infty \text{ m}$) with a load $P = 100 \text{ N}$, has a thermal contact conductance of $h \approx 7 \cdot 10^2 \text{ W m}^{-2} \text{K}^{-1}$.

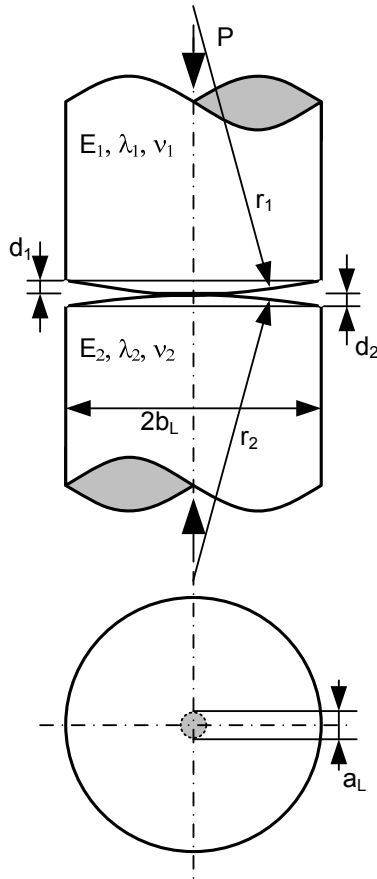
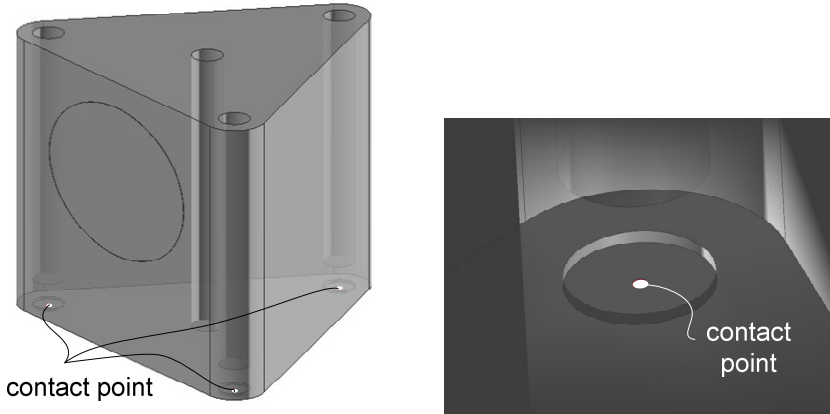


Figure E.1 Two smooth curved surfaces pressed together

In order to obtain an idea of the effect of this low thermal contact conductance, a finite element computation has been conducted using ANSYS. The analysis considers a triangular mirror (Figure E.2), which is mounted on an optical bench on three contact points. It is assumed that the three contact points are all fixed in 6 DOF to the optical bench, meaning that the mirror itself is over constrained.

The analysis is focused on analyzing a worst-case scenario, when, after launch, the mirror and the optical bench are exposed to space environment with background radiation temperature of 140 K, both will cool down from 293 K. However, the thermal response time of the mirror is assumed to be much lower, than that of the baseframe. If the thermal contact between the mirror and the

optical bench is poor, a temperature difference will occur, causing stress in each contact point, because of thermal expansion difference.



a) Complete mirror

b) A contact point (magnified)

Figure E.2 Mirror model for thermal contact analysis

In the worst case analysis the optical bench is 293 K. It is assumed that the base has such low thermal response in comparison to the mirror, that its transient behavior towards 140 K equilibrium temperature in space can be considered static. The mirror partly sees a temperature of 140 K and partly 4 K of deep space in radiation. The underside sees 293 K of the optical bench. Through thermal contact conductance heat is passed from the optical bench to the mirror.

In the case of a thermal contact conductance of $3600 \text{ W m}^{-2} \text{ K}^{-1}$ (which was taken from [109] as an aluminum-aluminum vacuum contact value) and a total effective thermal contact area of 0.85 mm^2 , the temperature difference between the optical bench and the mirror would become as much as 87 K. This will induce a thermal expansion difference of $8.7 \text{ }\mu\text{m}$, which will in a realistic situation cause slip in two of the three contact points, causing misalignment.

In order to prevent slip and thus misalignment, several measures can be taken:

- increase thermal contact area. This could be done by increasing the radius of the contacts, by using interstitial

thermal contact materials, or by using thermal straps. The latter is the most favorable option, because it will not fix additional DOF of the mirror;

- making a thermal tent for the optical bench and the mirrors, such that only the mirrors facing the telescopes (M3, M4, M7 and M8) will have only 1 side that sees 140 K radiative temperature;
- making the mirror design with a thermal center such that it will not lose alignment, like was done with the beamsplitter.

Bibliography

Chapter 1 – Introduction

- [1] <http://www.theoi.com/Ouranos/Gaia.html>
- [2] GAIA Science Advisory Group K.S. de Boer et al. *GAIA Composition, Formation and Evolution of the Galaxy Concept and Technology Study Report* (2002), ESA-SCI, France
- [3] GAIA SLTRS project team. *GAIA system level technical reassessment study final report*. Astrium, France, 2002
- [4] Braam, B.C. *Alignment and Test Results*. TNO TPD Space Instrumentation, Delft, doc.no. TPD-MLCS-OPD-RPT-04, 2000
- [5] GAIA PLM project team. *GAIA: BAM Opto-mechanical Assembly Requirements Specification*. EADS Astrium, France, 2005
- [6] Fortesque, P., Stark, J. *Spacecraft systems engineering*. 2nd ed., John Wiley and Sons Ltd., ISBN 0 471 95220 6, Chichester, 1995
- [7] Steele, D. *Theory of vibrational spectroscopy*. W.B. Saunders Company, London, 1971
- [8] Mangonon, P.C. *The principles of materials selection for engineering design*. Prentice-Hall, Inc., New Jersey, 1999, ISBN 0-13-242595-5
- [9] Pollard, A.F.C. *The Mechanical Design of Scientific Instruments*. Cantor Lectures, Imperial College of Science and Technology, Parsons Ltd., Hastings, 1992
- [10] Loewen, E.G. *Metrology problems in general engineering, a comparison with precision engineering*. Annals of the CIRP, Vol. 29/2, 1980, pp. 451 – 453

- [11] McKeown, P.A. *High precision manufacturing and the British economy*. James Clayton Lecture, Institute of Mech. Eng. Roc., vol. 200, no. 76, 1986
- [12] McKeown, P.A. *The role of Precision Engineering in Manufacturing of the Future*. Annals of the CIRP, Keynote paper, vol. 36/2, 1987
- [13] McKeown, P.A. *New and Advanced Materials*. Special Article, Nanotechnology, Emerging Technology Series, 1997
- [14] Teague, E.C., Evans, C. *Patterns for precision instrument design (mechanical aspects)*. National Institute of Standards and Technology, Tutorial Notes, ASPE Annual Meeting, Norfolk, Virginia, 1989
- [15] Teague, E.C. *Basic Concepts for Precision Instrument Design: Designing Instruments and Machines to have a high degree of repeatability*. National Institute of Standards and Technology, Tutorial Notes, ASPE Annual Meeting, Norfolk, Virginia, 1997
- [16] Teague, E.C. *Basic Concepts for Precision Instrument Design: Some Draft notes and papers*. National Institute of Standards and Technology, Tutorial Notes, ASPE Annual Meeting, Norfolk, Virginia, 1997
- [17] Schellekens, P., Rosielle, N., et al. *Design for precision: current status and trends*. Annals of the CIRP, Keynote paper, vol. 47/2, 1998, pp. 557 – 586
- [18] Lecture notes no. 4700. *Constructieprincipes 1, bedoeld voor het nauwkeurig bewegen en positioneren*. Technische Universiteit Eindhoven, Eindhoven, 1995, in Dutch
- [19] Maxwell, J.C. *General consideration concerning scientific apparatus*. Scientific Papers of James Clerk Maxwell, Ed. Dover Press, Reprint from the Handbook to the Special Loan Collection of Scientific Apparatus (1876), 1890
- [20] Marschall, C.W., Maringer, R.E. *Dimensional Instability. An introduction*. 22nd edition, Pergamon Press, New York, 1977, ISBN 0-08-021305-7

Chapter 2 – Silicon Carbide

- [21] K.A. Schwetz. *Silicon Carbide Based Hard Material*. Handbook of Ceramic Hard Materials, Riedel, R. (ed.), Wiley-VCH, Weinheim, 2000, ISBN 3-527-29972-6, Vol. 1, pp. 683 – 748

- [22] Breysse, J., et al. *All-SiC telescope technology. recent progress and achievements*. Proceedings of 5th International conference on Space Optics 2004, ESA, 2004, pp. 659 – 671
- [23] Bougoin, M. *SiC material and technology for space optics*. ICSO conference proceedings, 2000
- [24] Rashed, A.H. *Properties and Characteristics of Silicon Carbide*. POCO Graphite Inc., Decatur, 2002
- [25] Boostec, material properties leaflet, 2004
- [26] Touloukian, Y.S., Kirby, R.K., Taylor, R.E. *Thermal expansion: nonmetallic solids*. IFI/Plenum, 1977
- [27] Touloukian, Y.S., Kirby, R.K., Taylor, R.E. *Thermal conductivity: nonmetallic solids*. IFI/Plenum, 1970
- [28] Touloukian, Y.S., Kirby, R.K. Taylor, R.E., *Specific heat: nonmetallic solids*. IFI/Plenum, 1970, ISBN
- [29] http://www.rohmhaas.com/cvdmaterials/CVD_Sil_Carbide/CVD_Silicon_Carbide.html, 2006
- [30] Lawn, B. *Fracture of brittle solids*. 1st edition 1975, Cambridge University Press, Cambridge, 2nd edition 1993
- [31] Munz, D., Fett, T. *Ceramics: Mechanical Properties, Failure Behaviour, Materials Selection*. Springer Verlag, Heidelberg, 1999, ISBN 3-540-65376-7
- [32] Nestle, E., Westerheide, R. *The evolution of damage in ceramic materials for gas turbine applications under complex loading conditions*. Fraunhofer Institute for Mechanics of Materials, D-79108 Freiburg, Germany, 2000
- [33] Fischer-Cripps, A.C. *Introduction to contact mechanics*. Springer-Verlag Inc., New York, 2000, ISBN 0-387-98914-5
- [34] Auerbach, F. *Absolute Härtemessung*. Annalen der Physik und Chemie, vol. 43, 1891, pp. 61-100
- [35] Munro, R.G. *Material properties of a sintered alpha-SiC*. Journal of Physical and Chemical Reference Data, vol. 26, no.5, 1997, pp. 1195-1203
- [36] Dong, X., Jahanmir, S., Ives, L.K. *Wear transition diagram for Silicon Carbide*. Tribology International, vol. 28, no. 8, 1995, pp. 559 – 572
- [37] Yust, C.S., Carignan, F.J. *Observations on the sliding wear of ceramics*. ASLE Transactions, vol. 28, no. 2, 1984, pp. 245 – 252

- [38] Gee, M.G., Matharu, C.S., Almond, E.A., Eyre, T.S. *The measurement of sliding friction and wear of ceramics at high temperature*. Wear, vol. 138, 1990, pp. 169 – 187
- [39] Denape, J., Lamon, J. *Sliding friction of ceramics: mechanical action of the wear debris*. Journal of Materials Science, vol. 25, 1990, pp. 3592 – 3604
- [40] Takadoum, J., Zsiga, Z., Roques-Carmes, C. *Wear mechanism of silicon carbide: new observations*. Wear, vol. 174, 1994, pp. 239 – 242
- [41] Andersson, P., Blomberg, A. *Instability in the tribochemical wear of SiC in unlubricated sliding contacts*. Wear, vol. 174, 1994, pp. 1 – 7
- [42] Sasaki, S. *The effects of the surrounding atmosphere on the friction and wear of alumina, zirconia, silicon carbide and silicon nitride*. Wear, vol. 134, 1989, pp. 185 – 200
- [43] Miyoshi, K., Buckley, D.H. *Friction, deformation and fracture of single-crystal SiC*. ASLE Transactions, vol. 22, no. 1, 1977, pp. 79 – 90
- [44] Miyoshi, K., Buckley, D.H. *Friction and wear behaviour of single-crystal SiC in sliding contact with various metals*. ASLE Transactions, vol. 22, no. 3, 1978, pp. 245 – 256
- [45] Miyoshi, K., Buckley, D.H., Srinivasan, M. *Tribological properties of sintered polycrystalline and single-crystal silicon carbide*. American Ceramic Society Bulletin, vol. 62, no. 4, 1983, pp. 494 – 500
- [46] Stam, E. *Letter to M. van Veggel with subject: Static and dynamic coefficient of friction*. Reference no. MT-BRF-05-11232, April 4, 2005
- [47] Vukobratovich, D., Vukobratovich, S.M. *Introduction to opto-mechanical design*. Raytheon Systems Co., Tucson, Arizona, 2006
- [48] Bougoin, M. Presentation Boostec at TNO. 29 june 2006
- [49] Goela, J.S., Pickering, M.A., et al. *Chemical Vapor Deposited β -SiC for optics applications in severe environments*. Applied Optics, vol. 30, no. 22, 1991, pp. 3166 – 3175
- [50] Weber, M.J. *Handbook of optical materials*. CRC Press, Boca Raton, 2003, ISBN 0-8493-3512-4

-
- [51] Hasegawa, A., et al. *Critical issues and current status of SiC/SiC composites for fusion*. Journal of Nuclear Materials, vol. 283 – 287, 2000, pp. 128 – 137
- [52] Riccardi, B., et al. *Issues and advances of SiCf/SiC composites development for fusion reactors*. Journal of Nuclear Materials, vol. 329-333, 2004, pp. 56 – 65
- [53] Zinkle, S.J. *Fusion materials science: overview of challenges and recent progress*. Physics of Plasmas, vol. 12, Invited Tutorial 058101, 2005
- [54] Scholten, H.F. *Evaluation of multiaxial fracture models for technical ceramics*. PhD-thesis, Technische Universiteit Eindhoven, Eindhoven, 1993, ISBN 90-386-0192-1
- [55] Schwarcz, D., Keski-Ruha, R.A.M. *Efforts to control the EUV reflectance degradation of sputtered SiC films*. SPIE proceedings, vol. 2543, 1995, pp. 254 – 259
- [56] Onaka, T. et al. *Development of Lightweight Silicon Carbide Mirror at Cryogenic Temperatures for Infrared Imaging Surveyor (IRIS)*. 2004
- [57] Plummer, R., Bray, D. *Guidelines for design of SuperSiC® Silicon Carbide mirror substrates and precision components*. SPIE Proceedings, vol. 4771, 2002, pp. 265 – 275
- [58] Safa, F., Levallois, F., Bougoin, M., Castel, D. *Silicon Carbide technology for submillimetre space based telescopes*. Proceedings 48th International Astronautical Congress, Turin, 1997
- [59] Private communication with Fred Kamphues, TNO Science and Industry, 2006
- [60] Breidenthal, R.S., Galat-Skey, R., Geany, J.J. *Optical surfacing of one-meter class reaction bonded silicon carbide*. SPIE proc. Vol. 2543, 1995, pp. 248 – 253
- [61] Shih, C.J., Ezis, A. *The application of hot-pressed Silicon Carbide to large high-precision optical structures*. SPIE proc. Vol. 2543, 1995, pp. 24 – 37
- [62] Paquin, R.A. *Materials for mirror systems: an overview*. SPIE proc. vol. 2543, 1995, pp. 2 – 11
- [63] Fruit, M., et al. *Development of the SOFIA silicon carbide secondary mirror*. SPIE proc. vol. 4857, 2003, pp. 274 – 285

- [64] Gwo, D.-H. *Hydroxide-catalyzed bonding*. United States Patent no. US 6 548 176 B1, 2003
- [65] Gwo, D.-H. *Ultra-precision and reliable bonding method*. United States Patent no. US 6 284 085 B1, 2001
- [66] Rowan, S. Twyford, S.M. *Mechanical losses associated with the technique of hydroxide-catalysis bonding of fused silica*. Physics Letters A, vol. 246, 1998, pp. 471 – 478
- [67] Elliffe, E.J., Bogenstahl, J. et al. *Hydroxide-catalysis bonding for stable optical systems for space*. Classical and Quantum Gravity, vol. 22, 2005, pp. S257 – S267
- [68] Robertson, D., Killow, C., et al. *LTP interferometer – noise sources and performance*. Classical and Quantum Gravity, vol. 22, 2005, pp. S155 – S163
- [69] Heinzl, G., Braxmaier, C. et al. *Successful testing of the LISA Technology Package (LTP) interferometer engineering model*. Classical and Quantum Gravity, vol. 22, 2005, pp. S149 – S154

Chapter 3 – Optical design

- [70] Hecht, E. *Optics*. 4th ed, Addison-Wesley, Amsterdam, 2002, 1st ed. 1974, ISBN 0-8053-8566-5
- [71] F.Safa. *GAIA Interferometric Basic Angle Monitoring in Orbit*. Matra Marconi Space, internal report GAIA/MMS/TN/024.98, 1998
- [72] Kruizinga, B. *GAIA metrologie system*. TNO Science and Industry, internal report 2005, in Dutch

Chapter 4 – Optical benches

- [73] Mehta, P.K. *Flexural rigidity characteristics of light-weighted mirrors*. SPIE proceedings 748, no. 158, 1987, pp. 158 – 171
- [74] Barnes, W.P., Jr. *Optimal design of cored mirror structures*. Applied Optics, vol. 8, no. 6, 1969, pp. 1191 – 1196
- [75] Tobin, E., Magida, M. Kishner, S., Krim, M. *Design, fabrication and test of a meter-class reaction bonded SiC mirror blank*. SPIE proceedings, vol. 2543, 1995, pp. 12 – 21
- [76] Krödel, M., Kutter, G.S., Deyerler, M. *Short carbon-fiber reinforced ceramic – Cescic® – for optomechanical applications*. SPIE proceedings, vol. 4837, 2003, pp. 576 – 588

- [77] Kishner, S.J., Gardopee, G.J., Magida, M.B., Paquin, R.A. *Large stable mirrors: a comparison of glass, beryllium and silicon carbide*. SPIE proceedings vol. 1335, Dimensional Stability, 1990, pp. 127 – 139
- [78] Pearson, E., Stepp, L. *Response of large optical mirrors to thermal distributions*. SPIE proceedings, vol. 748, 1987, pp. 215 – 228
- [79] Paquin, R.A. *Dimensional stability: an overview*. SPIE proceedings, vol. 1335, 1990, pp. 2 – 19
- [80] Vukobratovich, D. *Rugged yet lightweight: how can we achieve both in optical instruments*. SPIE Critical Review 43, 1992, pp.18 – 60
- [81] Jacobs, S.F. *Variable invariables: dimensional stability with time and temperature*. SPIE Critical Review 43, 1992, pp. 181 – 204
- [82] Barnes, W.P. Jr. *Some effects of aerospace thermal environments on high-acuity optical systems*. Applied Optics, vol. 5, no. 5, 1966, pp. 701 – 712
- [83] Mehta, P.K. *Nonsymmetric thermal bowing of curved circular mirrors*. SPIE proceedings, vol. 748, 1987, pp. 187 – 205
- [84] Daryabeigi, K. *Heat transfer in adhesively bonded honeycomb core panels*. AIAA proceedings 2001 – 2825, 2001, pp. 1 – 10
- [85] Swann, R.T., Pittman, C.M. *Analysis of effective thermal conductivities of honeycomb-core and corrugated sandwich panels*. NASA technical note D-714, April 1961

Chapter 5 – Mounting of optical components

- [86] Johnson, K.L. *Contact Mechanics*. Cambridge University Press, London, 1985
- [87] Kropschot, R.H., Mikesell, R.P. *Strength and fatigue of glass at very low temperatures*. Journal of Applied Physics, vol. 28, no. 5, 1957, pp. 610 – 614
- [88] Schouten, C.H., Rosielle, P.C.J.N., Schellekens, P.H.J. *Design of a kinematic coupling for precision applications*. Precision Engineering, vol. 20, 1997, pp. 46 – 52

Chapter 6 – Experiments

- [89] Kamphues, F., *Test Report Beamsplitters*. Internal report TNO Science and Industry, TNO-GAIA-BAM-REP-005, 2006

- [90] ASTM norm C 1161-2C. *Standard test method for flexural strength of advanced ceramics at ambient temperature*. ASTM international, USA, 2006

Chapter 7 – Conclusions and recommendations

- [91] Veggel, A.A. van, et al. *Experimental set-up for testing alignment and measurement stability of a metrology system in Silicon Carbide for GAIA*. SPIE proceedings 5877-1, 2005, pp. 1 – 12
- [92] Private communication with Jim Hough and Sheila Rowan, University of Glasgow, November 2006

Appendix A – Additional material properties

- [93] Odegard, B.C., Thompson, A.W., *Low temperature creep of Ti-6Al-4V*, Metallurgical Transactions, vol. 5, 1974, pp. 1207 – 1213

Appendix D – Rolling kinematic couplings

- [94] Slocum, A.H. *Kinematic couplings for precision fixturing – Part 1: Formulation of design parameters*. Precision Engineering, vol. 10, no. 2, pp. 85 – 91, 1988
- [95] Slocum, A.H., Donmez, A. *Kinematic couplings for precision fixturing – Part 2: Experimental determination of repeatability and stiffness*. Precision Engineering, vol. 10, no. 3, 1988, pp. 115 – 122
- [96] Slocum, A.H. *Design of three-groove kinematic couplings*. Precision Engineering, vol. 14, no. 2, 1992, pp. 67 – 76
- [97] Schmiechen, P., Slocum, A.H. *Analysis of kinematic systems: a generalized approach*. Precision Engineering, vol. 19, 1996, pp. 11 – 18
- [98] Hale, L.C., Slocum, A.H. *Optimal design techniques for kinematic couplings*. Precision Engineering, vol. 25, 2001, pp. 114 – 127
- [99] Hart, A.J., Slocum, A.H., Willoughby, P. *Kinematic coupling interchangeability*. Precision Engineering, vol. 28, 2004, pp. 1 – 15
- [100] O'Connor, J.J., Johnson, K.L. *The role of surface asperities in transmitting tangential forces between metals*. Wear, vol. 6, 1963, pp. 118 – 139
- [101] Barraja, M., Vallance, R. *Tolerancing kinematic couplings*. Precision Engineering, vol. 29, 2005, pp. 101 – 112

- [102] Culpepper, M.L. *Design of quasi-kinematic couplings*. Precision Engineering, vol. 28, 2004, pp. 338 – 357

Appendix E – Thermal contact conductance

- [103] Madhusudana, C.V. *Thermal contact conductance*. Mechanical Engineering Series, Springer-Verlag, New-York, ISBN 0-387-94534-2, 1995
- [104] Incropera, F.P., DeWitt, D.P. *Fundamentals of heat and mass transfer*. 5th edition, Wiley, Chichester, 1st edition 1988, ISBN 0-471-38650-2, 2001
- [105] Gilmore, D.G. *Spacecraft thermal control handbook*. 2nd edition, The Aerospace Press, El Segundo, California, ISBN 1-884989-11-X (v. 1), 2002
- [106] Mikic, B.B. *Thermal contact conductance; theoretical considerations*. International Journal of Heat and Mass Transfer, vol. 17, no.2, 1974, pp. 205 – 214
- [107] Clausing, A.M., Chao, B.T. *Thermal contact resistance in a vacuum environment*. Journal of Heat Transfer, May 1965, pp. 243 – 251
- [108] Yovanovich, M.M. *Overall constriction resistance between contacting rough, wavy surfaces*. International Journal of Mass and Heat Transfer, vol. 12, 1969, pp. 1517 – 1520
- [109] Bejan, A., Kraus, A.D. *Heat transfer handbook*. Chapter 4, Thermal spreading and contact resistances, Yovanovich, M.M., Marotta, E.E., 1st ed. 1948, John Wiley & Sons, Inc., Hoboken, New Jersey, 2003
- [110] Bahrami, M., Culham, J.R., Yovanovich, M.M., Schneider, G.E. *Thermal contact resistance of nonconforming rough surfaces, part 1: contact mechanics model*. Journal of Thermophysics and Heat Transfer, vol. 18, no. 2, 2004, pp. 209 – 217
- [111] Bahrami, M., Culham, J.R., Yovanovich, M.M., Schneider, G.E. *Thermal contact resistance of nonconforming surfaces, part 2: thermal model*. Journal of Thermophysics and Heat Transfer, vol. 18, no. 2, 2004, pp. 218 – 227
- [112] Bahrami, M., Yovanovich, M.M., Culham, J.R. *Thermal joint resistances of nonconforming rough surfaces with gas-filled gaps*. Journal of Thermophysics and Heat Transfer, vol. 18, no. 3, 2004, pp. 326 – 332

- [113] Bahrami, M., Yovanovich, M.M., Marotta, E.E. *Modeling of thermal joint resistance of polymer-metal rough interfaces*. Proceedings of IMECE 2004, ASME International Mechanical Engineering Congress, Anaheim, CA, USA, paper IMECE2004-60131

Summary

GAIA is an ESA satellite (to be launched around 2011) which will make a map of the Galaxy with an accuracy of 5 micro-arcseconds (μas). This map will be made with two telescopes with viewing directions in a basic angle of 106° . The measured positions of stars in both telescopes must be linked using a Basic Angle Monitoring (BAM) system by measuring the variations of the basic angle with an accuracy of $0.5 \mu\text{as}$.

Three steps are taken to reach the required stability:

- GAIA operates in the Lagrange 2 point of the Sun and Earth;
- The BAM system is made of Silicon Carbide (SiC);
- The opto-thermo-mechanical design is made according to design principles.

The thesis has focused on the integration of mechanical design principles with the use of SiC as constructive material for the BAM system. Four main topics have been addressed to achieve this: the properties and possibilities of SiC, the optical design, the optical bench design and the design of the optical components.

Two types of SiC are considered: carbon felt SiC and sintered SiC. The possibilities of both materials are similar: in both the shape is machined in the green material before Si-infiltration or sintering.

The optical design must have specific properties to make the BAM system the least sensitive to relative rotation of the BAM optical benches: e.g. the interfering beams must be parallel and the optical path length difference (OPD) between interfering beams must be zero.

The sensitivity analysis leads to requirements on the stability after launch vibrations and cool-down and on the stability during actual 6 hour measurements. These are called alignment stability and measurement stability respectively. The alignment stability requirement for the OPD is $\pm 5 \mu\text{m}$ and for the tilt angle it is $\pm 6 \mu\text{rad}$. The measurement stability requirements are $\pm 0.65 \text{ pm}$ and $\pm 0.16 \mu\text{rad}$, respectively for the OPD and for the tilt angle.

The optical bench design must be a closed back honeycomb structure to provide an optimal stiffness to weight ratio. It is isostatically mounted onto the payload-module optical bench.

Thermal analysis of the optical bench shows that the alignment stability is threatened by spatial variations of the coefficient of thermal expansion. Based on a 0.1 mK thermal variation, measurement stability requirements are exceeded by far.

For mounting the optical components a mechanical clamping solution has been chosen in favor of other joining methods like hydroxide catalysis bonding. Mounting in the plane of light provides a better measurement stability than mounting on the reflective surface of the component. However, the design of mounting on the reflective surface is considered to be simpler and the probability of maintaining alignment stability through launch and cool-down is considered to be significantly larger.

Beamsplitters mounted on their reflective surface have been manufactured to test the alignment stability. Experiments show that the alignment stability is close to the required $1.2 \mu\text{rad}$, but is slightly higher due to abrasion of the contact points. Improvement can be obtained by increasing the clamping force.

Hydroxide catalysis bonding has been tested for experience and strength because it is still a highly experimental but also promising technique for stable bonding of SiC parts. The bonding itself has been conducted with reasonable success; however the sawing for the preparation of bending of the bars caused failure of many samples. The maximum strength that has been measured on the remaining samples is 30 N mm^{-2} .

Samenvatting

GAIA is een ESA satelliet (lancering rond 2011), die een kaart zal maken van de Melkweg met een nauwkeurigheid van ± 5 microboogseconden (μas). Deze kaart wordt met twee telescopen gemaakt met kijkrichtingen onder een basishoek van 106° . De sterposities, gemeten door beide telescopen, worden verbonden met het Basic Angle Monitoring (BAM) systeem door het meten van de variaties van de basishoek met $\pm 0.5 \mu\text{as}$.

Drie stappen zijn nodig om te komen tot voldoende stabiliteit:

- GAIA opereert in het Lagrange 2 punt van de Zon en Aarde;
- Het BAM systeem wordt gemaakt van Silicium Carbide (SiC);
- Opto-thermo-mechanisch ontwerp met ontwerp principes.

Het proefschrift is gericht op de integratie van mechanische ontwerp principes met het gebruik van SiC als constructief materiaal voor het BAM systeem.

Vier hoofdonderwerpen zijn daarbij bestudeerd: de eigenschappen en mogelijkheden van SiC, het optische ontwerp, het ontwerp van de optische banken en van de optische componenten.

Twee soorten SiC zijn in overweging genomen: koolstof vilt SiC en gesinterd SiC. De mogelijkheden van beide materialen zijn vergelijkbaar, omdat bij beiden de vorm gefreesd wordt voorafgaande aan Si-infiltratie of sinteren.

Het optische ontwerp moet specifieke eigenschappen hebben om het BAM systeem zo ongevoelig mogelijk te maken voor de relatieve rotatie van de optische banken: de interfererende bundels moeten parallel zijn en het optisch padlengte verschil (OPD) tussen interfererende bundels moet nul zijn.

De gevoeligheidsanalyse leidt tot eisen op de stabiliteit ten aanzien van de lancering en het afkoeltraject en van 6-uurs metingen. Deze eisen worden respectievelijk eisen op de uitlijnstabiliteit en op de meetstabiliteit genoemd. De vereiste uitlijnstabiliteit van het OPD is bepaald op $\pm 5 \mu\text{m}$ en van de tilthoek op $\pm 6 \mu\text{rad}$. De vereiste meetstabiliteit van het OPD en van de tilthoek is respectievelijk $\pm 0.65 \mu\text{m}$ en $\pm 0.16 \mu\text{rad}$.

De optische tafels moeten gesloten honingraat structuren zijn voor een optimale stijfheid-massa verhouding. Ze worden isostatisch opgehangen aan de optische tafel van de payload module.

Thermisch analyse van de optisch tafels laat zien dat de uitlijnstabiliteit in gevaar is door ruimtelijke variaties op de uitzettingscoëfficiënt. Gebaseerd op 0.1 mK thermische variatie, worden de meet-stabiliteitseisen ruim overschreden.

Een mechanische aanspanmethode is gekozen voor het monteren van optische componenten boven andere verbindingstechnieken zoals hydroxide catalysis bonding. Monteren in het vlak van het licht levert betere meetstabiliteit dan monteren op het reflecterende oppervlak van de component. Echter, het ontwerp van een component gemonteerd op het reflecterende oppervlak is eenvoudiger en de kans dat de uitlijnstabiliteit na lancering en afkoeling bewaard blijft, wordt groter geacht.

Beamsplitters, die op het reflecterende oppervlak zijn gemonteerd zijn geproduceerd om hun uitlijnstabiliteit te testen. De resultaten laten zien dat de uitlijnstabiliteit dicht bij de vereiste $1.2 \mu\text{rad}$ is, maar er iets boven zit door slijtage van de contactpunten. Een verbetering kan naar verwachting optreden door de aanspankracht te verhogen.

Hydroxide catalysis bonding is getest voor sterktemetingen, omdat het nog een experimentele techniek is, maar ook een goede optie voor het stabiel verbinden van SiC delen. Het verbinden op zich is redelijk succesvol verlopen, echter bij het zagen van staafjes voor de buigproeven zijn veel verbindingen gebroken. Sterkteproeven op de overgebleven proefstukken wezen een maximale sterkte van 30 N mm^{-2} uit.

Curriculum vitae

Mariëlle van Veggel was born in Deurne (the Netherlands) on 7 March 1979. She attended the Sint Willibrord Gymnasium in Deurne and received her VWO degree there in 1997. She started her study of Mechanical Engineering at the Technische Universiteit Eindhoven. In 2001 she worked on her internship at the Nationaal Lucht- en Ruimtevaart Laboratorium on “Analysis of controllers for the airconditioning system of aircraft”. In 2002, back in Eindhoven, she started her Master’s Project in the group Dynamics and Control on “Experimental dynamic modeling of a drill-string set-up”. In March 2003 she obtained her Master’s degree. Immediately, she started her Ph.D. project in the same group on “The Basic Angle Monitoring system: picometer stability with Silicon Carbide optics”. The project has been sponsored by the Netherlands Agency for Aerospace Programmes (NIVR) and conducted in close cooperation with TNO Science and Industry in Delft, resulting in this thesis.